



National Library
of Canada

Acquisitions and
Bibliographic Services Branch

395 Wellington Street
Ottawa, Ontario
K1A 0N4

Bibliothèque nationale
du Canada

Direction des acquisitions et
des services bibliographiques

395, rue Wellington
Ottawa (Ontario)
K1A 0N4

Your file Votre référence

Our file Notre référence

NOTICE

The quality of this microform is heavily dependent upon the quality of the original thesis submitted for microfilming. Every effort has been made to ensure the highest quality of reproduction possible.

If pages are missing, contact the university which granted the degree.

Some pages may have indistinct print especially if the original pages were typed with a poor typewriter ribbon or if the university sent us an inferior photocopy.

Reproduction in full or in part of this microform is governed by the Canadian Copyright Act, R.S.C. 1970, c. C-30, and subsequent amendments.

AVIS

La qualité de cette microforme dépend grandement de la qualité de la thèse soumise au microfilmage. Nous avons tout fait pour assurer une qualité supérieure de reproduction.

S'il manque des pages, veuillez communiquer avec l'université qui a conféré le grade.

La qualité d'impression de certaines pages peut laisser à désirer, surtout si les pages originales ont été dactylographiées à l'aide d'un ruban usé ou si l'université nous a fait parvenir une photocopie de qualité inférieure.

La reproduction, même partielle, de cette microforme est soumise à la Loi canadienne sur le droit d'auteur, SRC 1970, c. C-30, et ses amendements subséquents.

UNIVERSITY OF ALBERTA

FLOW OF EMULSIONS IN POROUS MEDIA

by



FUENGLARB KHAMBHARATANA

A THESIS SUBMITTED TO
THE FACULTY OF GRADUATE STUDIES AND RESEARCH
IN PARTIAL FULFILLMENT OF THE REQUIREMENTS
FOR THE DEGREE OF
DOCTOR OF PHILOSOPHY
IN
PETROLEUM ENGINEERING

DEPARTMENT OF MINING, METALLURGICAL AND PETROLEUM
ENGINEERING

EDMONTON, ALBERTA

SPRING, 1993



National Library
of Canada

Acquisitions and
Bibliographic Services Branch

395 Wellington Street
Ottawa, Ontario
K1A 0N4

Bibliothèque nationale
du Canada

Direction des acquisitions et
des services bibliographiques

395, rue Wellington
Ottawa (Ontario)
K1A 0N4

Your file Votre référence

Our file Notre référence

The author has granted an irrevocable non-exclusive licence allowing the National Library of Canada to reproduce, loan, distribute or sell copies of his/her thesis by any means and in any form or format, making this thesis available to interested persons.

L'auteur a accordé une licence irrévocable et non exclusive permettant à la Bibliothèque nationale du Canada de reproduire, prêter, distribuer ou vendre des copies de sa thèse de quelque manière et sous quelque forme que ce soit pour mettre des exemplaires de cette thèse à la disposition des personnes intéressées.

The author retains ownership of the copyright in his/her thesis. Neither the thesis nor substantial extracts from it may be printed or otherwise reproduced without his/her permission.

L'auteur conserve la propriété du droit d'auteur qui protège sa thèse. Ni la thèse ni des extraits substantiels de celle-ci ne doivent être imprimés ou autrement reproduits sans son autorisation.

ISBN 0-315-82071-3

UNIVERSITY OF ALBERTA

RELEASE FORM

NAME OF AUTHOR Fuenglarb Khambharatana

TITLE OF THESIS Flow of Emulsions in Porous Media

DEGREE FOR WHICH THESIS WAS PRESENTED DOCTOR OF PHILOSOPHY

YEAR THIS DEGREE WAS GRANTED SPRING, 1993

Permission is hereby granted to THE UNIVERSITY OF ALBERTA LIBRARY to reproduce single copies of this thesis and to lend or sell such copies for private, scholarly or scientific research purposes only.

The author reserves other publication rights, and neither the thesis nor extensive extracts from it may be printed or otherwise reproduced without the author's written permission.

(SIGNED) *Fuenglarb Khambharatana*

PERMANENT ADDRESS:

273 Soi 3 Navatani
Bangkok
Thailand

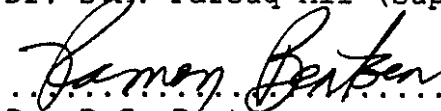
DATED *Dec. 31, 1992*


UNIVERSITY OF ALBERTA

FACULTY OF GRADUATE STUDIES AND RESEARCH

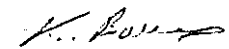
The undersigned certify that they have read and recommend to the Faculty of Graduate Studies and Research, for acceptance, a thesis entitled FLOW OF EMULSIONS IN POROUS MEDIA by Fuenglarb Khambharatana in partial fulfillment of the requirements for the degree of Doctor of Philosophy in Petroleum Engineering.



.....
Dr. S.M. Farouq Ali (Supervisor)

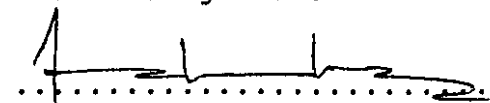

.....
Dr. R.G. Bentsen


.....
Dr. A.K. Ambastha


.....
Dr. W.S. Tortike


.....
Dr. K. Barron


.....
Dr. M.N. Oguztoreli


.....
Dr. A. Chakma (External Examiner)

DATED Nov. 27, 92

To My Parents

and

To My Grandmother

for their love and support

ABSTRACT

Emulsions constitute an important part of all EOR methods, yet the mathematical modelling of emulsions is still largely empirical. This is due to the lack of physical as well as mathematical descriptions of emulsion flow. This research addresses both aspects of this problem. Experimental work was first carried out to observe the physical mechanisms that occur when a stable emulsion flows in a porous medium. More comprehensive work was done on emulsion rheology and droplet capture for different kinds of emulsion flow in two types of porous media, especially for the system of comparable drop and pore sizes. The results show that the change in emulsion rheology in a porous medium has an overall trend similar to that in a viscometer for the shear rates of interest. Furthermore, the emulsion droplets were found to be captured according to a filtration process. These mechanisms were then represented mathematically and incorporated into a one-dimensional, three-phase (oleic, aqueous, and emulsion) model which accounts for interactions of a surfactant, oil, water, and the rock matrix. The developed model was used to simulate linear core floods of stable emulsions. Simulated and experimental production histories were compared. It was found that a multiphase, non-Newtonian rheological model of an emulsion with interfacial tension-dependent relative permeabilities and time-dependent capture gave the best predictions of the simulations of the experimental core floods.

ACKNOWLEDGEMENTS

I would like to thank Dr. S.M. Farouq Ali for his supervision, thoughtful guidance, and encouragement throughout my work.

I would also like to thank the examining committee for their helpful suggestions for improving the thesis.

I must also express my appreciation for the help provided by Sara Thomas whose expertise was invaluable in the completion of the core flood experiments.

I wish to extend my gratitude to Brian Doell and Ryan Zabel for their assistance in the completion of this work.

Finally, I would like to thank the Canadian International Development Agency (CIDA) and the Alberta Oil Sands Technology and Research Authority (AOSTRA) for their generous financial support.

TABLE OF CONTENTS

CHAPTER.....	PAGE
1. INTRODUCTION	1
2. REVIEW OF THE LITERATURE	3
2.1 Emulsions and Their Applications in Oil Recovery	3
2.2 Experimental and Field Studies on Emulsion Properties and Flow Mechanisms	6
2.3 Mathematical Modeling of Emulsion Flow in Porous Media.....	13
3.STATEMENT OF THE PROBLEM.....	22
4. EXPERIMENTAL WORK.....	23
4.1 Experimental Apparatus.....	23
4.2 Porous Medium Preparation and Determination of Its Properties	25
4.3 Emulsion Preparation and Characterization	29
4.3.1 Caustic Emulsions.....	30
4.3.1.1 Method of Preparation	30
4.3.1.2 Characterization of Emulsions.....	32
A. Quality.....	32
B. Rheological Behaviour of Emulsions..	32
C. Drop Size Distribution.....	35
4.3.2 Surfactant Emulsions.....	35
4.3.2.1 Petrostep Emulsions.....	38

A. Method of Preparation.....	38
B. Characterization of Emulsion S9T'...	39
B.1 Quality of Emulsion S9T'	39
B.2 Rheological Behaviour of Emulsion S9T'	39
B.3 Drop Size Distribution of Emulsion S9T'	41
C. Characterization of Emulsion S9B'...	41
C.1 Rheological Behaviour of Emulsion S9B'	41
C.2 Drop Size Distribution of S9B'	41
D. Characterization of Emulsion S10B...	41
4.3.2.2 SD1000 Emulsions.....	44
A. Preparation and Characterization....	44
4.4 Core Displacement Tests	47
4.4.1 Experimental Core Floods to Observe Rheological and Filtration Behaviour	47
4.4.1.1 Caustic Emulsion Floods.....	52
A. General Flood Description.....	52
B. Results.....	53
4.4.1.2 Surfactant Emulsion Floods.....	62
A. Flood Description.....	62
B. Results for Emulsion S9T' and S9B'	64
C. Results for Emulsion S10B.....	69
D. Results for Emulsion H3.....	75
4.4.2 Experimental Core Flood to Obtain Surfactant Recovery and Surfactant Adsorption on Porous Media	76

A. Flood Description of Emulsion H4	76
B. Flood Description of Emulsion H5	77
C. Results for Emulsions H4 and H5	78
4.4.3 Oil Recovery Experiments	81
4.4.3.1 Caustic Emulsion H2.....	81
4.4.3.2 Surfactant Emulsion H5.....	87
5. DEVELOPMENT OF THE MATHEMATICAL MODEL.....	96
5.1 Simulator Assumptions	96
5.2 Formulation of the Problem	97
5.3 Initial and Boundary Conditions.....	100
5.4 Flow Mechanisms During Oil Displacement by Emulsion Flooding.....	104
5.4.1 Emulsion Rheological Behaviour	108
5.4.2 Three-Phase Relative Permeabilities	113
5.4.2.1 Naar-Wygal-Henderson Model.....	113
5.4.2.2 Pope's Model.....	113
A. Interfacial Tensions	114
B. Residual Saturations.....	114
C. Relative Permeabilities.....	117
5.4.3 Adsorption	119
5.4.4 Droplet Capture.....	121
5.4.4.1 No Re-entrainment.....	121
5.4.4.2 With Re-entrainment.....	123
6.DEVELOPMENT OF THE COMPUTER MODEL	126
6.1 Main Program	126

6.2	Subroutine INPUT	132
6.3	Subroutine INIT	132
6.4	Subroutine PRINP	132
6.5	Subroutine TRANSC	133
6.6	Subroutine TRANS	133
6.7	Subroutine DISP	134
6.8	Subroutine PROP	134
6.9	Subroutine RATE	135
6.10	Subroutine ACCOEF	135
6.11	Subroutine RTERM	135
6.12	Subroutine TRIAN	135
6.13	Subroutine COEFFP	135
6.14	Subroutine MATRIX, DLSARG, CONVRT	135
6.15	Subroutine QPROD	136
6.16	Subroutine UPDATE	136
6.17	Subroutine PROUT, TABLE2	136
7.	RESULTS AND DISCUSSION	137
7.1	Validating the Simulator	137
7.1.1	Effect of Different Emulsion Viscosity Correlations	138
7.1.2	Effect of Different Relative Permeability Correlations	153
7.1.3	Effect of Oleic and Aqueous Relative Permeabilities and Emulsion Rheological Behaviour	159
7.1.4	Effect of Different Droplet Capture Models	161

7.1.5	Effect of Multiphase Emulsion Rheological Behaviour and Emulsion Relative Permeability	177
7.1.6	Effect of Droplet Capture Mechanism and Permeability Reduction.....	181
7.2	Sensitivity Study.....	192
7.2.1	Sensitivity Study of Injection Pressure.....	192
7.2.2	Sensitivity Study of Total Oleic Recovery.....	194
7.2.3	Sensitivity Study of Emulsion Breakthrough Time.....	197
8.	CONCLUSIONS	201
	REFERENCES	203
APPENDIX A:	Estimation of the Partition Coefficients of Each Component Between Phases.....	210
A.1	Sequence of Injection.....	210
A.2	Composition of Injected Emulsion H4....	210
A.3	Analysis of the Aqueous Phase During Waterflooding for Surfactant Content...	210
A.4	Calculation of the Partition Coefficient.....	211
APPENDIX B:	Mathematical Development of Flow Equations...	213
APPENDIX C:	Expansion of the Accumulation Terms in the Mass Balance Equation.....	216
C.1	Expansion of the Common Flowing (FLU _i) Term.....	217
C.2	Expansion of Adsorption (ADSP _S) Term.....	223
C.3	Expansion of Capture (CAPT _i) Term.....	224

C.3.1	Instantaneous Capture	224
C.3.2	Time-dependent Capture	225
APPENDIX D:	Expansion of the Remainder (R_i) Terms	228
D.1	Transmissibility Terms	234
D.2	Dispersion Terms	235
APPENDIX E:	Mass Fraction Constraint Expansion	237
APPENDIX F:	System of Equations and Solution	239
APPENDIX G:	Definition of Coefficients	248
APPENDIX H:	Estimation of Rheological Parameters	253
APPENDIX I:	Derivation of Single Phase non-Newtonian Rheological Model	255
I.1	Flow of Fluids Through Capillary Tubes	255
I.2	Flow of Fluids Through Porous Media	256

LIST OF TABLES

TABLE	PAGE
4.1	Capillary Pressure Curve Data for Berea Sandstone .26
4.2	Pore Size Distribution Data of Berea Sandstone28
4.3	Properties of the Horsefly Crude29
4.4	Rheological Data for Emulsions H1 and H233
4.5	Drop Size Distribution Data of Emulsion H136
4.6	Composition of Surfactant Emulsions47
4.7	Summary of Selected Core Floods Between 1-2149
4.8	Summary of Core Floods 23, 24, & 2550
4.9	Summary of Core Floods 27-3151
4.10	Characteristics of Injected and Produced Caustic Emulsions57
4.11	Drop-Size Distribution of Injected and Produced Emulsions S9B' (CF #19)66
4.12	Comparison of the K-values Obtained from Different Core Floods80
7.1	Simulation Input Data for Run 5/1 - 5/8139
7.2	Simulation Input Parameters for Run 5/2148
7.3	Simulation Input Parameters for Run 5/3155
7.4	Simulation Input Parameters for Run 5/4162
7.5	Simulation Input Parameters for Run 5/5166
7.6	Simulation Input Parameters for Run 5/6171
7.7	Simulation Input Parameters for Run 5/7179
7.8	Simulation Input Parameters for Run 5/8190

LIST OF FIGURES

FIGURE	PAGE
4.1	Schematic of Core Displacement Apparatus.....24
4.2	Capillary Pressure Curve of Berea Sandstone.....27
4.3	Log-Probability Plot of Berea Sandstone Pore Size Distribution.....27
4.4	Rheological Behaviour of Emulsion H1.....34
4.5	Rheological Behaviour of Emulsion H2.....34
4.6	Log-Probability Plot of Drop Size Distribution of Emulsion H1 (Batch 2).....37
4.7	Log-Probability Plot of Drop Size Distribution of Emulsion H2 (Batch 2).....37
4.8	Rheological Behaviour of Emulsion S9T'.....40
4.9	Log-Probability Plot of Drop Size Distribution of Emulsion S9T'.....40
4.10	Rheological Behaviour of Emulsion S9B'.....42
4.11	Log-Probability Plot of Drop Size Distribution of Emulsion S9B'.....42
4.12	Rheological Behaviour of Emulsion S10B.....43
4.13	Log-Probability Plot of Drop Size Distribution of Emulsion S10B.....43
4.14	Rheological Behaviour of Emulsion H3.....46
4.15	Rheological Behaviour of Emulsion H4.....46
4.16	Rheological Behaviour of Emulsion H5.....46
4.17	Summary Chart of the Selected Experiments.....48
4.18	Rheological Behaviour of Emulsion H1 (Batch 1) in Viscometer and in Porous Medium (CF #1 Sand Pack).....54

4.19	Rheological Behaviour of Emulsion H1 (Batch 2) in Viscometer and in Porous Medium (CF #9 Berea Sandstone).....	54
4.20	Rheological Behaviour of Emulsion H2 (Batch 1) in Viscometer and in Porous Medium (CF #2 Sand Pack).....	56
4.21	Rheological Behaviour of Emulsion H2 (Batch 2) in Viscometer and in Porous Medium (CF #11 Berea Sandstone).....	56
4.22	Log-Probability Plot of Drop Size Distribution of Produced Emulsion H2 at Low Flow Rate (CF #11).....	61
4.23	Log-Probability Plot of Drop Size Distribution of Produced Emulsion H2 at High Flow Rate (CF #11).....	61
4.24	Rheological Behaviour of Emulsion S9B' in Viscometer and in Porous Medium (CF #19 Fired Berea Sandstone).....	65
4.25	Rheological Behaviour of Emulsion S9T' in Viscometer and in Porous Medium (CF #20 Fired Berea Sandstone).....	65
4.26	Rheological Behaviour of Injected and Produced Emulsion S9T' (CF #20 Fired Berea Sandstone).....	68
4.27	Rheological Behaviour of Injected and Produced Emulsion S10B (CF #21 Unfired Berea Sandstone)....	68
4.28	Rheological Behaviour of Emulsion S10B in Viscometer and in Porous Medium (CF #21 Unfired Berea Sandstone).....	70
4.29	Log-Probability Plot of Drop Size Distribution of Produced Emulsion S10B at Flow Rate of 320 ml/hr.....	72
4.30	Log-Probability Plot of Drop Size Distribution of Produced Emulsion S10B at Flow Rate of 360 ml/hr	72
4.31	Log-Probability Plot of Drop Size Distribution of Produced Emulsion S10B at Flow Rate of 400 ml/hr	73

4.32	Loss of Surfactant to Porous Medium at Different Slug Sizes (CF #23, 24, 25)	79
4.33	Production History for Core Flood #4 Emulsion Flood at Secondary Stage	83
4.34	Production History for Core Flood #5 Emulsion Flood at Tertiary Stage	85
4.35	Production History for Core Flood #27 Waterflood Followed by Emulsion and Waterflood (Emulsion Slug Size = 0.2 PV)	89
4.36	Production History for Core Flood #28 Emulsion Followed by Waterflood (Emulsion Slug Size = 0.2 PV)	90
4.37	Production History for Core Flood #30 Emulsion Followed by Waterflood (Emulsion Slug Size = 0.1 PV)	91
4.38	Production History for Core Flood #31 Waterflood Followed by Emulsion and Waterflood (Emulsion Slug Size = 0.1 PV)	92
4.39	Effect of an Emulsion Slug Prior to Waterflood on Waterflood Recovery	94
6.1	Computer Program Flow Diagram	127
7.1	Comparison of Experimental and Simulated Injection Pressure History for Run 5/1 for Emulsion Flooding	140
7.2	Comparison of Experimental and Simulated Cumulative Oleic Recovery History for Run 5/1 for Emulsion Flooding	140
7.3	Comparison of Experimental and Simulated Oleic Phase Cut History for Run 5/1 for Emulsion Flooding	141
7.4	Comparison of Experimental and Simulated Aqueous Phase Cut History for Run 5/1 for Emulsion Flooding	141
7.5	Comparison of Experimental and Simulated Emulsion Phase Cut History for Run 5/1 for Emulsion Flooding	141

7.6	Simulated Saturation History at Production Block for Run 5/1	144
7.7	Simulated Saturation Profile for Run 5/1 at 0.1067 PV Injected	145
7.8	Simulated Saturation Profile for Run 5/1 at 0.1997 PV Injected	145
7.9	Simulated Saturation Profile for Run 5/1 at 0.3920 PV Injected	145
7.10	Simulated Saturation Profile for Run 5/1 at 0.6054 PV Injected	145
7.11	Oleic Relative Permeability vs. Oleic for Run 5/1	146
7.12	Aqueous Relative Permeability vs. Aqueous for Run 5/1	146
7.13	Emulsion Relative Permeability vs. Emulsion for Run 5/1	146
7.14	Comparison of Experimental and Simulated Injection Pressure History for Run 5/2 for Emulsion Flooding	149
7.15	Comparison of Experimental and Simulated Cumulative Oleic Recovery History for Run 5/2 for Emulsion Flooding	149
7.16	Comparison of Experimental and Simulated Oleic Phase Cut History for Run 5/2 for Emulsion Flooding	150
7.17	Comparison of Experimental and Simulated Aqueous Phase Cut History for Run 5/2 for Emulsion Flooding	150
7.18	Comparison of Experimental and Simulated Emulsion Phase Cut History for Run 5/2 for Emulsion Flooding	150
7.19	Simulated Saturation History at Production Block for Run 5/2	151
7.20	Simulated Saturation Profile for Run 5/2 at 0.1992 PV Injected.....	152

7.21	Simulated Saturation Profile for Run 5/2 at 0.5018 PV Injected.....	152
7.22	Simulated Saturation Profile for Run 5/2 at 0.8058 PV Injected.....	152
7.23	Simulated Saturation Profile for Run 5/2 at 0.9997 PV Injected.....	152
7.24	Comparison of Experimental and Simulated Injection Pressure History for Run 5/3 for Emulsion Flooding	156
7.25	Comparison of Experimental and Simulated Cumulative Oleic Recovery History for Run 5/3 for Emulsion Flooding	156
7.26	Comparison of Experimental and Simulated Oleic Phase Cut History for Run 5/3 for Emulsion Flooding	157
7.27	Comparison of Experimental and Simulated Aqueous Phase Cut History for Run 5/3 for Emulsion Flooding	157
7.28	Comparison of Experimental and Simulated Emulsion Phase Cut History for Run 5/3 for Emulsion Flooding	157
7.29	Simulated Saturation History at Production Block for Run 5/3	158
7.30	Simulated Saturation Profile for Run 5/3 at 0.1076 PV Injected	158
7.31	Simulated Saturation Profile for Run 5/3 at 0.3986 PV Injected	158
7.32	Simulated Saturation Profile for Run 5/3 at 0.8059 PV Injected	158
7.33	Comparison of Oleic Relative Permeability Predicted by Naar-Wygal-Henderson Model and Pope's Model.....	160
7.34	Comparison of Aqueous Relative Permeability Predicted by Naar-Wygal-Henderson Model and Pope's Model	160

7.35	Comparison of Emulsion Relative Permeability Predicted by Naar-Wygal-Henderson Model and Pope's Model	160
7.36	Comparison of Experimental and Simulated Injection Pressure History for Run 5/4 for Emulsion Flooding	163
7.37	Comparison of Experimental and Simulated Cumulative Oleic Recovery History for Run 5/4 for Emulsion Flooding	163
7.38	Comparison of Experimental and Simulated Oleic Phase Cut History for Run 5/4 for Emulsion Flooding	164
7.39	Comparison of Experimental and Simulated Aqueous Phase Cut History for Run 5/4 for Emulsion Flooding	164
7.40	Comparison of Experimental and Simulated Emulsion Phase Cut History for Run 5/4 for Emulsion Flooding	164
7.41	Simulated Saturation History at Production Block for Run 5/4	165
7.42	Simulated Saturation Profile for Run 5/4 at 0.0914 PV Injected	165
7.43	Simulated Saturation Profile for Run 5/4 at 0.3963 PV Injected	165
7.44	Simulated Saturation Profile for Run 5/4 at 0.9031 PV Injected	165
7.45	Comparison of Experimental and Simulated Injection Pressure History for Run 5/5 for Emulsion Flooding	167
7.46	Comparison of Experimental and Simulated Cumulative Oleic Recovery History for Run 5/5 for Emulsion Flooding	167
7.47	Comparison of Experimental and Simulated Oleic Phase Cut History for Run 5/5 for Emulsion Flooding	168
7.48	Comparison of Experimental and Simulated Aqueous Phase Cut History for Run 5/5 for Emulsion Flooding	168

7.49	Comparison of Experimental and Simulated Emulsion Phase Cut History for Run 5/5 for Emulsion Flooding	168
7.50	Simulated Saturation History at Production Block for Run 5/5	169
7.51	Comparison of Experimental and Simulated Injection Pressure History for Run 5/6 for Emulsion Flooding	173
7.52	Comparison of Experimental and Simulated Injection Pressure Histories for Runs 5/4 and 5/6 for Emulsion Flooding	173
7.53	Comparison of Experimental and Simulated Cumulative Oleic Recovery History for Run 5/6 for Emulsion Flooding	173
7.54	Comparison of Experimental and Simulated Oleic Phase Cut History for Run 5/6 for Emulsion Flooding	174
7.55	Comparison of Experimental and Simulated Aqueous Phase Cut History for Run 5/6 for Emulsion Flooding	174
7.56	Comparison of Experimental and Simulated Emulsion Phase Cut History for Run 5/6 for Emulsion Flooding	174
7.57	Simulated Saturation History at Production Block for Run 5/6	175
7.58	Simulated Saturation Profile for Run 5/6 at 0.1037 PV Injected	175
7.59	Simulated Saturation Profile for Run 5/6 at 0.4025 PV Injected	175
7.60	Simulated Saturation Profile for Run 5/6 at 0.8020 PV Injected	175
7.61	Simulated Absolute Permeability at Production Block for Run 5/6	176
7.62	Comparison of Experimental and Simulated Injection Pressure History for Run 5/7 for Emulsion Flooding	180

7.63	Comparison of Experimental and Simulated Cumulative Oleic Recovery History for Run 5/7 for Emulsion Flooding	180
7.64	Comparison of Experimental and Simulated Oleic Phase Cut History for Run 5/7 for Emulsion Flooding	182
7.65	Comparison of Experimental and Simulated Aqueous Phase Cut History for Run 5/7 for Emulsion Flooding	182
7.66	Comparison of Experimental and Simulated Emulsion Phase Cut History for Run 5/7 for Emulsion Flooding	182
7.67	Simulated Saturation History at Production Block for Run 5/7	183
7.68	Simulated Saturation Profile for Run 5/7 at 0.1988 PV Injected	183
7.69	Simulated Saturation Profile for Run 5/7 at 0.5062 PV Injected	183
7.70	Simulated Saturation Profile for Run 5/7 at 0.8059 PV Injected	183
7.71	Oleic Relative Permeability vs. Oleic Phase Saturation for Run 5/7	184
7.72	Aqueous Relative Permeability vs. Aqueous Phase Saturation for Run 5/7	184
7.73	Emulsion Relative Permeability vs. Emulsion Phase Saturation for Run 5/7	184
7.74	Emulsion Rheological Behaviour During Flow in Porous Medium for Run 5/7	178
7.75	Comparison of Experimental and Simulated Injection Pressure History for Runs 5/7 and 5/8 for Emulsion Flooding	185
7.76	Comparison of Experimental and Simulated Cumulative Oleic Recovery History for Run 5/7 and 5/8 for Emulsion Flooding	185
7.77	Comparison of Experimental and Simulated Oleic Phase Cut History for Run 5/7 and 5/8 for Emulsion Flooding	186

7.78	Comparison of Experimental and Simulated Aqueous Phase Cut History for Run 5/7 and 5/8 for Emulsion Flooding	186
7.79	Comparison of Experimental and Simulated Emulsion Phase Cut History for Run 5/7 and 5/8 for Emulsion Flooding	186
7.80	Simulated Saturation History at Production Block for Run 5/8	187
7.81	Simulated Saturation Profile for Run 5/8 at 0.1076 PV Injected	187
7.82	Simulated Saturation Profile for Run 5/8 at 0.4947 PV Injected	187
7.83	Simulated Saturation Profile for Run 5/8 at 0.8020 PV Injected	187
7.84	Predicted Water Droplet Capture History at Production Block for Run 5/8	188
7.85	Predicted Water Droplet Capture Profile for Run 5/8 at 0.1076 PV Injected	188
7.86	Predicted Water Droplet Capture Profile for Run 5/8 at 0.4947 PV Injected	188
7.87	Predicted Water Droplet Capture Profile for Run 5/8 at 0.8020 PV Injected	188
7.88	Predicted Total Droplet Capture History for Run 5/8	189
7.89	Sensitivity of Injection Pressure to Endpoint Aqueous Relative Permeability at High Interfacial Tension	193
7.90	Sensitivity of Injection Pressure to Endpoint Emulsion Relative Permeability	193
7.91	Sensitivity of Injection Pressure to Emulsion Viscosity Predicted by Single-Phase Non-Newtonian Correlation	193
7.92	Sensitivity of Injection Pressure to Emulsion Viscosity Predicted by Different Rheological Models	193

7.93	Sensitivity of Injection Pressure to Injection Rate	195
7.94	Sensitivity of Injection Pressure to Initial Oil Saturation in the Core	195
7.95	Sensitivity of Injection Pressure to Oil Viscosity	195
7.96	Sensitivity of Injection Pressure to Mass Fraction of Oil in Water-in-Oil Emulsion	195
7.97	Sensitivity of Total Oleic Recovery to Endpoint Aqueous Relative Permeability at High Interfacial Tension	196
7.98	Sensitivity of Total Oleic Recovery to Endpoint Emulsion Relative Permeability	196
7.99	Sensitivity of Total Oleic Recovery to Emulsion Viscosity Predicted by Single-Phase Non-Newtonian Correlation	198
7.100	Sensitivity of Total Oleic Recovery to Emulsion Viscosity Predicted by Different Rheological Models	198
7.101	Sensitivity of Total Oleic Recovery to Injection Rate	198
7.102	Sensitivity of Emulsion Breakthrough Time to Endpoint Aqueous Relative Permeability at High Interfacial Tension	199
7.103	Sensitivity of Emulsion Breakthrough Time to Endpoint Emulsion Relative Permeability	199
7.104	Sensitivity of Emulsion Breakthrough Time to Emulsion Viscosity Predicted by Single-Phase Non-Newtonian Correlation	199

NOMENCLATURE

A, A_x, A_y, A_z	cross-sectional area, m^2
ACC_i	accumulation terms for component i
$ADSP_i$	surfactant adsorption term
Aq_i	aqueous term for component i in FLU_i
C_{ij}	concentration of component i in phase j , mass fraction
C_{ij_i}	initial concentration of component i in phase j , mass fraction
C_{rs}	amount of surfactant adsorbed, kg of surfactant/kg of rock
C_{rs}^*	maximum adsorption capacity of rock, kg of surfactant/kg of rock
C_{rsm}	amount of surfactant adsorbed from emulsion phase, kg of surfactant/kg of rock
C_s	concentration of surfactant in any phase, kg of surfactant/ m^3 of phase
C_{sm}	concentration of surfactant in emulsion phase, kg of surfactant/ m^3 of emulsion
$C_{11}, C_{12}, \dots, C_{55}$	coefficients of system of equations
$C_{11}, C_{12}, \dots, C_{55}''''$	coefficients of triangularized system of equations
$CAPT_i$	capture term for component i
D	depth below sea level, m
D_{ij}, D_{is}, D_{im}	dispersion coefficient of component i in phase j , m^2/s
e_j	curvature of relative permeability curve for phase j
e_{jc}	curvature of relative permeability curve for high capillary number or low interfacial tension condition for phase j

e_{jw}	curvature of relative permeability curve for low capillary number or high interfacial tension condition for phase j
Em_i	emulsion term for component i in FLU_i
F	ratio of final permeability to initial permeability, fraction
FLU_i	common flowing terms in accumulation expression for component i
g	acceleration due to gravity, 9.80665 m/s^2
G_{11}, G_{12}, G_{13}	interfacial tension parameters in Eqn. (5.32)
G_{21}, G_{22}, G_{23}	interfacial tension parameters in Eqn. (5.33)
I	exponent of intercept in the logarithmic plot of ΔP_c versus \bar{V}_c , $\text{Pa}/(\text{m/s})^n$
I	identity matrix
k, k_x, k_y, k_z	absolute permeability, m^2
k_f	flowing or flushed permeability, m^2
k_{rj}	relative permeability to phase j
k_{rjc}	relative permeability to phase j at high capillary number or at low interfacial tension
k_{rjw}	relative permeability to phase j at low capillary number or at high interfacial tension
k_{rj}^o	end point relative permeability to phase j
K	universal consistency index, Pa.s^n
K'	consistency index obtained from viscometric data measured by Brookfield viscometer, Pa.s^n
K_{iam}	equilibrium constant of component i between aqueous and emulsion phases
K_{ilm}	equilibrium constant of component i between oleic and emulsion phases

K_1	kinetic rate constant for adsorption, m^3 of surfactant/(kg of rock.s)
K_2	kinetic rate constant for desorption, kg of surfactant/(kg of rock.s)
L_c	length of capillary tube, m
L_c	length of core or porous medium, m
\dot{m}_i	mass rate of injection of component i per unit volume, $\text{kg}/(\text{m}^3.\text{s})$
n	flow behaviour index, dimensionless
N_c	capillary number, dimensionless
Ol_i	oleic term of component i in FLU_i
p_j	pressure in phase j , Pa
p_{ji}	initial phase pressure, Pa
Δp_c	pressure drop across capillary tube, Pa
ΔP_c	pressure drop across core or porous medium, Pa
P_{cla}	capillary pressure between oleic and aqueous phases, Pa
P_{clm}	capillary pressure between oleic and emulsion phases, Pa
PV	pore volume, m^3
q_j	volumetric flow rate of phase j , m^3/s
\bar{q}_j	average volumetric flow rate of phase j , m^3/s
\dot{Q}_i	mass flow rate of component i , kg/s
r_c	capillary tube radius, m
r_{inner}	radius of inner cylinder, m
r_{outer}	radius of outer cylinder, m
R_1, R_2, R_3	remainder terms for oil, water, and surfactant equations

R_1, R_2, \dots, R_3''''	remainder terms for triangularized system of equations
S_j	phase saturation, fraction
S_{ji}	initial phase saturation, fraction
S_{jr}	residual phase saturation, fraction
S_{jrw}	residual saturation of phase j at low capillary numbers or at high interfacial tension
S_{nj}	normalized phase saturations, fraction
S_{oi}	initial oil saturation, fraction
S_{wir}	irreducible water saturation, fraction
S_{air}	irreducible aqueous saturation, fraction
t	time, s
T_i	transmissibility of component i
T_{ij}	transmissibility of component i in phase j
T_{ijk}	transmissibility of component i in phase j in k direction
T_{dijk}	$\frac{A_k \phi D_{ij}}{\Delta k}$ for component i in phase j in k direction
T_{j1}, T_{j2}	capillary desaturation parameters where $j=1, a, m$
u	superficial velocity or Darcy velocity, m/s
V_b	bulk volume, m ³
\bar{V}_c	average velocity in capillary tube, m/s
\bar{V}_C	average velocity in core or porous medium, m/s
\bar{V}_m	average superficial velocity of emulsion phase, m/s
w_{jx}, w_{jy}, w_{jz}	weighting factor for the upstream direction, 0 or 1
$w_{jx}^*, w_{jy}^*, w_{jz}^*$	weighting factor for the upstream direction, 0 or 1
x, y, z	coordinate directions

GREEK LETTERS

α	rheological parameter defined in Eqn.(5.30), dimensionless or flow redistribution parameter
β	rheological parameter defined in Eqn.(5.40), dimensionless or flow restriction parameter
$\beta'_{21}, \beta''_{31}, \dots, \beta''''_{54}$	coefficients of triangularized system of equations
ε	correction factor to convert K' to K
γ	interfacial tension, N/m
γ_{am}	interfacial tension between aqueous and emulsion phases, N/m
γ_c	$\frac{\rho_i^2 A_c}{(\rho_i + B_c \rho_m C_{im})^2}$ in capture term, where $i = 0$ or w
γ_d	$\frac{\rho_r A_d (1 - \phi_{inir})}{(1 + B_d \rho_m C_{dm})^2}$ in adsorption term
γ_{lm}	interfacial tension between oleic and emulsion phases, N/m
$\dot{\gamma}_{rc}$	shear rate at wall of capillary tube, s^{-1}
$\dot{\gamma}_c$	average shear rate in core or porous medium, s^{-1}
Δ	difference
δ	time difference operator
θ	emulsion quality or volume fraction of dispersed phase in continuous phase, fraction
η_j	transmissibility of phase j
λ_{rj}	relative mobility of phase j
λ_r	total relative mobility
λ_{sl_1}	straining and interception filter coefficient, m^{-1}

λ_{st_2}	straining and interception filter coefficient for re-entrainment, m^{-1}
μ_j	viscosity of phase j , Pa.s
μ_{eff}	effective viscosity, Pa.s
ϕ	porosity, fraction
ϕ_{init}	initial porosity, fraction
ϕ'	chord slope of porosity
Φ_j	potential of phase j , $\Phi_j = p_j - \rho_j g D$, Pa
ρ_j	density of phase j , kg/m^3
ρ_r	density of rock, kg/m^3
σ	local droplet retention, drop volume/bulk volume
τ_{rc}	shear stress at wall of capillary tube, N/m^2
$\bar{\tau}_c$	average shear stress in porous medium, N/m^2
ζ	ratio of outer radius to inner radius of an adaptor used for Brookfield viscometer, dimensionless
∇	del operator

SUBSCRIPTS

a	aqueous phase
c	capillary tube
C	core, porous medium
i	component i , where $i = o, w, s$
ij,k	block i, j, k
j	phase j , where $j = l, a, m$
l	oleic phase
m	emulsion phase

<i>n</i>	normalized
<i>o</i>	oil component
<i>s</i>	surfactant component
<i>w</i>	water component

SUPERSCRIPITS

<i>n</i>	time level
----------	------------

1. INTRODUCTION

Application of emulsions in the oil industry has received considerable attention for several decades. Recent investigations have shown that emulsions can be used in secondary recovery as blocking agents to improve waterflooding performance in layered reservoirs or under bottom-water conditions. Moreover, they occur in most enhanced oil recovery processes and are involved in certain modes of crude oil transportation. Recently, increasingly more complex compositional simulators have been developed for EOR processes. These require a detailed understanding of the mechanisms involved during the displacement process. Therefore, there is a need for understanding the physics controlling the flow of an emulsion in a porous medium. However, very little research has been carried out in the area of the flow mechanics of emulsions in porous media. Additionally, emulsion rheology and drop capture were investigated separately for certain conditions. These conditions restrict the model to specific applications. This leads to the question of how emulsion transport occurs in a porous medium in the case where emulsion drop size and the pore size are comparable, which is often the case. Furthermore, no attempt has been made in the literature to simulate macroemulsion flooding performance compositionally by including the physical property changes that occur simultaneously during multiphase displacement. The present

study investigates these subjects to achieve a better mechanistic understanding of emulsion flow and its mathematical representation. This will provide information that can be applied in any EOR process involving emulsion flow.

2. REVIEW OF THE LITERATURE

2.1 Emulsions and Their Applications in Oil Recovery

An emulsion is defined as the dispersion of one liquid (internal or dispersed phase) within another liquid (external or continuous phase) in the presence of surface-active agents (emulsifiers)¹. The emulsifier helps to form an extended interface by reducing the interfacial tension between the liquids and also helps to stabilize the dispersed droplets against coalescence. It can be classified as a macroemulsion if the droplet size is larger than 0.1 μm and as a microemulsion if the droplet size is smaller than 0.1 μm . Generally, most droplet diameters in macroemulsions are greater than 1 μm , which is of the same order of magnitude as the pore constrictions. There are two types of emulsions: water-in-oil (w/o) and oil-in-water (o/w). The former type has a viscosity higher than that of the oil and water constituents, while the latter has a viscosity lower than that of the oil constituent².

Most of the world's crude oil is produced in emulsion form because natural emulsifiers exist in petroleum reservoirs. These natural emulsifiers can be formed from the following materials: asphaltenes found in heavy crude^{3,4}; asphaltic and resinous materials found in crude⁵; oil-soluble organic acids such as naphthenic acids, fatty acids or aromatic acids⁶; or cyclic compounds (cyclic aromatics) such as toluene, benzene,

decalin, methylcyclohexane and cyclooctane in crude oil⁷. King and Flock proposed four hypothetical emulsion classifications⁸:

- (1) very viscous crudes, containing very high concentrations of asphaltenes and resinous acids;
- (2) viscous crudes with moderately high concentrations of asphaltenes and resinous acids;
- (3) moderately viscous crudes with intermediate concentrations of asphaltenes and resinous acids; and
- (4) low viscosity crudes with low concentrations of asphaltenes and/or resinous acids.

Crude oils from Group 1 (e.g. Athabasca bitumen) generally will not form emulsions at room temperature because of the high viscosity. Crude oils from Group 4 (e.g. Bonnie Glen crude) also will not form emulsions because of low natural surfactant content. Crude oils such as Wainwright and Chauvin crudes, from Group 3, readily form stable emulsions. However, if an artificial surfactant is employed, stable emulsions of crude oil from each category can be created.

Emulsions of produced crude oil are generally of the water-in-oil type, which are more viscous than either of their constituents. Therefore, chemical and heat treatment are applied in the oilfield to separate these emulsions into their less viscous components to maximize oil production. On the other hand, oil-in-water emulsions have lower viscosities than the oil constituents. This fact has been considered by

some investigators^{9,10} in the development of systems for producing and transporting crude oil as an oil-in-water emulsion. A surfactant can be injected with the produced water to form an oil-in-water emulsion downhole, which makes it easier for the oil to be pumped to the surface¹¹.

In addition, emulsions can be formed in-situ in many enhanced oil recovery methods such as chemical flooding, carbon dioxide flooding, steamflooding and fireflooding. The emulsion banks formed seem to improve oil displacement efficiency, under some conditions.

In chemical flooding, the mechanism by which spontaneous emulsification occurs is due to mass transfer of surfactant between the oil and water phases. The shearing action at the oil/water interface during surfactant flooding may be sufficient to cause emulsification⁷. In-situ emulsification and entrapment of emulsion droplets during caustic flooding results in reduced water mobility, which improves both vertical and areal sweep efficiencies¹². In immiscible carbon dioxide flooding, a narrow emulsion bank seems to form which improves oil displacement efficiency without appreciably increasing the pressure drop. Similarly, in hot water/steam injection experiments, emulsions are formed by the surface-active compounds generated from low temperature oxidation of oil, such as organic acids, phenols and sulphuric acid. Chung and Butler^{13,14} found a high emulsified water-oil ratio in the produced fluid in the steam-assisted gravity drainage

process in their laboratory experiments. The primary mechanism for in-situ water/oil emulsification during the thermal recovery process is the condensation of steam in contact with bitumen. Chen et al.¹⁵ presented both laboratory and field evidence for the in-situ formation and flow of emulsions in porous media.

In the further development of new methods of secondary recovery, high viscosity emulsions¹⁶, emulsion slugs^{17,18}, and controlled viscosity microemulsions¹⁹ can be injected externally to enhance oil recovery.

2.2 Experimental and Field Studies on Emulsion Properties and Flow Mechanisms

Many laboratory studies have been conducted to understand the rheological behaviour of emulsions and mechanisms of emulsion flow through porous media. This helps in the understanding of how oil recovery can be improved by in-situ emulsification or by injecting emulsion externally. The following is a review of experimental and field studies of emulsion flow in porous media.

Cartmill²⁰, with the aim of investigating the mechanism of oil migration through reservoir sandstones, carried out experiments on the flow of stable crude oil-in-water emulsions through packed beads having differing permeability zones in series. He found considerable amounts of oil drops retained at the junction of different permeability zones,

with maximum retention at the front portion of the low permeability zone. Consequently, permeability of the porous media was reduced. He also pointed out that electrostatic forces may be just as important as capillary forces in causing permeability reduction. Uzoigwe and Marsden²¹ observed no retention of droplets within porous media during the flow of oil-in-water emulsions through glass bead packs.

McAuliffe²² conducted laboratory studies to show that oil-in-water emulsions can be used as a selective plugging agent to improve oil recovery in waterfloods. The result from injecting caustic oil-in-water emulsions with various drop sizes into Berea sandstone under a constant pressure showed larger reduction in water permeability of sandstone with larger drop-size to initial permeability ratio. Furthermore, permanent permeability reduction was observed even when the emulsion was followed by many pore volumes of water. He also observed that the rate and amount of permeability reduction decreased with increasing injection pressure. He called this flow behaviour pseudo non-Newtonian, regardless of the oil content of the emulsion. For parallel cores of different permeabilities, an oil-in-water emulsion was found to reduce proportionally the permeability in high permeability cores more than low permeability cores. Finally, it was observed that oil-in-water emulsions displaced oil more efficiently than water. He postulated that the injected emulsion entered the more permeable zones first, restricting the flow, and

thereby causing the fluid to flow in the less permeable zones, resulting in improved sweep efficiency. It was also suggested that for an emulsion to be the most effective, the droplets of oil in the emulsion should be slightly larger than the pore-throat constrictions in the porous medium. Once oil droplets plug the pores, they can only be forced through the constrictions if the applied pressure can overcome the capillary retarding force. Field tests²³ substantiated the laboratory observations. Oil-in-water emulsions were found to reduce water channelling from injection to production wells, thus increasing oil recovery, lowering water-oil ratios, and considerably increasing the volumetric sweep efficiency.

Cooke et al.²⁴ argued that permeability reduction by the formation of water-in-oil emulsions was due to the formation of an oil film (lamella) across the pore throat, which restricted the flow path, reducing the mobility of the flowing fluid.

Johnson²⁵ suggested that either emulsions formed in-situ or emulsions injected externally were useful for recovering viscous oils and oils in heterogeneous reservoirs where sweep efficiency is poor. He pointed out that although the potential of emulsions for improving oil recovery was well established, the cost of oil for emulsification and injection was a serious deterrent to wider field use.

Radke and Somerton²⁶ suggested the alternative of using dilute emulsions, instead of polymers, to improve mobility control in caustic flooding. The advantage of using emulsions is that the emulsion effectiveness is quite insensitive to temperature and alkalinity. Emulsions would also be less expensive mobility-control agents than polymers because they can be easily prepared using acid California crude oil in alkaline water with no synthetic surfactants. They also studied emulsion displacement both in homogeneous cores and in heterogeneous systems to ascertain possible improvements in sweep efficiency.

Soo and Radke^{27,28} studied experimentally the flow mechanism of dilute, stable oil-in-water emulsions in porous media by determining the transient permeabilities, the pore size distribution of the porous medium, and the inlet and effluent drop concentrations and size distributions. The oil droplet migration in the porous medium was also observed by means of a visual micromodel. They argued that dilute, stable oil-in-water emulsions did not flow in porous media as continuous, viscous liquids or by being squeezed through pore constrictions; rather they flowed by the capture of the dispersed phase with a subsequent reduction of permeability to the continuous phase. This droplet capture mechanism was found to be similar to a filtration process. Soo and Radke explained that during the transient permeability reduction caused by droplet retention in pores, the drops not only

block pores with throat sizes smaller than their own (straining), but also are captured on the surface of sand grains and in crevices or pockets formed by the sand grains (interception). The capture of these small droplets on the rock surface depends on the surface chemistry of the drops and the porous matrix, especially the pH and ionic strength of the aqueous phase. Steady state is reached, once all capture sites are occupied, because liquid droplets cannot be captured on top of one another. Soo and Radke concluded that the overall permeability reduction is controlled by two factors: the volume of drops retained, and how effective these drops are in restricting flow. As the drop size of the emulsion increased, the drop retention also increased because of the higher probability of capture. However, at identical volume retentions, smaller-sized drops were more effective in restricting flow during the transient state. Once steady state flow was obtained, the larger droplets caused a larger permeability reduction than the smaller droplets due to the combination of these two factors. Finally, it was noted that the viscosity of the oil phase had little effect on both effluent concentration and transient permeability histories.

Schmidt et al.²⁹ proposed the hypothesis that for continuous, linear, secondary oil displacement by an oil-in-water emulsion, the displacement was improved by microscopic mobility control through entrapment or local permeability reduction, not through viscosity ratio improvement. For

parallel core flooding, displacement was improved through macroscopic mobility control by diverting flow to the lower permeability core.

French et al.³⁰ suggested the use of emulsions for mobility control during steamflooding. Their observations support the emulsion flow mechanism proposed by Soo and Radke. They observed that there was a permeability reduction caused by plugging of emulsion droplets both larger and smaller than the pore throat size, and that a permeability reduction occurred when a waterflood followed an emulsion flood. They also showed that emulsions formed in-situ did not perform as well as those prepared externally.

Islam and Farouq Ali^{31,32,33,34} investigated the blocking mechanism of emulsions and their effectiveness in controlling mobility, while waterflooding an oil reservoir, both with and without a bottom-water zone. They concluded that the reservoir and fluid properties, such as oil-to-water zone thickness, oil-to-water permeability ratio, oil viscosity, and emulsion slug size, affected the blocking action of emulsions as well as their oil content in a reservoir with a bottom-water zone. The study showed that the lower the oil-to-water zone thickness was, the lower was the ultimate oil recovery for low to moderate oil-to-water permeability ratios. However, for high oil-to-water permeability ratios, the oil recovery was found to increase slightly as the thickness of the bottom-water zone increased. For high-

viscosity oils, significant improvement in performance was observed by using an emulsion flood, as compared to that obtained using a conventional waterflood. A minimum of one pore volume (bottom-water zone) of emulsion slug was required for successful blockage with emulsion, while the optimum slug size was 2.5 pore volumes.

Yeung and Farouq Ali^{35,36} suggested three different displacement processes, the Emulsion Slug Process (ESP), the Alternating Water Emulsion Process (AWE), and the Dynamic Blocking Procedure (DBP), to improve vertical sweep efficiency during the waterflooding of bottom-water formations. For low surfactant emulsions (0.016 to 0.04%) the DBP and AWE processes were found to give higher oil recoveries than the ESP process under bottom-water conditions. The reverse was true for emulsions with higher surfactant concentrations (0.4%). Furthermore, the higher the viscosity of the injected fluid, the greater the amount of crossflow that occurred ahead of the flood front. Yeung and Farouq Ali also found that a high surfactant concentration did not necessarily give a higher oil recovery for both homogeneous and bottom-water conditions.

Mendoza et al.³⁷ found that oil recovery was sensitive to injection rate for both oil-in-water and water-in-oil emulsion floods. The flood rate determined the extent of mobility ratio variation, which in turn depended on the drop size, type, and rheological behaviour of the emulsion. Oil

recovery, as a function of flood advance rate, showed a minimum about a rate of 10 m/day. The type of emulsion slug (water-in-oil or oil-in-water) determined whether recovery increased or decreased with an increase in slug size. They concluded that water-driven emulsion slugs may provide a viable alternative to thermal recovery of moderately viscous oils.

Fiori and Farouq Ali³⁸ proposed the use of solvents in adjusting the emulsion characteristics for increased oil displacement efficiency. Emulsion slugs were then injected into partially waterflooded cores resulting in incremental recoveries of up to 70%. They concluded that carefully designed crude oil emulsions (water-in-oil) can be used as oil recovery agents for heavy oil reservoirs with low primary conductivity, poor response to waterflooding, and low potential for thermal recovery applications.

2.3 Mathematical Modelling of Emulsion Flow in Porous Media

As mentioned previously, emulsions are formed in-situ in most EOR processes or injected externally, alone or alternating with other fluids, to improve displacement efficiency by way of their mobility control properties. Therefore, quantitative representation of emulsion flow in porous media becomes increasingly important, especially since more comprehensive simulators for these EOR processes are being developed. Thus, an understanding of the flow behaviour,

transport properties of emulsions, and the physical laws controlling flow is necessary to model emulsion flow. These characteristics of emulsion flow must be included in EOR simulators to predict reservoir performance more accurately.

There are three main mechanisms describing emulsion flow behaviour postulated by Uzoigwe and Marsden²¹, and later by Alvarado and Marsden^{2,39}, McAuliffe²², and Soo and Radke^{27,28}, based on their laboratory observations. A review of the mathematical models formulated for the postulated mechanisms is given below.

Alvarado and Marsden^{2,39} developed the bulk viscosity model in which emulsion is viewed as a homogeneous, single-phase fluid. They studied experimentally the flow of oil-in-water macroemulsions through both porous media and capillary tubes. They found that the rheological behaviour of the flow of these oil-in-water macroemulsions through porous media is practically the same as that of flow through capillary viscometers. Results showed that emulsions with oil concentrations less than 50% behaved like Newtonian fluids, while those with concentrations greater than 50% behaved like pseudoplastic fluids for the range of shear rates from 10^3 to 10^4 sec^{-1} . The value of the emulsion quality associated with the transition from Newtonian to non-Newtonian rheological behaviour depended on the emulsifier concentration. Alvarado and Marsden derived a simple correlation to describe successfully the flow of non-Newtonian oil-in-water

macroemulsions through porous media for the range of shear rates investigated, 10^3 to 10^4 sec^{-1} . This correlation can be reduced to Darcy's law for oil-in-water Newtonian macroemulsions including permeability reduction caused by partial plugging. The parameter $\beta = \alpha^{(n+1)}$, which depended on both the tortuosity of the porous medium (α) and the rheological nature of the flowing fluid (n), was proposed for calculation in a trial-and-error graphical algorithm that brought the two rheograms from the capillary tubes and the porous medium into agreement.

In conclusion, this model considered an emulsion as a homogeneous, non-Newtonian fluid that did not follow Darcy's law due to the change in bulk viscosity with shear rate. The final permeability was used to account for the plugging effect which caused permeability reduction. Alvarado and Marsden pointed out that the above limiting value of permeability depended on the emulsion quality. The tortuosity and pore size distribution of the porous medium, and the rheological nature, drop size distribution, and quality of the emulsion influenced only the bulk emulsion viscosity, resulting in a simple correlation of pressure drop and average flow velocity. Therefore, the viscosity model was limited to a description of the flow of high-concentration emulsions with small drop-size to pore-size ratios which approached steady state quickly.

Devereux⁴⁰ proposed a droplet retardation model, based on the mechanism postulated by McAuliffe, for describing the flow of stable oil-in-water emulsions in porous media, including capillary effects, but neglecting gravitation and compression. In Devereux's study, continuous injection into a solid saturated with the external phase of the emulsion under conditions of constant saturation and pressure drop yielded a closed-form equation for the total volume of emulsion injected versus time with three experimental parameters. These were the flow constants for each phase and the capillary factor. A fit of experimental data to this equation provided these parameters. The capillary factor was seen to represent a real force per unit volume, capable of physical interpretation. This relation was compared with results from experimental studies of crude oil-in-water emulsion flow in sandstone⁴¹. Emulsion concentration and pressure difference across the experimental system were varied. It was found that Devereux's relation provided an accurate description of the results except for high emulsion concentrations, where the high saturation values observed were presumed to cause interaction of the emulsion droplets, and for low pressure differences, where the capillarity factor (capillarity force per unit volume of porous solid) became dominant and restrictions in the simplistic model became detrimental.

In conclusion, Devereux considered the flow of two phases, dispersed and continuous, in porous solids with the capillary effect included. He proposed that the emulsion drops flowed slower than the continuous phase because of a capillary resistance force encountered during their flow through pore throats smaller than themselves. Therefore, this capillary retarding force, which depends on the drop size distribution, was included in the pressure driving force of the dispersed oil phase in this model. The model derived for the case of constant velocity flow⁴² can properly predict transient permeability reduction. That is, the model predicts larger permeability reduction with lower flow rate and higher drop size-to-pore size ratio. However, this retardation model could not predict the permanent permeability reduction observed in the laboratory when an emulsion flood was followed by many pore volumes of water. Instead, the permeability prior to the emulsion flood was predicted.

Abou-Kassem and Farouq Ali^{43,44,45} modified the viscosity model, making it practical for both Newtonian and non-Newtonian emulsions and suitable for use in numerical simulations of EOR processes. For non-Newtonian emulsions, the correlation was presented in the form of a modified Darcy's law which is suitable for incorporating into reservoir simulators. The correlation provides for a quantitative description of the effect of pore size distribution and tortuosity of porous media on flow. It also

gives pressure drop predictions accurate to within 2.4% of the average absolute relative deviation based on Alvarado and Marsden's experimental data. The proposed model is recommended for use in the one-dimensional, isothermal, single-phase flow of non-Newtonian fluids in porous media.

In conclusion, the model was derived using assumptions similar to those used by Alvarado and Marsden in their viscosity model. The difference is that Abou-Kassem and Farouq Ali replaced the flushed permeability (k_f) with $Fk_{initial}$, where F is the ratio of damaged permeability-to-original permeability, and included the effect of interaction between the flowing fluid and the porous medium (F) in the parameter γ , where $\gamma = \alpha\sqrt{F}$. They also introduced a simpler and more direct analytical procedure for estimating the parameter γ than the trial-and-error graphical procedure used by Alvarado and Marsden to force agreement between the core rheogram and the capillary rheogram. This parameter, γ , which depends on pore size distribution and tortuosity of the porous medium, and reflects reduction in permeability, accounts for the shifting of the capillary viscometer rheogram and the porous medium rheogram. It is important to note that this model should be used only in describing emulsion flow in porous media, where the average shear rate is in the range that the rheological parameters K and n are estimated.

Soo and Radke^{42,46-48} proposed a flow model describing the flow of stable, dilute emulsions in unconsolidated porous

media based on deep-bed filtration concepts. This model takes into account the interactions between the flowing droplets and the pore constrictions. This helps to predict more accurately how emulsions are transported in porous media. In the model, emulsion droplets can be captured in pores by both straining and interception, causing permeability reduction. Transient flow behaviour is characterized by three parameters, namely a filter coefficient, a flow-redistribution parameter, and a flow-restriction parameter. The filter coefficient controls the sharpness of the emulsion front. The flow-redistribution parameter dictates the steady-state retention as well as the flow redistribution phenomenon. The flow-restriction parameter describes the effectiveness of retained drops in reducing permeability. Expressions for these filtration parameters were derived and compared with those measured experimentally. Good agreement was achieved and it was concluded that the dependence of these parameters on retention was weak. Therefore, they may be treated as functions of drop size and pore size distribution only. Comparisons among the filtration model and the previously developed emulsion flow models showed that only the filtration model successfully represented all the experimental observations, such as permanent permeability reduction. This model represents the underlying physical mechanisms correctly and is reliable for predicting emulsion flow behaviour in porous media.

Islam and Farouq Ali³⁴ introduced a model to investigate emulsion flow in a multiphase system. A fully-implicit, three-phase, three-dimensional black oil reservoir simulator was developed to simulate emulsion flooding in the presence of a bottom-water zone. They assumed that the effective permeabilities were only functions of the saturation of each phase. Thus, there was no interference effect among the three phases. History matching with experimental data was conducted by changing the relative permeability curve for the emulsion. This model incorporated permeability reduction as a function of the initial permeability of the porous medium. The transient permeability reduction was not included in the simulation. An empirical correlation was used for the permanent permeability reduction which was restricted to a particular set of fluid/porous medium systems and led to difficulty in matching emulsion breakthrough. Also, this model could not explain the relationship between pore throat size and emulsion droplet size, even if excellent agreement was obtained with experimental results for a particular oil-in-water emulsion.

Later, a more complete formulation, including the blocking mechanism of the emulsion, transient permeability reduction, and emulsion breaking and formation, was presented. Islam and Farouq Ali⁴⁹ developed three different models, one for a stable emulsion and the other two for in-situ generation of emulsions. In the stable emulsion model, two-phase flow (oil

and aqueous phases) was formulated, and included drop capture with local permeability reduction based on the filtration theory of Soo and Radke. The stable emulsion model showed a better agreement with the experimental results than the previous simplified model. The first model of in-situ generation of emulsion used a multiphase formulation incorporating surfactant propagation. The surfactant adsorption, capillary number and relative permeability were treated as functions of the surfactant concentration. This model could not predict an increase in injection pressure due to in-situ emulsion generation in the porous medium. The reason for this unexpected behaviour was the absence of mass transfer between the oil and water, even if surfactant was allowed to partition in both phases. Therefore, the flow restriction, caused by the blocking mechanism and which increases the injection pressure, was not properly formulated. The second model of in-situ generation of emulsion was a single-phase treatment, which included an increase in the aqueous phase viscosity due to the concentration of the oil droplets formed in the aqueous phase. Because of the high aqueous viscosity predicted by this model, the high injection pressure which occurred after emulsion generation was obtained.

3. STATEMENT OF THE PROBLEM

The transport of a macroemulsion in a porous medium is complex and is not yet fully understood, especially for the case of multiphase flow. This study was carried out with the purpose of investigating the following problems.

1. To observe the mechanisms of the emulsion flooding process for the recovery of light and medium gravity oils, for the same emulsion characteristics. The case in which the pore and drop sizes are approximately the same is of particular interest as it is commonly encountered in oil recovery.
2. To analyze the existing limited physical property models and extend their application to the present system.
3. To develop a multiphase emulsion flow simulator consisting of a three-phase system with a stable emulsion and incorporating observed physical property models as well as other property models.
4. To employ the experimental data obtained to validate the developed numerical simulator, to determine to what extent the experimental results can be simulated, and to determine what effect these mechanisms have in improving the simulated result.

4. EXPERIMENTAL WORK

A number of experimental core floods were conducted in this study. This chapter describes the experimental apparatus, the preparation of the cores and the emulsions, the procedures for determining the properties of the porous media and the emulsions used, and the results of the core floods.

4.1 Experimental Apparatus

Figure 4.1 shows a schematic of the core displacement apparatus. It consists of a piston-type constant rate ISCO pump, cylinders for injected fluid, a cylindrical core holder, an automatic sample collector, and a recorder for the continuous monitoring of the core injection pressure and the differential pressure across the two taps 2.5 cm apart midway along the core.

The desired fluid was injected into the core by displacing it with mercury, which was in turn displaced by water, pumped by the ISCO pump. At the same time, the injection pressure and the differential pressure were measured by pressure transducers and recorded on the chart recorder. The effluent was then collected in an automatic sample collector, and the produced fluids were characterized.

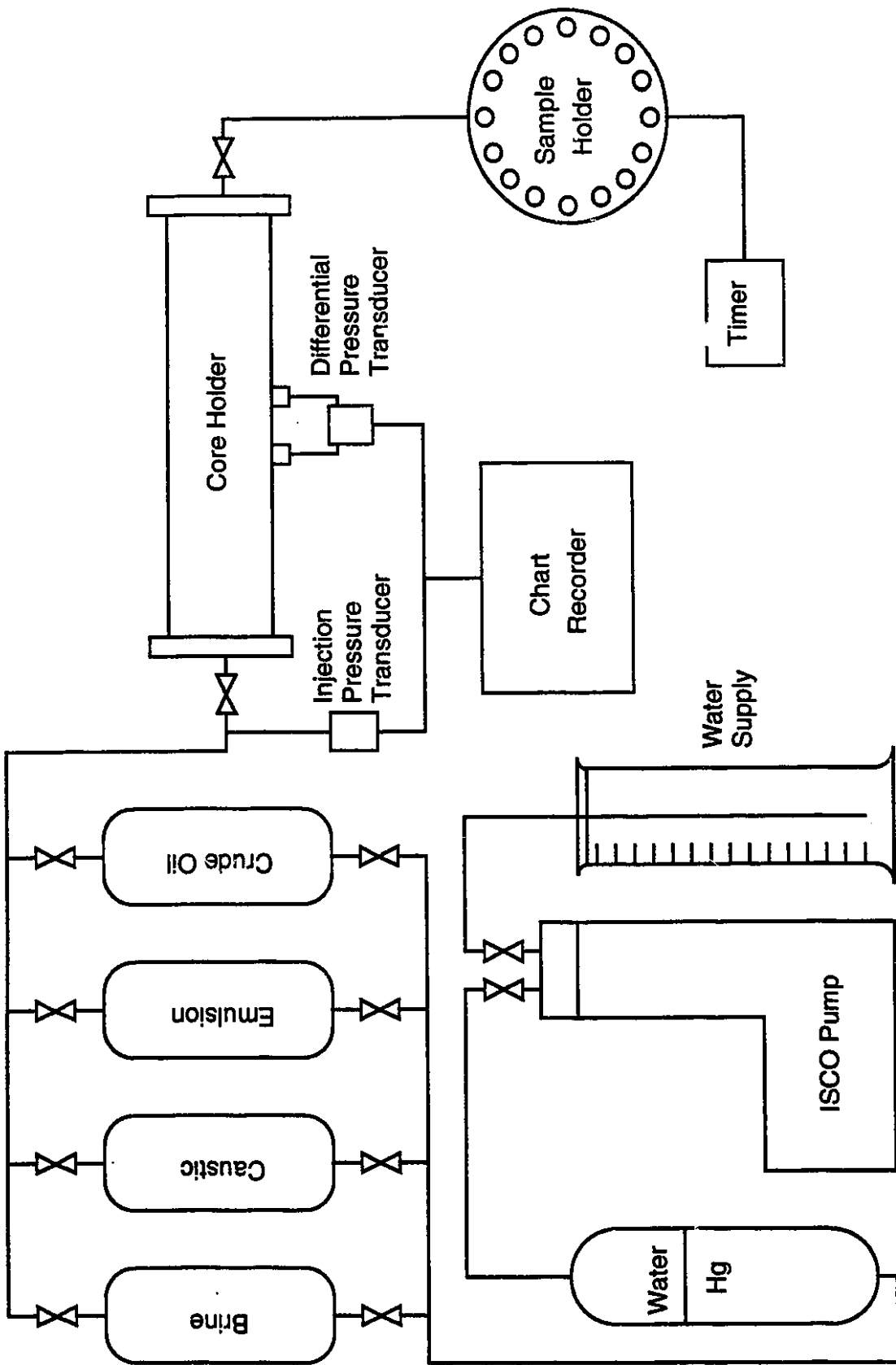


Fig. 4.1 Schematic of Core Displacement Apparatus.

4.2 Porous Medium Preparation and Determination of Its Properties

Ottawa sand and Berea sandstone were used as the porous media in the core displacement tests. The Ottawa sand packs were prepared by dry packing in stainless steel core holders, 61 cm in length and 6.26 cm in diameter. Berea sandstone cores of the same length and 5 cm in diameter were prepared by painting them with epoxy resin and casting them in stainless steel coreholders using Cerrobend, an alloy with a low melting point (158°F). The ends were machined and the cores were fitted with flanges.

The cores were placed under vacuum for twelve hours and then the core properties, namely pore volume, permeability, and porosity, were determined. Pore volume was determined by imbibition of brine with a concentration of 1% or 2% by weight brine. The absolute permeability was found using Darcy's law at several flow rates. Once the core properties were found, the cores were saturated with the same brine and the core displacement tests were begun.

The pore size distribution of a porous medium has a significant influence on the flow of emulsion through it. The pore size distribution of the Berea core was determined by the Purcell mercury injection method. The method involves forcing mercury under pressure into the evacuated pores of the core. This yields the pressure-volume

Table 4.1
Capillary Pressure Curve Data for Berea Sandstone

(1)	(2)	(3)	(4)	(5)	(6)
Pressure (kPa)	Volume (m ³ ×10 ⁶) w/o Sample	Volume (m ³ ×10 ⁶) w Sample	Vol. of Injected Mercury (3) - (2)	S _{Hg} * $\frac{(4)}{0.834} \times 100$	P _c ** (kPa)
377	0.060	0.140	0.080	9.59	380
653	0.060	0.278	0.218	26.14	656
929	0.070	0.420	0.350	41.97	932
1205	0.082	0.568	0.486	58.27	1208
1480	0.091	0.667	0.576	69.06	1483
2170	0.113	0.805	0.692	82.97	2173
2859	0.135	0.888	0.753	90.29	2862
3549	0.165	0.940	0.775	92.93	3552
4238	0.196	0.990	0.794	95.20	4241
4928	0.220	1.034	0.814	97.60	4931
5617	0.248	1.068	0.820	98.32	5620
6307	0.270	1.100	0.830	99.52	6310
6996	0.298	1.132	0.834	100.00	6999

$$* S_{Hg} = \frac{\text{Volume of Injected Hg}}{\text{Total Volume of Hg (Total PV)}}$$

$$** P_c = p + \rho_{Hg} \cdot \frac{g}{g_c} \cdot h,$$

where

P_c = capillary pressure, Pa

p = exerted pressure, Pa

ρ_{Hg} = mercury density = 13,597 kg/m³, and

h = height from the upper reference line to the core sample = 0.02 m

g_c = conversion factor = 1 (kg.m)/(N.s²)

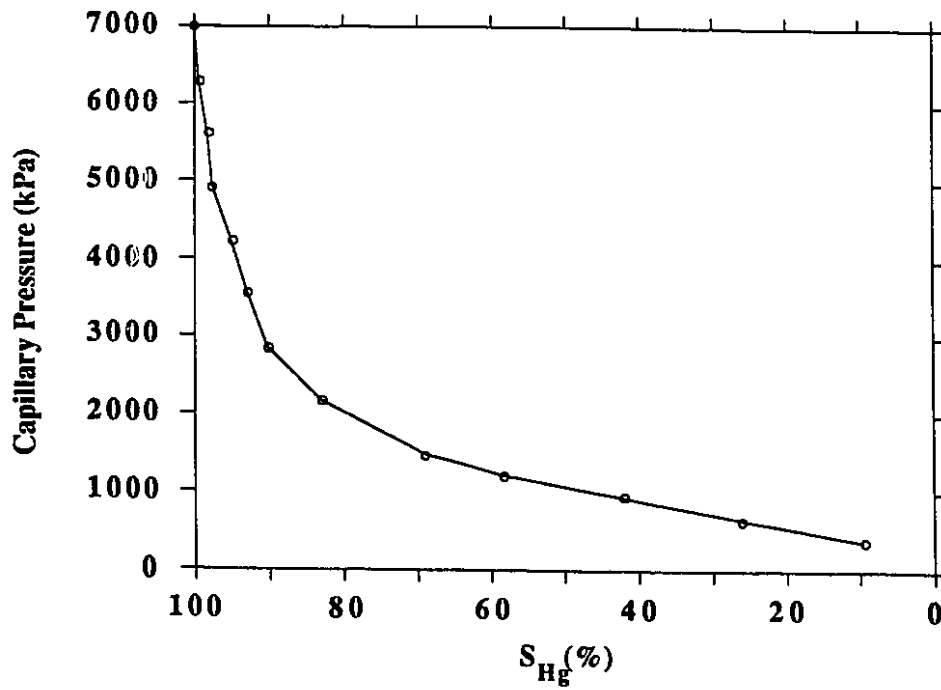


Fig. 4.2 Capillary Pressure Curve of Berea Sandstone.

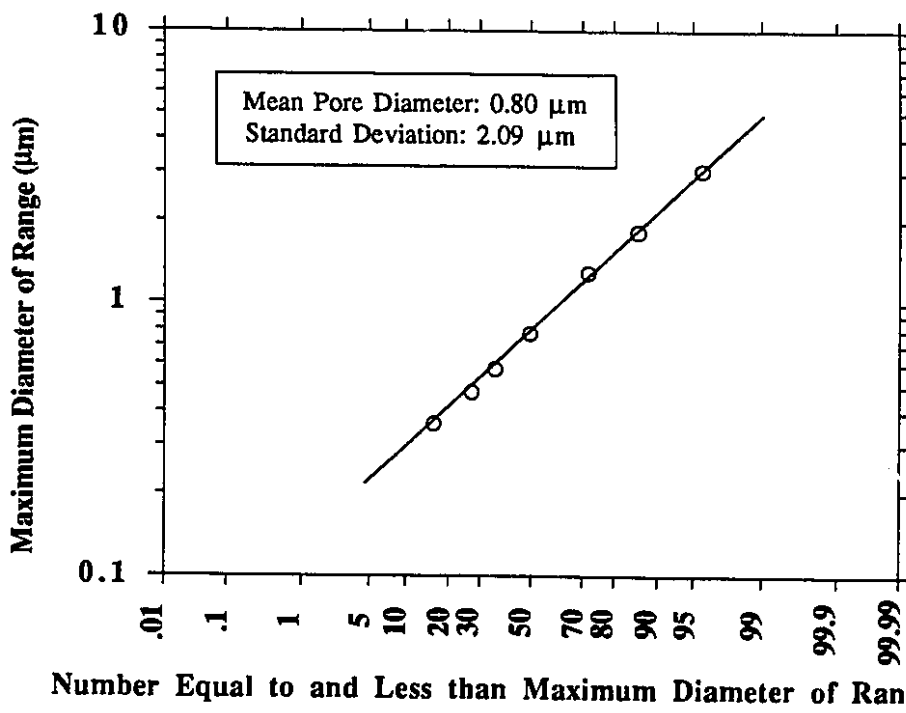


Fig. 4.3 Log-Probability Plot of Berea Sandstone Pore Size Distribution.

Table 4.2
Pore Size Distribution Data of Berea Sandstone

Range of Saturation	Range of Radius (μm)	Mean Radius* (μm)	Mean Diameter (μm)	Frequency Percentage** (%)
0.00 - 0.20	> 1.55	2.67	5.34	4.23
0.20 - 0.40	1.55 - 0.93	1.24	2.48	9.75
0.40 - 0.60	0.93 - 0.65	0.79	1.58	14.83
0.60 - 0.80	0.65 - 0.39	0.52	1.04	22.70
0.80 - 0.88	0.39 - 0.29	0.34	0.68	13.46
0.88 - 0.92	0.29 - 0.24	0.27	0.53	8.53
0.92 - 0.96	0.24 - 0.18	0.21	0.42	10.71
0.96 - 1.00	0.18 - 0.12	0.15	0.30	15.79

$$* \quad r = \frac{2\delta \cos \theta}{P_c},$$

where

P_c = Capillary pressure (N/m^2), and

δ = Interfacial tension of mercury = 0.48 N/m

θ = Contact angle of mercury = 140°

** The frequency-percentage of occurrence of pores in the interval $r_2 - r_1$ is given by

$$f(r_2 - r_1) = \frac{\int_{r_1}^{r_2} P_c dS}{\int_0^{r_2} P_c dS} \times 100.$$

The integral is determined by using the Simpson rule,

$$\int_a^b f(x) dx = \frac{h}{3} [f(0) + 4f(1) + 2f(2) + 4f(3) + f(4)],$$

where

$$h = \frac{b - a}{4}.$$

relationship given in Table 4.1 and the capillary pressure curve shown in Fig. 4.2. Table 4.2 shows how the pore size distribution was obtained from this data, and the log-probability plot of the distribution is plotted in Fig. 4.3. The mean pore size was found to be $0.80\ \mu\text{m}$.

4.3 Emulsion Preparation and Characterization

The type and properties of an emulsion are, to a great extent, dependent on the type of surfactant used as well as the method employed for creating the emulsion. Two kinds of emulsions, caustic and surfactant, were formulated and investigated in the core displacement tests. An Alberta crude oil, "Horsefly crude", was used for the preparation of both emulsions. Table 4.3 shows the properties of this crude.

Table 4.3
Properties of the Horsefly Crude⁵⁹

Density at 24°C	0.886 g/ml
Viscosity at 24°C	18 mPa.s
Water content	0.2% by volume
Acid number	1.88 mg KOH/100 g crude
Interfacial tension between crude and 2% (wt.) NaCl	22.1 mN/m

A detailed description of the methods used to obtain the above properties is given in Ref. 59. Density was measured by a Paar Digital Densitymeter; viscosity was measured using a Brookfield LV viscometer with the UL adaptor. Water content was determined by the method of Dean and Stark which was done by distillation of the crude with excess toluene until no more water was collected as distillate. Water content was then calculated from the volume of the crude distilled and the volume of water collected. The acid number was found according to the ASTM Standard D 1962-67. The interfacial tension between the crude and the 2% (wt.) NaCl was measured using a Du Nuoy tensiometer.

4.3.1 Caustic Emulsions

When sodium hydroxide (caustic) is in contact with a crude oil that contains acid compounds, a surfactant forms as a result, and the interfacial tension between the crude oil and the aqueous solution is reduced. An emulsion can then be formed when the mixture is agitated. Because of the availability and relatively low cost of caustic, caustic emulsions were chosen for use in some of the core displacement tests in this study.

4.3.1.1 Method of Preparation

Emulsions were prepared by the agent-in-water method. The crude oil and caustic solutions were mixed in known proportions and homogenized for five to ten minutes using

the Brinkmann homogenizer. The emulsions were then transferred to graduated cylinders and allowed to equilibrate over several hours until the phase volumes became constant. The phase volumes were noted periodically and the different phases were examined under the microscope to determine the type of emulsion formed; that is, water-in-oil (w/o) or oil-in-water (o/w).

A series of emulsions were prepared using various ratios of Horsefly crude and caustic solutions having concentrations of 0.1% and 1.0% (weight/volume, or w/v; e.g., 0.1% = 1 g/litre). When the emulsions were allowed to equilibrate over twelve hours, water-in-oil emulsions were formed in the oil-rich phase and oil-in-water emulsions in the water-rich phase. The emulsions were then aged at room temperature for two weeks. The stability of the emulsions is classified based upon the phase volume changes at the end of this aging period. The stable water-in-oil emulsions, named H1 and H2, were chosen for further investigation of their properties, and were also used in core displacement tests. Emulsion H1 is the upper phase of a mixture of one part oil to three parts 0.1% w/v caustic solution. Similarly, emulsion H2 is the upper phase of a mixture of one part oil to three parts 1% w/v caustic solution.

4.3.1.2 Characterization of Emulsions

Characterization of the emulsions H1 and H2 consists of determination of the percent quality, the rheological properties, and the drop size distribution.

A. Quality

The emulsion quality is the volume percentage of the dispersed phase in the emulsion (percentage of water in water-in-oil emulsions, for example). The quality of water-in-oil emulsions was found by distilling a known volume of the emulsion with excess toluene until no water was collected as distillate. The volume of emulsion distilled and the volume of water collected were then used to calculate the quality. Emulsion H1 had an average quality of 29%, while emulsion H2 had an average of 55%.

B. Rheological Behaviour of Emulsions

The Brookfield LV model viscometer was used with the UL adaptor or spindle #1 to measure apparent viscosities of the emulsions at different shear rates (Table 4.4). All measurements were performed at room temperature. The shear stress-shear rate relationships for injected emulsions H1 and H2 are shown in Figures 4.4 and 4.5, respectively. Both emulsions generally displayed pseudoplastic behaviour. However some batches were found to behave like a dilatant fluid, e.g. Batch 3 of emulsion H2 had the n value of

Table 4.4
Rheological Data for Emulsions H1 and H2

Emulsion H1

RPM	Shear Rate (s ⁻¹)	Dial Reading	Factor	μ_{app}^{62} (mPa.s)	Shear Stress (N/m ²) $\tau = \mu_{app}(\text{Pa.s}) \times \dot{\gamma}(\text{s}^{-1})$
0.3	0.36	4.7	19.1282	89.90	0.03236
0.6	0.73	5.1	9.5641	48.78	0.03561
1.5	1.83	12.3	3.8256	47.06	0.08612
3.0	3.67	25.3	1.9128	48.39	0.17759
6.0	7.34	51.6	0.9564	49.35	0.36223

Brookfield LV Model Viscometer with UL Adaptor was used.

Emulsion H2

RPM	Shear Rate (s ⁻¹)	Dial Reading	Factor	μ_{app}^{62} (mPa.s)	Shear Stress (N/m ²) $\tau = \mu_{app}(\text{Pa.s}) \times \dot{\gamma}(\text{s}^{-1})$
0.3	0.36	1.0	200	200.0	0.0720
0.6	0.73	1.7	100	166.7	0.1217
1.5	1.83	4.2	40	166.7	0.3051
3.0	3.67	8.5	20	169.3	0.6213
6.0	7.34	17.1	10	171.3	1.2573

Brookfield LV Model Viscometer with Spindle #1 was used.

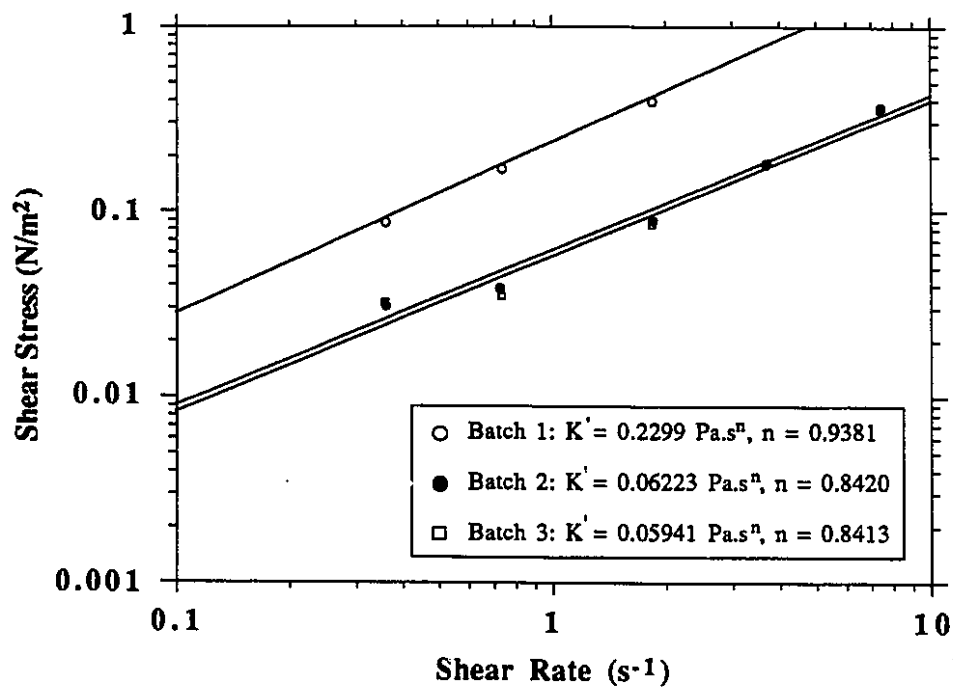


Fig. 4.4 Rheological Behaviour of Emulsion H1.

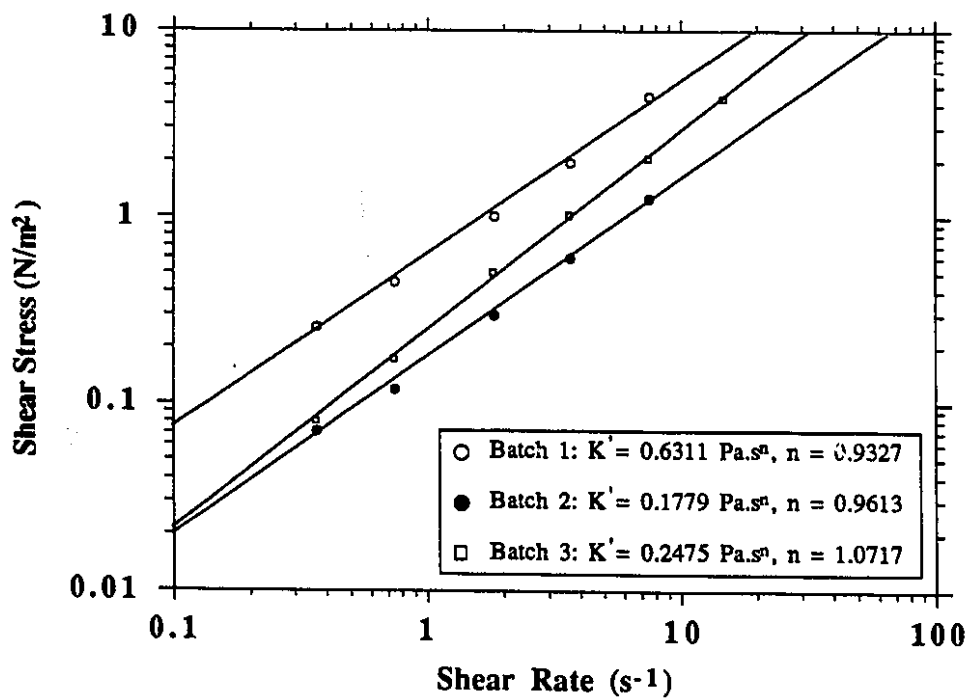


Fig. 4.5 Rheological Behaviour of Emulsion H2.

1.0717, even though the same preparation technique was applied.

C. Drop Size Distribution

The drop size distribution of an emulsion has a strong influence on its characteristics and effectiveness as an EOR agent. The Alpha Omnicon Image Analyzer was used to determine the drop size distribution. Drop-size distribution data, which is shown in Table 4.5, was obtained by examining photomicrographs of the emulsions under the Image Analyzer.

Emulsion H1 was found to contain small, medium, and large droplets that were loosely packed. Most of the particles were between 1 and 3 μm in size. A log-probability plot of the size distribution gives a mean drop diameter of 1.91 μm (Fig. 4.6). Emulsion H2 had mostly small particles that were densely packed, with most of them between 0.9 and 1.9 μm in size and a mean drop diameter of 1.44 μm (Fig. 4.7).

4.3.2 Surfactant Emulsions

A number of surfactant stabilized emulsions were prepared using the Horsefly crude oil, various surfactants, and brine. These emulsions can be grouped into two types according to the trade name of surfactant used, Petrostep emulsions and SD1000 emulsions. Emulsions were characterized by stability, quality (percent dispersed phase), rheological behaviour, and drop size distribution in

Table 4.5
Drop Size Distribution Data of Emulsion H1

Drop Size Range (μm)	Number of Drops	Frequency of Drops (%)	Cumulative Frequency
0.0 - 0.5	0.0	0.0	0.0
0.5 - 1.0	6.0	8.4	8.4
1.0 - 1.5	17.5	24.5	32.9
1.5 - 2.0	14.5	20.3	53.2
2.0 - 2.5	13.5	18.9	72.1
2.5 - 3.0	9.5	13.3	85.4
3.0 - 3.5	2.0	2.8	88.2
3.5 - 4.0	1.5	2.1	90.3
4.0 - 4.5	2.0	2.8	93.1
4.5 - 5.0	4.0	5.6	98.7
5.0 - 5.5	1.0	1.4	100.1

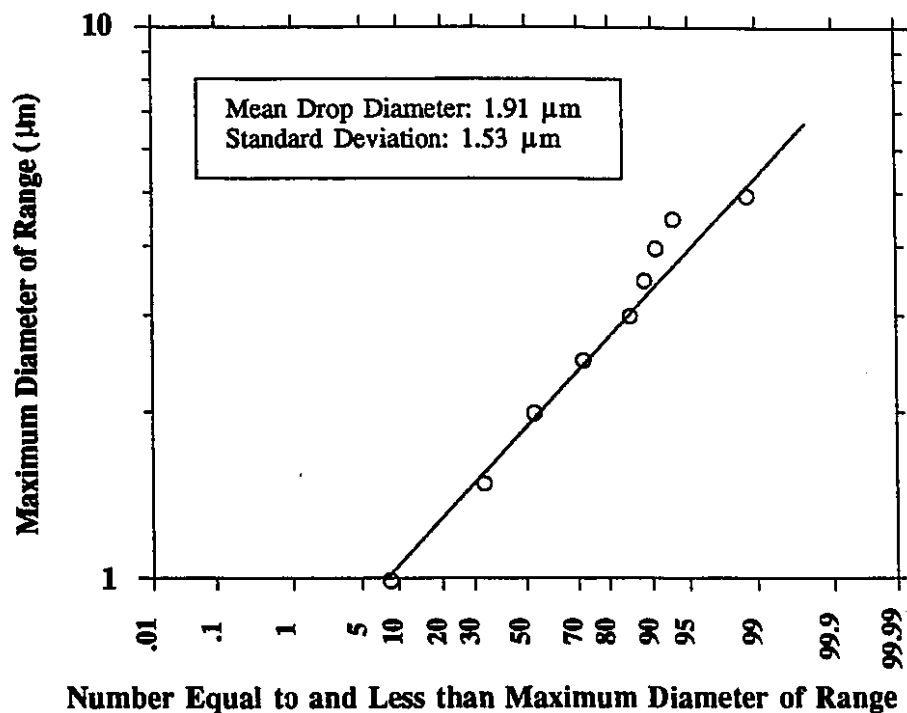


Fig. 4.6 Log-Probability Plot of Drop Size Distribution of Emulsion H1 (Batch 2).

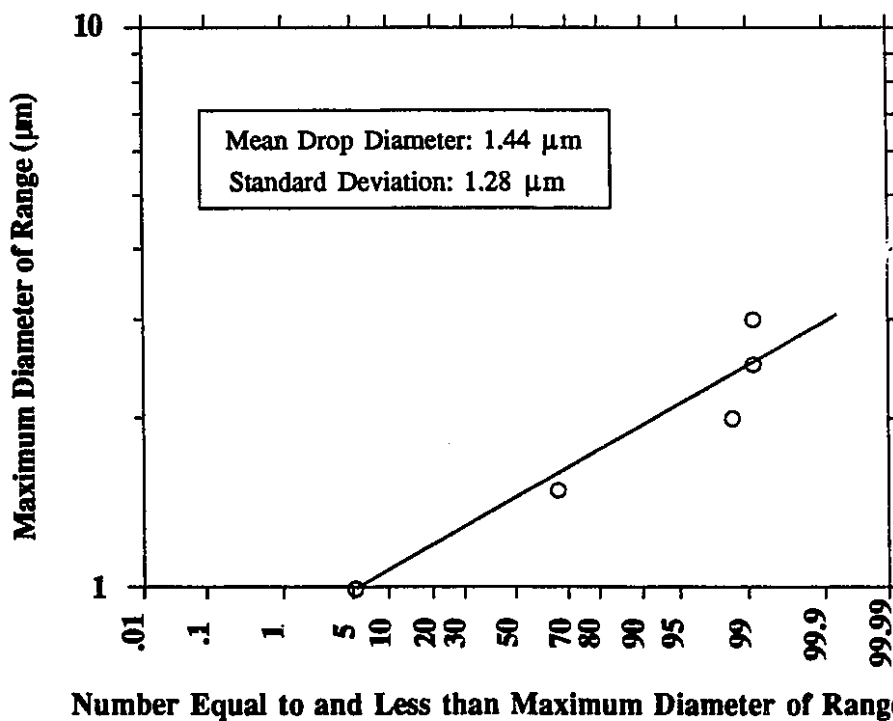


Fig. 4.7 Log-Probability Plot of Drop size Distribution of Emulsion H2 (Batch 2).

order to select suitable emulsions for core displacement tests.

4.3.2.1 Petrostep Emulsions

A. Method of Preparation

Emulsions were prepared by homogenizing the crude oil and aqueous solutions in a Brinkmann homogenizer for five minutes at 5000 rpm. The surfactant was dispersed in the oil first. The aqueous phase was then added with continuous agitation in the homogenizer. The solutions were transferred to graduated cylinders and sealed. They were allowed to equilibrate over a period of 24 hours at room temperature (24°C), and the phase volumes were noted. The top and bottom phases were then sampled and characterized.

Of the various surfactant emulsions prepared, a water-in-oil emulsion (S9T') and an oil-in-water emulsion (S9B') were chosen for core displacement tests. These emulsions were the equilibrium phases formed upon mixing the Horsefly crude, 1% sodium chloride brine, and petroleum sulfonate (Petrostep B100) in the following proportions (% volume).

Horsefly crude	-	31.65
1% sodium chloride brine	-	63.35
Petrostep B100	-	5.00

Another petroleum sulfonate emulsion (S10B) was prepared by the agent-in-oil method. Water was added to a mixture of

Horesfly crude and 1% (by weight) Petrostep B110 (o:w = 1:8), and mixed by a homogenizer at 5000 rpm for 25 minutes. The bottom phase, which was a dilute oil-in-water type emulsion, was chosen for characterization and use in core flood #21.

B. Characterization of Emulsion S9T'

This water-in-oil type emulsion was stable at room temperature and showed no signs of phase separation over a period of two months. Its quality, rheological behaviour, and drop size distribution were determined.

B.1 Quality of Emulsion S9T'

The quality (volume percent dispersed phase) of the emulsion was found by distilling 25 ml of the emulsion with excess toluene for six hours. The quality range of the emulsion S9T' prepared three times was calculated to be 1 to 6%.

B.2 Rheological Behaviour of Emulsion S9T'

Emulsion rheological behaviour was determined with a Brookfield viscometer. The shear stress-shear rate relationship of emulsion S9T' is shown in Fig. 4.8. Dilatant behaviour was apparent from the value of 1.1383 for the flow behaviour index. The reproducibility of the rheological properties of this emulsion was rather poor. Although they were prepared using the same procedure, some batches were pseudoplastic, while others were dilatant.

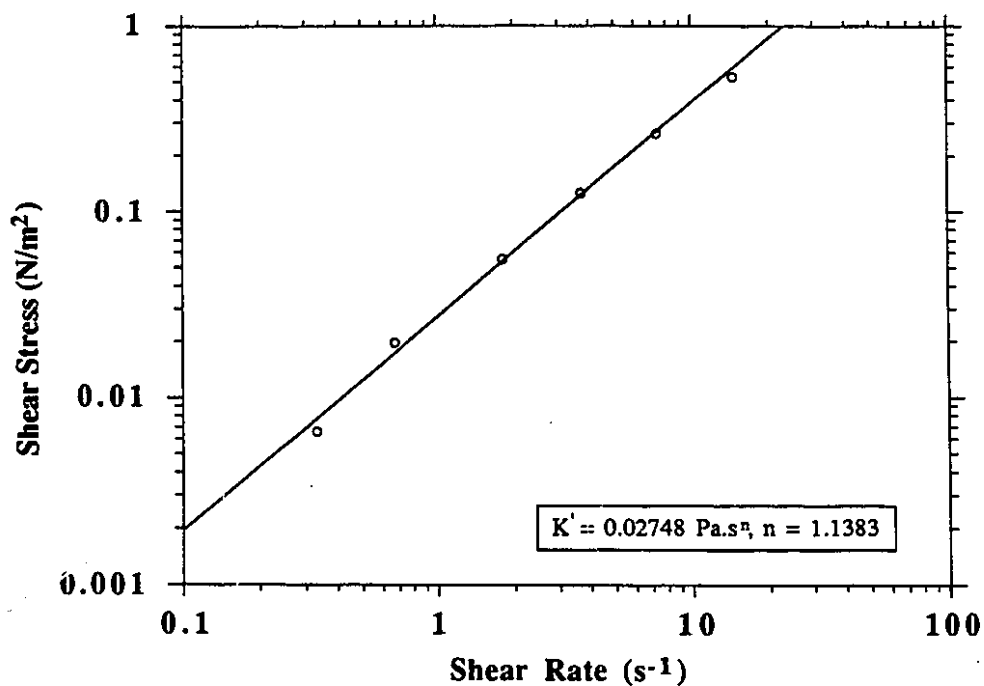


Fig. 4.8 Rheological Behaviour of Emulsion S9T'.

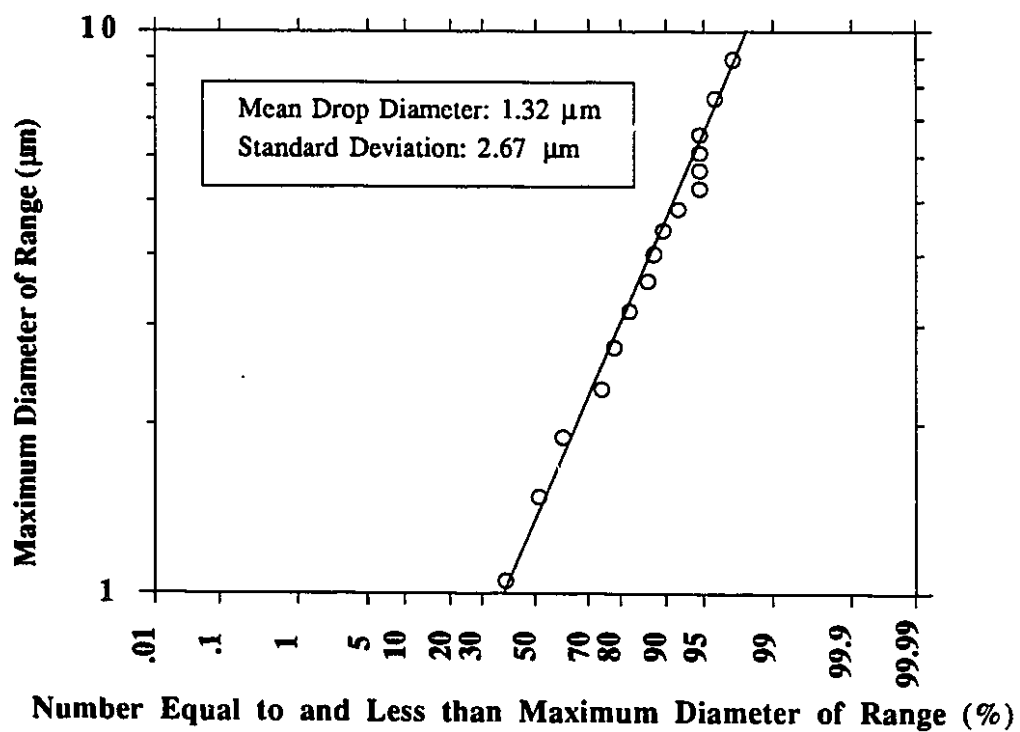


Fig. 4.9 Log-Probability Plot of Drop Size Distribution of Emulsion S9T'.

B.3 Drop Size Distribution of Emulsion S9T'

Drop size distribution of the emulsion was determined from photomicrographs using an Alpha Omnicon Image Analyzer. It was found that most of the droplets were between 0.9 and 1.2 μm in size, with less than 3% of the droplets larger than 2 μm and a mean diameter of 1.32 μm (Fig. 4.9).

C. Characterization of Emulsion S9B'

This oil-in-water type emulsion showed good stability at room temperature, and was characterized by rheological behaviour and drop size distribution.

C.1 Rheological behaviour of Emulsion S9B'

The emulsion showed pseudoplastic characteristics ($n = 0.7239$, shown in Fig. 4.10).

C.2 Drop Size Distribution of S9B'

Based on an analysis of photomicrographs, it was found that this emulsion had a drop size distribution smaller than that of the water-in-oil type emulsion S9T'. Most of the droplets were between 0 and 0.8 μm in size, with a mean drop diameter of 0.50 μm (Fig. 4.11).

D. Characterization of Emulsion S10B

The rheological behaviour and drop size distribution were found using the previously described procedures. The emulsion showed pseudoplastic behaviour ($n = 0.6388$, shown in Fig. 4.12). Furthermore, it had a relatively small drop

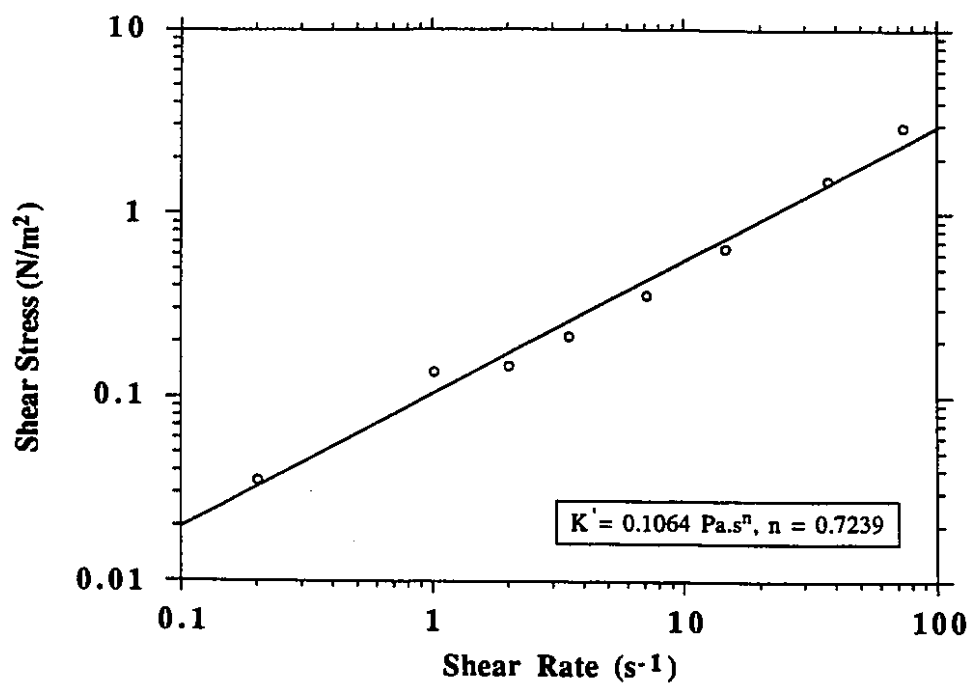


Fig. 4.10 Rheological Behaviour of Emulsion S9B'.

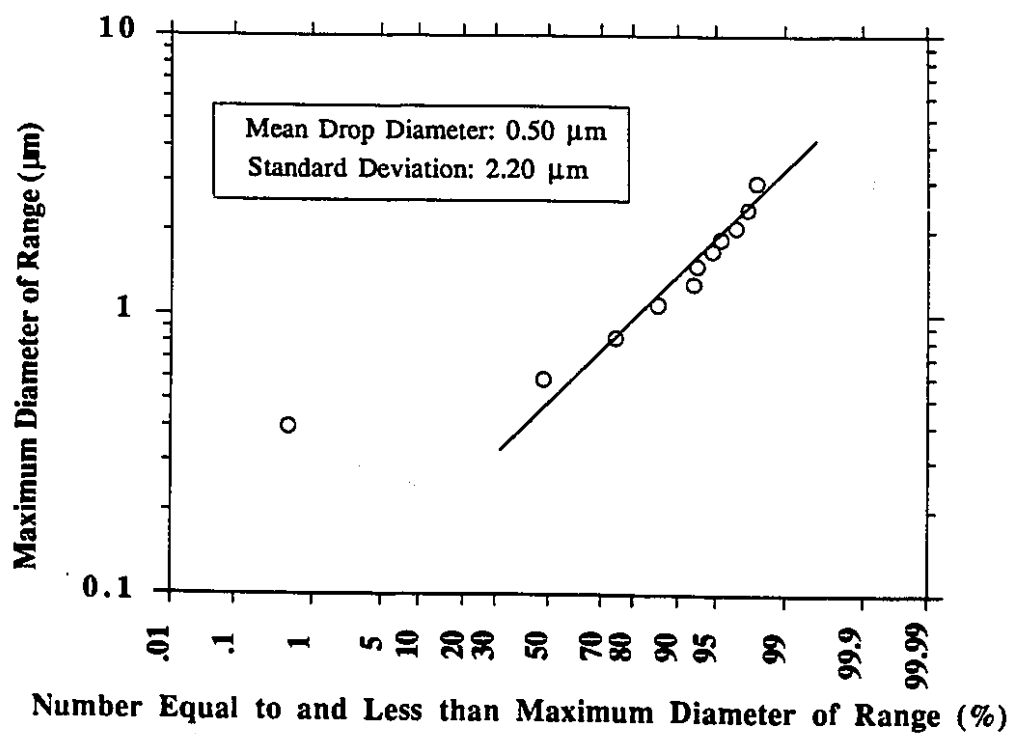


Fig. 4.11 Log-Probability Plot of Drop Size Distribution of Emulsion S9B'.

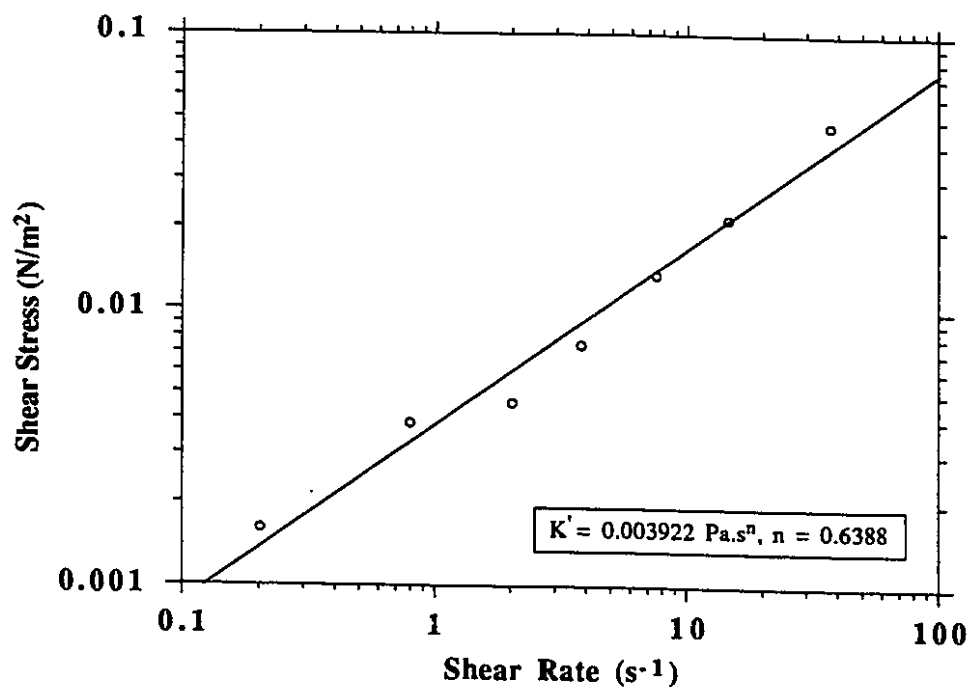


Fig. 4.12 Rheological Behaviour of Emulsion S10B.

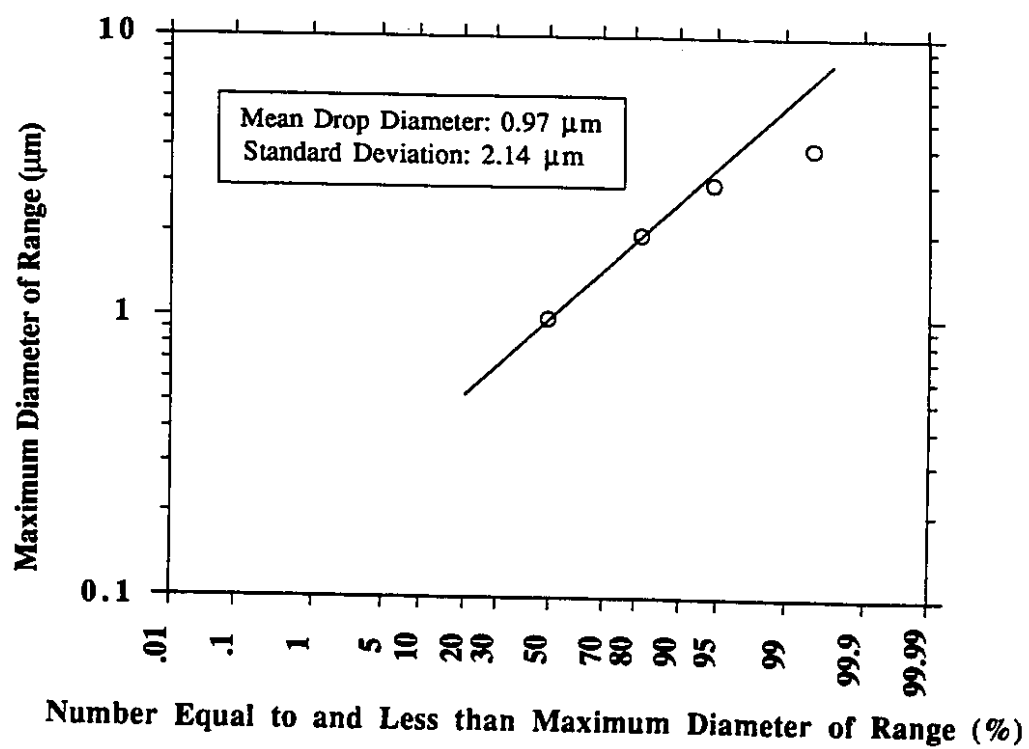


Fig. 4.13 Log-Probability Plot of Drop Size Distribution of Emulsion S10B.

size, with most of the droplets between 0 and 1 μm in size. A mean drop diameter of 0.97 μm is shown in the log-probability plot (Fig. 4.13).

4.3.2.2 SD1000 Emulsions

The surfactant used was Chevron Chaser SD1000, manufactured by the Chevron Chemical Company, which is an anionic alkyl sulfonate. It is a hydrophilic surfactant, meaning it forms good oil-in-water type emulsions with crude oil and brine.

A. Preparation and Characterization

Emulsion H3 was prepared using the agent-in-oil method. It was a (water-in-oil)-in-water type double emulsion, meaning that it is essentially an oil-in-water type emulsion except that the oil droplets have smaller water droplets dispersed in them. The formation of this double emulsion is thought to be due to the surfactant being dispersed in a medium contrary to its characteristics. That is, in preparing the emulsion, the SD1000, a hydrophilic surfactant, was first dispersed in the oil. The aqueous phase was then gradually added to the oil-surfactant mixture. No significant signs of flocculation or coalescence were observed, although many of the oil droplets were irregular in shape and not perfectly spherical. The emulsion remained stable to phase separation over several weeks. The emulsion was pseudoplastic ($n = 0.4702$) with the consistency index of 0.3425 $\text{Pa}\cdot\text{s}^n$. The apparent viscosity ranged from 450 to 31

mPa.s for shear rates between 0.36 and 73.40 s^{-1} , which is the maximum rpm of the Brookfield viscometer used. Emulsion batches prepared at different times showed good rheological reproducibility. In fact, the change in apparent viscosity was between 0 and 2 mPa.s for all shear rates used. The rheological behaviour of the emulsion is shown in Fig. 4.14.

Emulsion H4, an oil-in-water type emulsion, was prepared using the agent-in-water method. Some flocculation and coalescence were observed. Excess brine separated from the emulsion about eight hours after it was prepared. The emulsion was pseudoplastic ($n = 0.4685$) with the consistency index of 0.3590 Pa.s^n . The apparent viscosity ranged from 500 to 33 mPa.s at shear rates between 0.36 and 73.40 s^{-1} . The emulsion rheological behaviour is shown in Fig. 4.15.

Emulsion H5 was the stable emulsion formed when emulsion H4 was aged for two days. The free water that separated from H4 was removed and the top phase, emulsion H5, was used in core flooding experiments. The emulsion composition was found using material balance and UV methods for surfactant content. This water-in-oil type emulsion had pseudoplastic characteristics ($n = 0.4381$, shown in Fig. 4.16). The apparent viscosity was higher than that of H3 and H4 at the same shear rates. This can be seen from the consistency index of 1.5174 in comparison with that of 0.3425 for emulsion H3 and that of 0.3590 for emulsion H4.

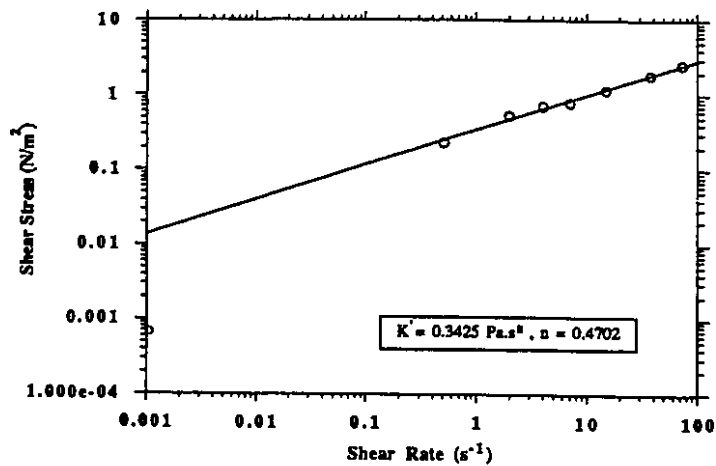


Fig. 4.14 Rheological Behaviour of Emulsion H3.

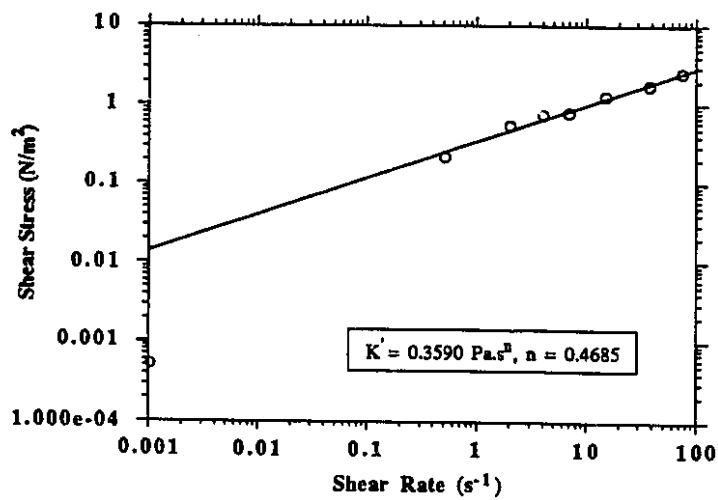


Fig. 4.15 Rheological Behaviour of Emulsion H4.

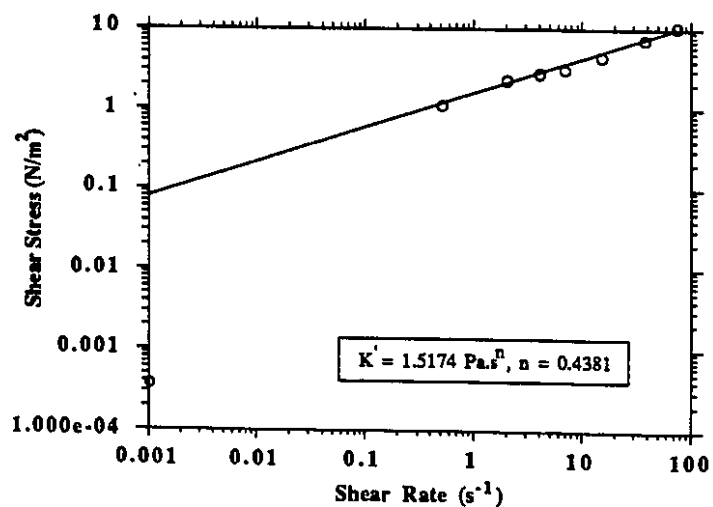


Fig. 4.16 Rheological Behaviour of Emulsion H5.

Compositions of the surfactant emulsions H3, H4, and H5 are shown in Table 4.6.

Table 4.6
Composition of Surfactant Emulsions

Emulsions	Composition (% volume)			
	Type	Horsefly Crude	1% w/v NaCl	Surfactant SD1000
H3	o/w	41.0	50.0	9.0
H4	o/w	44.5	47.8	7.7
H5	w/o	57.7	38.1	4.25

4.4 Core Displacements Tests

The following is a discussion of the core floods chosen from the core displacement tests carried out in Ref. 59, which are grouped according to their objectives. A summary chart of the selected runs is shown in Fig. 4.17. Summaries of these core floods are shown in Tables 4.7, 4.8, and 4.9.

4.4.1 Experimental Core Floods to Observe Rheological and Filtration Behaviour

The following set of core floods was carried out with the purpose of observing rheological behaviour and confirming the filtration process postulated by Soo and Radke^{47,48}. This occurs during the flow of both oil-in-water and water-in-oil emulsions through porous media.

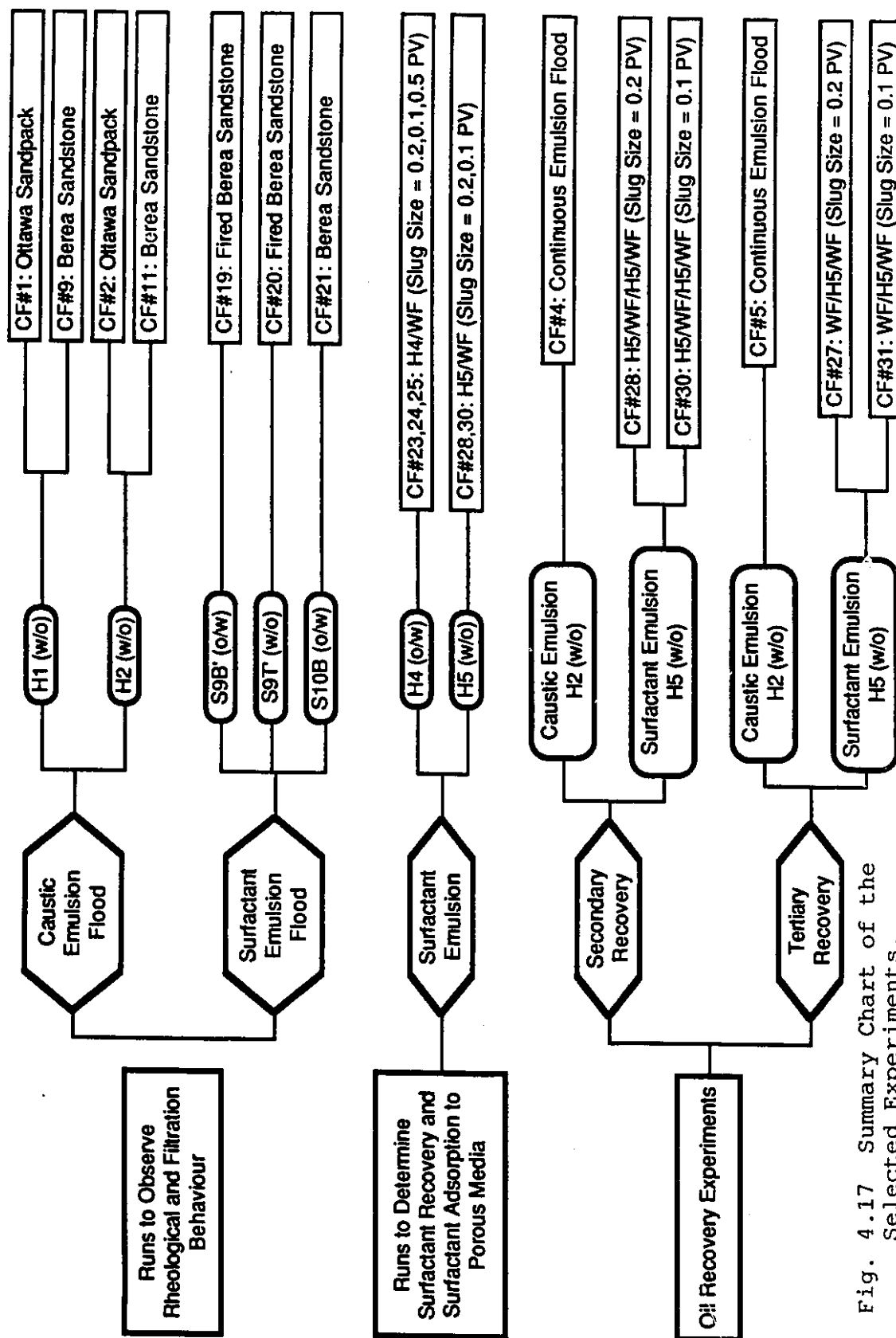


Fig. 4.17 Summary Chart of the Selected Experiments.

Table 4.7
Summary of Selected Core Floods between 1 - 21

No.	Properties of Porous Media			Flood Description	Emulsion	Parameters Investigated	Findings
	Type	PV (ml)	k (d)	Porosity (% PV)			
1	Ottawa sand	501	6.61	26.90	H1	Rheology behaviour of injected and produced emulsions	Rheological behaviour of inj. & prod. emulsions was similar
2	Ottawa sand	781	6.60	41.60	H2	Same as above	Same as above
4	Ottawa sand	729	8.25	38.82	H2	Oil displacing efficiency of emulsion H2	Sec. Rec. (emulsion H2) = 34 %OOIP
5	Ottawa sand	723	7.95	38.51	H2	Same as above	Sec. Rec. (waterflood) = 71.34 %OOIP, Tert. Rec. (emulsion H2) = 82.6 %OIP
9	Berea	171	0.38	14.28	H1	Same as above	Inj. & prod. emulsions showed similar rheology. Larger drops plugged the pores.
11	Berea	256	0.59	21.37	H2	Same as above	Same as above
19	Fired Berea	266	0.41	22.21	S9B'	Characterize and compare emulsions injected and produced	Double emulsions formed in situ were reconstituted to original emulsion with time
20	Fired Berea	251	0.51	20.96	S9T'	Same as above	Emulsion rheology in porous media varied slightly from that observed externally
21	Unfired Berea	224	0.42	18.70	S10B	Flow behaviour of emulsion with smaller drop size than pore size	Small oil drops could be captured on pore walls and produced at high flow rates

Table 4.8

Summary of Core Floods (23, 24, & 25)

(Loss of Crude and Surfactant to the Porous Medium)

No.	Run Type	PV (ml)	Perm. (μm^2)	Porosity (%)	Front Velocity (m/day)	Emulsion		Surf. Loss (mg/g Sand)	Loss of Crude	
						Type	Size (% PV)		% Inj.	mg/100 g Sand
23	Core saturated with 1% NaCl	768	11.07	40.91	7.62	H4	20	0.22	55.6	1.25
24	Core saturated with 1% NaCl	733	7.15	39.04	7.99	H4	10	0.09	35.54	0.38
25	Core saturated with 1% NaCl	722	18.58	41.12	7.59	H4	50	3.22	63.28	3.67

Table 4.9

Summary of Core Floods 27 - 31

(Emulsion Flood)

No.	Run Type	PV (ml)	Perm. (μm^2)	Porosity (%)	Sol (% PV)	Sor (% PV)	Front. Velocity (m/day)	Emulsion Slug			WF Rec. & IOIP	Tert. Rec. & OIP	Process Efficiency	
								Type	Size	% HCPV			ml/ml Emul.	ml/g Surf.
27	WF													
	Emul.; WF	530	9.33	28.23	98.11	-	11.05	-	-	-	75.50	-	-	-
	"	"	"	"	"	22.68	"	H5	88.3	20.0	-	-7.15	3.99	83.27
28	Emul.; WF	663	9.92	35.31	93.06	-	8.83	H5	21.6	20.0	78.50	-	3.59	74.82
30	Emul.; WF (Sec.)	694	12.67	36.97	90.78	-	8.43	H5	13.0	11.5	76.8	-	6.05	126.34
31	WF													
	Emul.; WF	659	7.75	35.10	88.01	-	8.89	-	-	-	71.55	-	-	-
	"	"	"	"	"	25.04	8.89	H5	40.0	10.0	-	2.24	0.20	3.16

Definitions:

Emul. Emulsion
HCPV Hydrocarbon Pore Volume %
Surf. Surfactant
Tert. Tertiary Recovery
WF Waterflood

Tertiary Recovery (% OIP) = Oil Recovered - (Oil in place at the start of the flood
+ Oil in the Emulsion Injected)

4.4.1.1 Caustic Emulsion Floods

Two types of caustic emulsions, H1 and H2, were used in this set of five core floods. Emulsion H1 was used in core floods #1 and #9, while emulsion H2 was used in core floods #2, and #11.

A. General Flood Description

The porous medium was initially saturated with 2% NaCl brine. The desired emulsion was then injected at varying flow rates until approximately two pore volumes had been injected. During this period, the injection pressure and differential pressure between two taps midway along the core were measured using pressure transducers and recorded by the chart recorder. These data were later analyzed to compare the rheological behaviour of emulsion flow in a porous medium with the rheological behaviour of an injected emulsion as measured by a viscometer. The produced emulsions were characterized and compared with the injected emulsions, which permitted an interpretation of the emulsion transport mechanism in porous media to be made. The pH of the produced water was also measured in each core flood to distinguish between the water in the emulsions and the reservoir water.

In addition to a general flood description for core floods #9 and #11, a 2% NaCl waterflood followed the emulsion flood at varying flow rates until about two pore volumes of the

brine were injected. The effluent emulsion produced during the waterflood was characterized and compared with the effluent emulsion produced during the emulsion flood in order to observe the effect of injection flow rate on captured droplets.

B. Results

The emulsion breakthrough occurred at 0.8 to 0.9 pore volumes (PV). The rheological behaviour of the injected emulsion H1 (Batch 1 and Batch 2) is shown in a plot of shear stress versus shear rate (Fig. 4.18 for core flood #1 and Fig. 4.19 for core flood #9), while the rheological behaviour of the same emulsion during the flow through porous media is shown in a plot of pressure drop versus velocity (Fig. 4.18 for core flood #1, which used Ottawa sand, and Fig. 4.19 for core flood #9, which used Berea sandstone). By comparing the two rheological behaviours within the same average shear rate range, emulsion H1 was found to exhibit non-Newtonian behaviour in the same degree of deviation from Newtonian behaviour. This can be seen from the almost identical slope in the two rheograms within the average shear rate range of 4 to 40 s^{-1} for the Ottawa sand for the velocity range of 3.6×10^{-6} to 3.6×10^{-5} m/s, and 50 to 500 s^{-1} for the Berea core for the velocity range of 5.7×10^{-6} to 5.7×10^{-5} ml/hr. A similar result was found for emulsion H2, which was used in two different porous media, namely Ottawa sand and Berea sandstone. These

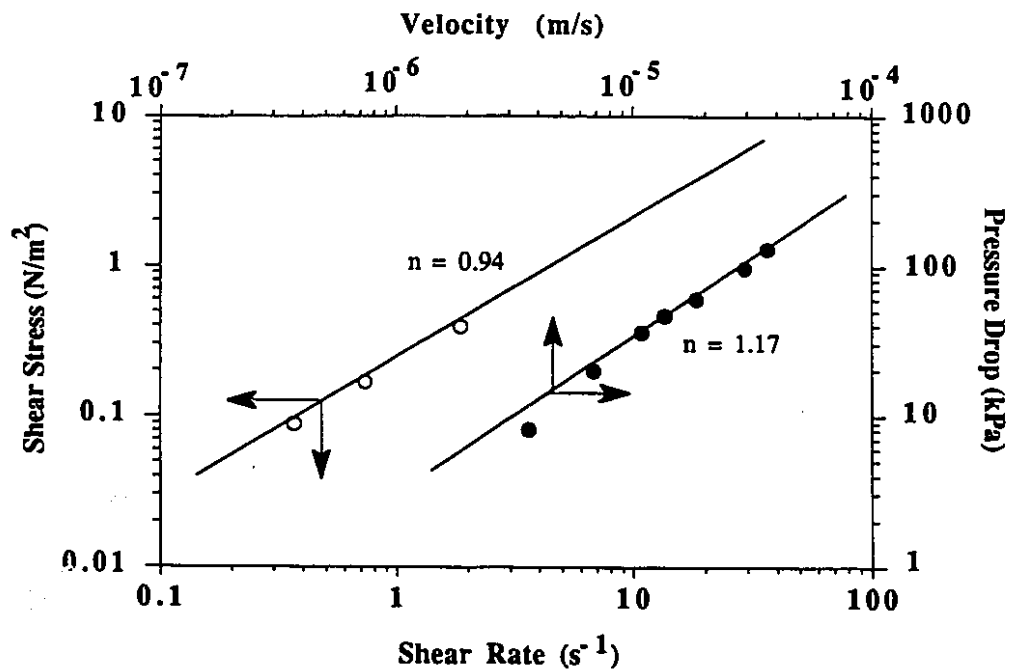


Fig. 4.18 Rheological Behaviour of Emulsion H1 (Batch 1) in Viscometer and in porous Medium (CF #1 Sand Pack).

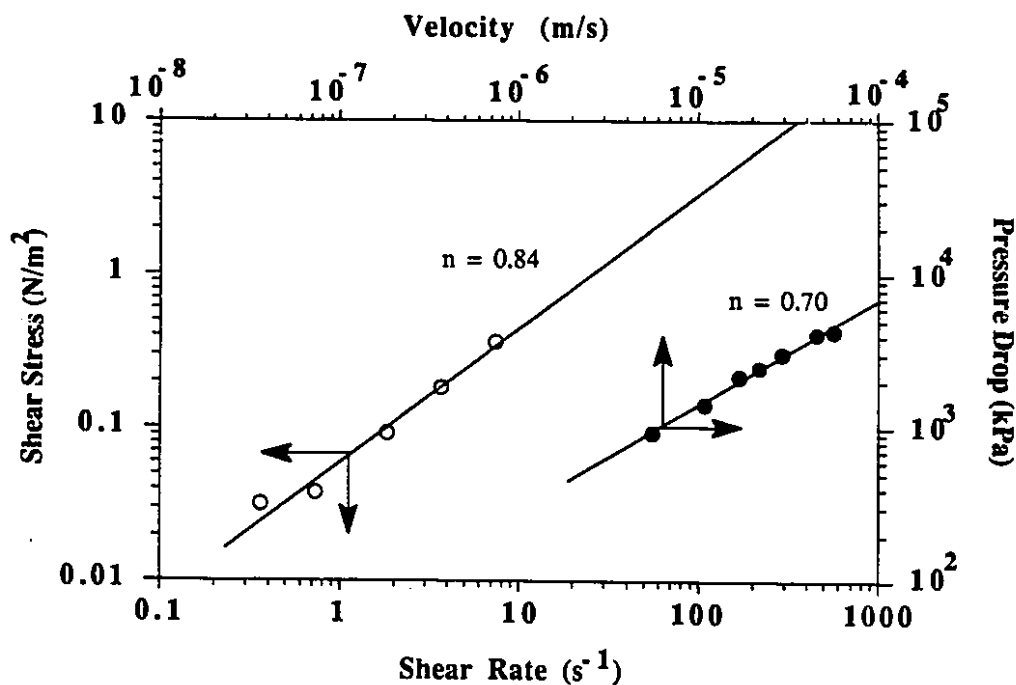


Fig. 4.19 Rheological Behaviour of Emulsion H1 (Batch 2) in Viscometer and in Porous Medium (CF #9 Berea Sandstone).

media were used in core floods #2 and #11, respectively (Figs. 4.20 and 4.21). In conclusion, these results show that the rheological behaviour of emulsions H1 and H2 during flow in porous media is practically the same as that in a viscometer over the same range of average shear rates.

The characteristics of the injected and produced emulsions, which are the quality, rheological behaviour, and drop-size distribution, were compared to determine how emulsion droplets are transported through porous media and to determine if the droplet capture mechanism described by Soo and Radke could explain what was observed. A summary of these characteristics for each core flood is given in Table 4.10. All of the produced emulsions obtained during emulsion flooding at various flow rates were used to determine the produced emulsion characteristics.

The quality and viscosity of the produced emulsions were lower than those of the injected emulsions. Furthermore, the droplet size of the produced emulsions was smaller than that of the injected emulsions. The only exception to this trend was observed in core flood #9. In spite of the fact that the water content of the effluent was only 1% during the emulsion flood and the subsequent waterflood for this core flood, the viscosities of the produced emulsions in both cases were surprisingly higher than those of the injected emulsions.

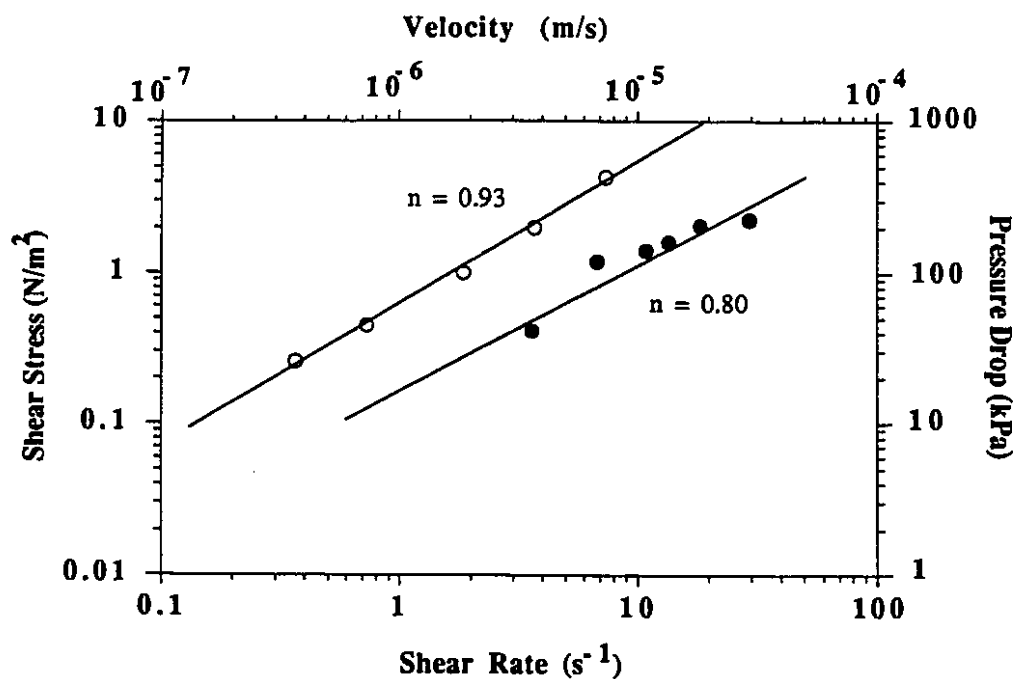


Fig. 4.20 Rheological Behaviour of Emulsion H2 (Batch 1) in Viscometer and in porous Medium (CF #2 Sand Pack).

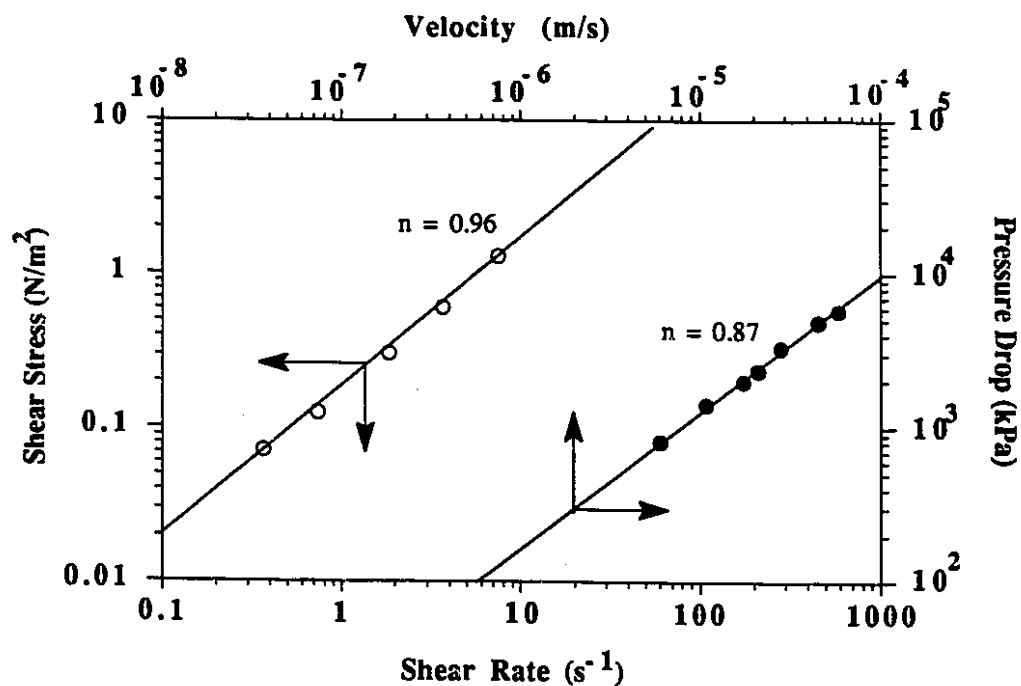


Fig. 4.21 Rheological Behaviour of Emulsion H2 (Batch 2) in Viscometer and in Porous Medium (CF #11 Berea Sandstone).

Table 4.10
Characteristics of Injected and Produced Caustic Emulsions

Core Flood No.	Emulsion Injected & Produced	Properties				
		Type	Quality (% Disp. Phase)	Rheology	% Change in Viscosity	Drop Size Distribution Mean Drop Diameter (μm) Standard Deviation (μm)
1	H1 - inj. -prod.	w/o w/o	29.3 3.6	pseudoplastic pseudoplastic	-62	- -
2	H2 - inj. -prod.	w/o w/o	52.8 56.8	pseudoplastic pseudoplastic	-25	- -
3	H2 - inj. -prod.	w/o w/o	57.5 47.5	pseudoplastic pseudoplastic	-57	- -
9	H1 - inj. -prod. -prod. (WF)	w/o w/o w/o	4.8 1.0 1.0	pseudoplastic pseudoplastic pseudoplastic	70 82	1.91 - -
11	H2 - inj. -prod. -prod. (WF)	w/o w/o w/o	33.2 8.8 5.5	pseudoplastic pseudoplastic pseudoplastic	-4 0	1.44 - 0.53* 1.52** 1.28 - 1.86* 1.35**

* Emulsion produced at low flow rate.

** Emulsion produced at high flow rate.

By analyzing the foregoing observed characteristics of the injected water-in-oil emulsions, the emulsion flow mechanisms can be interpreted as follows. The lower quality of the produced emulsion before steady state is attained indicates that the dispersed phase must encounter constrictions in the core that delays its flow relative to the continuous phase. In other words, the loss of water droplets due to filtration in the porous medium accounts for the lower quality and the reduction in produced emulsion viscosity. Further evidence of this filtration process was found by comparing the drop size distribution of the injected emulsions to that of the produced emulsions when they flow through porous media of a known pore size distribution. Core floods #9 and #11, which used emulsions H1 and H2, respectively, and Berea sandstone cores, were used to investigate this aspect of the flow mechanism.

The pore size distribution of the Berea core was calculated from the capillary pressure curve data. Capillary pressure curve data and the pore size distribution data of the Berea core are shown in Tables 4.1 and 4.2, respectively. Figure 4.3 shows the log-probability plot to the pore size distribution of the Berea core, which has a mean pore diameter of 0.80 μm .

Figure 4.6 shows the log-probability plot of the drop size distribution for the injected emulsion H1 (Batch 2 for core

flood #9). The injected emulsion has a mean drop diameter of $1.91\text{ }\mu\text{m}$, which is larger than the mean pore diameter observed for the Berea sandstone. The emulsion produced during emulsion flooding in core flood #9 had only a 1% quality, and appeared as clear oil under the microscope. This confirms that the straining mechanism described by Soo and Radke was dominant. This can be explained in that the injected emulsion droplets had a mean diameter that was large relative to the mean pore diameter. Therefore, these large droplets plugged the smaller pore throats. Since the mean drop size to pore size ratio for this system is 2.39, Soo's findings verify the use of the straining mechanism as an explanation for the experimental results. Only small droplets would be able to percolate ahead of the larger ones in the porous medium, and this would explain the low water content in the effluent emulsion. Given the size of the droplets relative to the pores, it would take a long time for this system to reach steady state. The produced water during the waterflood was more alkaline ($\text{pH} = 9.35$) than the in-place brine ($\text{pH} = 8.01$). The increase in pH might be due to the larger droplets, that had previously plugged the pores, being forced out during the waterflood.

The drop size distribution of emulsion H2 shown in Fig. 4.7 gave a mean drop diameter of $1.44\text{ }\mu\text{m}$ and a mean drop to pore size ratio of 1.80. According to Soo's observations, this ratio indicates that the drop capture which took place

during the initial emulsion flooding in core flood #11 was predominantly due to straining. During the waterflood that followed the emulsion flood, the emulsion that was produced at a low frontal velocity of 11.44 m/day had a mean drop diameter of $0.53\text{ }\mu\text{m}$ (Fig. 4.22), whereas the emulsion that was produced at a high frontal velocity of 22.88 m/day had a mean size of $1.52\text{ }\mu\text{m}$ (Fig. 4.23). These observations can be explained by droplet squeezing. At the initially low waterflood rate, the larger drops in the injected emulsion become plugged in the pore throats, while the smaller drops are able to move ahead through the core. Thus, only the smaller drops are eluted, and the resulting produced emulsion has a mean drop size of about one-half of that of the injected emulsion. When the flow rate is doubled, the pressure gradient experienced by the drops plugged in the pore throats becomes sufficient to squeeze these drops through the constrictions and cause them to be eluted. Hence, the resulting emulsion effluent has a mean pore size which is slightly greater than that of the injected emulsion.

Summarizing the previous findings, when the mean drop diameter to mean pore diameter ratio is very high, the produced emulsion will contain only the very smallest drops, the rest being captured in the pore throats. In the case where drop size is comparable to pore size, an increase in flow rate can raise the pressure gradient within the porous

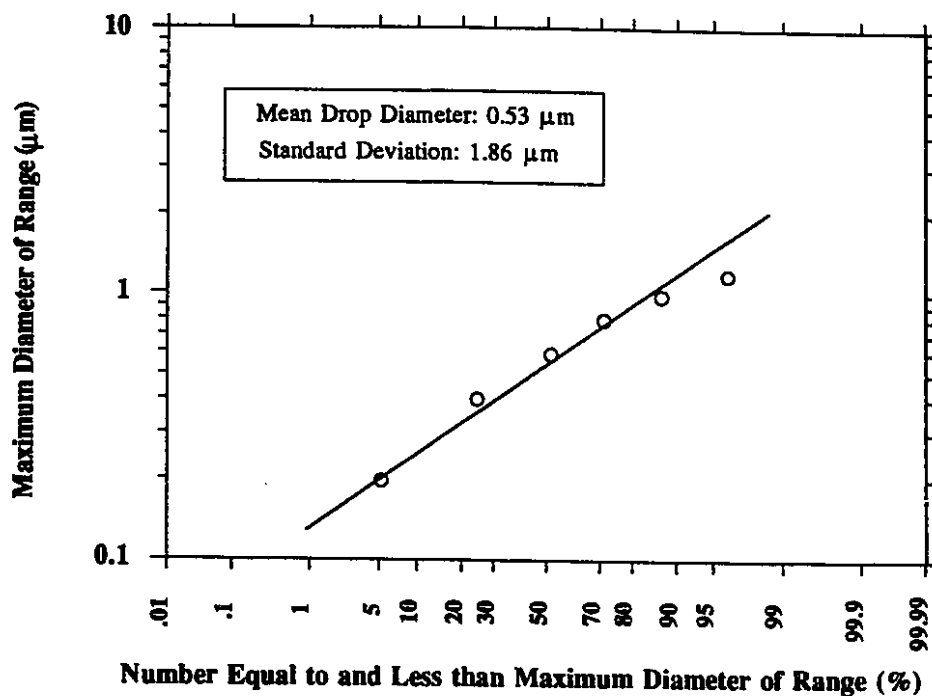


Fig. 4.22 Log-Probability Plot of Drop Size Distribution of Produced Emulsion H2 at Low Flow Rate (CF#11).

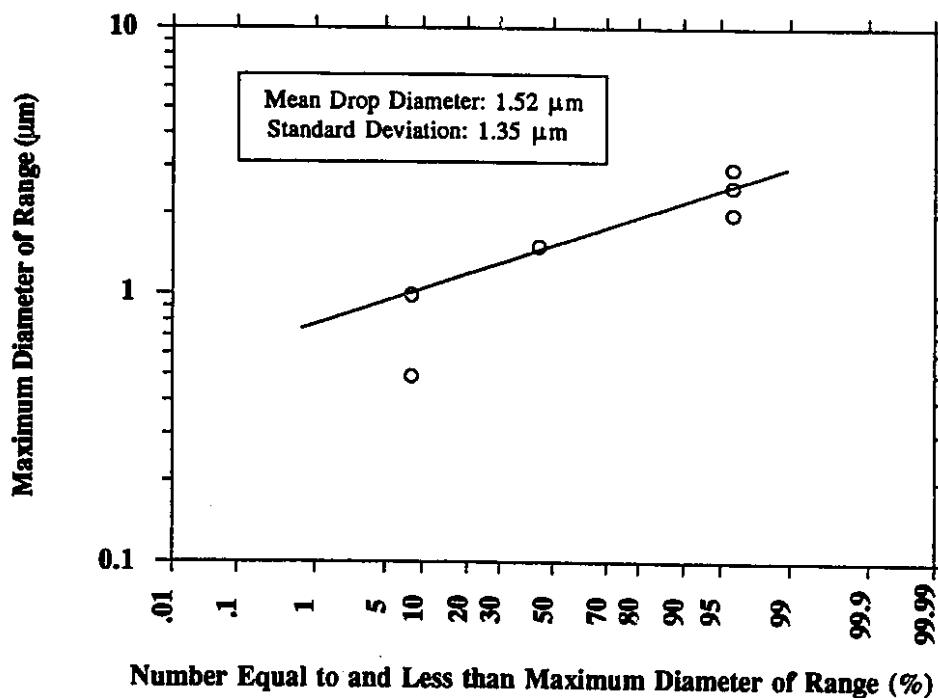


Fig. 4.23 Log-Probability Plot of Drop Size Distribution of Produced Emulsion H2 at High Flow Rate (CF#11).

medium sufficiently to squeeze captured drops through the pore constrictions and cause them to elute.

4.4.1.2 Surfactant Emulsion Floods

Surfactant emulsions S9T', S9B', S10B, and H3 were used for this set of experimental runs. As described in earlier sections, emulsions S9T' (water-in-oil) and S9B' (oil-in-water) are the equilibrium phases formed upon mixing Horsefly crude, 1% NaCl brine, and petroleum sulfonate (Petrostep B100), while emulsion S10B (oil-in-water) is the bottom phase formed upon mixing Horsefly crude, brine, and Petrostep B110. Core floods #19 and #20 were chosen to represent the study of the flow of oil-in-water and water-in-oil surfactant emulsions (S9B' and S9T'), respectively, in a fired Berea core. Furthermore, core flood #21 was carried out to examine the flow mechanism of emulsion S10B, which has a drop-size that is small relative to the pore-size of the core. The final run for this group of studies was core flood #22, in which the surfactant emulsion H3, a mixture of Horsefly crude, brine, and SD1000, was used in an Ottawa sand.

A. Flood Description

For core floods #19 and #20, the cores were initially saturated with brine (2% sodium chloride in distilled water). The emulsion flood was then started at a rate of 400 ml/hr and continued until emulsion breakthrough.

Following breakthrough, the rate was varied from 400 down to 40 ml/hr in several steps to examine the effect of pressure gradient on the produced emulsion characteristics. The effluent was sampled at the different flow rates and its drop size distribution analyzed. The injection pressure and the core mid-point pressure differential were monitored throughout the flooding process. The rheological behaviour of the emulsion before, during, and after flow through the porous medium was compared using viscosity measurements and correlations of shear stress versus shear rate and pressure drop versus velocity. The flood description for core flood #21 is similar to that of the previous core floods, except that the brine used to saturate the core was 0.2% (w/v) sodium chloride in distilled water. The flooding rate was 75 ml/hr initially, and was increased to 400 ml/hr in several steps.

For core flood #22, a continuous emulsion flood was performed in an Ottawa sand pack core saturated with 1% NaCl brine at a rate of 400 ml/hr until emulsion breakthrough. The flood rate was varied in a similar way as described above until about 2.5 PV of the emulsion were injected. Following the emulsion flood, a 1% NaCl waterflood was carried out until about 5.2 PV were injected.

B. Results for Emulsions S9T' and S9B'

Emulsion breakthrough occurred at 0.96 PV injected and an injection pressure of 439 kPa for the flow of the oil-in-water emulsion S9B' in core flood #19. It occurred at 0.73 PV injected and an injection pressure of 2928 kPa for the flow of the water-in-oil emulsion S9T' in core flood #20. Injection pressure varied from 439 to 212 kPa in core flood #19, compared with 2928 to 460 kPa in core flood #20 for flow rates between 400 and 40 ml/hr. The higher injection pressure is required to make the more viscous emulsion flow at the same rate.

Figures 4.24 and 4.25 show the rheological behaviour of the injected emulsion S9B' in core flood #19 and that of injected emulsion S9T' in core flood #20, respectively. The rheological behaviours of the same emulsions flowing in fired Berea cores are also shown in Figs. 4.24 and 4.25, respectively. The rheograms for the oil-in-water emulsion S9B' and the water-in-oil emulsion S9T' were compared within the same shear rate range. The resemblance between the rheological behaviour of the emulsions in the porous media and those formed in a viscometer was not as close as it was in the case of the caustic emulsions. This can be seen from the greater difference between the slopes in Figs. 4.24 for emulsion S9B', and Figs. 4.25 for emulsion S9T'.

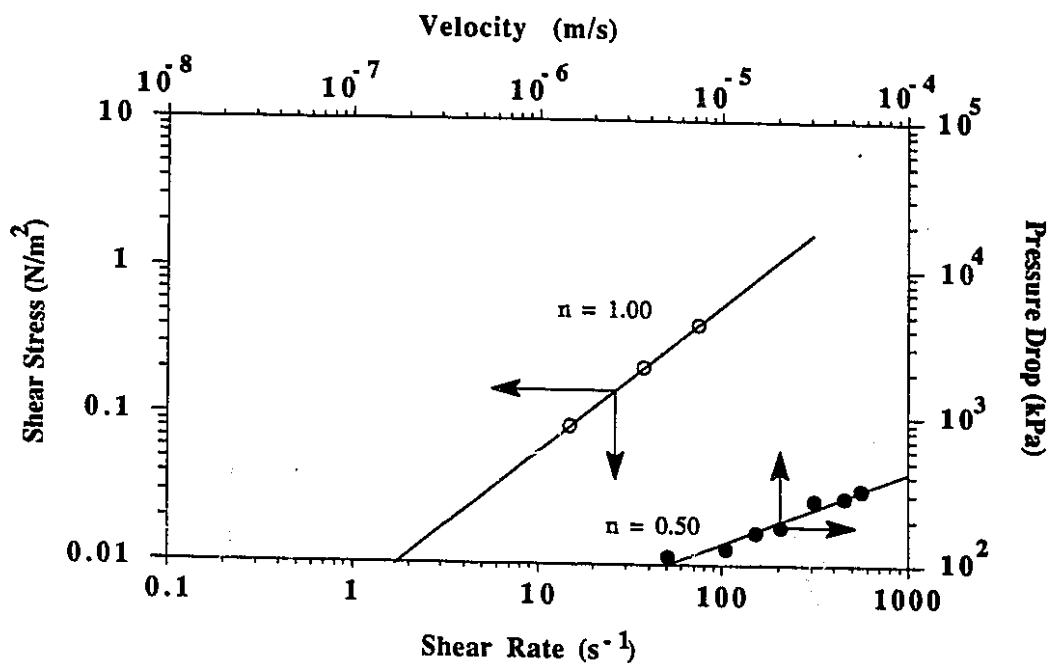


Fig. 4.24 Rheological Behaviour of Emulsion S9B' in Viscometer and in Porous Medium (CF #19 Fired Berea Sandstone).

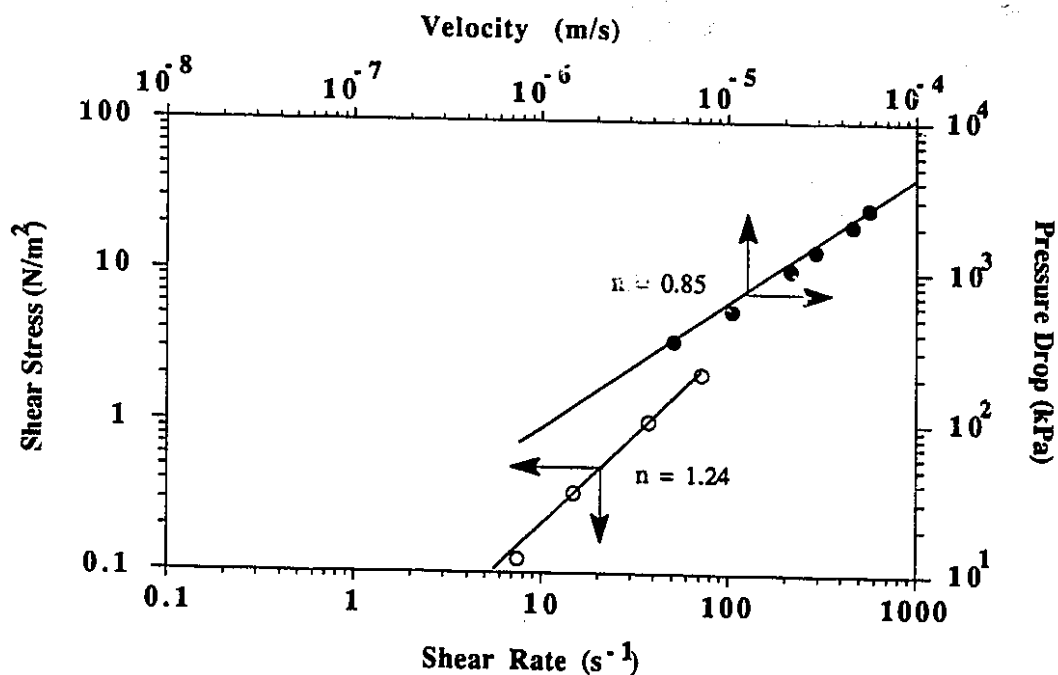


Fig. 4.25 Rheological Behaviour of Emulsion S9T' in Viscometer in Porous Medium (CF #20 Fired Berea Sandstone).

The characteristics of injected and produced emulsions for core flood #19 were found to be Newtonian with viscosities of 6 mPa.s and 5.4 mPa.s, respectively. When viewed under the microscope, the effluent at various shear rates was an unstable double emulsion. That is, it was a (water-in-oil)-in-water, (w/o)/w, and an (oil-in-water)-in-oil, (o/w)/o, co-existing with small droplets of oil dispersed in water. The double emulsion droplets were unstable, large, and irregular in shape. However, when this emulsion was allowed to settle at room temperature for several hours (about 12 hours), the droplets became redistributed and formed an oil-in-water type emulsion, similar to the injected emulsion. A comparison of the drop size distribution of the injected emulsion and a cumulative sample of the produced emulsion, as shown in Table 4.11 below, revealed a higher percentage of smaller droplets in the produced emulsion than in the injected emulsion.

Table 4.11

Drop-Size Distribution of Injected and Produced Emulsions

S9B' (CF #19)

Size Range (μm)	% Drops in Injected Emulsion	% Drops in Produced Emulsion
0 - 1	73	84
1 - 2	14	10
> 2	13	6

The mean drop size of emulsion S9B' to mean pore size is found to be 0.63. This indicates that interception, or the capture of small droplets on the surface of the sand grains, is most likely a key mechanism for this fluid-rock system. The high flow rates used during the flood enabled the viscous force to overcome the van der Waals force, thereby making the small emulsion droplets more difficult to capture. Furthermore, the large droplets were broken into smaller ones which added to the number of small droplets.

Emulsion S9T' showed generally pseudoplastic behaviour in both the injected and produced emulsions, with the exception of core flood #20 which showed dilatant behaviour. For this core flood, the injected emulsion behaved like a dilatant fluid with the n value of 1.2379, while the produced emulsion behaved like a dilatant fluid with the n value of 1.0272 (Fig. 4.26). Since the mean drop size of emulsion S9T' to mean pore size is 1.65 for core flood #20, the straining mechanism was dominant. This is confirmed by examining the drop size distribution of the effluent at different flow rates. The results showed that only small droplets, 1 μm or less in size, were produced at low flow rates (40 to 120 ml/hr). The larger droplets, 2 to 3 μm in size, were retained at the low flow rate and produced at the higher rates (200 to 400 ml/hr). The droplets which were larger than the pore size of the porous medium may have been

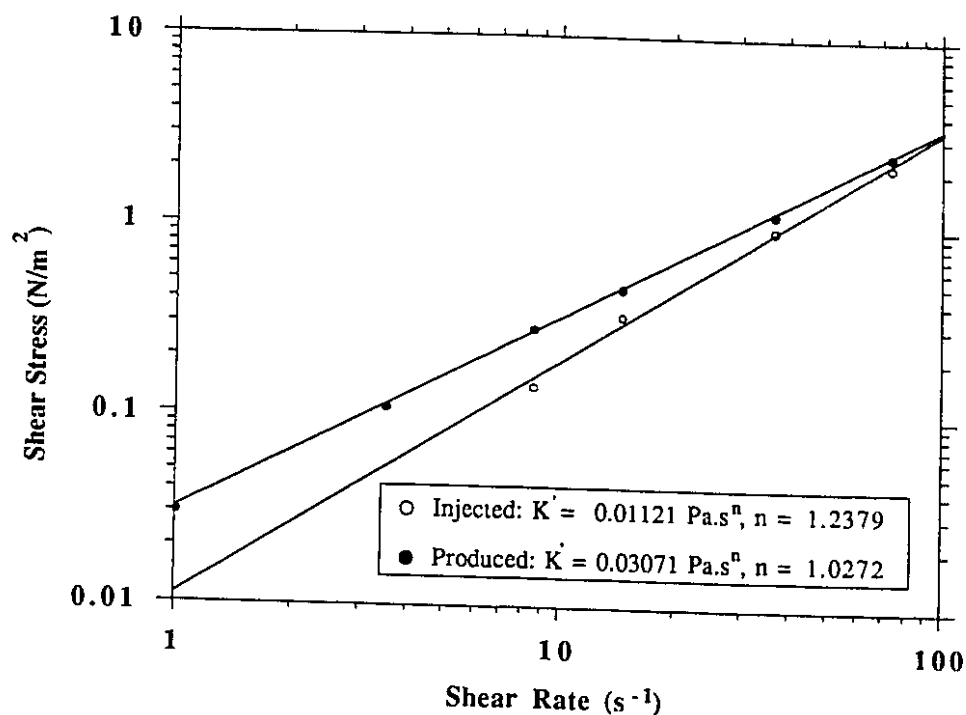


Fig. 4.26 Rheological Behaviour of Injected and Produced Emulsion S9T' (CF #20 Fired Berea Sandstone).

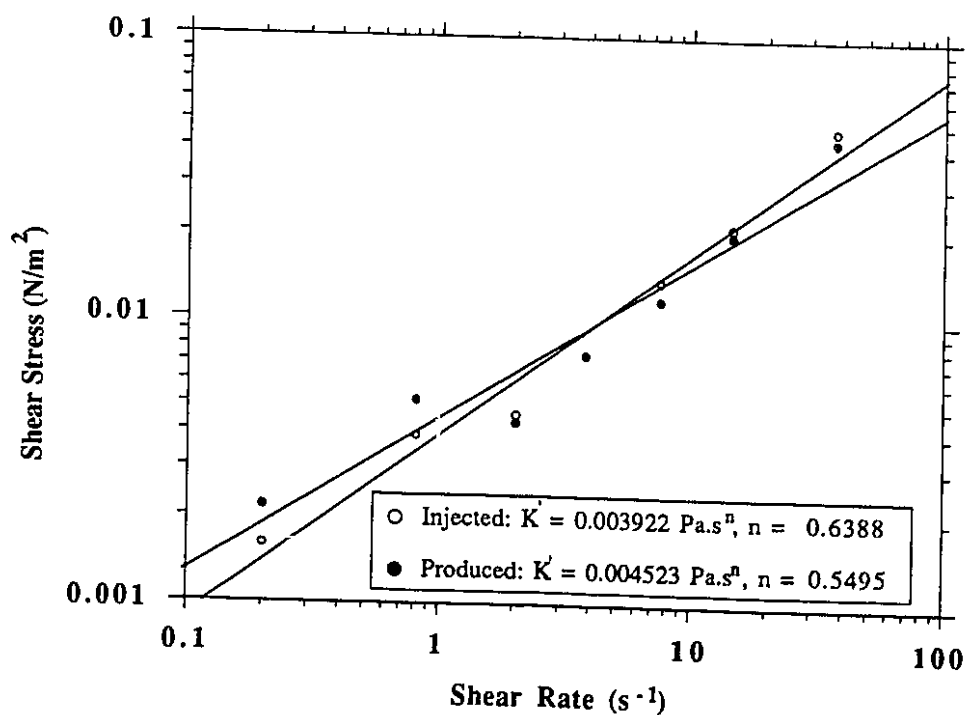


Fig. 4.27 Rheological Behaviour of Injected and Produced Emulsion S10B (CF #21 Unfired Berea Sandstone).

lodged in the pore throats and retained at low flow rates. Under a large enough pressure gradient, these droplets were mobilized and produced.

C. Results for Emulsion S10B

For core flood #21, which utilized oil-in-water emulsion S10B in Berea sandstone, the injection pressure varied between 219 and 460 kPa for flow rates between 75 and 400 ml/hr; the breakthrough pressure was 219 kPa. This core flood had a ratio of mean drop size to mean pore size of 1.21, which meant that interception dominated the flow mechanism for this fluid-rock system.

Both the injected and produced emulsions showed pseudoplastic behaviours with the flow behaviour indices of 0.6388 and 0.5495, respectively. Figure 4.27 shows the similarity of the rheological behaviours of the injected emulsion and the produced emulsion at high flow rates (360 and 400 ml/hr). The similarity of the emulsion rheological behaviour in the porous medium to that in a viscometer is also shown by the slopes of the plots of shear stress versus shear rate and pressure drop versus velocity (Fig. 4.28).

As mentioned earlier, interception dominated the flow mechanism, and had a capture behaviour of moderate ionic strength (0.03 M). The 0.2% NaCl brine was used as a drive fluid. The log-probability plots of drop size distribution of the produced emulsion at flow rates of 320, 360, and 400

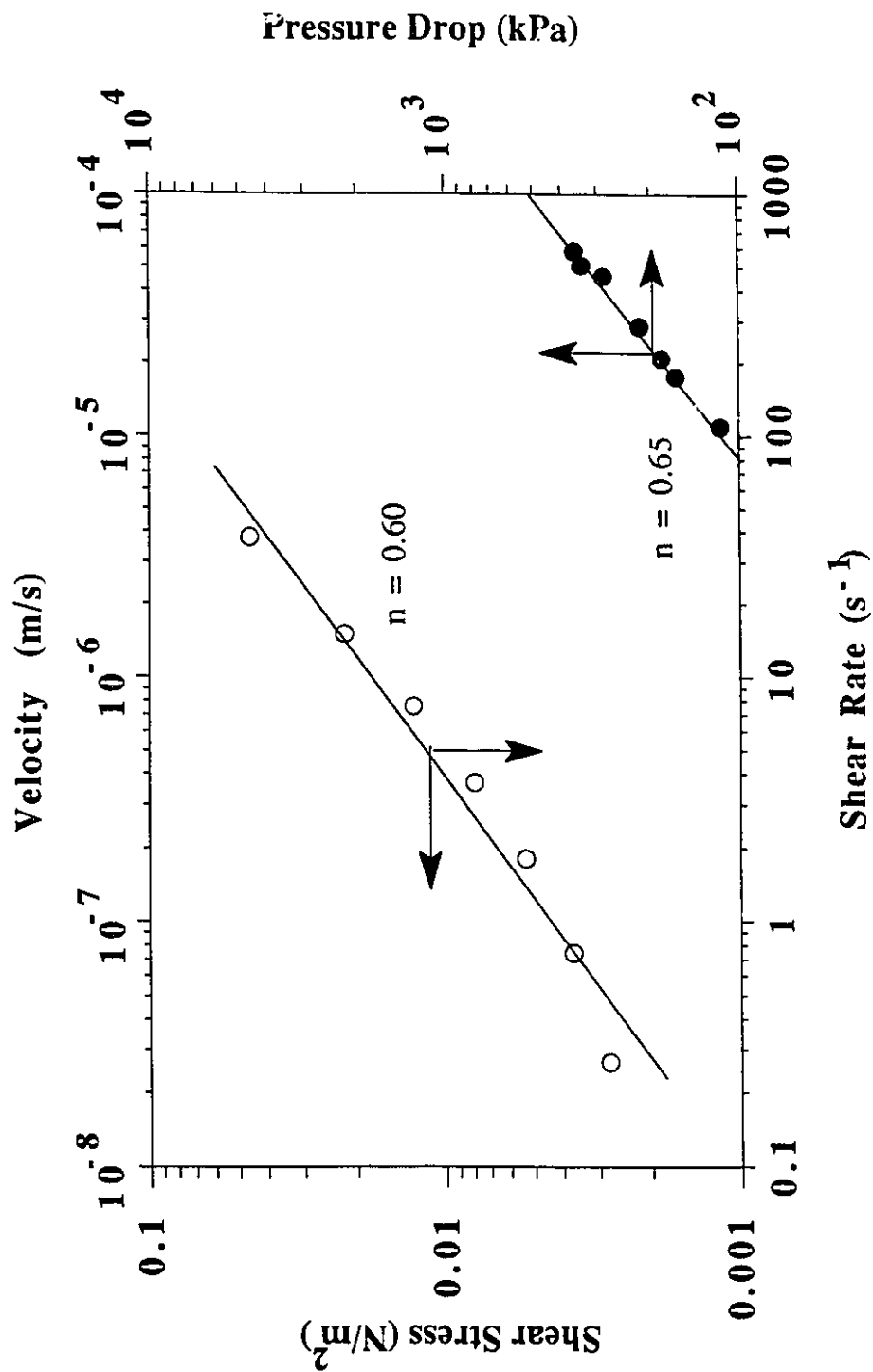


Fig. 4.28 Rheological Behaviour of Emulsion S10B in Viscometer in Porous Medium (CF #21 Unfired Berea Sandstone).

ml/hr are shown in Figs. 4.29, 4.30, and 4.31, respectively. The flow behaviour of surfactant emulsion S10B in Berea sandstone can be understood by comparing these drop size distributions and explained using the double layer theory of particle capture behaviour.

Emulsion breakthrough occurred at 1 PV injected. The pH of the effluent was found to be higher than that of the brine in place, and approached that of the injected emulsion (pH = 8.45). All of the droplets were captured and only the continuous phase of the emulsion was produced at low flow rates (75, 120, and 150 ml/hr). The aqueous phase of the reservoir brine and the continuous phase of the emulsion were distinguished by their different pH values. Therefore, when the pH value of the produced aqueous phase changed, it indicated that emulsion breakthrough had occurred; only the continuous phase of the emulsion was being produced, leaving all of the droplets in the porous medium. According to double layer theory⁴², weak capture of small droplets can occur in the secondary minimum at low velocities or under small hydrodynamic forces.

At a moderate flow rate (200 ml/hr), some small droplets were produced because these droplets were pulled out of the secondary minimum and re-entered the flow stream at a higher velocity.

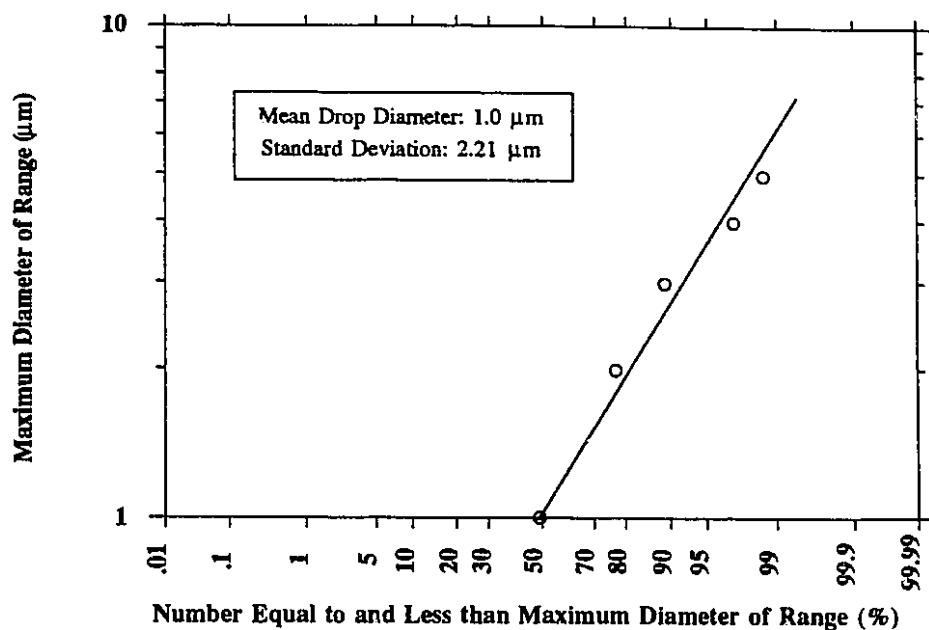


Fig. 4.29 Log-Probability Plot of Drop Size Distribution of Produced Emulsion S10B at Flow Rate of 320 ml/hr.

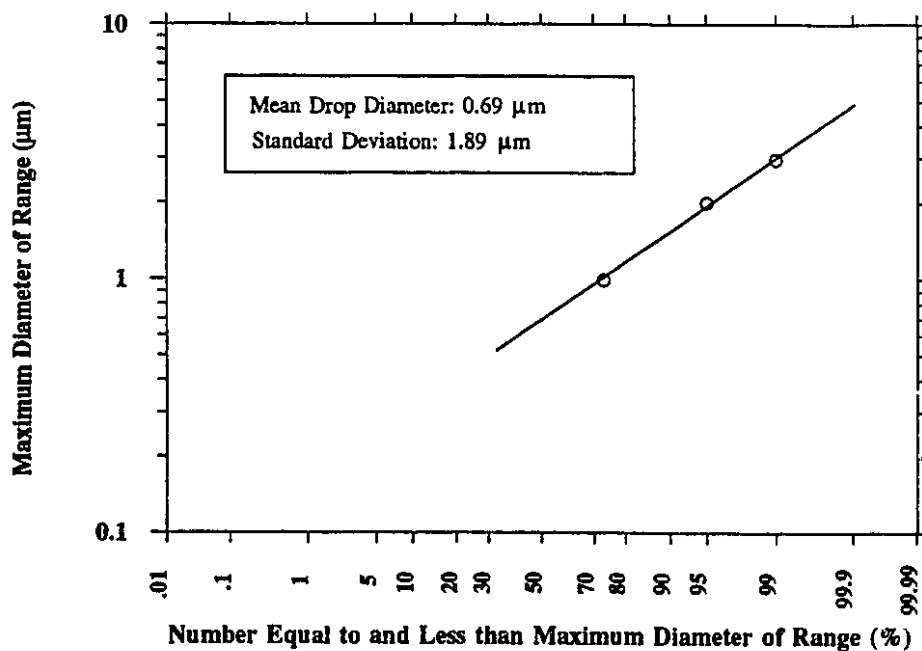


Fig. 4.30 Log-Probability Plot of Drop Size Distribution of Produced Emulsion S10B at Flow Rate of 360 ml/hr.

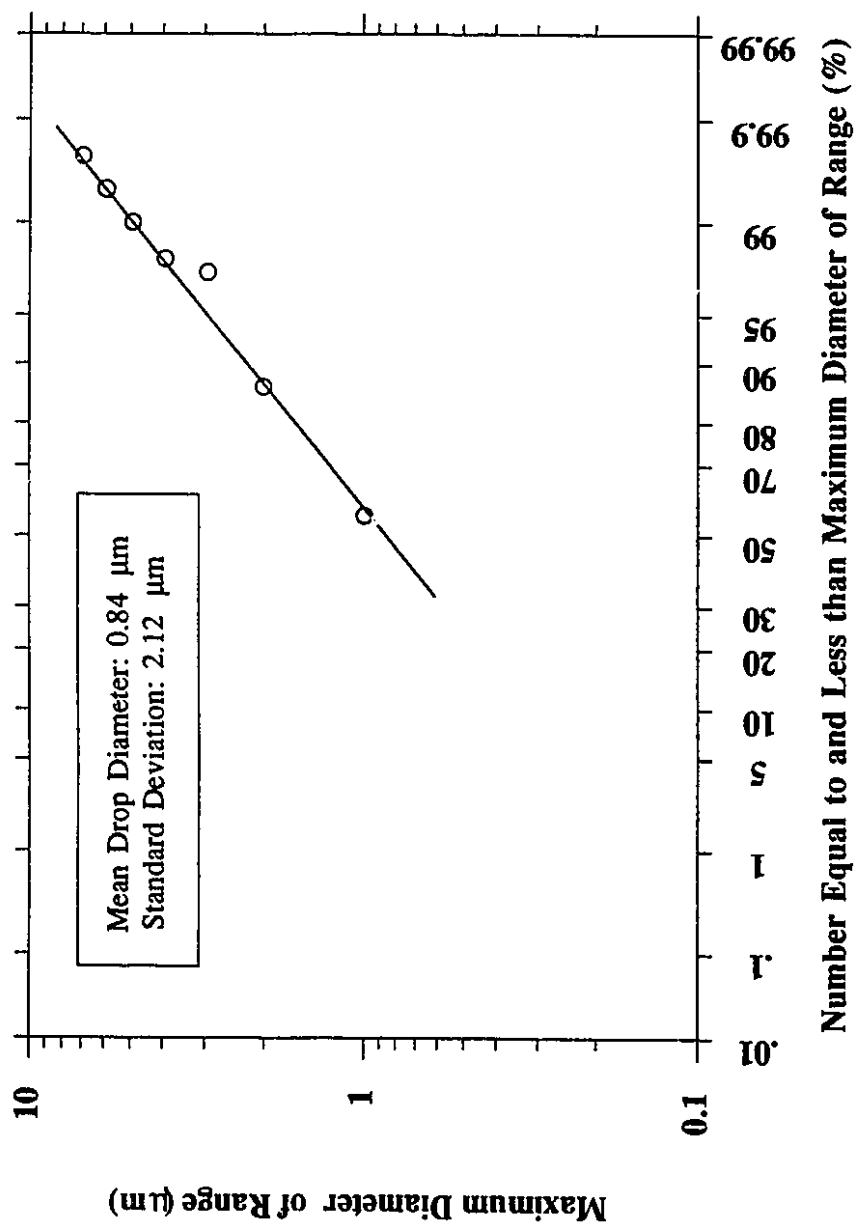


Fig. 4.31 Log-Probability Plot of Drop Size Distribution of Produced Emulsion S10B at Flow Rate of 400 ml/hr.

At a higher flow rate (320 ml/hr), the effluent contained more droplets. Furthermore, the drop size distribution of the produced emulsion is similar to that of the injected emulsion with close values of mean drop sizes (Figs. 4.13 and 4.29), except that a higher percentage of large droplets was produced at a flow rate of 320 ml/hr. These large droplets may be the ones that were retained in the porous medium during the low flow rates, and were eluted when a high enough pressure gradient was applied.

The flow rate of 360 ml/hr produced a greater viscous force than the interfacial force, and caused the captured droplets to break up. This is why, the drop size distribution (Fig. 4.30) shows a high percentage of small particles and a smaller percentage of large particles with the mean drop size of 0.69 μm .

The drop size distribution of the produced emulsion at a flow rate of 400 ml/hr, illustrated in Figure 4.31, shows the combined effect of drop breakup and strong capture of small droplets in the primary minimum. Drop breakup is indicated by the lower percentage of large droplets. Strong capture is shown by an eluted percentage of small droplets that is lower than that found at a flow rate of 360 ml/hr. This strong capture of small droplets in the primary minimum occurs once the hydrodynamic force is high enough to overcome the repulsive energy barrier.

D. Results for Emulsion H3

Emulsion H3, an oil-in-water emulsion, had an apparent viscosity of 174 to 31 mPa.s at shear rates of 3.67 to 73.40 s⁻¹. The emulsion produced during emulsion flooding was a stable, water-in-oil type with some double emulsion of the (water-in-oil)-in-water type. Surprisingly, the quality of the emulsion (% dispersed phase) increased from 50 to 66% vol., and the viscosity of the pseudoplastic produced emulsion more than doubled, reaching values from 390 to 70 mPa.s. However, the emulsion that was produced during the waterflood following the emulsion flood remained pseudoplastic; its viscosity decreased to a range of 50 to 16 mPa.s, and its quality dropped from 66 to 60% vol.

Similarly to the previous core floods, core flood #22 was carried out to confirm that oil droplets of a size smaller than the mean pore diameter could be retained on the pore surface. Hence, an Ottawa sand pack, which has a mean pore diameter greater than that of Berea sandstone, was used as the porous medium. The effluent at emulsion breakthrough and at 2.5 PV of emulsion injected resembled each other in drop-size distribution.

The flushed permeability after injecting 5.2 PV of 1% NaCl brine was calculated using Darcy's law and was found to be 3.4 μm^2 , compared to an initial value of 5.7 μm^2 . This

confirms that the captured drops caused a permanent permeability reduction.

In conclusion, both the caustic and surfactant emulsion rheologies of emulsions flowing through either consolidated or unconsolidated cores behave very much like those under the same shear initiated in a viscometer. The similarity was found to be closer for flow in a Berea sandstone core. Furthermore, both the straining and interception capture mechanisms postulated by Soo and Radke can be used to explain observations of the flow of emulsions with both low and high drop size to pore size ratio through a porous medium with a known pore size distribution.

4.4.2 Experimental Core Flood to Obtain Surfactant Recovery and Surfactant Adsorption to Porous Media

As regards the transport of the surfactant in the emulsion, it is desirable to know how much surfactant could transfer between phases during displacement and how much could adsorb onto the rock surface. The following core floods were carried out to determine adsorption of surfactant SD1000 on the rock surface and its distribution among the oleic, aqueous, and emulsion phases.

A. Flood Description of Emulsion H4

Core floods #23, #24, and #25 were performed using emulsion H4, an oil-in-water type emulsion. This emulsion behaved as a pseudoplastic fluid with the flow behaviour index (n) of

0.4685. An Ottawa silica sand pack was used as the porous medium. The cores were initially saturated with 1% NaCl brine. Emulsion slugs of 20%, 10%, and 50% PV were injected for core floods #23, #24, and #25, respectively, each at a rate of 400 ml/hr. This was followed by a brine flood until about 5 PV of brine was injected. The summary of these core floods is given in Table 4.8. The effluent in all three floods was observed to be a dilute oil-in-water type emulsion. The produced emulsion was broken by adding salt. The oil and water phases were then analyzed by infrared and ultraviolet spectroscopy to determine the surfactant concentration.

B. Flood Description of Emulsion H5

Core floods #28 and #30 were conducted similarly to core floods #23 and #24, except that emulsion H5 was used and an oleic phase was introduced to the system. Ottawa sand packs were used as the porous media, and they were initially saturated with 1% NaCl brine and flooded with oil to irreducible water saturation. An emulsion slug was used under secondary conditions by injecting a 20% PV-size slug in core flood #28 and a 10% PV-size slug in core flood #30, each followed with a 1% NaCl brine flood. An emulsion slug of the same size as the first one was then injected for each core flood, followed by another brine flood. The resulting effluent was treated with an emulsion breaker to separate it into oil and water. The oil recoveries were then

calculated, and surfactant loss and distribution between the phases were determined by analyzing the effluent using the Infrared method.

C. Results for Emulsions H4 and H5

Almost all of the surfactant partitioned into the water phase, and almost no surfactant was recovered from the oil phase. This was because surfactant SD1000 is preferentially soluble in water. The partition coefficients of the surfactant between the different phases, as well as that of oil and water, were calculated (Appendix A). Figure 4.32 shows the loss of surfactant to the porous medium versus the slug size of the injected emulsions for core floods #23, #24, and #25.

It can be seen in Table 4.12 that the ratio of surfactant SD1000 partitioned between the aqueous and emulsion phases was approximately within the same range for all these core floods. Therefore, a constant partition coefficient may be used for surfactant SD1000 during its transport through a porous medium. A similar result was obtained for the distribution of oil and water among phases. The partition coefficient for each component is approximately constant when the emulsion is stable enough so that there is no change in the number of phases in the system.

For core flood #25, the brine flood following the emulsion flood was continued until about 10 PV of the brine was

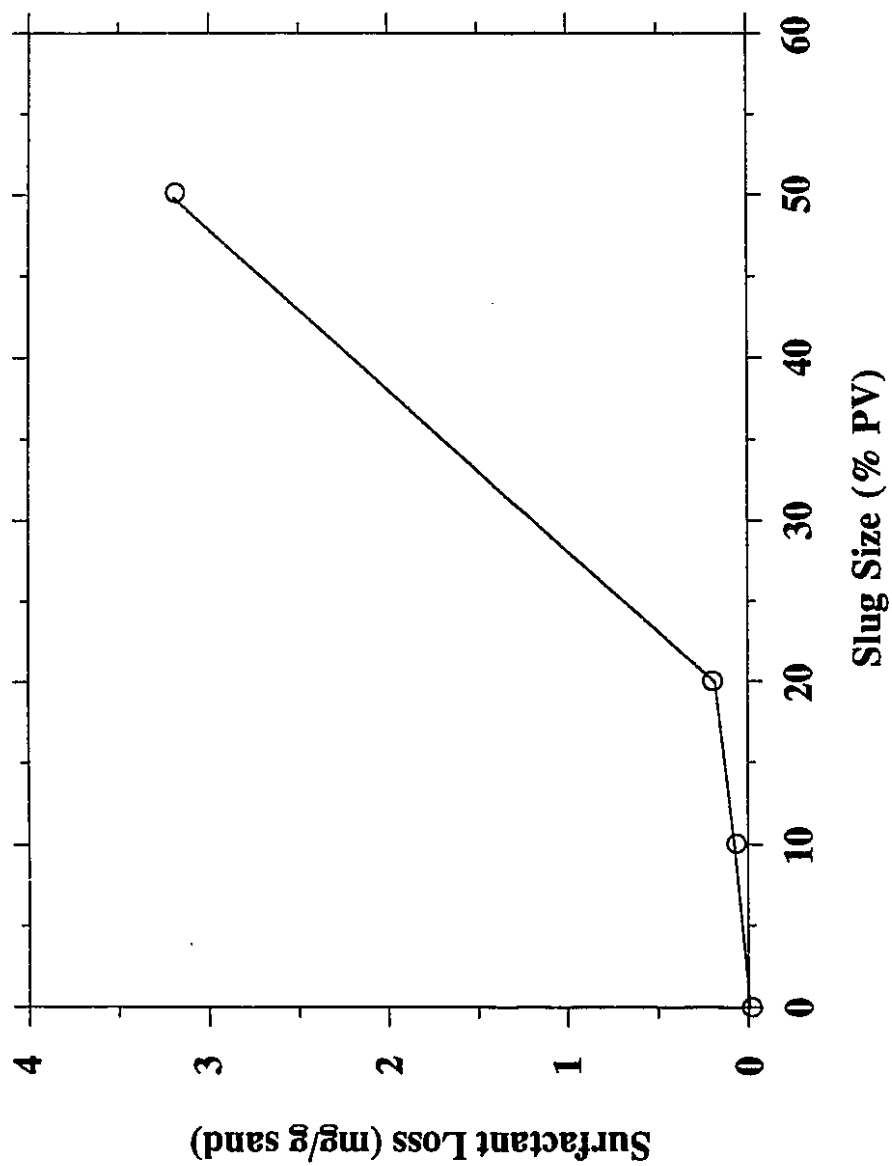


Fig. 4.32 Loss of Surfactant to Porous Medium
at Different Slug Sizes (CF #23, 24, 25).

Table 4.12
Comparison of the K -values Obtained
from Different Core Floods

Core Flood	K_{oam}	K_{wam}	K_{sam}	K_{olm}	K_{wlm}	K_{slm}
24	0	1.7037	0.0484	2.4390	0	0
25	0	1.6976	0.1333	2.4390	0	0
28	0	1.6984	0.0769	2.4390	0	0
30	0	1.6948	0.0697	2.4390	0	0

injected to determine if more of the surfactant could be recovered. No additional surfactant was recovered by injecting additional brine.

In conclusion, the emulsions used in the laboratory core floods were sufficiently stable so that no breakdown occurred. The effect of gravity, which could cause coalescence of the droplets, was negligible for the high flow rates used. In other words, the emulsion always flowed as an independent phase in the system, with a constant partition coefficient for each component between the emulsion and the other phases.

4.4.3 Oil Recovery Experiments

The experimental runs to determine how effective the caustic and surfactant emulsions were in enhancing oil recovery are discussed below. The oil recovery core floods are grouped according to the emulsion type used.

4.4.3.1 Caustic Emulsion H2

Core flood #4 was carried out to evaluate the performance of the emulsion in the porous medium at an irreducible water saturation. Emulsion H2 was used in an Ottawa sand pack, at a frontal velocity of 8 m/day. The core was initially saturated with 2% NaCl brine. An irreducible water saturation was established ($S_{oi} = 83.68\%$ PV) by pumping several pore volumes of the Horsefly crude. The emulsion

flood was then started and continued until 1.86 PV of H₂ were injected.

The production history of core flood #4 is shown in Fig. 4.33. It can be seen that there is a change in the slope of the injection pressure as time proceeds. It is also apparent that the injection pressure at later times increases more slowly than that at earlier times. This can be explained in that fewer droplet capture sites are available as time proceeds. Therefore, the absolute permeability reduction is decreased, which reduces the injection pressure required to maintain a constant flow rate. Emulsion breakthrough occurred at 0.88 PV injected. It can be seen that the injection pressure drops slightly near the end of the flood. This could be due to elution of the captured drops and the trapped oil. The captured drops caused the pressure gradient to increase to the point that it was able to squeeze these drops and the trapped oil out of the core. This opened new contiguous channels for the emulsion to flow through, reducing the required pressure gradient and increasing the oleic recovery slightly. The effluent was sampled and analyzed for emulsion type, quality, and rheological behaviour. The effluent emulsion was a water-in-oil type, with small droplets packed tightly. The effluent emulsion quality was 10% lower than that of the injected emulsion. The injected emulsion was pseudoplastic ($n = 0.8676$), while the produced emulsion had dilatant

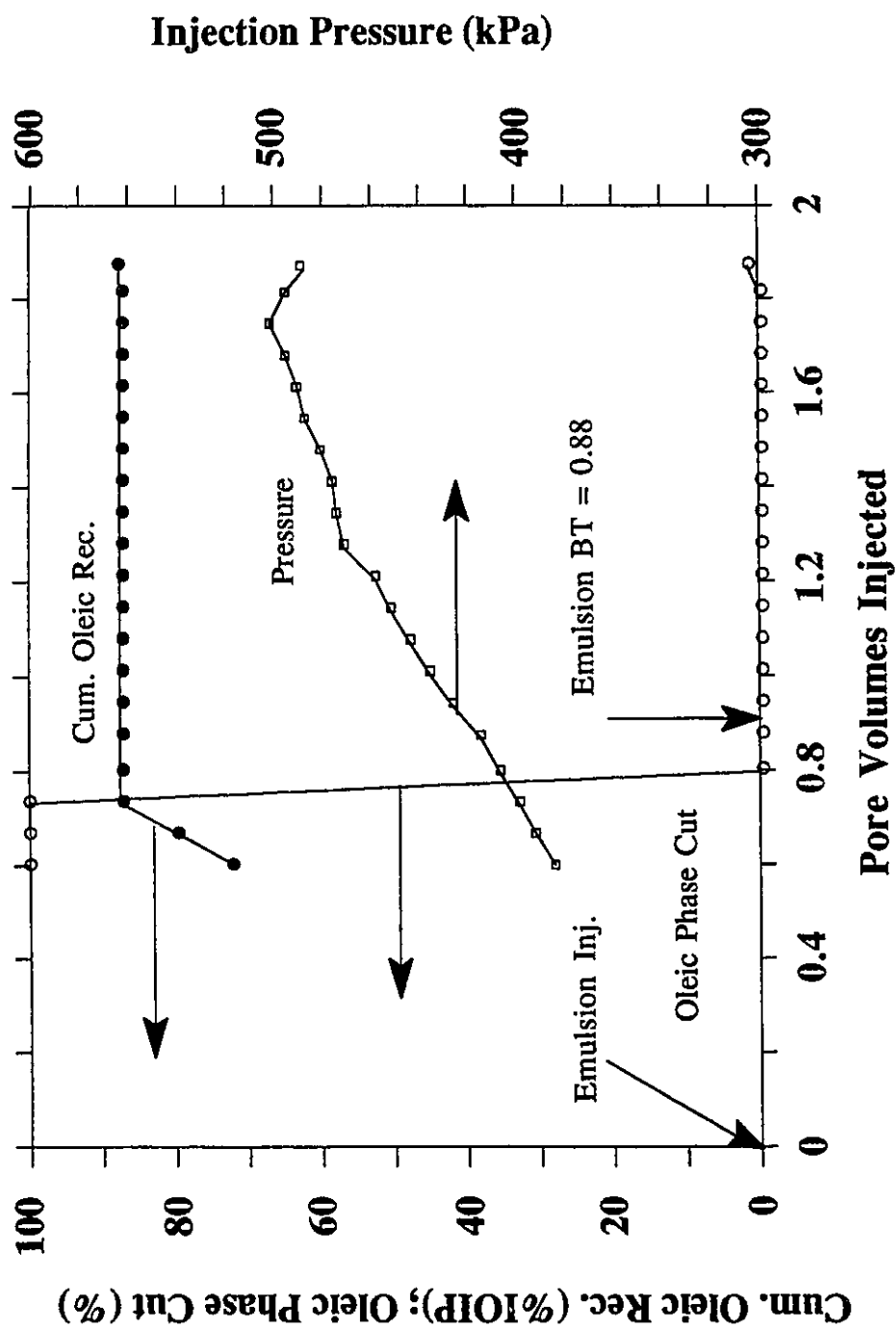


Fig. 4.33 Production History for Core Flood #4
Emulsion Flood at Secondary Stage.

behaviour ($n = 1.1528$). Cumulative oleic recovery is also shown in Fig. 4.33, with a maximum recovery of 87.54% IOIP. Oleic recovery includes the recovery of the oil in place and the oil from injected emulsion. The oil recovery after correcting for the amount of oil injected in the emulsion was 34% of the original oil in place.

Core flood #5 was designed to observe the performance of emulsion H2 in an unconsolidated porous medium at residual oil saturation. This flood was analyzed in detail using the simulator developed in this study (Chapter 7). The core was first waterflooded with 2% NaCl brine to establish a residual oil saturation ($S_{or} = 24.9\%$ PV at WOR of 18.2:1). This was followed by a continuous emulsion flood until 1.8 PV of emulsion H2 was injected.

The production history of core flood #5 is shown in Fig. 4.34. During the emulsion flood, the pressure drop across the core increased from 163 to 653 kPa. This increase in injection pressure is larger than that observed in the secondary stage (core flood #4), and can be attributed to the higher flow resistance force due to the trapped oil. This was confirmed by the late emulsion breakthrough, which occurred at 1.01 PV injected of emulsion, as opposed to 0.88 PV injected of emulsion in core flood #4. In tertiary recovery, some of the pore space is initially occupied by residual oil which is trapped during waterflooding.

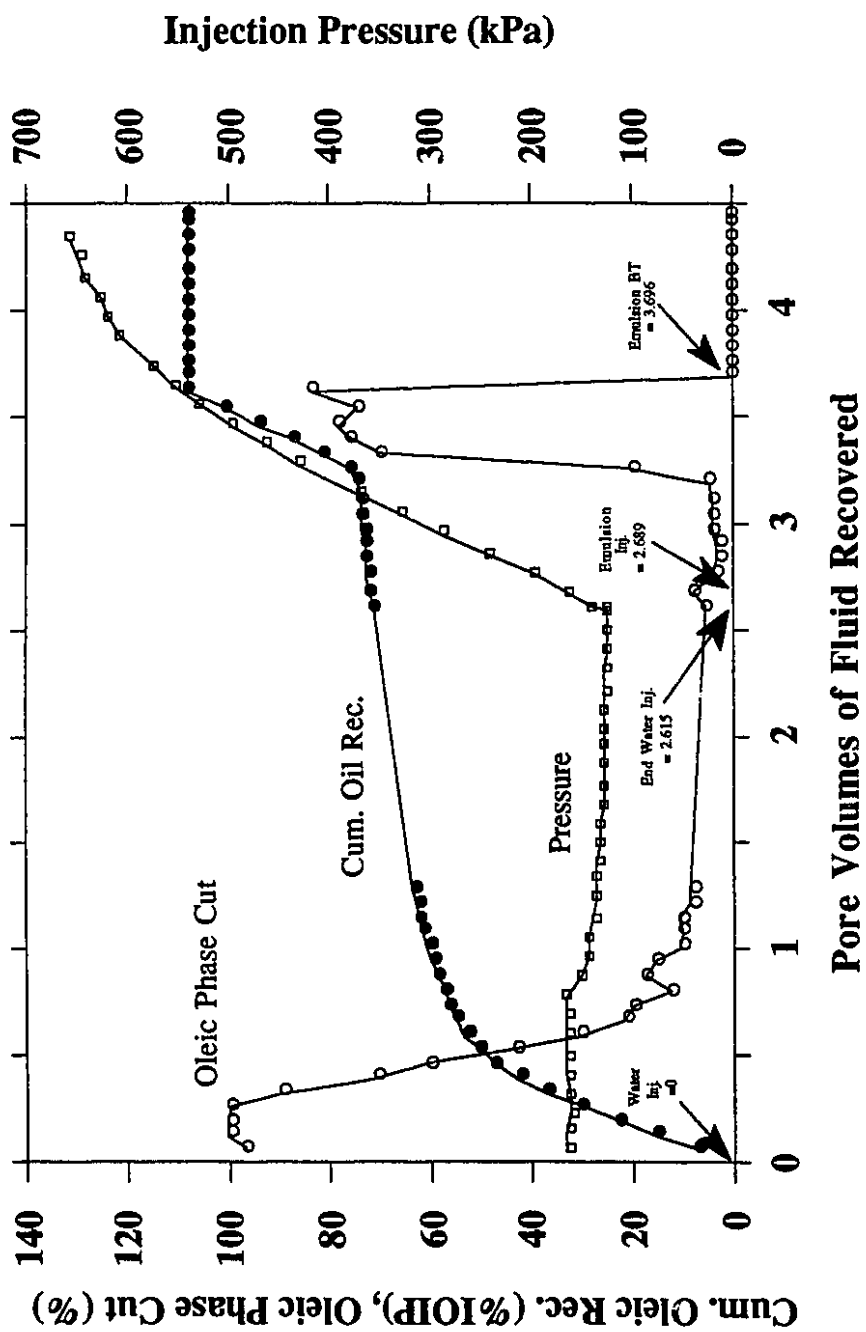


Fig. 4.34 Production History for Core Flood #5
Emulsion Flood at Tertiary Stage.

Therefore, there is less pore space available for droplet capture, which means that there should be fewer droplets captured during emulsion flooding under tertiary recovery. Analysis of the effluent emulsion shows that there was only a 6% reduction in quality, compared to 10% in core flood #4. The injected and produced emulsions displayed dilatant ($n = 1.0717$, shown in Fig. 4.5) and pseudoplastic behaviours ($n = 0.8443$), respectively. This is contrary to what was observed in core flood #4. Emulsions prepared at different times showed significant variations in rheological properties. This is possibly due to fluctuations in the ambient conditions. It is shown in Fig. 4.34 that the maximum oleic recovery is over 100% IOIP. This indicates that some oil from injected emulsion was produced together with the residual oil. Oleic recovery in this flood was 128% of the residual oil in place, while oil recovery after correcting for the oil in injected emulsion was 82.6% of the residual oil in place.

The above results indicate that the recovery efficiency of water-in-oil emulsions was higher under tertiary flooding conditions. It could be that the trapped oil was mobilized by reduced interfacial tension caused by the surfactant in the emulsion. Another possible explanation is that when drops plug the pore throats of pores containing trapped oil, the increased pressure gradient causes the trapped oil to mobilize.

Core flood #5 is used for comparisons with the simulation results in Chapter 7 to determine whether the mathematical model developed based upon the physical properties and mechanisms observed gives results comparable to the experimental data.

4.4.3.2 Surfactant Emulsion H5

This set of core floods was performed to evaluate the oil displacing characteristics of the emulsions. Emulsion slugs were used before and after waterflooding to determine the effect on oil recovery. The composition and properties of emulsion H5 are described in Section 4.3.2.2.

Four core floods, viz. #27, #28, #30, and #31, were conducted using emulsion H5 to evaluate its effectiveness in displacing oil. The cores were initially saturated with 1% NaCl brine and flooded with oil to irreducible water saturation. Emulsions were used under secondary conditions, with 10% and 20% PV emulsion slug being injected for core floods #30 and #28, respectively. Each slug was followed with a 1% NaCl brine flood. A second emulsion slug of the same size as the first was then injected for each core flood, followed by another brine flood. For core floods #31 and #27, the emulsion slug was used under tertiary conditions by first waterflooding the cores to residual oil saturation. Emulsion slugs 10% and 20% PV in size were injected for core floods #31 and #27, respectively, followed

with brine flooding. The effluent was treated with an emulsion breaker, and the oil recoveries were calculated. The summary of these core floods is shown in Table 4.9. The production histories for core floods #27, #28, #30, and #31 are shown in Fig. 4.35 to Fig. 4.38, respectively.

In core flood #27, waterflooding was carried out for about 3.4% PV injected and followed by injecting a 20% PV emulsion slug. It is shown in Fig. 4.35 that once the emulsion slug was injected, a large increase in injection pressure was observed. This indicates flow restriction due to the droplet capture mechanism and also the flow of a higher viscosity fluid in the porous medium. It is followed by a decline in the injection pressure once water was injected. The emulsion breakthrough occurred after injecting water for about 0.6 PV. It was found that the waterflood recoveries in these experiments were 77 and 72% of original oil in place for core floods #27 and #31, respectively. A similar trend in injection pressure for core flood #31 was observed. There was only a slight increase in cumulative oleic recovery at the tertiary stage (8% of oil in place) after waterflooding was stopped at an oil cut of 1.5%.

There was a sharp increase in injection pressure when an emulsion slug was injected in core floods #28 and #30 (Fig. 4.36 and Fig. 4.37). This was followed by a sharp decrease in injection pressure during waterflooding. Emulsion

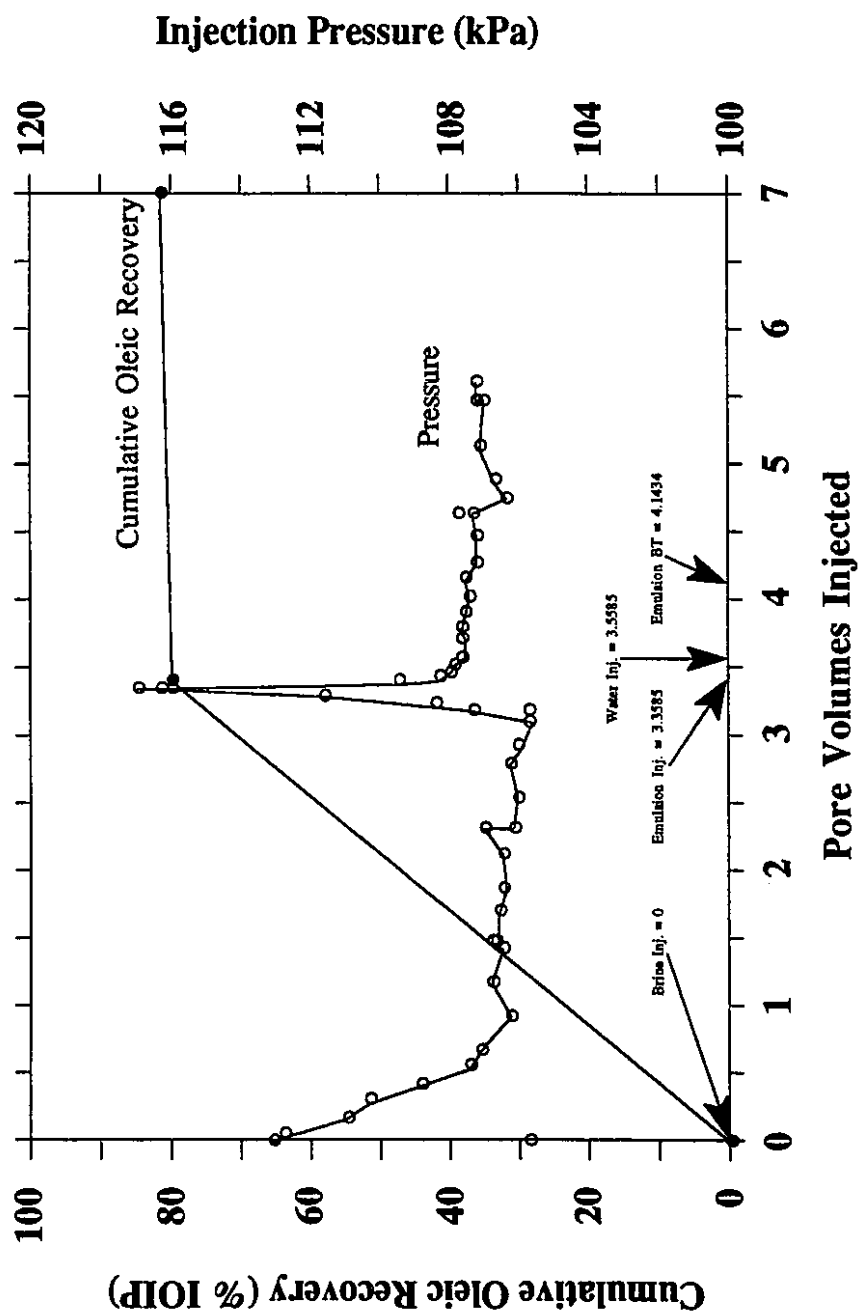


Fig. 4.35 Production History for Core Flood #27

Waterflood Followed by Emulsion and Waterflood
(Emulsion Slug Size = 0.2 PV).

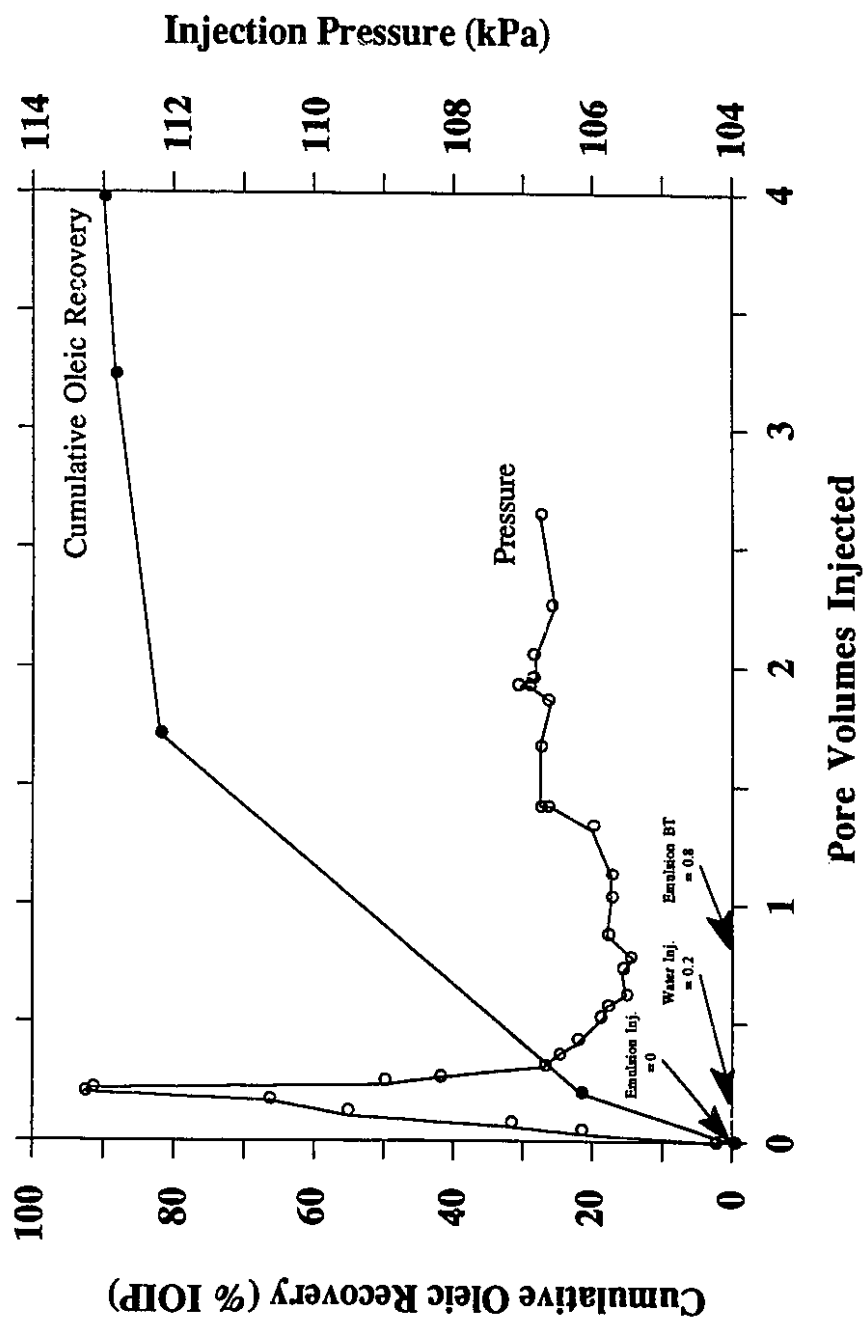


Fig. 4.36 Production History for Core Flood #28
Emulsion Followed by Waterflood
(Emulsion Slug Size = 0.2 PV).

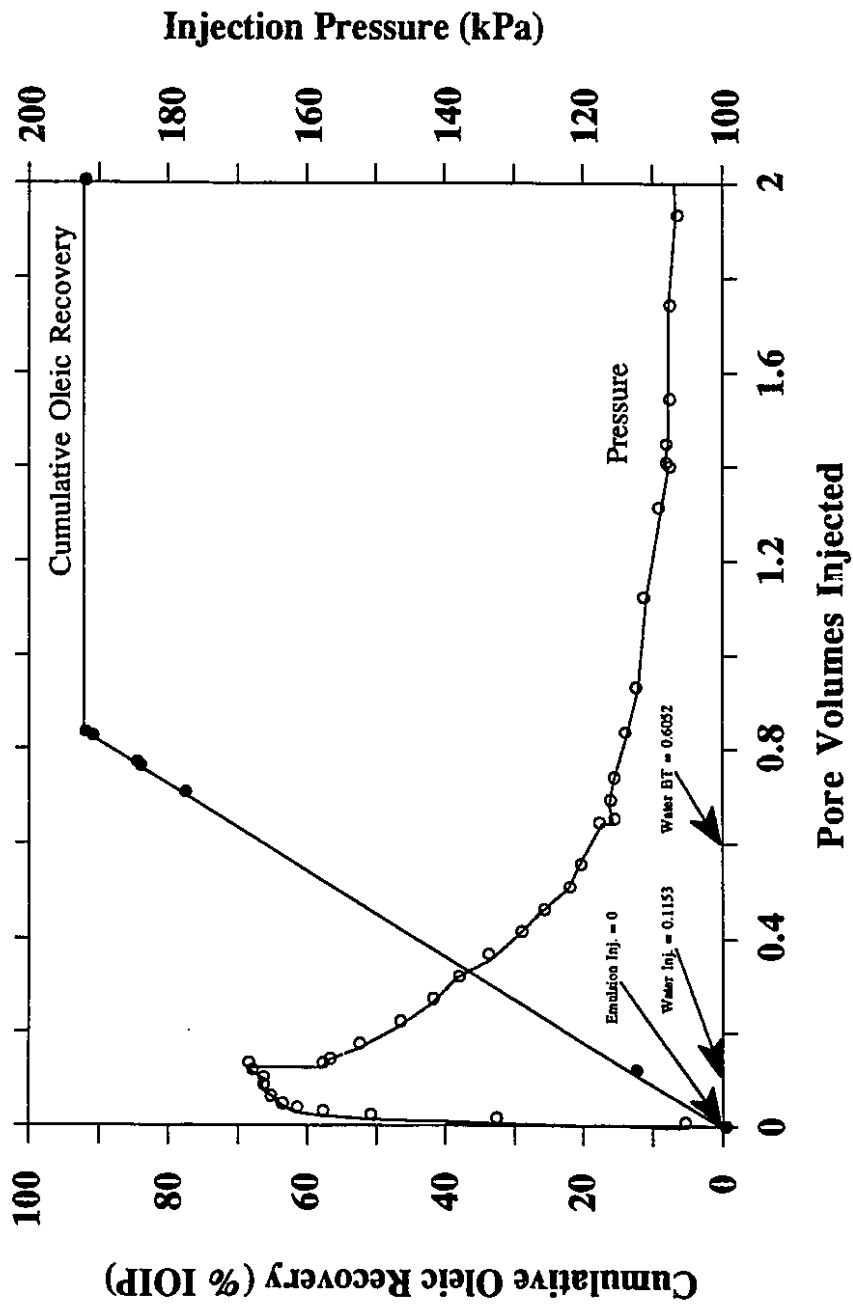


Fig. 4.37 Production History for Core Flood #30
Emulsion Followed by Waterflood
(Emulsion slug Size = 0.1 PV).

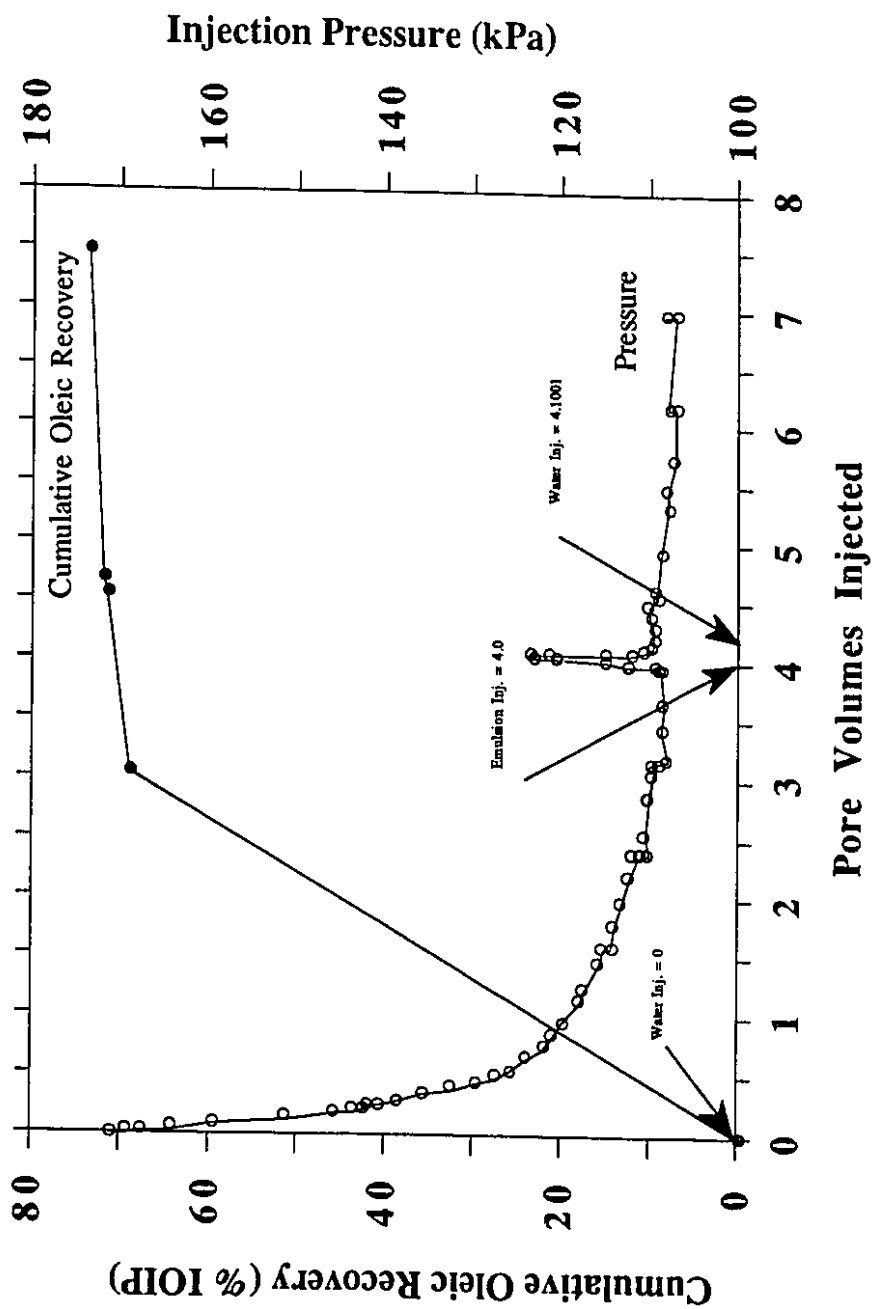


Fig. 4.38 Production History for Core Flood #31
Waterflood Followed by Emulsion and Waterflood
(Emulsion Slug Size = 0.1 PV).

breakthrough occurred after 0.6 PV of water was injected for core flood #28 and about 0.5 PV for core flood #30. The cumulative oleic recoveries for core floods #28 and #30 are shown in Fig. 4.36 and Fig. 4.37, respectively. However, after correcting for the amount of oil injected with the emulsions, the oil recoveries were found to be 79 and 77% of original oil in place for core floods #28 and #30, respectively. This indicates that an emulsion slug prior to the waterflood did not improve recovery by any significant amount. Fig. 4.39 compares the waterflood recovery and the oil recovery when an emulsion slug is used prior to a waterflood. Injecting emulsion as a slug prior to waterflood did not seem to improve the recovery.

In conclusion, as emulsion H5 is viscous and has a 38% quality, it was first thought that it should be a good mobility control agent. However, only a slight improvement in oil recovery was observed when it was injected as a slug. The drop size-to-pore size ratio may not have provided sufficient permeability reduction, the slug size may have been too small, or that it should have been followed by a polymer buffer. Further experimental investigations need to be done to find a suitable injected emulsion and the best injection sequence.

The preceding observations may be summarized as follows. First, observations were made of the rheological behaviour

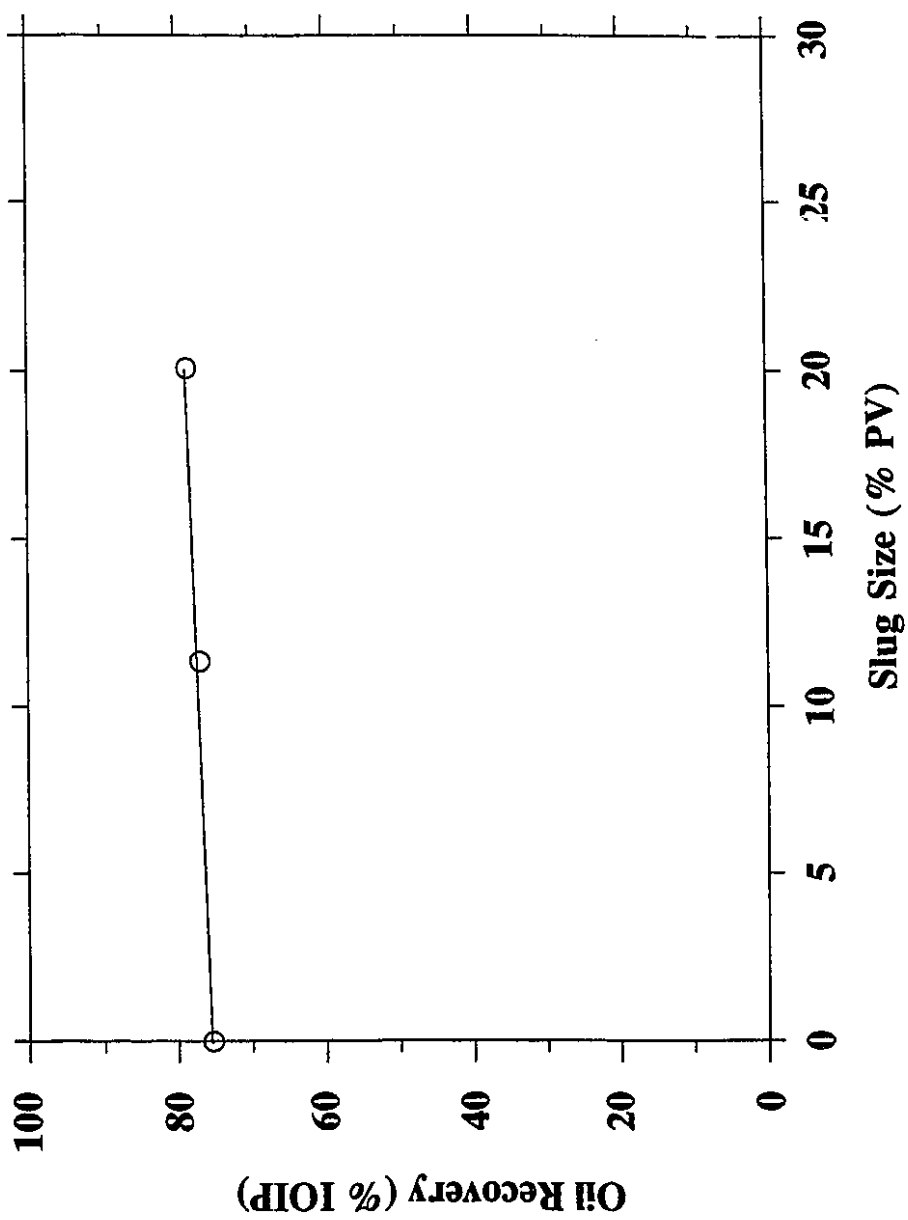


Fig. 4.39 Effect of an Emulsion Slug Prior to Waterflood on Waterflood Recovery.

of the caustic and surfactant emulsions for the system of comparable drop to pore size. Slight differences were seen when the emulsions flowed in porous media and in a viscometer. This is probably due to an interaction between drops and pores. Rheological similarities were closer for flow in a Berea sandstone than for flow in an Ottawa sand pack. The similarities were also closer for a caustic emulsion than for a surfactant emulsion. Second, for the system of drop size-to-pore size ratio investigated, observations indicated that the capture mechanism operated by a filtration process. Third, for a system with the condition that three phases must exist at all times, the partition coefficient between the emulsion and the other phases for each component was found to be approximately constant. Finally, it was found that the recovery efficiency of water-in-oil emulsions was higher under tertiary flooding conditions for a continuous emulsion flood. However, an emulsion slug injected prior to the waterflood was found not to improve recovery significantly.

5. DEVELOPMENT OF THE MATHEMATICAL MODEL

A three-dimensional, three-phase, three-component simulator was developed to simulate the emulsion flooding process. The simulator was based on the mechanisms occurring in the displacement of oil and water by an externally injected stable emulsion. A one-dimensional version of the model was validated by comparing the simulation results with the experimental results. Afterwards, the sensitivities of the injection pressure, oil recovery, and breakthrough time to the key variables were studied.

5.1 Simulator Assumptions

The model developed allows for the flow of three phases, oleic, aqueous, and emulsion, simultaneously with interphase mass transfer of three components, oil, water, and surfactant, among the phases. Emulsion flooding is a complex EOR process involving several mechanisms that occur at the same time during displacement. To represent the flow of multiphase, multicomponent fluids and the control mechanisms mathematically, the following assumptions were made to simplify and limit the scope of the study.

1. The flow is isothermal.
2. All phases are incompressible fluids.
3. No change in volume results from mixing.

4. There is no salinity gradient in the system; i.e., reservoir brine, water in emulsion phase, and drive water have the same salinity and physical properties.
5. Compositions, equilibrium coefficients, and fluid properties are pressure independent.
6. There are always three phases present in the system (emulsion injected is sufficiently stable that no breakdown or coalescence occurs).
7. Instantaneous equilibrium between phases occurs. The partition coefficients are assumed to be constant or independent of phase compositions because three-phase flow is assumed at all times.
8. Adsorption, desorption, and retention of surfactant occur instantaneously, and the amount adsorbed is controlled by the adsorptive capacity of the rock.
9. Only molecular diffusion is considered which is allowed only in the case of the surfactant.

5.2 Formulation of the Problem

The mass balance for each component in three dimensions can be written as,

$$\begin{aligned}
 & \nabla \cdot \left(C_{ii} \rho_i \frac{kk_{ri}}{\mu_i} \nabla \Phi_i \right) + \nabla \cdot \left(C_{ia} \rho_a \frac{kk_{ra}}{\mu_a} \nabla \Phi_a \right) + \nabla \cdot \left(C_{im} \rho_m \frac{kk_{rm}}{\mu_m} \nabla \Phi_m \right) \\
 & + \nabla \cdot [D_{ii} \nabla (\rho_i C_{ii})] + \nabla \cdot [D_{ia} \nabla (\rho_a C_{ia})] + \nabla \cdot [D_{im} \nabla (\rho_m C_{im})] + m_i^* \\
 & = \frac{\partial}{\partial t} (\phi C_{ii} \rho_i S_i + \phi C_{ia} \rho_a S_a + \phi C_{im} \rho_m S_m) \text{ for } i = o, w, s, \quad (5.1)
 \end{aligned}$$

where m_i^* is the mass injection rate of component i per unit volume ($\text{kg.m}^{-3}.\text{s}^{-1}$). Equation 5.1 is shown as a generalized parabolic equation with second order derivatives of highly nonlinear terms on the left hand side.

The potentials for oleic, aqueous, and emulsion phases are replaced by phase pressures as follows:

$$\Phi_l = p_l - \rho_l g D, \quad (5.2)$$

$$\Phi_a = p_a - \rho_a g D, \quad (5.3)$$

and

$$\Phi_m = p_m - \rho_m g D. \quad (5.4)$$

Equation 5.1 becomes,

$$\begin{aligned} & \nabla \cdot \left[C_{il} \rho_l \frac{kk_{rl}}{\mu_l} (\nabla p_l - \rho_l g \nabla D) + C_{ia} \rho_a \frac{kk_{ra}}{\mu_a} (\nabla p_a - \rho_a g \nabla D) \right. \\ & + \left. C_{im} \rho_m \frac{kk_{rm}}{\mu_m} (\nabla p_m - \rho_m g \nabla D) \right] + \nabla [D_{il} \nabla (\rho_l C_{il}) + D_{ia} \nabla (\rho_a C_{ia}) \\ & + D_{im} \nabla (\rho_m C_{im})] + m_i^* = \frac{\partial}{\partial t} (\phi C_{il} \rho_l S_l + \phi C_{ia} \rho_a S_a \\ & + \phi C_{im} \rho_m S_m) \text{ for } i = o, w, s. \end{aligned} \quad (5.5)$$

For the oil mass balance, oil capture, $\rho_o \sigma$, is added in the accumulation term for an oil-in-water emulsion. Similarly, $\rho_w \sigma$ is added for a water-in-oil emulsion. For the surfactant mass balance, surfactant adsorption, $\rho_r (1-\phi) \frac{A_d \rho_m C_{sm}}{1 + B_d \rho_m C_{sm}}$, will be included in an accumulation term.

The above mass balance equations for a system of three components in three phases involve the following fifteen unknown variables:

p_l = oleic phase pressure,

p_a = aqueous phase pressure,

p_m = emulsion phase pressure,

S_l = oleic phase saturation,

S_a = aqueous phase saturation,

S_m = emulsion phase saturation,

C_{il} = mass fraction of component i
in the oleic phase ($i = o, w, s$),

C_{ia} = mass fraction of component i
in the aqueous phase ($i = o, w, s$),

and

C_{im} = mass fraction of component i
in the emulsion phase ($i = o, w, s$).

In order to solve for these unknowns, the following independent relationships are required in addition to the mass balance of oil, water, and surfactant to complete the formulation of this system. The relationships are the phase saturation constraint,

$$S_l + S_a + S_m = 1, \quad (5.6)$$

the capillary pressure relationships,

$$P_{ca} = p_l - p_a, \quad (5.7)$$

for a preferentially water-wet rock, and

$$P_{dm} = p_l - p_m, \quad (5.8)$$

the mass fraction constraints,

$$\sum_{i=1}^3 C_{il} = 1, \quad (5.9)$$

$$\sum_{i=1}^3 C_{ic} = 1, \quad (5.10)$$

and

$$\sum_{i=1}^3 C_{im} = 1, \quad (5.11)$$

and the phase equilibrium relationships,

$$K_{ilm} = \frac{C_{il}}{C_{im}} \text{ for } i=o,w,s, \quad (5.12 - 5.14)$$

and

$$K_{iam} = \frac{C_{ia}}{C_{im}} \text{ for } i=o,w,s. \quad (5.15 - 5.17)$$

5.3 Initial and Boundary Conditions

The initial conditions can be stated as follows.

$$p_l(x,y,z,0) = p_{l_i},$$

$$p_a(x,y,z,0) = p_{a_i},$$

$$p_m(x,y,z,0) = p_{m_i},$$

$$S_l(x,y,z,0) = S_{l_i},$$

$$S_o(x,y,z,0) = S_{o_i},$$

$$S_m(x,y,z,0) = S_{m_i},$$

and

$$\left. \begin{aligned} C_{il}(x, y, z, 0) &= C_{il_i} \\ C_{ia}(x, y, z, 0) &= C_{ia_i} \\ C_{im}(x, y, z, 0) &= C_{im_i} \end{aligned} \right\} \text{ for } i = o, w, s.$$

Generally, the initial conditions of a reservoir are those before the secondary stage when it is oil flooded. Therefore, the initial conditions for the uniform system are as follows:

$$\begin{aligned} p_l(x, y, z, 0) &= p_i, \\ S_l(x, y, z, 0) &= S_{o_i}, \\ S_a(x, y, z, 0) &= S_{w_{ir}}, \\ S_m(x, y, z, 0) &= 0, \\ C_{ol}(x, y, z, 0) &= 1, \\ C_{wl}(x, y, z, 0) &= 0, \\ C_{sl}(x, y, z, 0) &= 0, \\ C_{oa}(x, y, z, 0) &= 0, \\ C_{wa}(x, y, z, 0) &= 1, \\ C_{sa}(x, y, z, 0) &= 0, \\ C_{om}(x, y, z, 0) &= C_{om_{ini}}, \\ C_{wm}(x, y, z, 0) &= C_{wm_{ini}}, \end{aligned}$$

and

$$C_{sm}(x, y, z, 0) = C_{sm_{ini}}.$$

The initial aqueous and emulsion pressure values can be obtained through capillary pressure relationships and correlations.

For the case of a waterflooded reservoir, the following initial conditions are given.

$$\begin{aligned}
 p_a(x,y,z,0) &= p_{a_i}, \\
 S_i(x,y,z,0) &= S_{o_i}, \\
 S_a(x,y,z,0) &= 1 - S_{o_i}, \\
 S_m(x,y,z,0) &= 0, \\
 C_{oi}(x,y,z,0) &= 1, \\
 C_{wi}(x,y,z,0) &= 0, \\
 C_{si}(x,y,z,0) &= 0, \\
 C_{oa}(x,y,z,0) &= 0, \\
 C_{wa}(x,y,z,0) &= 1, \\
 C_{sa}(x,y,z,0) &= 0, \\
 C_{om}(x,y,z,0) &= C_{om_{ini}}, \\
 C_{wm}(x,y,z,0) &= C_{wm_{ini}},
 \end{aligned}$$

and

$$C_{sm}(x,y,z,0) = C_{sm_{ini}}.$$

Similarly, oleic and emulsion pressure values can be calculated through capillary pressure relationships and correlations. It should be noted that all these pressures can be assigned the same initial pressure.

In this model, the reservoir boundaries are assumed to be closed with no flow of fluid crossing them. Thus, the necessary boundary conditions along the entire exterior surface of the reservoir normal to the x , y , and z directions for all phases are

$$\left. \begin{aligned} \frac{\partial p_i}{\partial \bar{n}} &= 0 \\ \frac{\partial S_i}{\partial \bar{n}} &= 0 \\ \frac{\partial C_{ij}}{\partial \bar{n}} &= 0 \end{aligned} \right\} \text{ for } i=o,w,s \text{ and } j=l,a,m,$$

where \bar{n} is a unit vector normal to the boundary and points outwards away from the boundary surface.

The fifteen equations of the component mass balances and auxiliary relations with specified initial and boundary conditions are solved by the method developed by Coats et al.⁵⁰, and Farouq Ali and Ferrer⁵¹, and modified by Al-Seehati⁵² to simulate a micellar/polymer process. This method involves reducing the above system to five equations with five unknowns. These unknowns are written in the form δf , which is the change in f at the consecutive time steps ($f^{n+1} - f^n$). The new system of equations are given in the following forms with the five variables δp_l , δS_l , δS_a , δC_{om} , and δC_{wm} .

$$C_{11}\delta C_{om} + C_{12}\delta C_{wm} + C_{13}\delta S_l + C_{14}\delta S_a + C_{15}\delta p_l = \Delta(T_o^n \Delta \delta p_l) + Q_o^{*n+1} + R_1, \quad (5.18)$$

$$C_{21}\delta C_{om} + C_{22}\delta C_{wm} + C_{23}\delta S_l + C_{24}\delta S_a + C_{25}\delta p_l = \Delta(T_w^n \Delta \delta p_l) + Q_w^{*n+1} + R_2, \quad (5.19)$$

$$C_{31}\delta C_{om} + C_{32}\delta C_{wm} + C_{33}\delta S_l + C_{34}\delta S_a + C_{35}\delta p_l = \Delta(T_s^n \Delta \delta p_l) + Q_s^{*n+1} + R_3, \quad (5.20)$$

$$C_{41}\delta C_{om} + C_{42}\delta C_{wm} + C_{43}\delta S_l + C_{44}\delta S_a + C_{45}\delta p_l = 0, \quad (5.21)$$

and

$$C_{51}\delta C_{om} + C_{52}\delta C_{wm} + C_{53}\delta S_l + C_{54}\delta S_a + C_{55}\delta p_l = 0. \quad (5.22)$$

where the definition of the accumulation coefficients C_{ij} is given in Appendix G. These definitions are derived from the time-difference expansions of the accumulation terms shown in Appendix C, while the definition of R_i is given in Appendix D. The derivation of Eqns. (5.18) to (5.22) is shown in Appendices B through E.

5.4 Flow Mechanisms During Oil Displacement by Emulsion Flooding

Emulsion flooding can be used as a secondary recovery process to recover the oil left in a reservoir after it has been depleted of its energy through primary production. Emulsion flooding can also function as a tertiary recovery process to recover the residual oil left behind after waterflooding. Care should be taken in creating a mathematical representation of the displacement process physics to match the experimental results. The following is a description of the modeling of the process mechanisms, the fluid properties, and the rock-fluid properties involved in the simultaneous flow of oil, water, and emulsion in a given reservoir.

First to be considered are the microscopic processes taking place in a unit element as proposed by Payatakes et al. and reported in Soo⁴². Such an element in a porous medium can be described as a bundle of tubes of different diameters and

lengths. The pore size is generally proportional to the pore length. That is, the larger pores tend to be longer than the smaller ones. For simplicity, a unit bed element is used to represent the tube bundle. This element retains the various tube diameters, but uses the same weighted average length for all the tubes to ensure the pressure drop across each tube is the same.

Next, consider the injection of a polydisperse emulsion into a reservoir with oil and brine in place and a pore-size distribution. At first the larger emulsion droplets are captured in pore throats that range in size from about twice the drop diameter down to the smallest pore throat diameter. Because the number of capture sites is greater for the large droplets than for the small ones, the smaller droplets are able to move ahead through the reservoir. As the emulsion that first breaks through is only composed of these smaller droplets, the eluted emulsion concentration will initially be less than that of the injected emulsion. This has been observed in laboratory core flood tests. As the emulsion flood proceeds, the larger droplets will continue to flow through the porous medium, occupying the remaining capture sites until they too begin to elute. The droplets that are captured will either block or restrict pores such that the flow will be redirected to a contiguous network of larger pores. As the number of available capture sites for the larger droplets decreases, more of the larger droplets will

be eluted, and the effluent emulsion concentration will increase until at steady state it will be equivalent to the injected concentration.

Returning to a typical unit bed element in this reservoir, the element first experiences the encroaching flood as an emulsion consisting of smaller droplets with a low concentration relative to that of the injected emulsion. This emulsion exhibits non-Newtonian behaviour at the local average shear rate inside the porous medium. When the larger droplets reach the element, some of them will be captured in the tubes, and the flow will be redirected to the larger tubes. Since the capture sites of the small pores are now occupied, the larger droplets can proceed through the element. This increases the emulsion concentration and causes it to flow with a different rheological behaviour for that particular concentration and shear rate. The droplet capture mechanism just described also causes a reduction in absolute permeability of the porous medium in the zone swept by the emulsion flood. The reduced permeability in the displacing zone will lower the mobility of the displacing fluid in a homogeneous reservoir. In a heterogeneous reservoir, the blocking effect will enhance the redistribution of fluid from the higher permeability layers to the lower permeability layers, resulting in better sweep efficiency. In summary, displacement is improved by microscopic mobility control through local permeability

reduction for a homogeneous reservoir, and through macroscopic mobility control by diverting flow to less permeable layers for a stratified reservoir. Besides losing droplets through the capture mechanism, the emulsion phase can also lose surfactant because this component can diffuse, disperse, and adsorb onto the sand grain surfaces. At the flood front, where the emulsion is in contact with the reservoir oil and brine, interphase mass transfer of surfactant to the oleic or aqueous phases can occur, depending on the affinity of the surfactant. For a low concentration hydrophilic surfactant, the amount of oil that dissolves in the aqueous phase is negligible. Similarly, for a lipophilic surfactant, it is assumed that a negligible amount of water is transferred into the oleic phase. The oleic and aqueous phases are always immiscible, and hence cannot transfer surfactant to each other. Changes in the physical properties of each phase, namely density and viscosity, are influenced only by changes in the phase composition, not by changes in the phase pressure. For the rock-fluid properties, such as the relative permeabilities of each phase and the capillary pressure between phases, the presence of surfactant will reduce interfacial tension between the phases. This brings about lower residual saturations in each phase and enhances the relative permeability because the two-phase relative permeability curves approach those of complete miscibility as the amount of surfactant present is increased. In conclusion, the mass

balance of each component must be maintained when all of the mechanisms and properties just described are included in the mathematical model. The following section explains how each of the mechanisms and properties are modeled.

5.4.1 Emulsion Rheological Behaviour

As explained earlier, there are more capture sites available for the larger droplets than for the smaller ones. Therefore, the smaller droplets percolate ahead of the larger droplets and are the first to be produced in the effluent. During this flow of small droplets, the emulsion can be viewed as a homogeneous fluid with a low concentration and no interaction between the droplets and the pores. Hence, only one set of rheological behaviour data is required for the emulsion for this low concentration at different shear rates. As the larger droplets flow through the porous medium, more of the small pores are blocked and the flow is redistributed to the larger pores. An increasing number of the larger droplets can now move through the porous medium without being captured, and therefore the emulsion quality in these large pores increases with time. Eventually, steady state is reached, and the emulsion flows with the same injected concentration throughout the porous medium through the remaining open channels. It is clear that what is required for modeling the non-Newtonian behaviour of the local emulsion in the porous medium is a rheological correlation as a function of emulsion quality and shear rate. This function

can be independent of the droplet size due to the homogeneous nature of the emulsion during flow.

The emulsion rheological behaviour for single phase, one-dimensional flow will first be derived. The derivation is shown in Appendix I. It will then be modified to describe three-dimensional, multiphase flow. The rheological model used for single-phase, one-dimensional flow is based on the correlation developed by Alvarado and Marsden³⁹, later modified by Abou-Kassem and Farouq Ali^{43,44,45}.

The apparent viscosity of the emulsion for single phase and one-dimensional flow is as follows.

$$\mu_m = \frac{8K}{(\alpha\sqrt{F})^2} \left(\frac{3n+1}{4n} \right) (\bar{\gamma})^{n-1}, \quad (5.23)$$

where

$$\bar{\gamma} = \left(\frac{3n+1}{4n} \right) \frac{4\bar{V}}{\phi \left(\frac{\alpha^2 F k}{\phi} \right)^{1/2}}. \quad (5.24)$$

Eqns. (5.23) and (5.24) were derived based on the assumption that emulsions are viewed as homogeneous fluids and on the observation that the rheological behaviour of emulsions during flow in porous media is similar to that in a viscometer. That means Equations (5.23) and (5.24) can be

applied only for the emulsion with small droplet sizes in comparison to pore sizes.

For the mathematical model describing emulsion flow in porous media developed in the present work, the system dealt with is for the case in which drop size is comparable to the pore size. This rheological model cannot describe the rheological flow behaviour for this system on a macroscopic level. However, the model can be applied microscopically for the flow of small emulsion droplets inside the large pores. This occurs when the small pore openings are plugged and the flow is redirected to larger pores. As time passes, the droplet capture sites are occupied, the drop retention decreases, and more and more of the larger drops flow through the large pore openings. The concentration or quality of the emulsion in the large pores changes with time and position in the porous medium. The change in emulsion quality in the pores may affect the change in emulsion rheological behaviour during its flow in a porous medium. This is supported by the experimental results described in Chapter 4, which compare the rheological behaviour of the emulsion during its flow in the porous medium to shearing in a viscometer. It is shown in Chapter 4 that within a given range of shear rates, the slope of the porous medium rheogram varies slightly while the slope of the viscometry rheogram is constant. This difference is probably due to the fact that the viscometry data were obtained for a particular emulsion composition

while there is a change in emulsion quality during flow in the porous medium due to the filtration process. Therefore, one set of K and n values from viscometry data is not enough to describe emulsion rheological behaviour in a porous medium throughout the whole range of shear rates of interest. This is true when the emulsion drop sizes are about the same as the pore sizes of the medium. Although the change in K and n as a function of emulsion quality should be further investigated to understand this relationship in greater detail, overall the two rheograms have very similar slopes. Therefore, constant values of K and n were used for an injected emulsion composition to model the emulsion rheological behaviour in the porous medium.

The correlation in Eqn. (5.23) will be referred to as a single phase non-Newtonian correlation later on in the discussion of the simulation results. In the case of multiphase flow, the shear rate correlation is modified to account for the shear rate in the emulsion phase only and the following equation for one dimension will be referred to as the multiphase non-Newtonian correlation.

$$\mu_m = \frac{8K}{(\alpha\sqrt{F})^2} \left(\frac{3n+1}{4n} \right) (\bar{\gamma}_m)^{n-1}, \quad (5.25)$$

where,

$$\bar{\gamma}_m = \left(\frac{3n+1}{4n} \right) \frac{4\bar{V}_m}{\phi \left(\frac{\alpha^2 F k}{\phi} \right)^{1/2}}. \quad (5.26)$$

For one dimension and neglecting capillary and gravity effects, the superficial velocity of the emulsion phase is as follows.

$$\bar{V}_m = \frac{\lambda_m}{\lambda_n} \bar{V}. \quad (5.27)$$

For three-dimensional flow in porous media, the average velocity in block i, j, k is given by

$$\begin{aligned} \bar{V}_{m_{i,j,k}} = \left(\frac{\bar{q}_m}{A} \right)_{i,j,k} = & \left\{ \left[\left(\frac{q_m}{A} \right)_{i+1,j,k} + \left(\frac{q_m}{A} \right)_{i-1,j,k} \right]^2 \right. \\ & + \left[\left(\frac{q_m}{A} \right)_{i,j+1,k} + \left(\frac{q_m}{A} \right)_{i,j-1,k} \right]^2 \\ & \left. + \left[\left(\frac{q_m}{A} \right)_{i,j,k+1} + \left(\frac{q_m}{A} \right)_{i,j,k-1} \right]^2 \right\}^{1/2}. \end{aligned} \quad (5.28)$$

The average shear rate $\bar{\gamma}$ in each block, which corresponds to the average velocity in that block, is calculated using Eqn. (5.26). The apparent viscosity of the emulsion at that position and time can then be obtained from Eqn. (5.25).

5.4.2 Three-Phase Relative Permeabilities

The following correlations were used for modelling three phase relative permeabilities

5.4.2.1 Naar-Wygal-Henderson Model⁶⁰

The simplified forms for the relative permeabilities to oleic (k_{rl}), aqueous (k_{ra}), and emulsion (k_{rm}), by considering the emulsion phase as a middle phase, are as follows.

$$k_{rl} = \frac{S_l^3(2 - S_l - 2S_{air})}{(1 - S_{air})^4}, \quad (5.29)$$

$$k_{ra} = \left(\frac{S_a - S_{air}}{1 - S_{air}} \right)^4, \quad (5.30)$$

$$k_{rm} = \frac{S_m^3(1 - S_l + S_a - 2S_{air})}{(1 - S_{air})^4}, \quad (5.31)$$

5.4.2.2 Pope's Model^{53,54}

The mathematical model in the present study was developed by considering the three phases in the system as immiscible. These three phases are the oleic (oil-rich) phase, the aqueous (water-rich) phase, and the emulsion (surfactant-rich) phase. In reality, the oil-in-water emulsion is usually miscible in water and the water-in-oil emulsion tends to be miscible with the oil which is the continuous phase. This partial miscibility is incorporated into the model through the lower interfacial tension between phases due to the presence of surfactant. Furthermore, the reduced

interfacial tension helps to reduce the residual saturation and thus increase the relative permeability.

A. Interfacial Tension

The interfacial tension is calculated using the empirical relations of Reed and Healy as quoted in Camilleri⁵⁵ which can be summarized as follows. The interfacial tension between two phases is a function of the amount of solubilized water or oil relative to the amount of surfactant in the emulsion phase. For three-phase compositions, two interfaces are present and the interfacial tensions are computed using

$$\log \gamma_{am} = G_{12} + \frac{G_{11}}{G_{13} \left(\frac{C_{wm}}{C_{sm}} \right) + 1}, \quad (5.32)$$

and

$$\log \gamma_{lm} = G_{22} + \frac{G_{21}}{G_{23} \left(\frac{C_{om}}{C_{sm}} \right) + 1}. \quad (5.33)$$

Interfacial tensions are used in the calculation of capillary numbers. The residual saturations are then calculated from a capillary desaturation correlation.

B. Residual Saturations

The capillary number is defined as

$$N_c = \frac{u\mu}{\gamma},$$

where

u = Darcy velocity [m/s],

μ = viscosity [Pa.s],

and

γ = interfacial tension [N/m].

The residual saturations are calculated from capillary desaturation curves which are modeled using the following equation for two-phase flow^{54,56},

$$\frac{S_{jr}}{S_{jrw}} = T_{j1}(\log N_c + T_{j2}) \quad \text{for} \quad 0 \leq \frac{S_{jr}}{S_{jrw}} \leq 1 \quad (5.34)$$

where S_{jrw} is equal to the residual phase saturation at low capillary numbers or high interfacial tension for an oil/water system.

The parameters T_{ji} depend on fluid/rock properties, such as contact angle and pore-size distribution, and to a lesser degree on viscosity, which will be neglected in this case.

The capillary desaturation curves as conceptualized for two-phase flow can be further extended to three-phase flow without any theoretical or experimental justification. This follows from the assumption that for three-phase flow where the third phase has intermediate wettability between the other two, a third curve can be drawn such that for any capillary number, the residual saturation of the third phase is between the residual saturation of the other two.

Pope's model^{53,54} as mentioned in Camilleri⁵⁵, an empirical model which quantifies the residual saturation, was used for calculating the residual saturations and relative permeabilities. Pope's model assumes that the third phase is trapped according to a function similar to that used for the two-phase flow. Therefore, the residual saturations for the three phases are

$$S_{lr} = S_{lrw} T_{l1} \left(\log \frac{u\mu_l}{\gamma_{lm}} + T_{l2} \right), \quad (5.35)$$

$$S_{ar} = S_{arw} T_{a1} \left(\log \frac{u\mu_a}{\gamma_{am}} + T_{a2} \right), \quad (5.36)$$

and

$$S_{mr} = T_{m1} + T_{m2} \log N_c. \quad (5.37)$$

It can be seen from the above equations that the residual saturations for the oleic and aqueous phases are calculated in the same manner as used for two-phase flow. Furthermore, the residual saturation of the third phase is independent of the other two phases and is only a function of the capillary number. The capillary number used in Eqn. (5.37) is the larger of the two possible for the three-phase case. Parameters T_{m1} and T_{m2} are adjusted to give a residual saturation S_{mr} between that of the aqueous and the oleic phases for a given capillary number.

The normalized saturations (S_{nj}), which require values of the residual saturations of each phase, can be calculated using

$$S_{nj} = \frac{S_j - S_{jr}}{1 - \sum_{j'} S_{j'r}} \quad \text{where } j' = l, a, m. \quad (5.38)$$

That is,

$$S_{nl} = \frac{S_l - S_{lr}}{1 - (S_{lr} + S_{ar} + S_{mr})}, \quad (5.39)$$

$$S_{na} = \frac{S_a - S_{ar}}{1 - (S_{lr} + S_{ar} + S_{mr})}, \quad (5.40)$$

and

$$S_{nm} = 1 - S_{nl} - S_{na}. \quad (5.41)$$

Note that the condition $S_{lr} + S_{ar} + S_{mr} < 1$ is necessary, which sets an upper limit on S_{mr} if S_{lr} and S_{ar} are given.

C. Relative Permeabilities

The relative permeabilities for three-phase flow are modeled using relations similar to those for two-phase flow, namely

$$k_{rj} = k_{rj}^o (S_{nj})^{e_j}, \quad (5.42)$$

where

k_{rj}^o = end point relative permeability of phase j , and

e_j = curvature of relative permeability for phase j .

The simple functionality shown above has the following merits.

1. When $S_j = S_{jr}$, $k_{rj} = 0$.

2. When $S_{ir} = 1 - S_{ar} - S_{mr}$, $k_{ri} = k_{ri}^o$ (the end point), and similarly for the aqueous and emulsion phases.
3. k_{ij} reduces to k_{ri} and k_{ra} when $S_{mr} = 0$, that is, when there is no emulsion phase.

The basic requirement that k_{ij} approaches the proper limit as the capillary number, and hence S_{jr} , changes for three-phase flow is similar to the requirements for two-phase flow. The requirements are:

1. k_{ij} should approach the water-oil (with no surfactant) value as the capillary number decreases.
2. k_{ij} should approach the phase saturation as the capillary number increases (straight line relative permeabilities where $S_{jr} = 0$).

The end points k_{ij}^o must change as residual saturations change because of detrapping. However, the relative permeabilities must approach the proper limits. Therefore, linear interpolations of the end point relative permeability and curvature between the high tension or low N_c values and the low tension or high N_c values are performed based on the change in the residual phase saturations S_{jr} as follows:

$$k_{ri}^o = k_{riw}^o + \frac{S_{arw} - S_{ar}}{S_{arw}} (k_{ric}^o - k_{riw}^o), \quad (5.43)$$

$$k_{ra}^o = k_{raw}^o + \frac{S_{irw} - S_{ir}}{S_{irw}} (k_{rac}^o - k_{raw}^o), \quad (5.44)$$

$$e_i = e_{hw} + \frac{S_{arw} - S_{ar}}{S_{arw}}(e_{ic} - e_{hw}), \quad (5.45)$$

and

$$e_a = e_{aw} + \frac{S_{irw} - S_{ir}}{S_{irw}}(e_{ac} - e_{aw}). \quad (5.46)$$

Subscript *w* designates a water-oil (no surfactant) system with a low capillary number or high interfacial tension, while subscript *c* designates a large capillary number or low interfacial tension. Generally, k_{rjc}^o and e_{jc} are assigned the value of 1.0, which corresponds to a high capillary number and zero residual saturation for the trapped phase. That is, the system behaves like a single-phase flow.

In the present work, e_i and e_a are calculated by setting e_{ic} and e_{ac} equal to 1.0 and obtaining e_{hw} and e_{aw} from the oil-water relative permeability curves. Alternatively, e_i and e_a can be read in as an input data directly. Similarly, k_{rm}^o and e_m can be read in directly.

5.4.3 Adsorption

Surfactant adsorption is allowed to occur according to the Langmuir isotherm

$$C_{rs} = \frac{A_d C_s}{1 + B_d C_s}. \quad (5.47)$$

The above Langmuir equilibrium adsorption isotherm is derived from the Langmuir adsorption kinetic equation,

$$\frac{d}{dt}C_{rs} = K_1\left(1 - \frac{C_{rs}}{C_{rs}^*}\right)C_s - K_2\frac{C_{rs}}{C_{rs}^*}. \quad (5.48)$$

Using the initial condition of $C_{rs}=0$ at $t=0$, the general solution for constant C_s is

$$C_{rs} = \frac{K_1 C_s C_{rs}^* \left[1 - e^{-\left(\frac{K_1 C_s + K_2}{C_{rs}^*}\right)t} \right]}{K_1 C_s + K_2}. \quad (5.49)$$

Simulation time is assumed to be much longer than the time needed to achieve equilibrium; i.e., t approaches ∞ . Hence, the general solution is reduced to the Langmuir equilibrium adsorption isotherm,

$$C_{rs} = \frac{K_1 C_s C_{rs}^*}{K_1 C_s + K_2}, \quad (5.50)$$

or

$$C_{rs} = \frac{A_d C_s}{1 + B_d C_s}, \quad (5.51)$$

The present model assumes that surfactant is adsorbed on the rock surface only through the emulsion phase. Hence, the adsorption model used is

$$C_{rsm} = \frac{A_d C_{sm}}{1 + B_d C_{sm}}, \quad (5.52)$$

Thus, the total amount of surfactant adsorbed [kg of surfactant] is

$$V_b \rho_r (1 - \phi_{init}) C_{rsm} = V_b \rho_r (1 - \phi_{init}) \frac{A_d C_{sm}}{1 + B_d C_{sm}}, \quad (5.53)$$

5.4.4 Droplet Capture Mechanism

It was found in the experimental work described in Chapter 4 that the droplet capture mechanism proposed by Soo and Radke can explain the flow of emulsions through porous media for the system investigated. Therefore, it was decided to modify the filtration model^{47,48} to include the re-entrainment effect and then incorporate it into the numerical simulator to account for the droplet capture mechanism. The following is a summary of the filtration model derived by Soo and Radke^{47,48} and a description of the extended model to include the re-entrainment effect.

5.4.4.1 No Re-entrainment

Listed below are the assumptions of the filtration model for the case of no re-entrainment of captured droplets into the flowing stream.

Assumptions:

1. There is no re-entrainment when there is significant electrical double layer repulsion between drops, and between drops and sand grains, high drop tensions, and relatively low flow rates.
2. For highly stable emulsions, it can be assumed that droplet coalescence does not need to be accounted for.

3. For dilute, monodisperse emulsions, drops will be captured one at a time; i.e., there is no simultaneous multiple-drop capture. Hence, the filter coefficient for a given pore throat size is independent of drop-volume concentration.
4. Drops are not captured on previously retained drops.

The drop capture kinetics can be written as

$$\frac{d\sigma}{dt} = \lambda_{sl} \left(1 - \frac{\alpha\sigma}{\phi_i} \right) u\theta. \quad (5.54)$$

The solution with no drop retention as an initial condition is

$$\sigma = \frac{\phi_i}{\alpha} \left(1 - e^{-\lambda_{sl} u \theta \frac{\alpha}{\phi_i}} \right). \quad (5.55)$$

Local permeability is expressed as

$$\frac{k}{k_i} = 1 - \frac{\beta\sigma}{\phi_i}. \quad (5.56)$$

The above correlations for drop retention σ and permeability ratio $\frac{k}{k_i}$ are for the case of one dimension and single phase flow.

5.4.4.2 With Re-entrainment

The above drop capture kinetics can be modified to account for the re-entrainment of droplets into the flowing stream. When this is done, the following equation is obtained:

$$\frac{d\sigma}{dt} = \lambda_{sl_1} \left(1 - \frac{\alpha\sigma}{\phi_i}\right) u\theta - \lambda_{sl_2} u \left(\frac{\alpha\sigma}{\phi_i}\right). \quad (5.57)$$

The solution with no drop retention as an initial condition is

$$\sigma = \frac{\lambda_{sl_1} \phi_i \theta}{\alpha(\lambda_{sl_1} \theta + \lambda_{sl_2})} \left[1 - e^{\frac{-\alpha u}{\phi_i} (\lambda_{sl_1} \theta + \lambda_{sl_2}) t} \right]. \quad (5.58)$$

The above drop retention equation will be referred to as the time-dependent capture correlation which is for the case of one dimension and a single phase. It can be modified for multiphase flow by assuming that drops are captured only from the emulsion phase. Hence, for one dimension and neglecting capillary and gravity effects, $u_m = \frac{\lambda_{rm}}{\lambda_r} u$ will be used instead of u . Then, for three dimensions, the expression can be modified further by using the following average velocity \bar{u}_m for an emulsion phase:

$$\begin{aligned}
\bar{u}_{m,i,j,k} &= (u_{mx}^2 + u_{my}^2 + u_{mz}^2)^{1/2} \\
&= \left[(u_{m,i+1,j,k} + u_{m,i-1,j,k})^2 + (u_{m,i,j+1,k} + u_{m,i,j-1,k})^2 + (u_{m,i,j,k+1} + u_{m,i,j,k-1})^2 \right]^{1/2} \\
&= \left\{ \left[-k_x \frac{k_{rm}}{\mu_m} \right]_{i+\frac{1}{2}} \left(\frac{\Phi_{m,i+1} - \Phi_{m,i}}{\Delta x} \right) - k_x \frac{k_{rm}}{\mu_m} \left[\left(\frac{\Phi_{m,i} - \Phi_{m,i-1}}{\Delta x} \right) \right]_{i-\frac{1}{2}} \right]^2 \\
&\quad + \left[-k_y \frac{k_{rm}}{\mu_m} \right]_{j+\frac{1}{2}} \left(\frac{\Phi_{m,i+1} - \Phi_{m,i}}{\Delta y} \right) - k_y \frac{k_{rm}}{\mu_m} \left[\left(\frac{\Phi_{m,i} - \Phi_{m,i-1}}{\Delta y} \right) \right]_{j-\frac{1}{2}} \right]^2 \\
&\quad + \left[-k_z \frac{k_{rm}}{\mu_m} \right]_{k+\frac{1}{2}} \left(\frac{\Phi_{m,i+1} - \Phi_{m,i}}{\Delta z} \right) - k_z \frac{k_{rm}}{\mu_m} \left[\left(\frac{\Phi_{m,i} - \Phi_{m,i-1}}{\Delta z} \right) \right]_{k-\frac{1}{2}} \right]^2 \right\}^{1/2}. \quad (5.59)
\end{aligned}$$

Similar to the case with no re-entrainment, local permeability can be calculated from the following equation.

$$\frac{k}{k_i} = 1 - \frac{\beta \sigma}{\phi_i}. \quad (5.60)$$

Equation (5.58) can be simplified to a form similar to the Langmuir Adsorption Isotherm by considering that the capture time is quite small compared to simulation time; i.e., t approaches ∞ . Thus, the following instantaneous droplet capture correlation is obtained.

$$\sigma = \frac{\lambda_{sl_1} \phi_i \theta}{\alpha (\lambda_{sl_1} \theta + \lambda_{sl_2})} \quad \text{or} \quad \sigma = \frac{A_c \theta}{1 + B_c \theta}, \quad (5.61)$$

where,

$$B_c = \frac{\lambda_{sl_1}}{\lambda_{sl_2}}, \quad (5.62)$$

$$A_c = \frac{\phi_i}{\alpha} B_c, \quad (5.63)$$

and

$$\theta = \frac{\rho_m}{\rho_i} C_{im}. \quad (5.64)$$

6. DEVELOPMENT OF THE COMPUTER MODEL

The mathematical model developed in Chapter 5 is transformed into a computer program which consists of a main program and twelve subroutines. The program flow diagram is shown in Fig. 6.1. The following is a description of the main program and all the subroutines.

6.1 Main Program

The reservoir data and initialization data are first read in and then printed out as the input data. The constant part of the transmissibilities is then calculated. The transmissibilities and the dispersion term are written at time level n in the mass balance equations. Therefore, properties, such as the phase density, phase viscosity, and relative permeability, are found using the variables at the previous time level. These calculations are then followed by the computation of the transmissibilities and the dispersion coefficients, which remain the same during an iteration.

The cycle of computation is started by setting the time step, the number of reduced time step sizes, and the iteration number. The values of the unknown variables at time level $n+1$ are assigned by extrapolation for the first iteration. Next, the rock-fluid and fluid properties are recalculated as functions of the new time level variables which are required during the computation of chord slopes. The mass flow rates

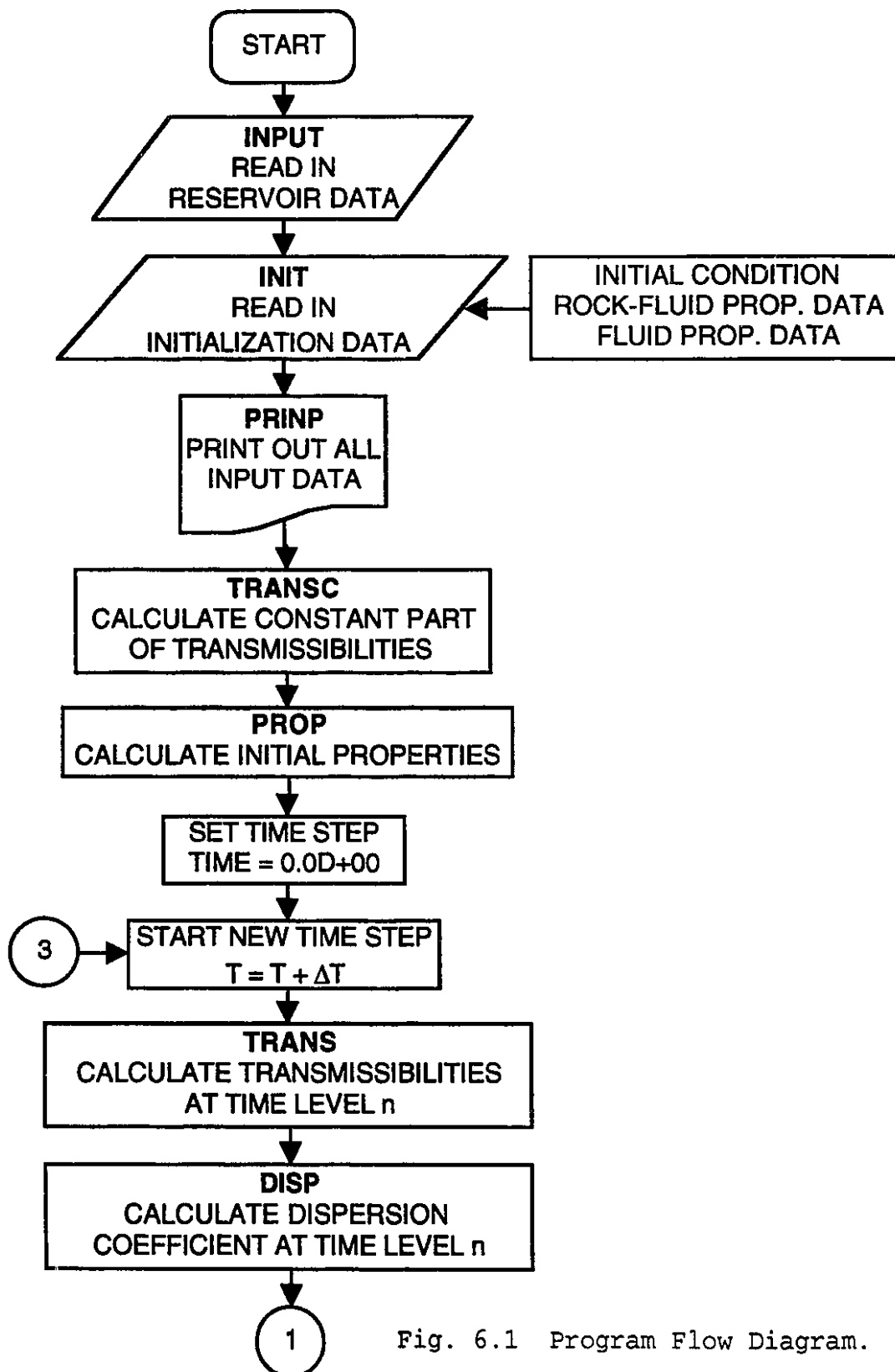


Fig. 6.1 Program Flow Diagram.

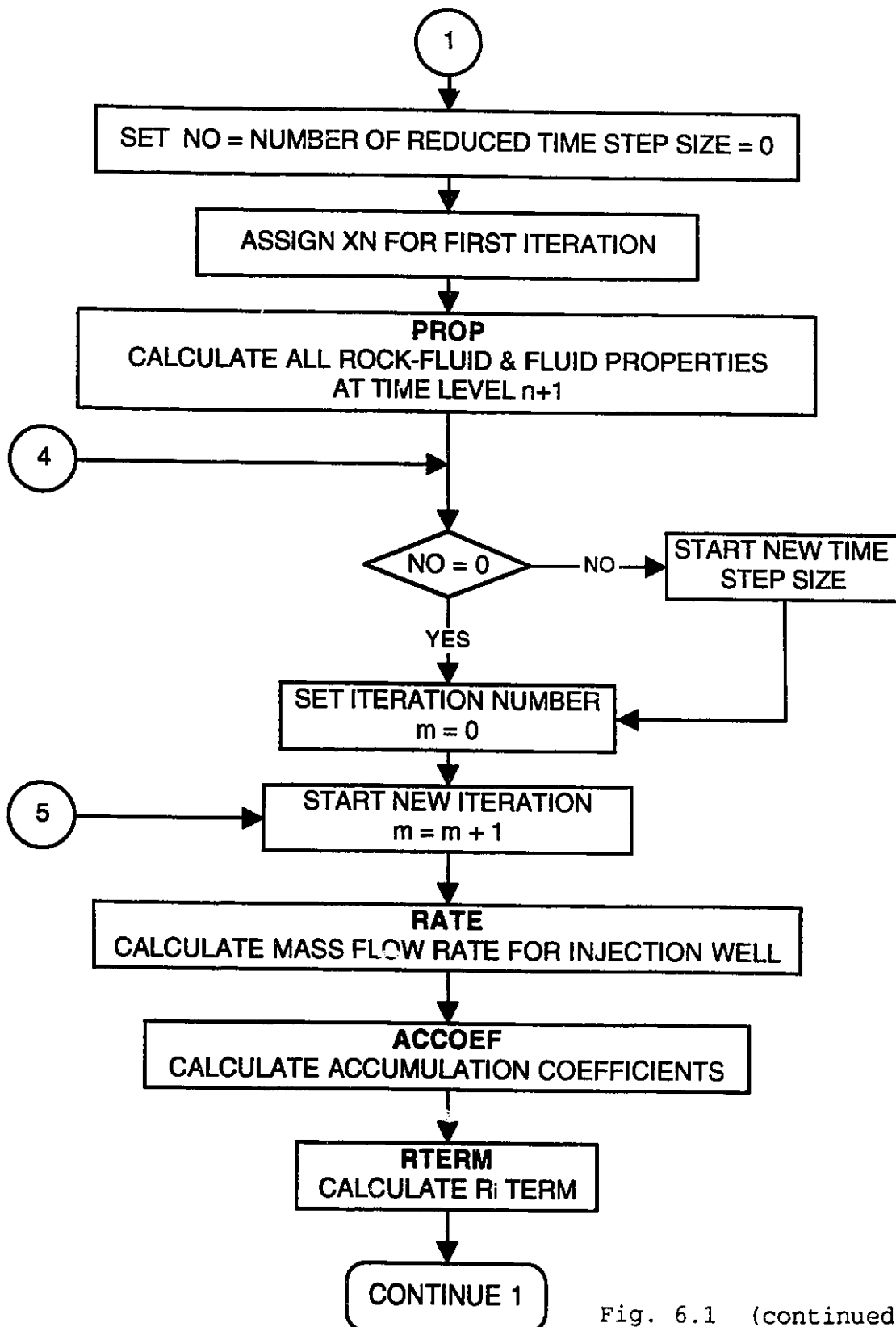


Fig. 6.1 (continued).

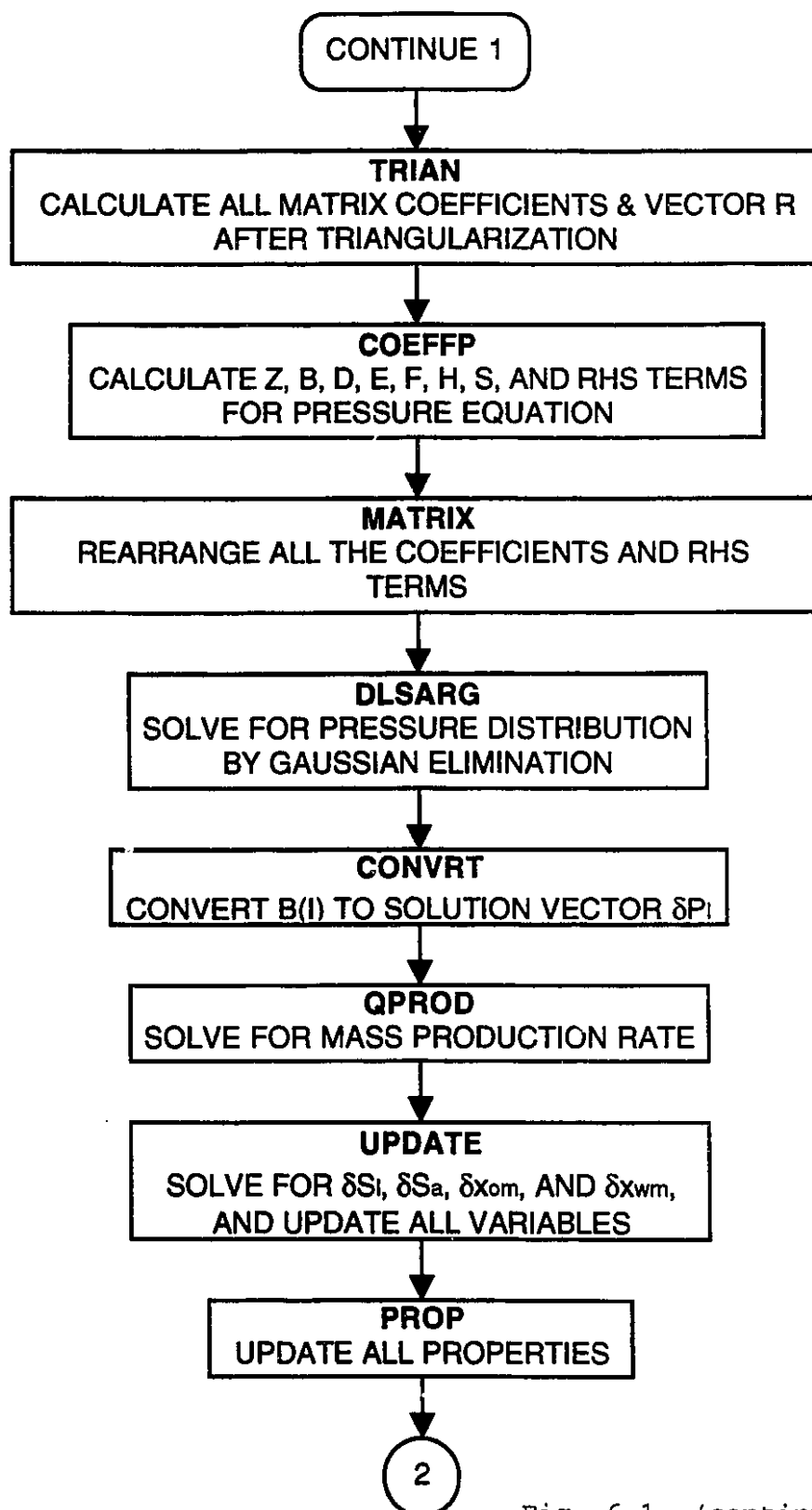


Fig. 6.1 (continued).

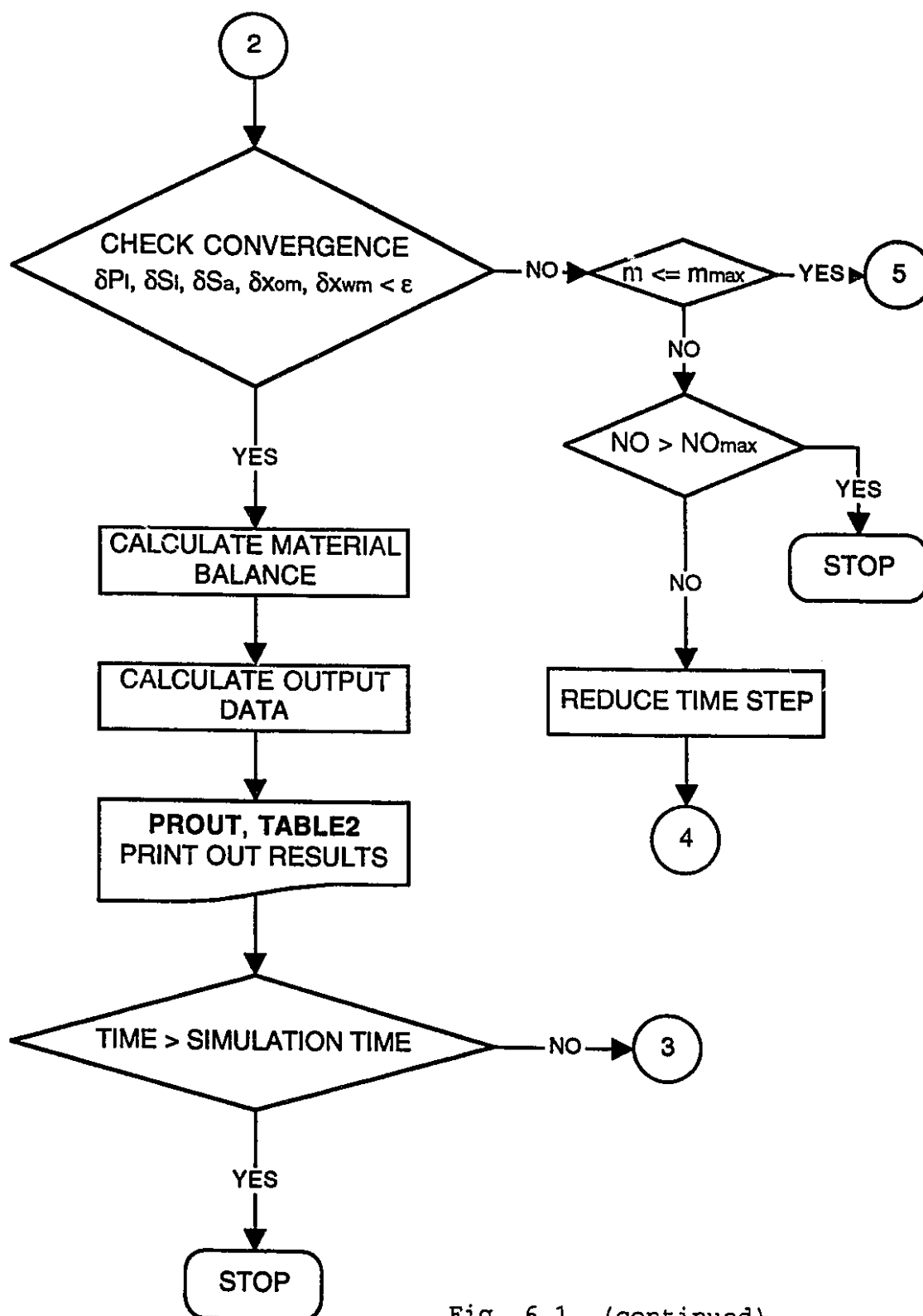


Fig. 6.1 (continued).

for each component for an injection well are then calculated. This includes the calculation of flow rates in each layer depending on the mobilities of the injected fluid in that layer for a stratified reservoir. Following this, the accumulation coefficients C_{ij} and the R_i terms, shown in Appendices G and D, respectively, are calculated. The matrix coefficients and the R_i terms of the system are then triangularized. The pressure equation (Eqn. F.10) described in Appendix F is then solved for δp_i by Gaussian elimination, followed by the mass production rates for each component. Finally, the remaining unknowns, which are δS_i , δS_a , δC_{om} , and δC_{wm} , are solved explicitly by back substitution, followed by an update in all the variables at time level $n+1$.

Once all the unknowns are solved and all the properties are updated, the convergence of these variables is checked. The tolerances used for the changes in the absolute values of the variables over one iteration, i.e. $\delta p_i^{(m)}$, $\delta S_j^{(m)}$, and $\delta C_{ij}^{(m)}$ are 115, 0.0001, and 0.0001, respectively. If all the variables converge, the mass balances of the oil, water, and surfactant are calculated, and the output data computed and printed out. The program computation then proceeds to the new time interval or stops if the simulation time has elapsed. If the solution does not converge, the updated variables and properties are used for the next iteration. If convergence is still not achieved after reaching the maximum number of iterations allowed, the time step size is reduced and the

calculation procedure in the cycle is repeated. An error message is printed if convergence is not reached within a given maximum number of reduced time steps.

6.2 Subroutine INPUT

The following reservoir data are read in: number of dimensions, number of blocks in the x , y , and z directions, grid index, block length in x , y , and z directions, depth below sea level, permeabilities in x , y , and z directions, porosity, rock compressibility, rock density, pore volume of the core, and well information including the number of wells, the location of the wells, and the injection rate and composition.

6.3 Subroutine INIT

This subroutine reads in the initialization data. The initial condition data of pressure, saturation and phase composition, and original oil in place are first read in. The rock-fluid and fluid property data are then read in. These property data are the relative permeability parameters, viscosity of each component, emulsion rheological parameters, density of each component, dispersion coefficient of each component in each phase, surfactant adsorption data, and filtration parameters.

6.4 Subroutine PRINP

All the reservoir and initialization data read in earlier are printed out by this subroutine.

6.5 Subroutine TRANSC

The purpose of this subroutine is to calculate the constant part of the transmissibility in the x , y , and z directions depending on the number of dimensions.

6.6 Subroutine TRANS

The transmissibilities of oil, water, and surfactant in the oleic, aqueous, and emulsion phases are calculated by this subroutine in the x , y , and z directions. The phase potentials for an upstream block are first checked. The transmissibilities of each component in that phase are then calculated using the upstream properties. For instance, the transmissibility of the oleic phase for component i can be computed as follows.

$$T_{ilx, i-\frac{1}{2}, j, k}^n = w_{lx} T_{ilx, i, j, k}^n + (1 - w_{lx}) T_{ilx, i+1, j, k}^n \quad \text{for } i = o, w, s,$$

where

$$w_{lx} = 1 \text{ if } \Phi_{i, j, k}^n > \Phi_{i+1, j, k}^n,$$

and

$$T_{ilx, i, j, k}^n = \frac{A_x k_x}{\Delta x} \bigg|_{i-\frac{1}{2}, j, k} \left(\frac{\rho_l C_{il} k_{rl}}{\mu_l} \right)_{i, j, k}^n.$$

The constant part, $\frac{A_x k_x}{\Delta x} \bigg|_{i-\frac{1}{2}, j, k}$, is obtained from subroutine TRANSC.

6.7 Subroutine DISP

This subroutine calculates the coefficient of the dispersion term. For constant dispersion coefficients, the harmonic mean is used for averaging, as shown in the following example.

$$T_{dix}^n = \frac{A_x \phi D_{il}}{\Delta x} \bigg|_{i+\frac{1}{2},j,k}^n$$

$$= \frac{2A_{x_{i+1,j,k}}(\phi D_{il})_{i+1,j,k} A_{x_{i,j,k}}(\phi D_{il})_{i,j,k}}{A_{x_{i+1,j,k}}(\phi D_{il})_{i+1,j,k} \Delta x_{i,j,k} + A_{x_{i,j,k}}(\phi D_{il})_{i,j,k} \Delta x_{i+1,j,k}}.$$

6.8 Subroutine PROP

The purpose of this subroutine is to calculate the following rock-fluid and fluid properties using the selected physical property correlations:

1. Phase densities using a weighted-average correlation.
2. Oleic and aqueous phase viscosities using a weighted-average correlation.
3. Relative permeabilities to the oleic, aqueous, and emulsion phases using the Naar-Wygal-Henderson model or Pope's model.
4. Emulsion viscosity using a weighted-average correlation, a single-phase non-Newtonian correlation, or a multiphase non-Newtonian correlation.
5. Absolute permeability correlation using the filtration model.

6.9 Subroutine RATE

This subroutine can also handle the calculation of the volumetric injection flow rate for each block in the case that a well penetrates more than one block. The mass flow rate is then calculated.

6.10 Subroutine ACCOEF

The calculation of the accumulation coefficients shown in Appendix G is performed in this subroutine.

6.11 Subroutine RTERM

The calculation of the R_i term derived in Appendix D is carried out in this subroutine.

6.12 Subroutine TRIAN

The purpose of the subroutine is to determine all the coefficients of the matrix C , the identity matrix, and the vector R after the triangularization shown in Appendix F.

6.13 Subroutine COEFFP

The purpose of the subroutine is to calculate Z , B , D , E , F , H , S , and the RHS terms for the pressure Eqn. (F.10).

6.14 Subroutines MATRIX, DLSARG, and CONVRT

The subroutine MATRIX rearranges the coefficients Z , B , D , E , F , H , and S from δp_i and the RHS terms of the pressure equation into the form, $AA \cdot \delta p_i = BB$. This matrix equation is then solved by Gaussian elimination using the subroutine DLSARG to provide the solution vector. Finally, the

subroutine CONVRT is used to convert the solution vector into the block dimensions of $\delta p_{i,jk}$.

6.15 Subroutine QPROD

Volumetric production rates at time level $n+1$ for the oleic, aqueous, and emulsion phases are calculated for the production block with a specified pressure according to the equations in Appendix F for a linear core flood. The mass production rates for each component at time level $n+1$ are then calculated.

6.16 Subroutine UPDATE

Subroutine UPDATE is called to solve the remaining unknowns, δS_a , δS_l , δC_{wm} , and δC_{om} , according to Eqns. (F.15), (F.17), (F.19), and (F.21), respectively shown in Appendix F. The values of all unknown variables, oleic pressure, phase saturations, mass fraction of the emulsion phase, are then updated for the new time level. This is followed by a calculation of the mass fractions of the oleic and aqueous phases.

6.17 Subroutines PROUT and TABLE2

The subroutine PROUT is called to print out the results, including the calculated values of the unknown variables, a well summary, and a time step summary at the selected value of pore volumes injected.

7. RESULTS AND DISCUSSION

Although the multiphase simulator described in Chapter 5 was three-dimensional, only the one-dimensional version was tested. This simulator was validated by comparing the simulation results with the results from a linear core flood performed in the laboratory. The comparison was made using different physical property models and testing different mechanisms to determine which combination best followed the core flood observations and measurements. The experimental data of laboratory core flood #5 was chosen for verifying the simulator developed. It was carried out for tertiary oil recovery by injecting caustic emulsion H2 (water-in-oil) continuously. A discussion of the validation of the emulsion flood simulator developed and the sensitivity study is presented in the following sections.

7.1 Validating the Simulator

Simulator validation was undertaken by comparing the experimental and simulated production history of core flood #5. It was tested by incorporating different physical property models, such as the relative permeability model, the emulsion rheological model, and the drop capture and permeability reduction model. The effects of these physical properties on the prediction of the emulsion flooding performance in comparison to the experimental observations are discussed below.

7.1.1. Effect of Different Emulsion Viscosity

Correlations

Simulation Runs 5/1 and 5/2 (5 refers to core flood #5) were carried out using the Naar-Wygal-Henderson correlation for three-phase relative permeabilities (Eqns. 5.29 - 5.31), but using different rheological correlations to calculate emulsion viscosity. The purpose was to determine the rheological effect on the production history prediction. Other rheological correlations which better predict emulsion viscosity were used in subsequent investigations. The emulsion viscosity for Run 5/1 was calculated from the weighted average of the viscosities of the three components:

$$\frac{1}{\mu_m} = \frac{C_{om}}{\mu_o} + \frac{C_{wm}}{\mu_w} + \frac{C_{sm}}{\mu_s}. \quad \text{This run simulated core flood \#5,}$$

neglecting capillarity, emulsion droplet capture and absolute permeability reduction, and surfactant adsorption. Table 7.1 shows the input data for Run 5/1 and Fig. 7.1 to Fig. 7.5 show the comparisons of the experimental and the simulation results.

It is shown in Fig 7.1 that the simulated pressure required for injecting emulsion at a constant flow rate of 0.0096 m³/day (400 cc/hr) was quite low in comparison with the experimental pressure. Also, the shape of the curve does not follow the trend found in the experimental data. This indicates that either the three-phase relative permeability

Table 7.1

Simulation Input Data for Run 5/1 - 5/8

A.1 Core Data

Dimensions of Ottawa Sandpack	0.05 m ² area × 0.61 m length
Pore Volume, m ³	723 × 10 ⁻⁶
Porosity, fraction	0.3851
Absolute Permeability, m ²	0.7950 × 10 ⁻¹¹
Initial Oil in Place, m ³	627 × 10 ⁻⁶
Irreducible Water Saturation, % PV	13.28
Residual Oil Saturation, % PV	24.86

A.2 Pressure After Waterflooding (kPa)

Block No.	1	2	3	4	5	6	7	8	9	10
Pres.	128.90	125.84	122.77	119.71	116.65	113.58	110.52	107.45	104.40	101.33

B. Horsefly Crude Oil Data

Density, kg/m ³	886
Viscosity, Pa.s	0.018

C. 2% (wt.) NaCl Brine Data

Density, kg/m ³	1000
Viscosity, Pa.s	0.107 × 10 ⁻²

D. Injected Emulsion Data

Type	w/o	
Composition	Horsefly Crude Oil, vol %	51.61
	1% (wt.) NaOH, vol %	48.39
Injection Rate, m ³ /s	0.1111 × 10 ⁻⁶	
Frontal Velocity, m/s	0.9373 × 10 ⁻⁴	

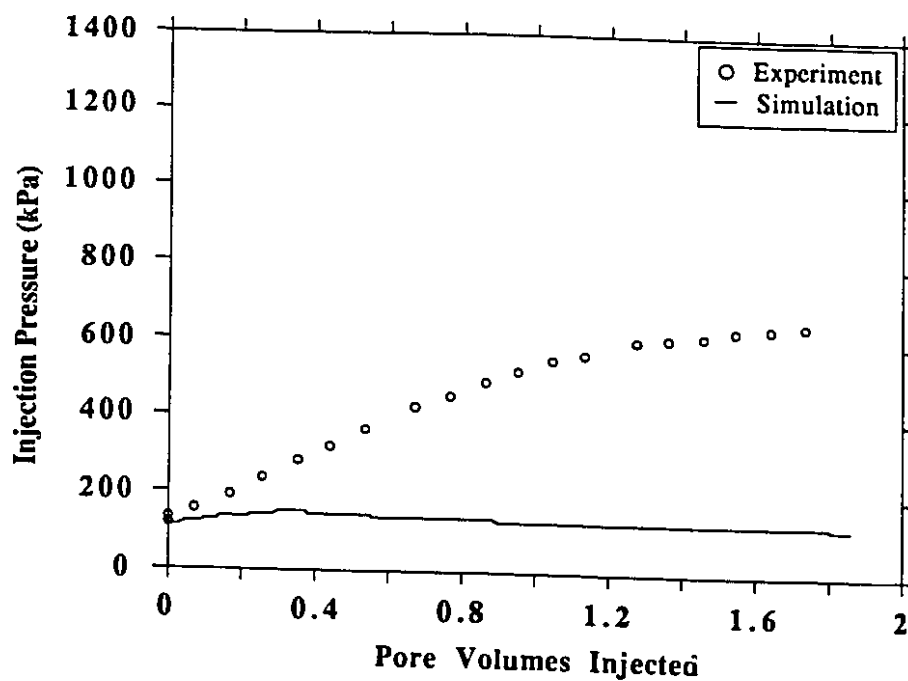


Fig. 7.1 Comparison of Experimental and Simulated Injection Pressure History for Run 5/1 for Emulsion Flooding.

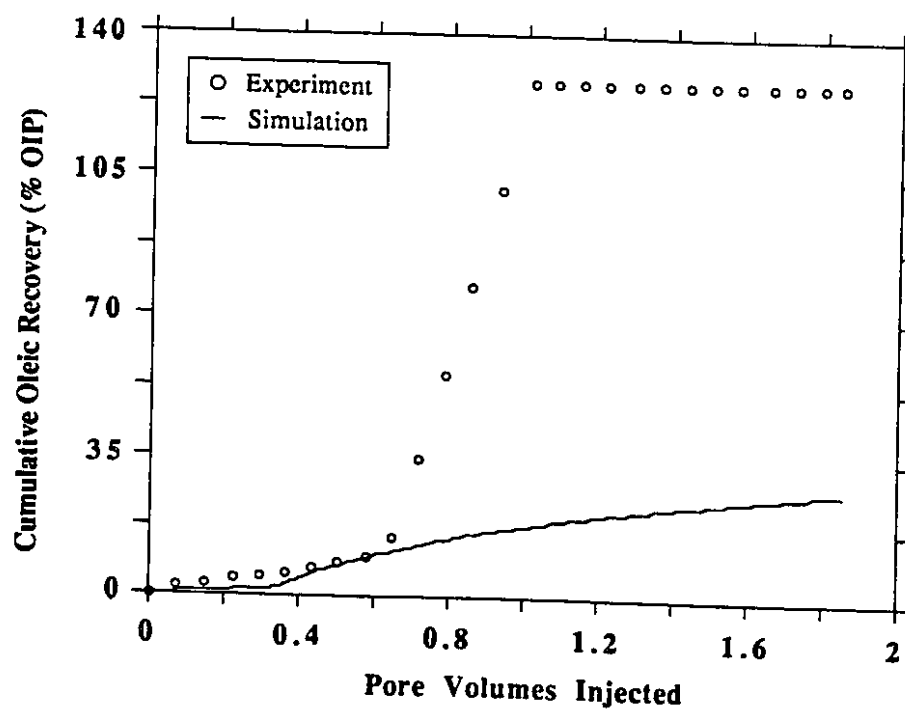


Fig. 7.2 Comparison of Experimental and Simulated Cumulative Oleic Recovery History for Run 5/1 for Emulsion Flooding.

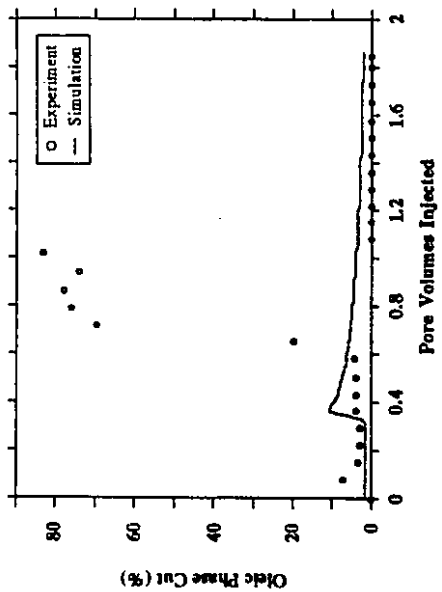


Fig. 7.3 Comparison of Experimental and Simulated Oleic Phase Cut History for Run 5/1 for Emulsion Flooding.

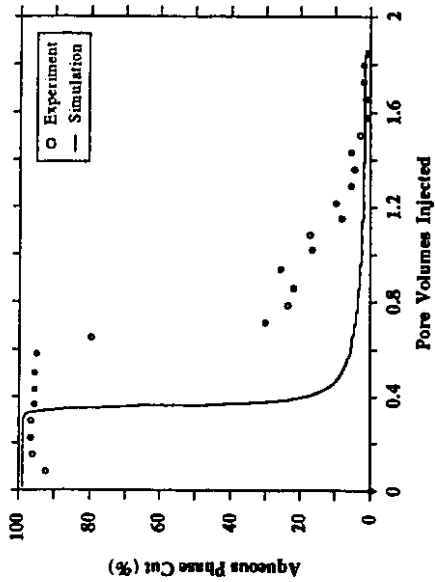


Fig. 7.4 Comparison of Experimental and Simulated Aqueous Phase Cut History for Run 5/1 for Emulsion Flooding.

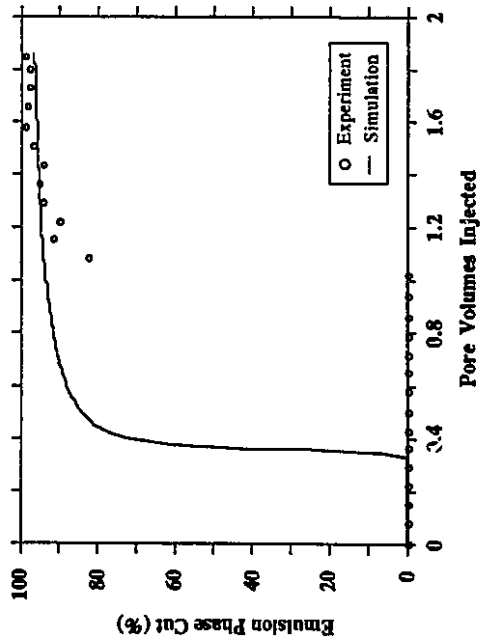


Fig. 7.5 Comparison of Experimental and Simulated Emulsion Phase Cut History for Run 5/1 for Emulsion Flooding.

model, the emulsion rheological model, or both of the models are inadequate.

The comparisons in cumulative oleic recovery (Fig. 7.2) and phase cuts (Fig. 7.3 to Fig. 7.5) provide further information about the simulation. The shift of the simulated oleic, aqueous, and emulsion cuts to the left of the experimental ones indicates that the mobilities of these three phases were greater than those which actually occurred in the core flood. It indicates that the Naar-Wygal-Henderson correlation predicts relative permeabilities that are too high. It is also shown that oil and emulsion breakthrough times are about the same. The early breakthrough of the emulsion phase might be explained by a predicted emulsion viscosity that is too low. The low simulated oil cut and cumulative oleic recovery are attributed to poor mobility control during the displacement. A comparison of simulator and experimental data shows this to be the case. The average emulsion viscosity is calculated by the simulator to be 0.018 Pa.s, whereas the injected emulsion in fact has an average viscosity of 0.264 Pa.s. The corresponding breakthroughs occurred at 0.35 PV injected in the simulation and at about 1 PV injected in the laboratory. Based on these observations, it is clear that both the relative permeability model and the emulsion viscosity correlation are unsuitable for modeling flow in the core flood.

The simulated saturation history is shown in Fig. 7.6, while saturation profiles at four different pore volumes injected, namely 0.1067, 0.1977, 0.3920, and 0.6054, are shown in Figs. 7.7 to 7.10. These saturation profiles sequentially show the flow of each phase through the core. It is easily observed that only a very slight oil bank is formed. The relative permeability for each phase as predicted by the Near-Wygal-Henderson correlation for Run 5/1 is plotted versus the phase saturation in Figs. 7.11 to 7.13.

Since the simple weighted average correlation for the emulsion viscosity does not provide a good approximation for the emulsion viscosity, Run 5/2 was conducted to correct this problem. The experimental work showed that on the whole, there was a similarity between the rheological behaviour of emulsion H2 when it was sheared in a viscometer and when it flowed in a porous medium, as described in Chapters 4 and 5. This information can provide a reasonable approximation of the rheological parameters that are sufficient to properly model the emulsion rheological behaviour. Viscosity measurement of the injected emulsion H2 showed non-Newtonian behaviour ($n = 1.0717$) within the range of 0.220 to 0.289 Pa.s for shear rates of 0.36 to 14.68 s^{-1} (Fig. 4.5). A single phase non-Newtonian correlation, given by Eqns. (5.23) and (5.24) in Chapter 5, represents the non-Newtonian behaviour of an emulsion during single phase flow. This

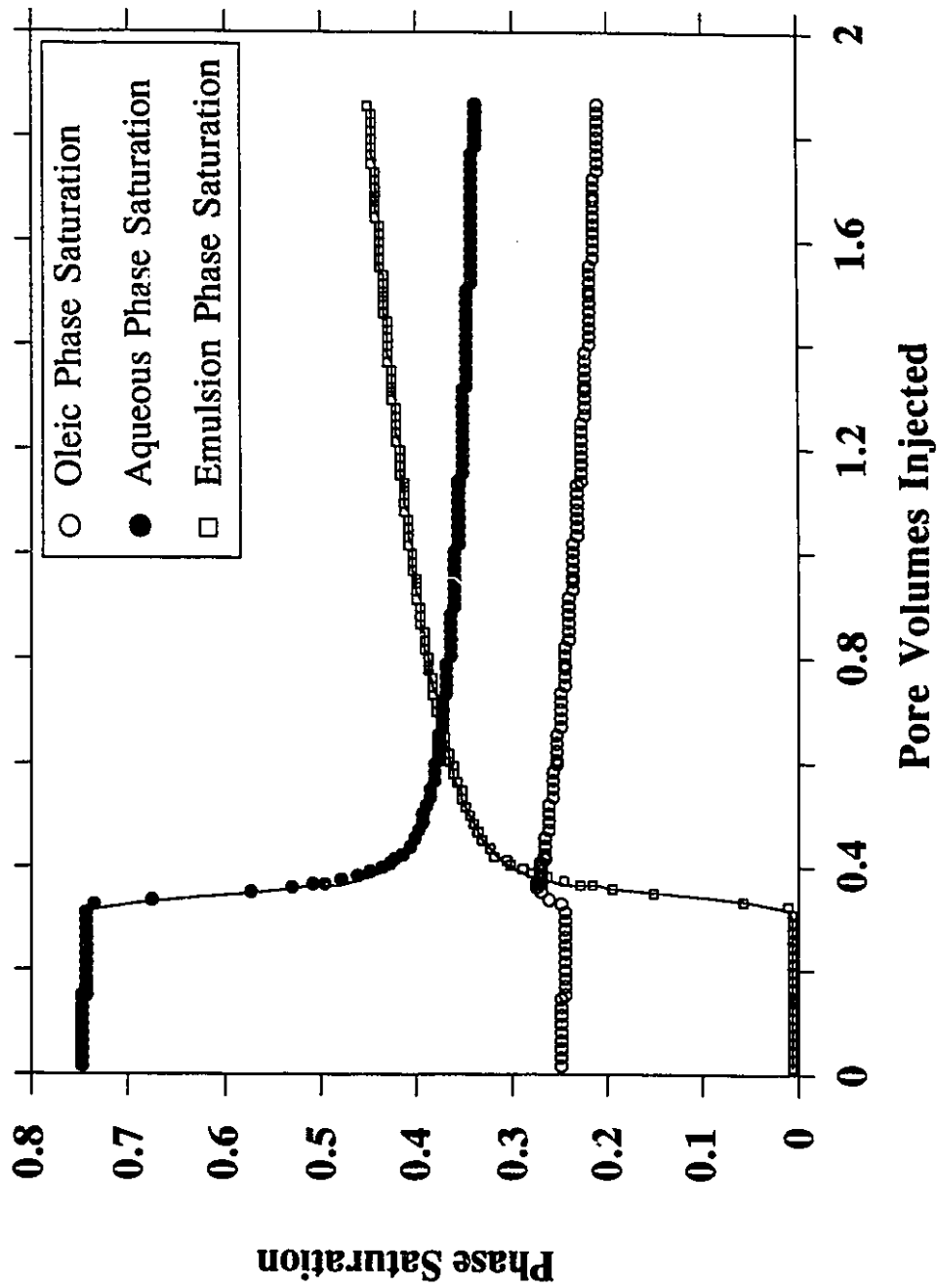


Fig. 7.6 Simulated Saturation History at Production
Block for Run 5/1.

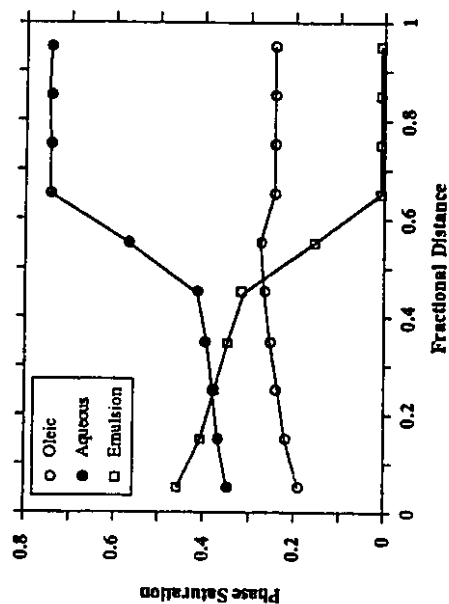


Fig. 7.8 Simulated Saturation Profile for Run 5/1 at 0.1977 pv Injected.

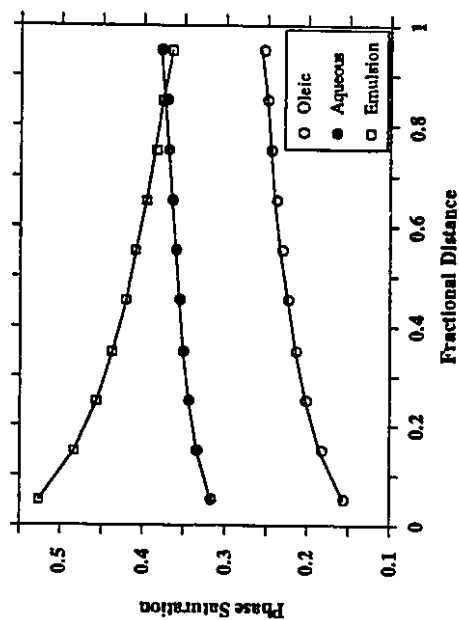


Fig. 7.10 Simulated Saturation Profile for Run 5/1 at 0.6054 pv Injected.

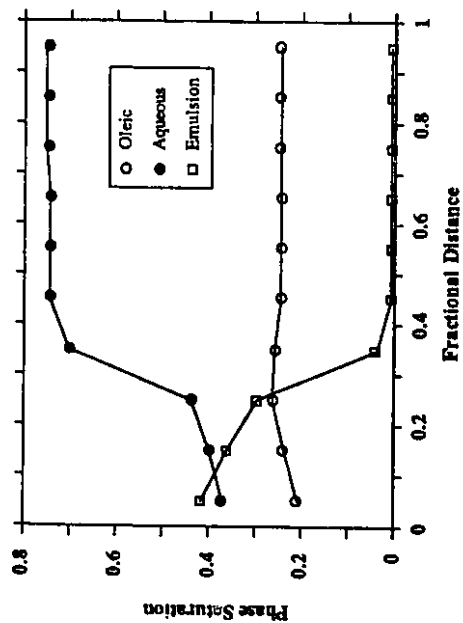


Fig. 7.7 Simulated Saturation Profile for Run 5/1 at 0.1067 pv Injected.

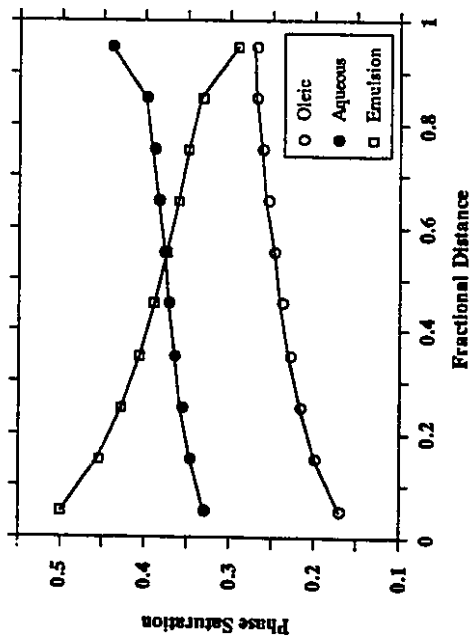


Fig. 7.9 Simulated Saturation Profile for Run 5/1 at 0.3920 pv Injected.

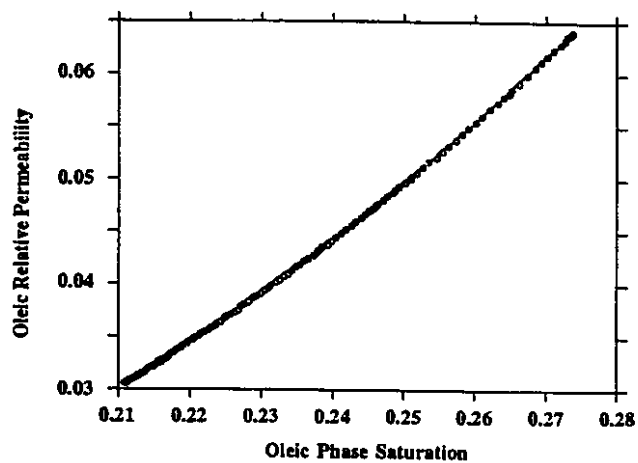


Fig. 7.11 Oleic Relative Permeability Vs. Oleic Saturation for Run 5/1.

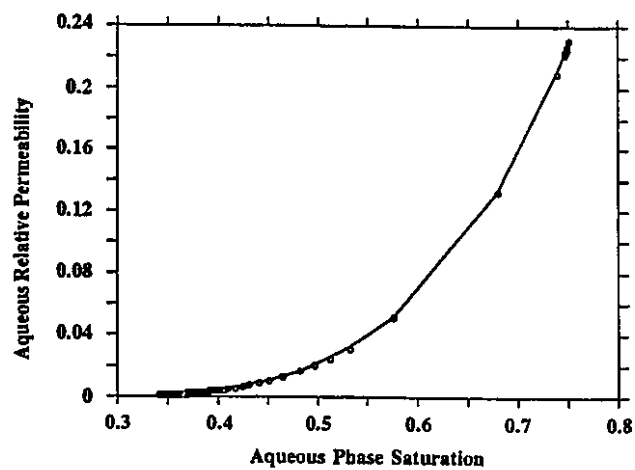


Fig. 7.12 Aqueous Relative Permeability Vs. Aqueous Saturation for Run 5/1.

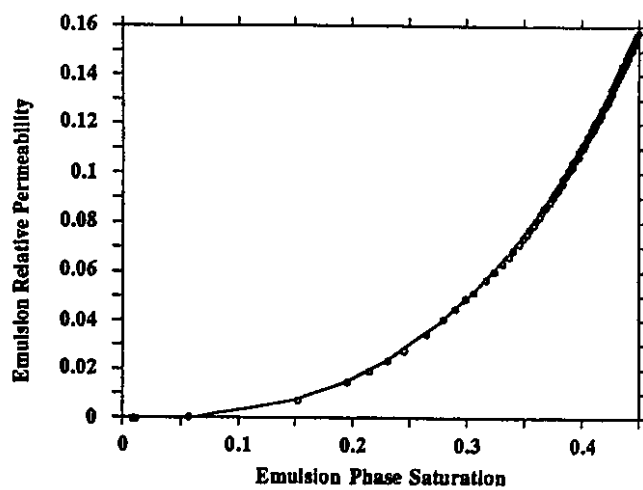


Fig. 7.13 Emulsion Relative Permeability Vs. Emulsion Saturation for Run 5/1.

correlation was incorporated into the simulator to model emulsion viscosity during the displacement.

Table 7.1, which was previously shown, and Table 7.2 show the input data for Run 5/2. Appendix H shows how to estimate the value of the rheological parameter $\alpha\sqrt{F}$ from the experimental data. This correlation and the parameters predict an emulsion viscosity of 0.278 Pa.s compared to the actual value of 0.264 Pa.s for the injected emulsion. For one dimension and a constant flow rate with a specific consistency K and a flow behaviour index n for the injected emulsion composition, it predicts a single value of emulsion viscosity. This correlation may not represent emulsion viscosity precisely, but an improvement is apparent in the production histories shown in Figs. 7.14 to 7.18.

Figure 7.14 shows an increased injection pressure due to a prediction of higher emulsion viscosity. This high viscosity emulsion is a better mobility control agent, giving a sharp increase in the cumulative oleic recovery (Fig. 7.15). The superiority of the mobility control in Run 5/2 over that of Run 5/1 is confirmed by viewing the saturation profiles, namely Figs. 7.7 to 7.10 for Run 5/1 and Figs. 7.20 to 7.23 for Run 5/2. When the higher viscosity emulsion of Run 5/2 displaced the oil, a larger oil bank was formed with a lower residual oil saturation behind the bank. However, there is still a decline in the injection pressure when emulsion

Table 7.2
Simulation Input Parameters for Run 5/2
Non-Newtonian Rheology

Viscosity Parameter	Value
K, Pa.s ⁿ	0.63105
n	0.6948
$\alpha\sqrt{F}$	2.5

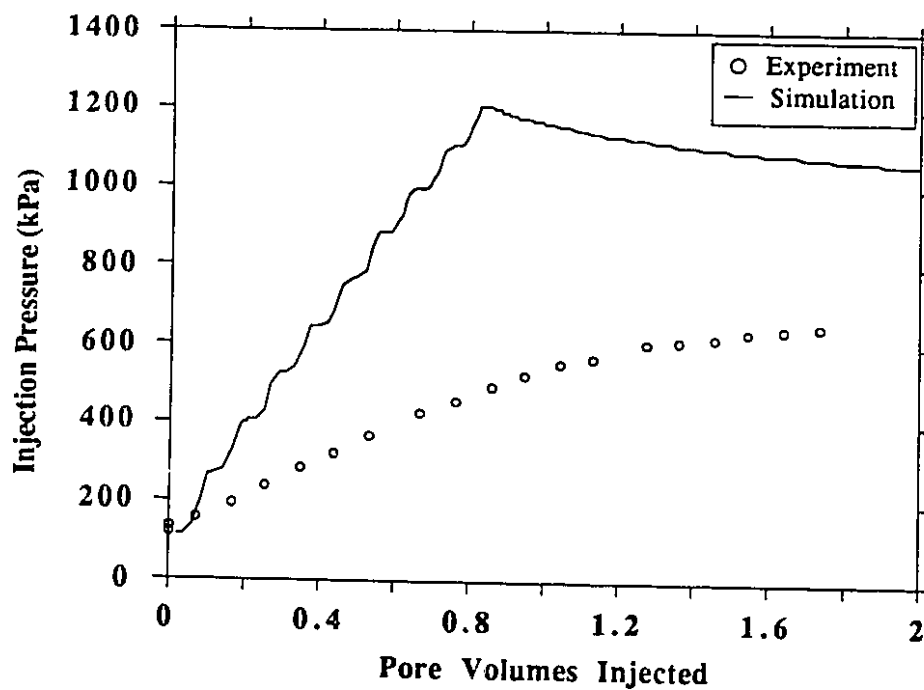


Fig. 7.14 Comparison of Experimental and Simulated Injection Pressure History for Run 5/2 for Emulsion Flooding.

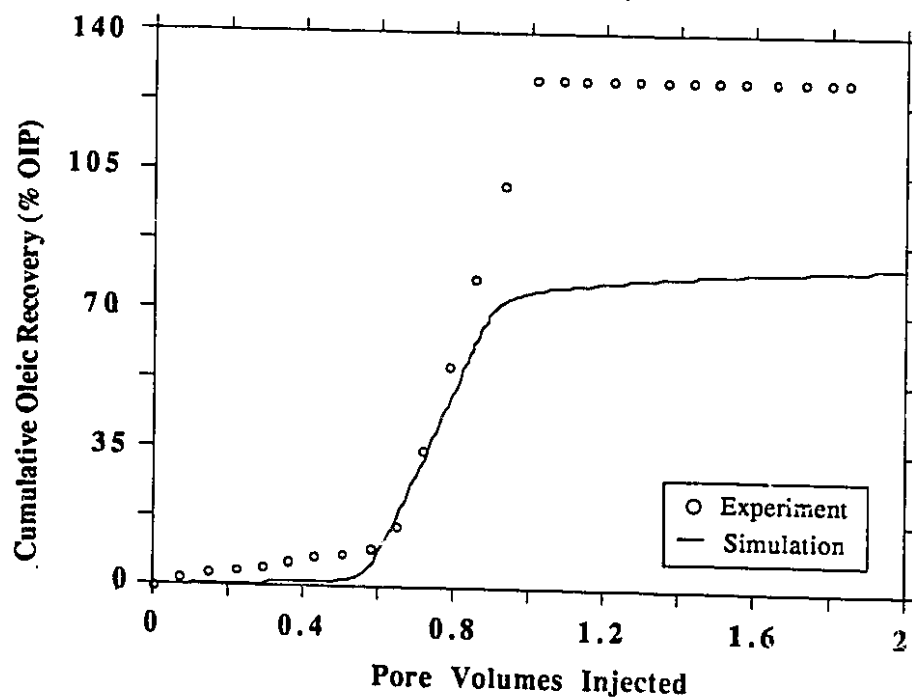


Fig. 7.15 Comparison of Experimental and Simulated Cumulative Oleic Recovery History for Run 5/2 for Emulsion Flooding.

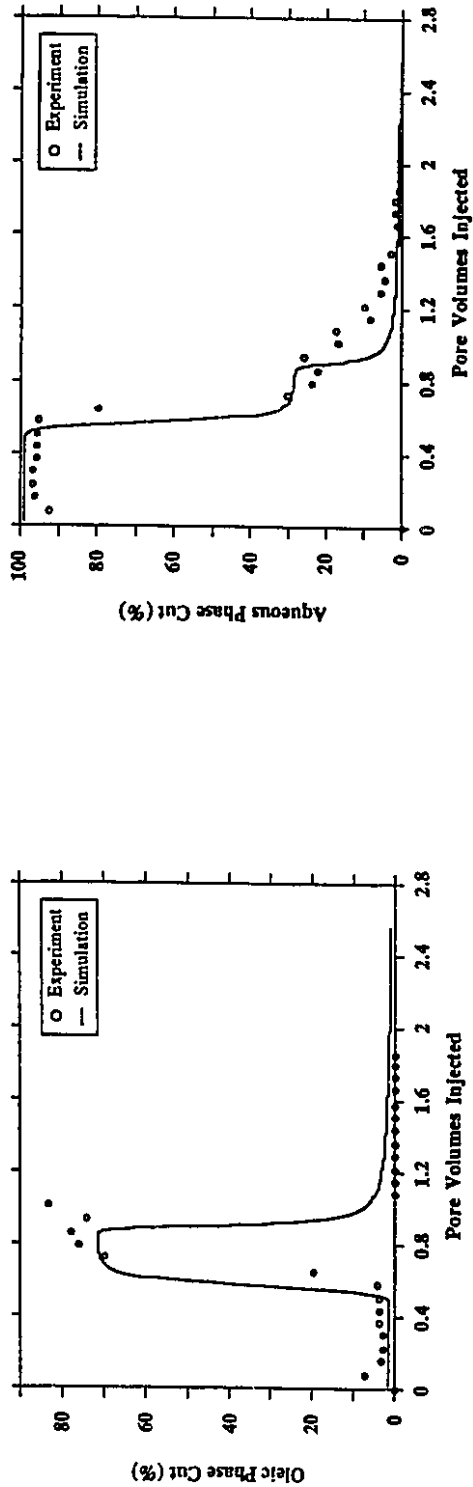


Fig. 7.16 Comparison of Experimental and Simulated Oleic Phase Cut History for Run 5/2 for Emulsion Flooding.

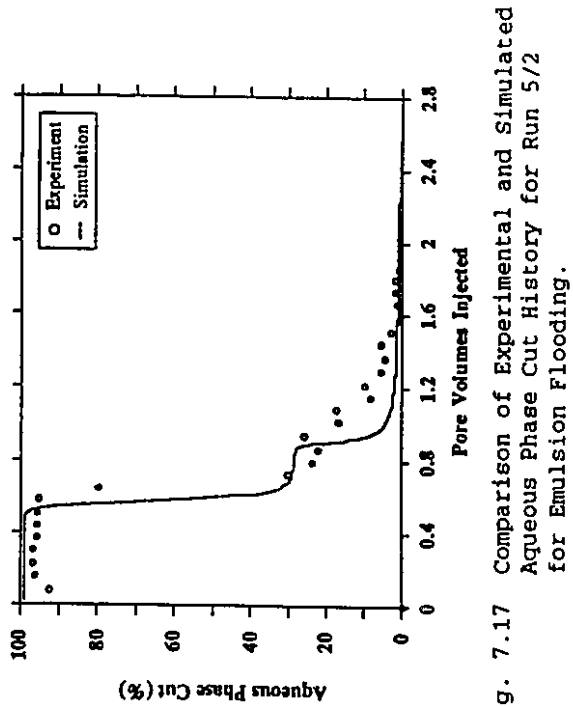


Fig. 7.17 Comparison of Experimental and Simulated Aqueous Phase Cut History for Run 5/2 for Emulsion Flooding.

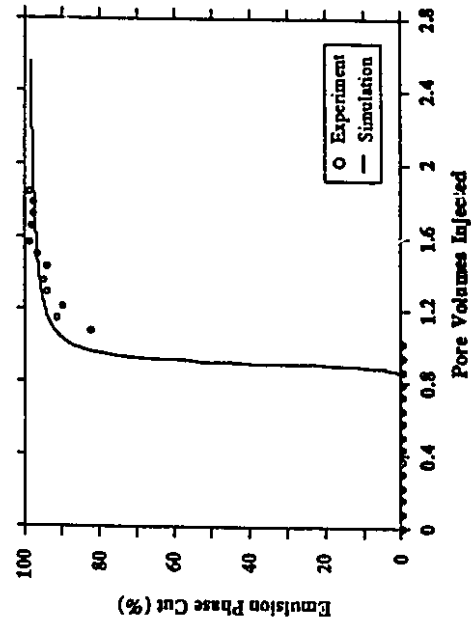


Fig. 7.18 Comparison of Experimental and Simulated Emulsion Phase Cut History for Run 5/2 for Emulsion Flooding.

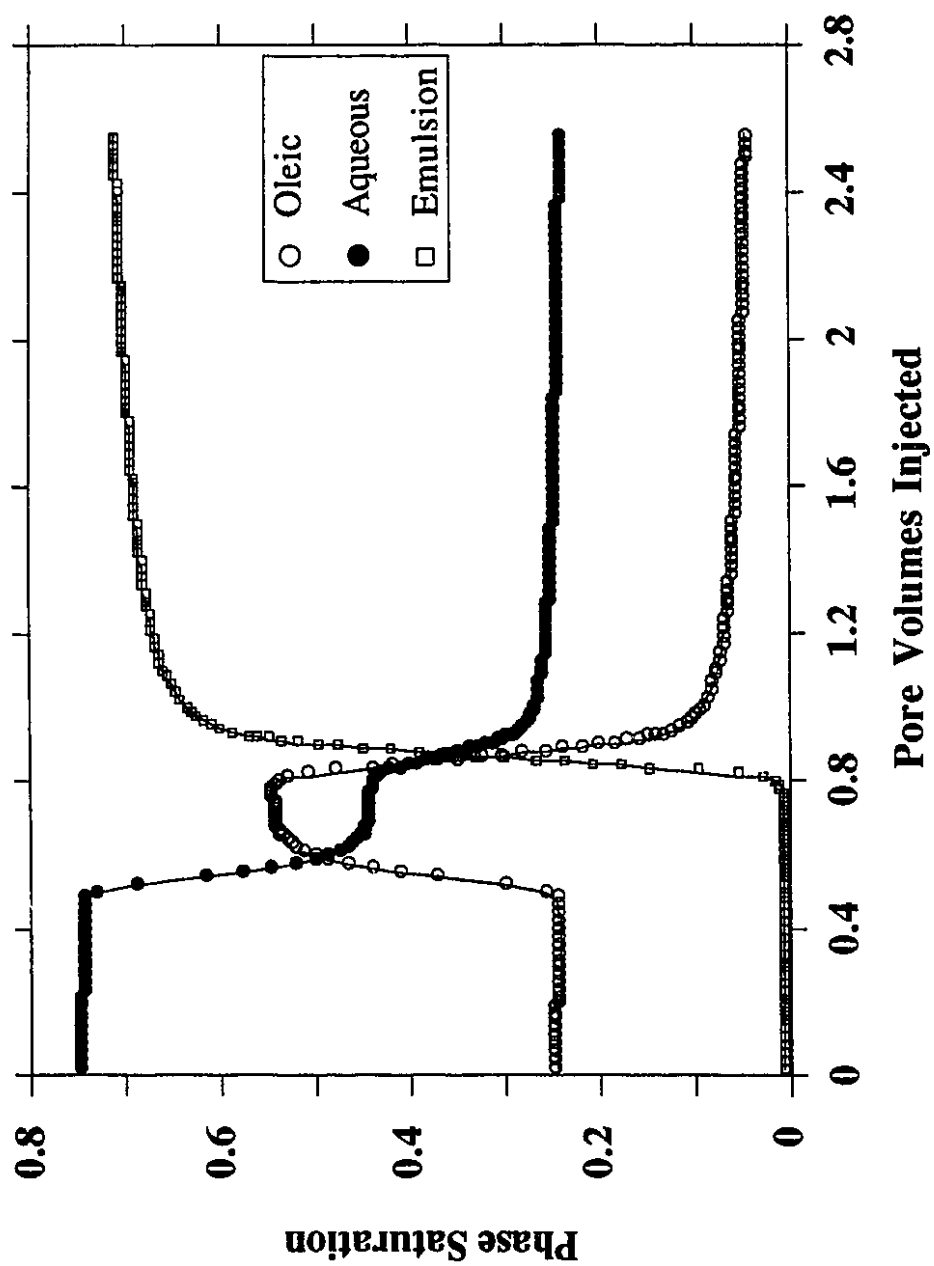


Fig. 7.19 Simulated Saturation History at Production
Block for Run 5/2.

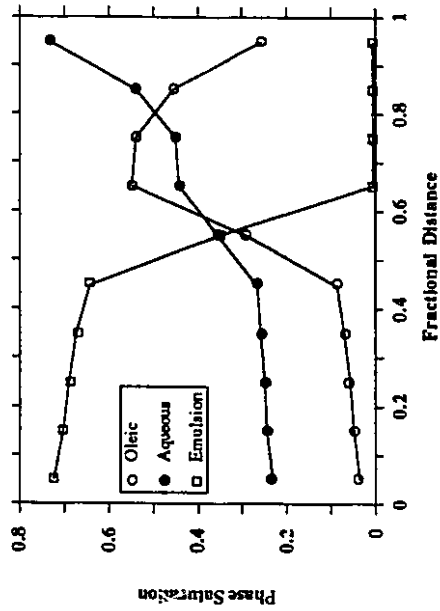


Fig. 7.21 Simulated Saturation Profile for Run 5/2 at 0.5018 pv Injected.

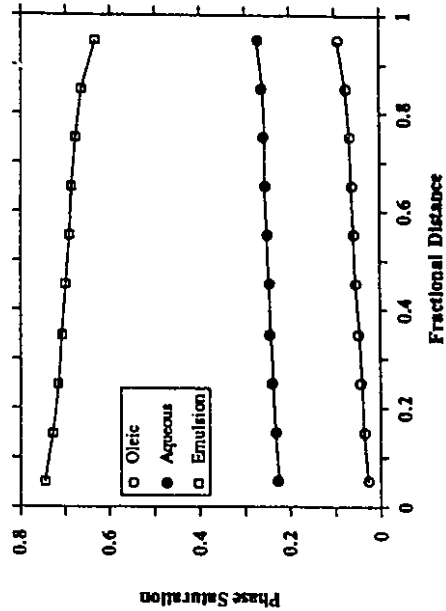


Fig. 7.23 Simulated Saturation Profile for Run 5/2 at 0.9997 pv Injected.

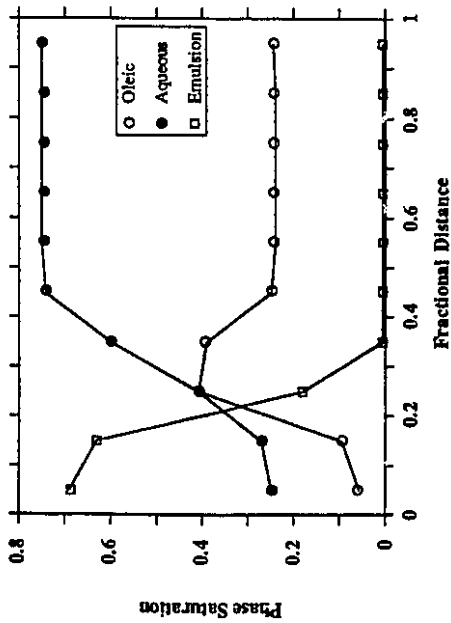


Fig. 7.20 Simulated Saturation Profile for Run 5/2 at 0.1992 pv Injected.

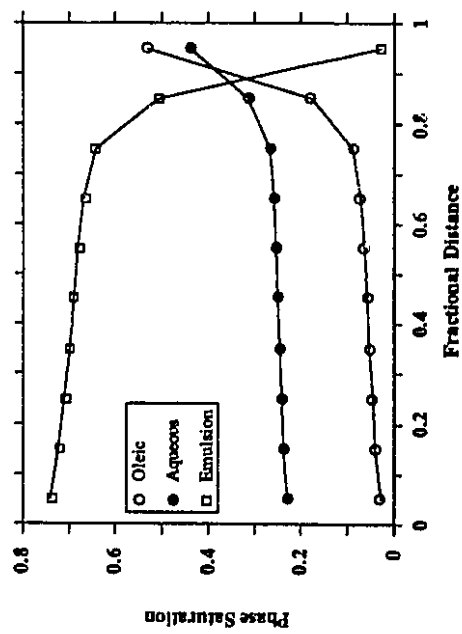


Fig. 7.22 Simulated Saturation Profile for Run 5/2 at 0.8058 pv Injected.

breakthrough occurs corresponding to a gradual increase in the cumulative oleic recovery. This is due to the use of the Naar-Wygal-Henderson relative permeability model. This effect can be seen more clearly by observing the saturation profiles after emulsion breakthrough, both for Run 5/1 in Figs. 7.9 and 7.10, and Run 5/2 in Figs. 7.22 and 7.23. These profiles show that the Naar-Wygal-Henderson model predicts a gradual decline in the oleic phase saturation to a new residual oil saturation. This explains the gradual increase in the cumulative oleic recoveries for Runs 5/1 and 5/2. Obviously, if there is less oil to be displaced, a lower injection pressure is required; hence, the decline in injection pressure. The oleic, aqueous, and emulsion phase cuts shown in Figs. 7.16 to 7.18 indicate a better mobility control predicted by using the single phase non-Newtonian correlation. This can be seen from the later emulsion breakthrough time for Run 5/2, which occurs at 0.85 PV injected compared to 0.33 PV injected for Run 5/1, and the much higher oleic cut for Run 5/2. However, all three phases still break through sooner than is indicated by the experimental data.

7.1.2 Effect of Different Relative Permeability Correlations

Since the single phase non-Newtonian correlation used in Run 5/2 gave a good match to the experimental data, it was used again in Run 5/3. However, Run 5/3 utilized a different relative permeability model. This model, developed by Pope,

incorporates the effect of interfacial tension. This is especially important in the case of trapped oil, and can reduce the residual oil saturation. Table 7.3 gives the relative permeability parameters and rheological parameters for Run 5/3 in addition to the base input data shown in Table 7.1. It should be pointed out that the same value of $\alpha\sqrt{F} = 2.5$ was used in both Run 5/2 and Run 5/3.

Figs. 7.24 to 7.28 show the injection pressure, cumulative oleic recovery, and the oleic, aqueous, and emulsion phase cuts for Run 5/3, respectively. The improvement brought about by using Pope's relative permeability model can be seen in that it improves the cumulative oleic recovery from a maximum value of 82.3 to 96.3% OIP and predicts a stabilized injection pressure after emulsion breakthrough. This differs from the Naar-Wygal-Henderson prediction in Run 5/2 which predicts the decline in injection pressure after emulsion breakthrough. This is not unexpected because the Naar-Wygal-Henderson model does not include the effect of interfacial tension. The saturation profile following emulsion breakthrough, shown in Figs. 7.30 to 7.32, is consistent with these observations. That is, instead of a long, gradual decline in the oleic phase saturation behind the oil bank, the decline to a new residual oil saturation is much more rapid. The faster decline to a constant residual oil saturation combined with a constant aqueous phase saturation following emulsion breakthrough requires an emulsion injected

Table 7.3

Simulation Input Parameters for Run 5/3

A. Pope's Relative Permeability Model Parameters

A.1 Interfacial Tension and Capillary Desaturation Parameters

Parameter	Value	Parameter	Value
GL1	13.1	TL1	-0.5
GL2	-14.0	TL2	0.222
GL3	0.0221	TA1	-0.428
GA1	13.1	TA2	-0.415
GA2	-14.0	TM1	0.0
GA3	0.0221	TM2	0.0
IFTW	-1.70		

A.2 End Point Relative Permeabilities and Relative Permeability Exponents for Each Phase

End Point Relative Permeability	Value	Relative Permeability Exponent	Value
$k_{rl_{WT}}^o$	0.57	e_l	1.5
$k_{rl_{LT}}^o$	1.0	e_a	1.3
$k_{ra_{WT}}^o$	0.1	e_m	1.0
$k_{ra_{LT}}^o$	1.0		
k_{rm}^o	0.8		

B. Non-Newtonian Rheology

Viscosity Parameter	Value
$K, \text{ Pa.s}^n$	0.63105
n	0.6948
$\alpha\sqrt{F}$	2.5

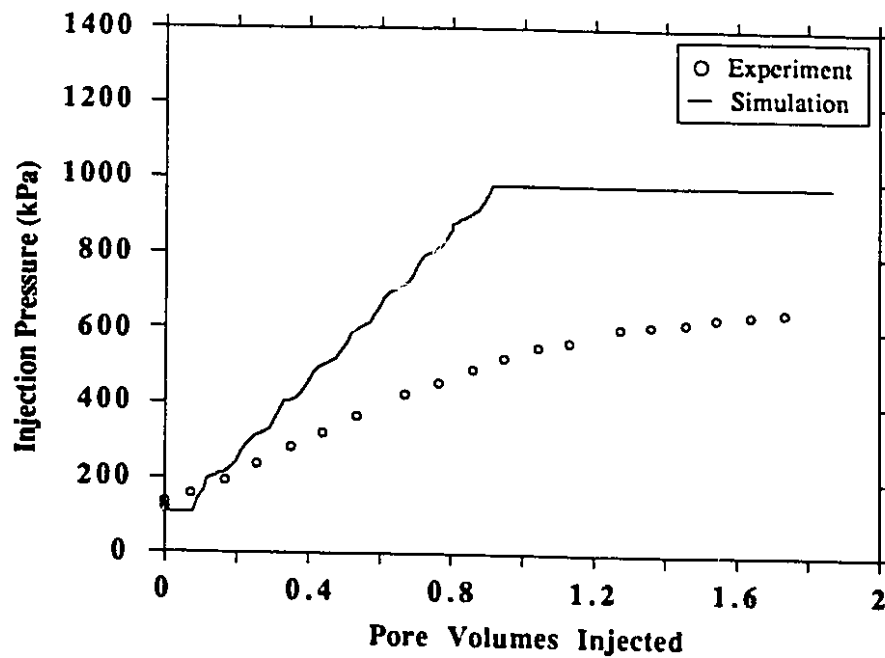


Fig. 7.24 Comparison of Experimental and Simulated Injection Pressure History for Run 5/3 for Emulsion Flooding.

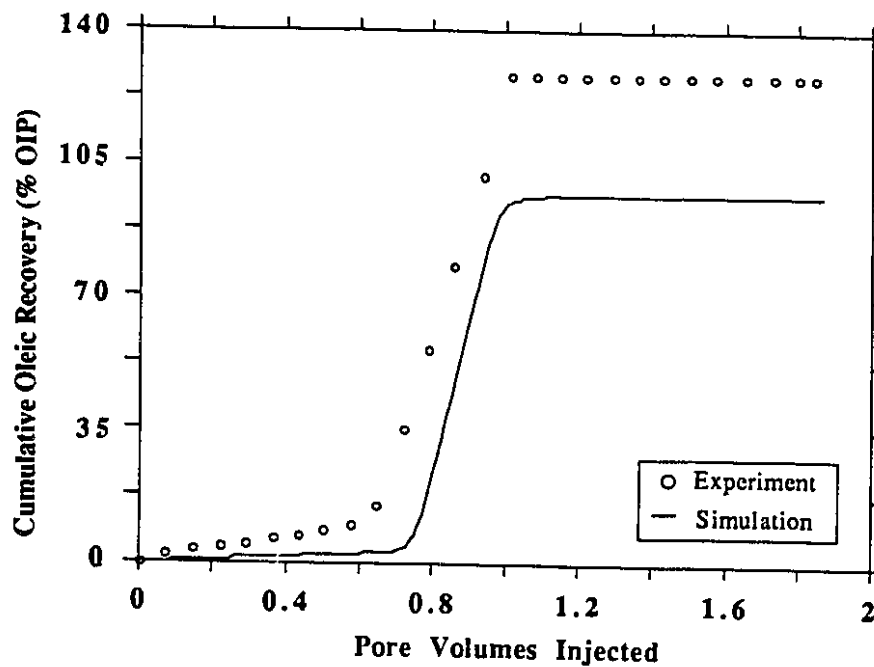


Fig. 7.25 Comparison of Experimental and Simulated Cumulative Oleic Recovery History for Run 5/3 for Emulsion Flooding.

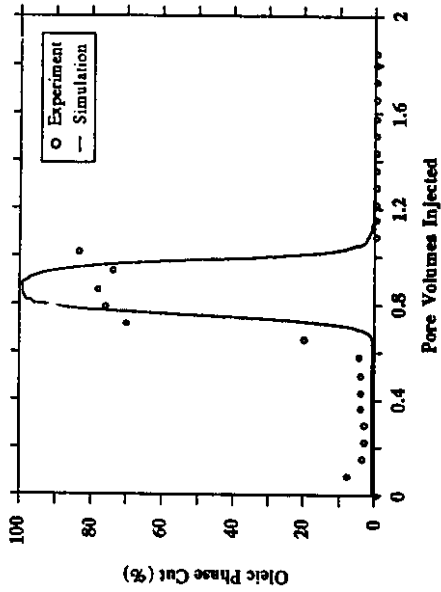


Fig. 7.26 Comparison of Experimental and Simulated Oleic Phase Cut History for Run 5/3 for Emulsion Flooding.

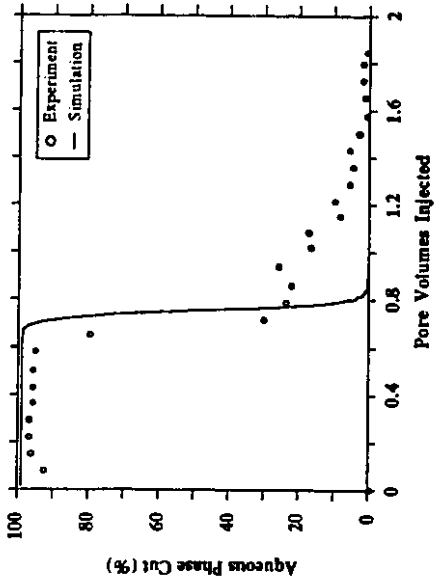


Fig. 7.27 Comparison of Experimental and Simulated Aqueous Phase Cut History for Run 5/3 for Emulsion Flooding.

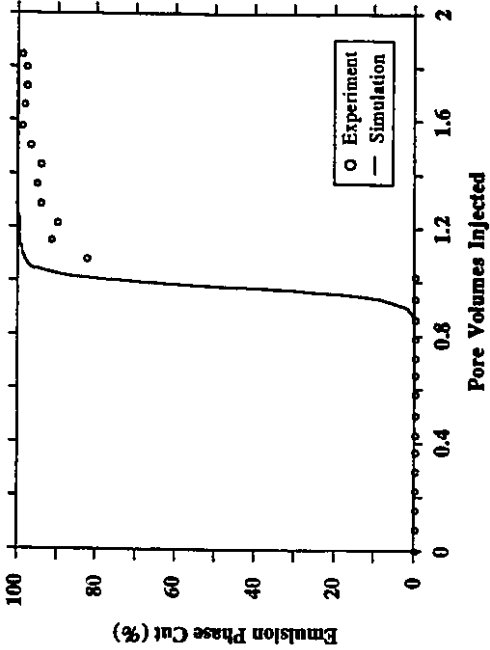


Fig. 7.28 Comparison of Experimental and Simulated Emulsion Phase Cut History for Run 5/3 for Emulsion Flooding.

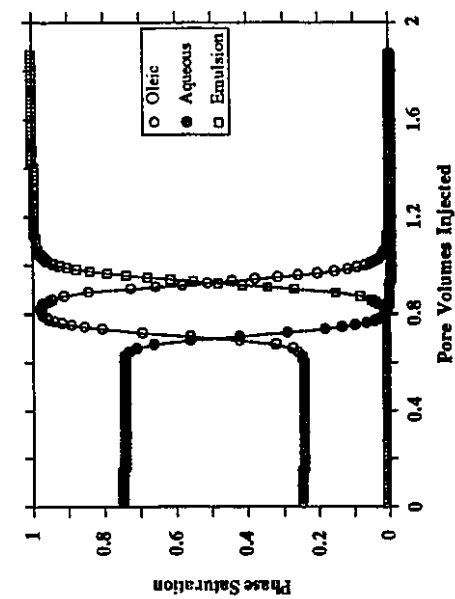


Fig. 7.29 Simulated Saturation History at Production Block for Run 5/3.

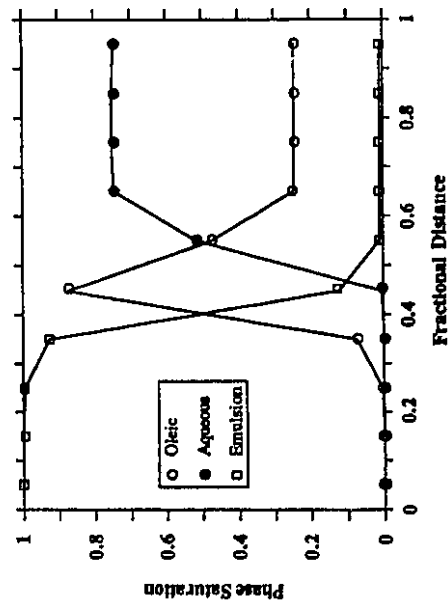


Fig. 7.31 Simulated Saturation Profile for Run 5/3 at 0.3986 PV Injected.

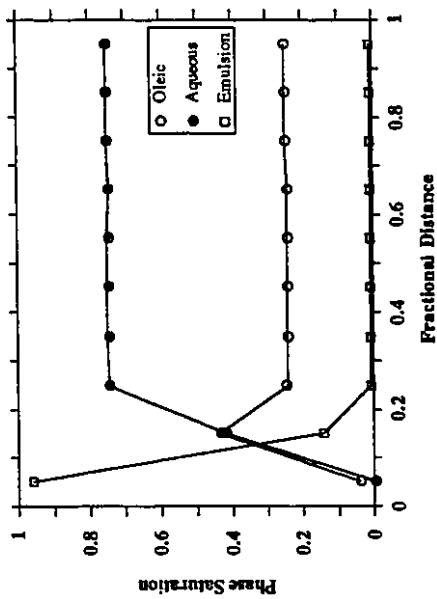


Fig. 7.30 Simulated Saturation Profile for Run 5/3 at 0.1076 PV Injected.

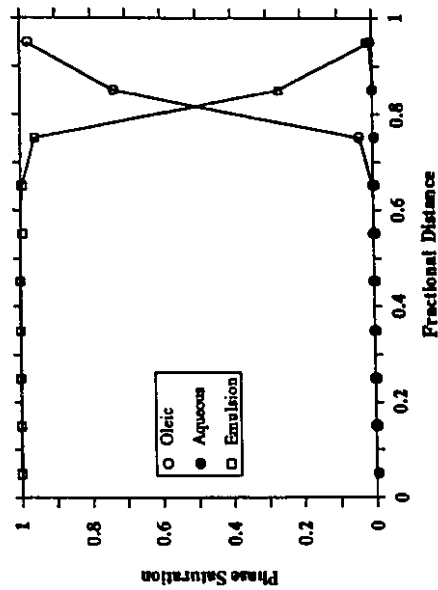


Fig. 7.32 Simulated Saturation Profile for Run 5/3 at 0.8059 PV Injected.

at a constant pressure to displace the oleic and aqueous phases in the core. These factors also account for the almost constant cumulative oleic recovery. Furthermore, the oleic and aqueous phase relative permeability curves (Figs. 7.33 and 7.34) seem to predict lower relative permeabilities than those that occurred in the core and cause the delay in oleic phase breakthrough time (Figs. 7.26 and 7.27). However, the emulsion phase still breaks through sooner than observed experimentally. The emulsion breaks through in Run 5/3 at about the same time as in Run 5/2 due to the same predicted value of the emulsion viscosity.

7.1.3 Effect of Oleic and Aqueous Relative Permeabilities and Emulsion Rheological Behaviour

Up to this point in the investigation, Pope's relative permeability model generally predicts the relative permeability of each phase better than the Naar-Wygal-Henderson approach because the latter does not include the interfacial tension effects. However, the injection pressure required for displacement in Run 5/3 is higher than that found during the core flood. An emulsion viscosity of 0.278 Pa.s is produced by setting the value of $\alpha\sqrt{F}$ to 2.5. Therefore, Run 5/4 was carried out to see the effect of emulsion rheological behaviour on the injection pressure. The value of 5.0 for $\alpha\sqrt{F}$ was used which produces an emulsion viscosity of 0.086 Pa.s. The simulation predicts a lower injection pressure, with a stabilized pressure of 700 kPa in

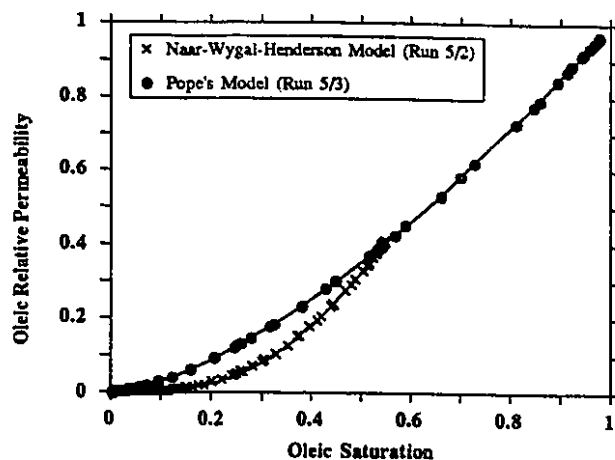


Fig. 7.33 Comparison of Oleic Relative Permeability Predicted by Naar-Wygal-Henderson Model and Pope's Model.

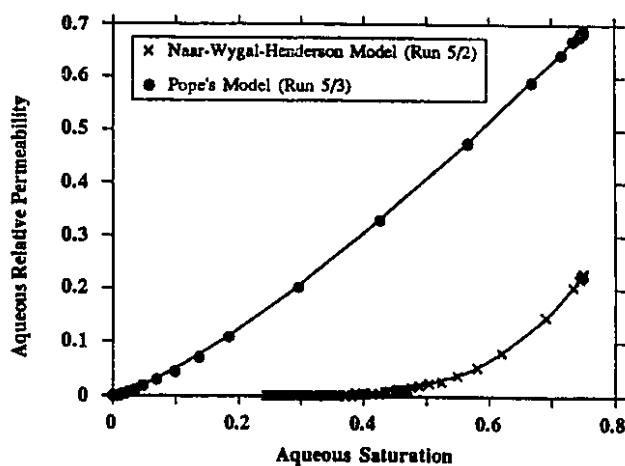


Fig. 7.34 Comparison of Aqueous Relative Permeability Predicted by Naar-Wygal-Henderson Model and Pope's Model.

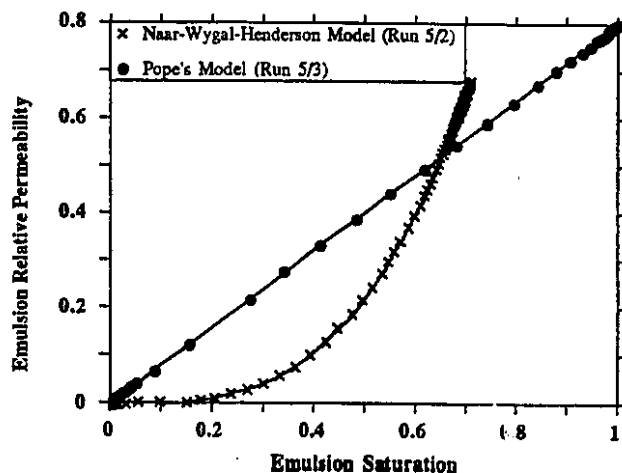


Fig. 7.35 Comparison of Emulsion Relative Permeability Predicted by Naar-Wygal-Henderson Model and Pope's Model.

Run 5/4 (Fig. 7.36) compared to that of 980 kPa found in Run 5/3 (Fig. 7.24). Furthermore, the effect of the oleic and aqueous phase relative permeabilities on the phase breakthrough time is observed. The lower oleic and aqueous relative permeabilities, through increasing the exponents of the relative permeability curves, predict a later oleic phase breakthrough time (Figs. 7.38 and 7.39). Consequently, the emulsion breaks through at a later time (Fig. 7.40). As a result, a slightly higher total oleic recovery is obtained (Fig. 7.37).

7.1.4 Effect of Different Droplet Capture Models

Thus far only the effects of the phase mobilities on the simulated results have been analyzed. The effects of other mechanisms, such as droplet capture and absolute permeability, were not considered. The inclusion of these mechanisms can enhance the predictive capabilities of the simulator. To investigate this possibility, Run 5/5 was performed by incorporating a droplet capture model. This capture model is simplified for the case of instantaneous equilibrium (Eqn. 5.61), and yields a correlation similar to the Langmuir adsorption isotherm.

Table 7.5 shows the simulation input parameters for Run 5/5. The injection pressure is given in Fig. 7.45, cumulative oleic recovery in Fig. 7.46, and oleic, aqueous, and emulsion phase cuts in Fig. 7.47 to Fig. 7.49, respectively. There is

Table 7.4

Simulation Input Parameters for Run 5/4

A. Pope's Relative Permeability Model Parameters

A.1 Interfacial Tension and Capillary Desaturation Parameters

Parameter	Value	Parameter	Value
GL1	13.1	TL1	-0.5
GL2	-14.0	TL2	0.222
GL3	0.0221	TA1	-0.428
GA1	13.1	TA2	-0.415
GA2	-14.0	TM1	0.0
GA3	0.0221	TM2	0.0
IFTW	-1.70		

A.2 End Point Relative Permeabilities and Relative Permeability Exponents for Each Phase

End Point Relative Permeability	Value	Relative Permeability Exponent	Value
k_{rlr}^o	0.57	e_l	1.7*
k_{rlr}^o	1.0	e_a	1.5*
k_{rar}^o	0.1	e_m	1.0
k_{rar}^o	1.0		
k_{rm}^o	0.8		

B. Non-Newtonian Rheology

Viscosity Parameter	Value
K, Pa.s ⁿ	0.63105
n	0.6948
$\alpha\sqrt{F}$	5.0*

* Values changed in Run 5/4 compared to Run 5/3

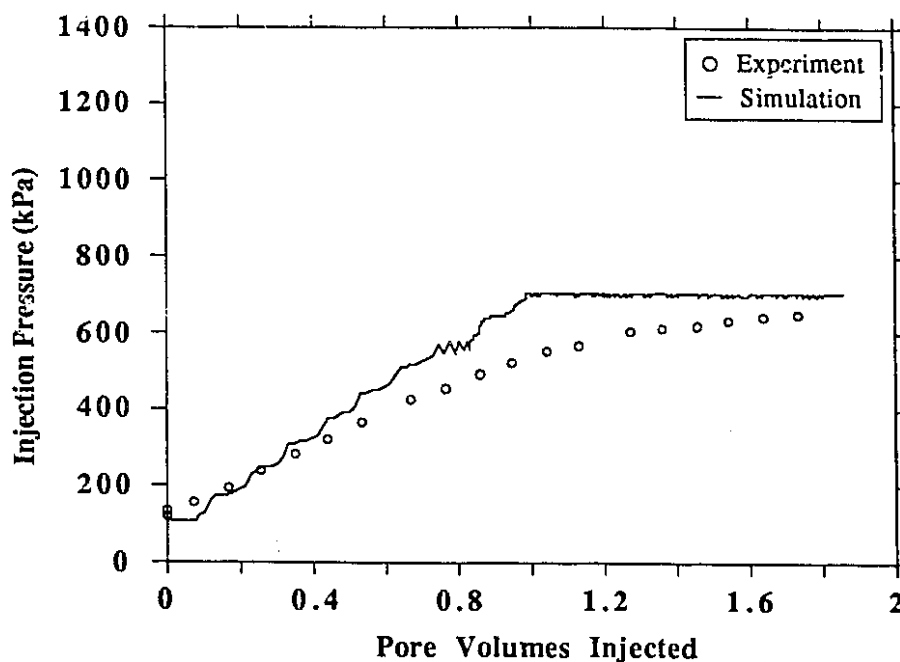


Fig. 7.36 Comparison of Experimental and Simulated Injection Pressure History for Run 5/4 for Emulsion Flooding.

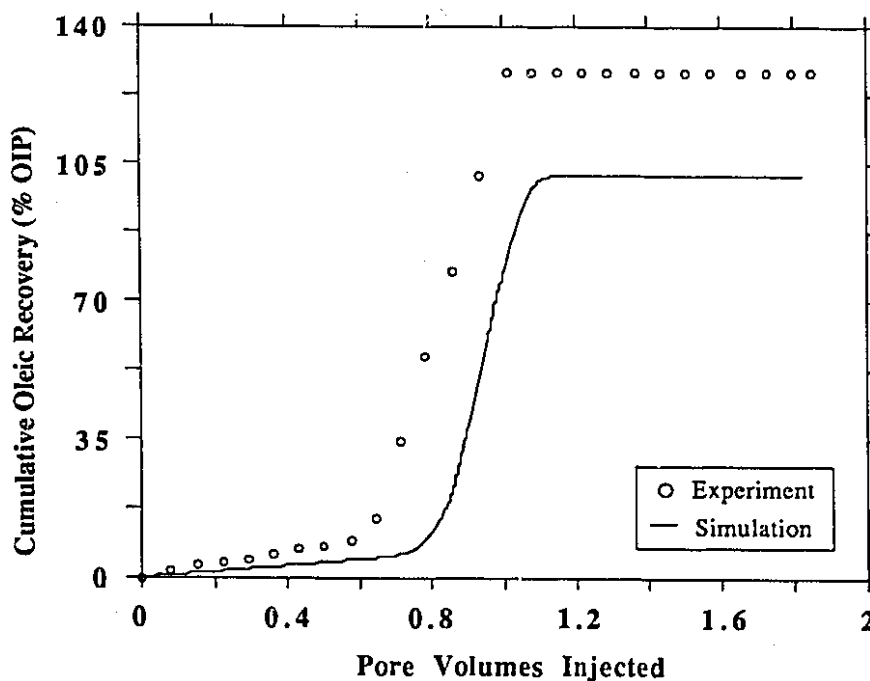


Fig. 7.37 Comparison of Experimental and Simulated Cumulative Oleic Recovery History for Run 5/4 for Emulsion Flooding.

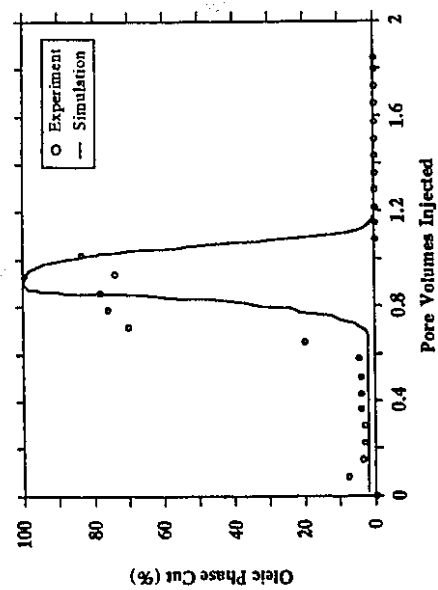


Fig. 7.38 Comparison of Experimental and Simulated Oleic Phase Cut History for Run 5/4 for Emulsion Flooding.

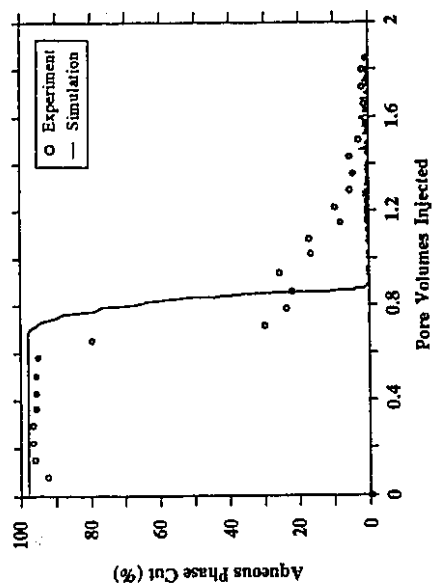


Fig. 7.39 Comparison of Experimental and Simulated Aqueous Phase Cut History for Run 5/4 for Emulsion Flooding.

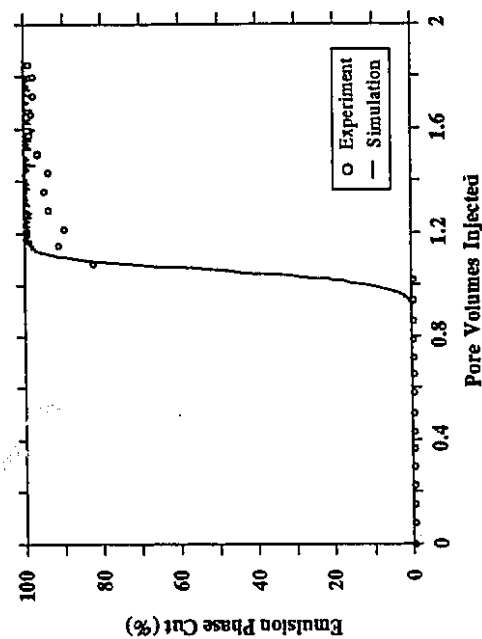


Fig. 7.40 Comparison of Experimental and Simulated Emulsion Phase Cut History for Run 5/4 for Emulsion Flooding.

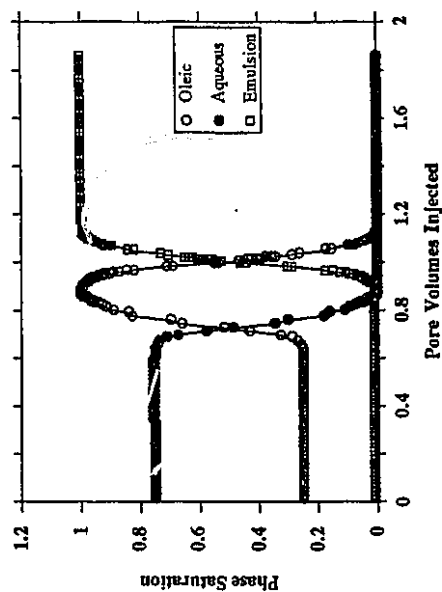


Fig. 7.41 Simulated Saturation History at Production Block for Run 5/4.

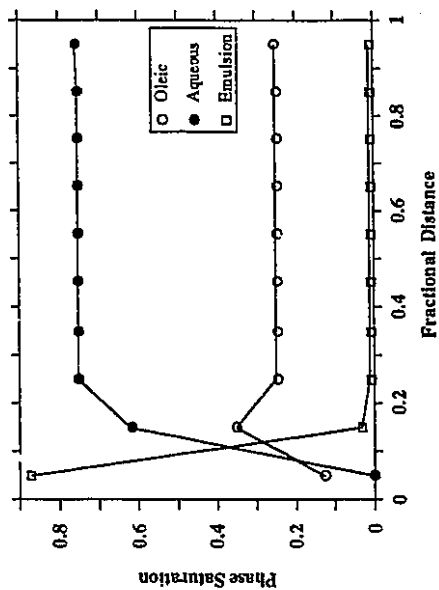


Fig. 7.42 Simulated Saturation Profile for Run 5/4 at 0.0914 PV Injected.

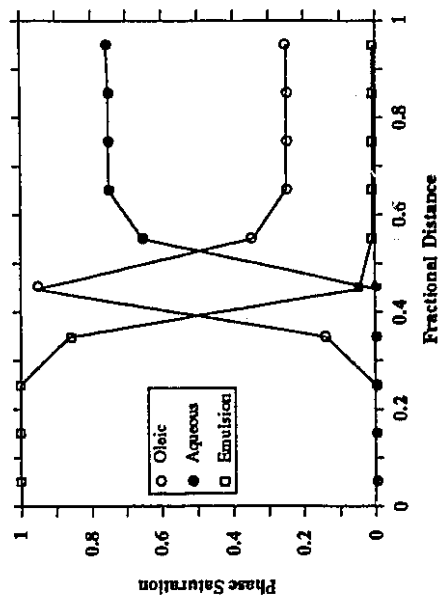


Fig. 7.43 Simulated Saturation Profile for Run 5/4 at 0.3963 PV Injected.

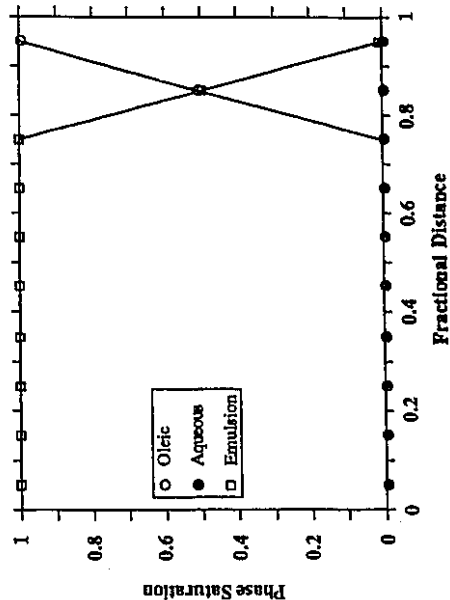


Fig. 7.44 Simulated Saturation Profile for Run 5/4 at 0.9031 PV Injected.

Table 7.5

Simulation Input Parameters for Run 5/5

A. Pope's Relative Permeability Model Parameters

A.1 Interfacial Tension and Capillary Desaturation Parameters

Parameter	Value	Parameter	Value
GL1	13.1	TL1	-0.5
GL2	-14.0	TL2	0.222
GL3	0.0221	TA1	-0.428
GA1	13.1	TA2	-0.415
GA2	-14.0	TM1	0.0
GA3	0.0221	TM2	0.0
IFTW	-1.70		

A.2 End Point Relative Permeabilities and Relative Permeability Exponents for Each Phase

End Point Relative Permeability	Value	Relative Permeability Exponent	Value
$k_{rl_{wt}}^o$	0.57	e_1	1.7*
$k_{rl_{lt}}^o$	1.0	e_a	1.5*
$k_{ra_{wt}}^o$	0.1	e_m	1.0
$k_{ra_{lt}}^o$	1.0		
k_{rm}^o	0.8		

B. Non-Newtonian Rheology

Viscosity Parameter	Value
K, Pa.s ⁿ	0.63105
n	0.6948
$\alpha\sqrt{F}$	5.0*

* Values changed in Run 5/5 compared to Run 5/3
Run 5/5 also included droplet capture mechanism.

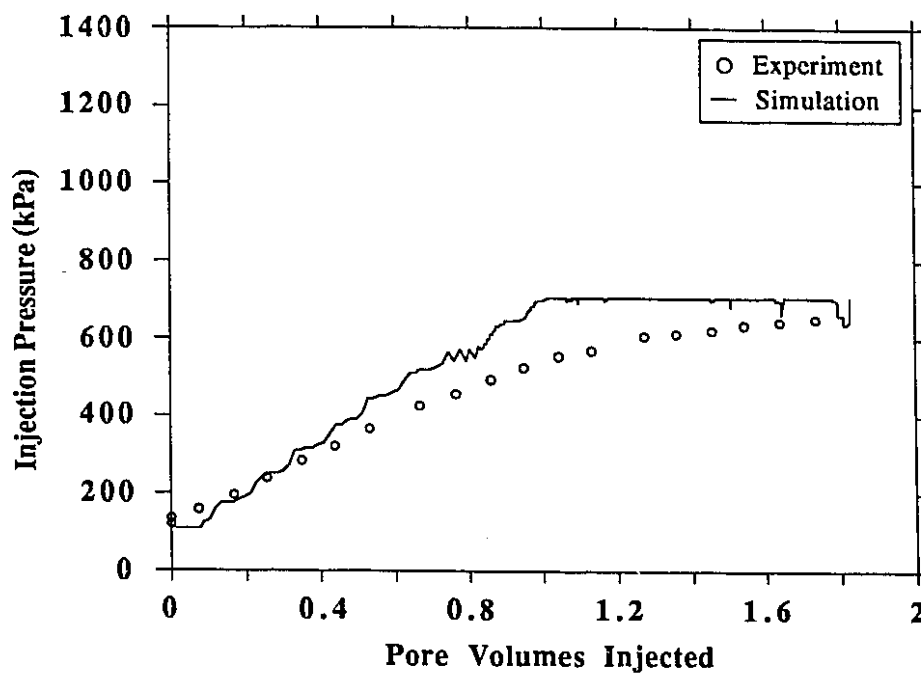


Fig. 7.45 Comparison of Experimental and Simulated Injection Pressure History for Run 5/5 for Emulsion Flooding.

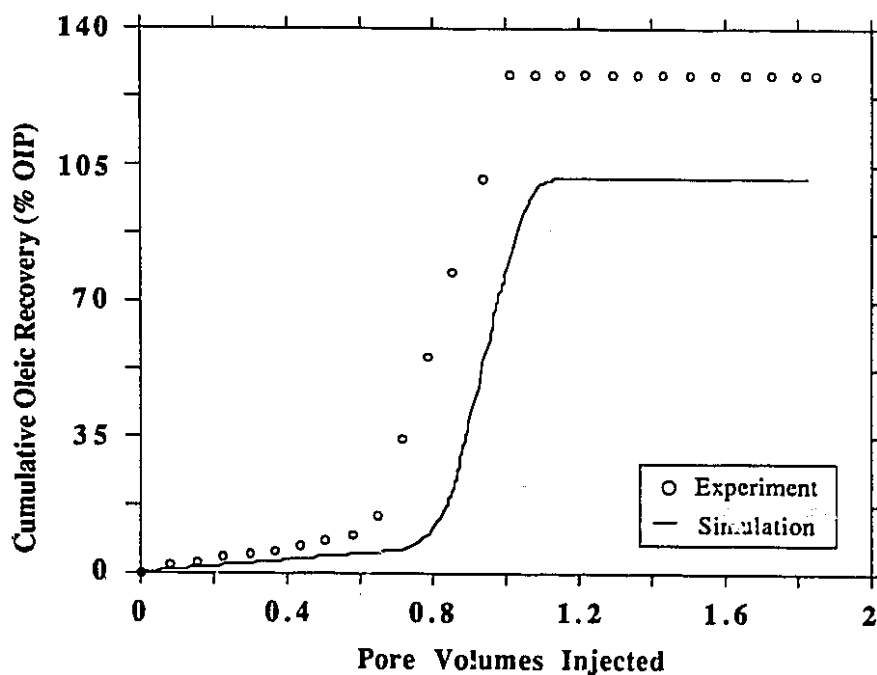


Fig. 7.46 Comparison of Experimental and Simulated Cumulative Oleic Recovery History for Run 5/5 for Emulsion Flooding.

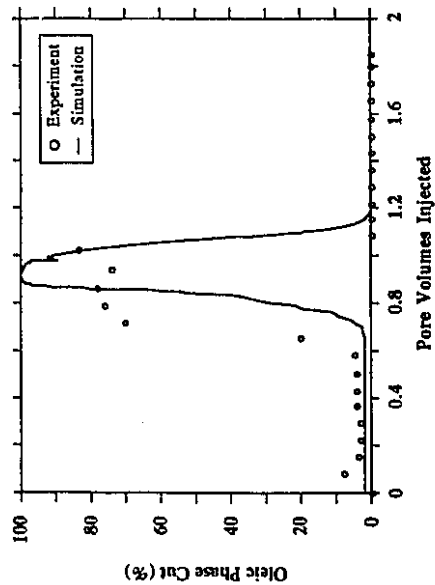


Fig. 7.47 Comparison of Experimental and Simulated Oleic Phase Cut History for Run 5/5 for Emulsion Flooding.

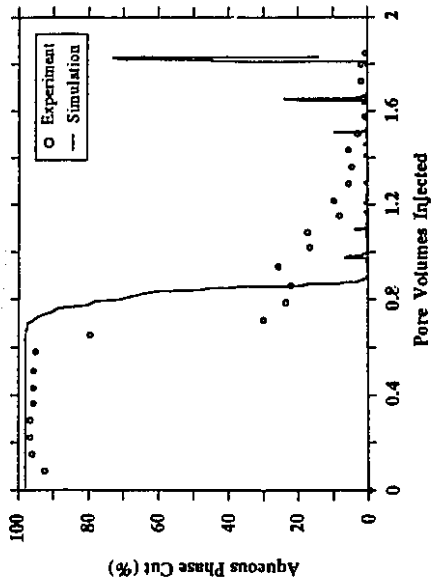


Fig. 7.48 Comparison of Experimental and Simulated Aqueous Phase Cut History for Run 5/5 for Emulsion Flooding.

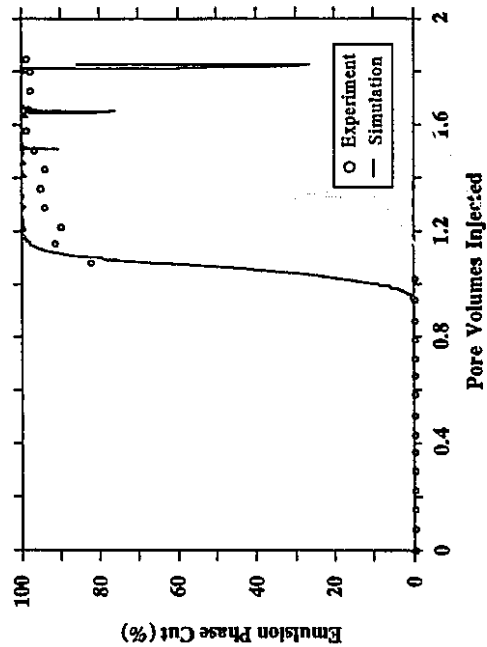


Fig. 7.49 Comparison of Experimental and Simulated Emulsion Phase Cut History for Run 5/5 for Emulsion Flooding.

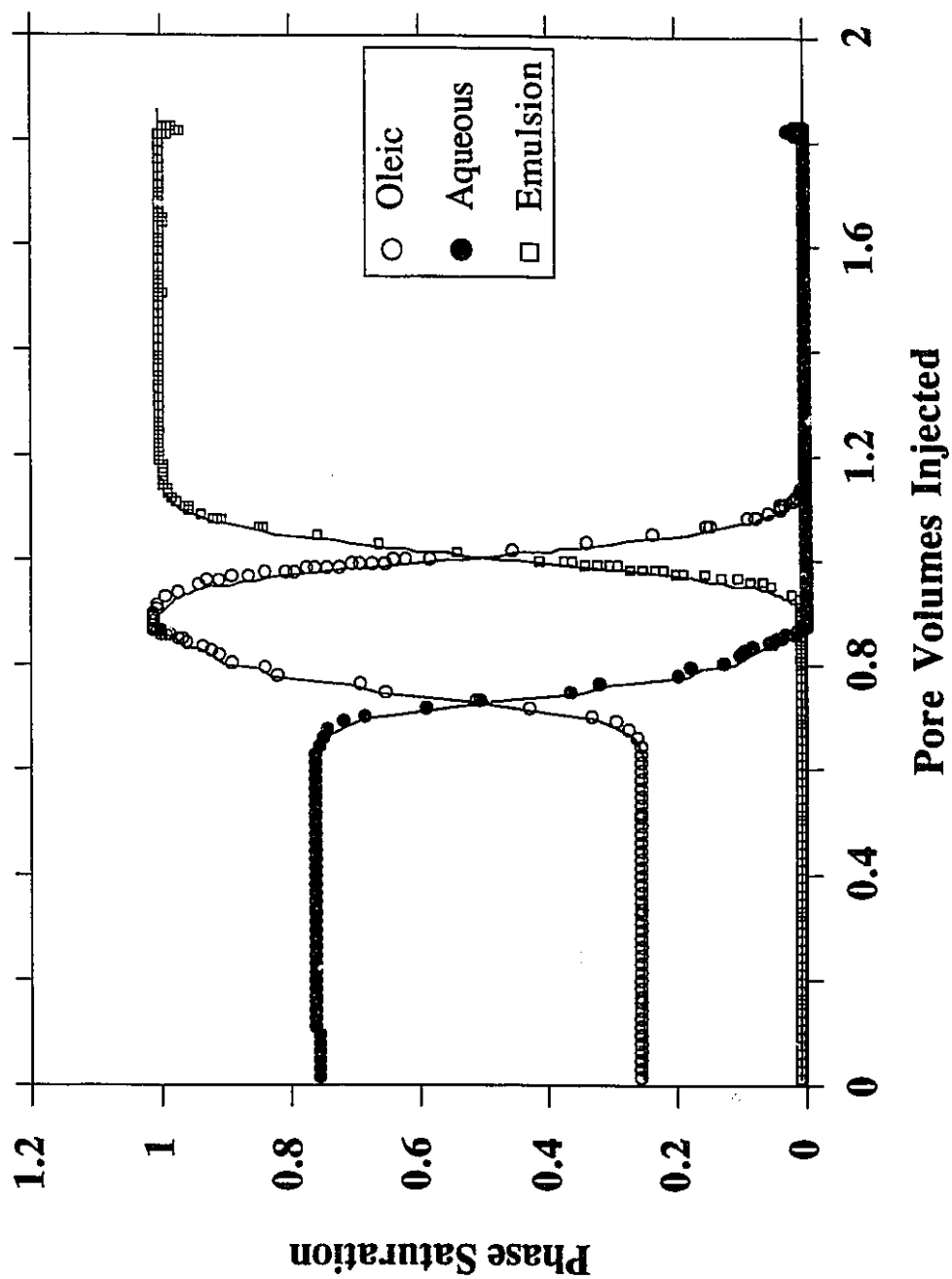


Fig. 7.50 Simulated Saturation History at Production Block for Run 5/5.

some fluctuation in the simulation results for the injection pressure and the aqueous and emulsion phase cuts. The capture mechanism model may be inadequate and has a convergence problem. It is also possible that an instantaneous equilibrium capture assumption is not suitable or over simplified. It could also be that the flow rate in the system is so high that when the droplets in the flow stream come in contact with the pore constrictions, equilibrium cannot be achieved instantaneously. Another notable feature is that all the plots of the simulated results, whether or not they include capture and permeability reduction, generally coincide. This can be explained in that the instantaneous drop capture correlation does not depend on the velocity of the emulsion phase. It depends only on the quality of the emulsion and the ability of the given rock and fluid system to capture droplets. Therefore, no change in the injection pressure or saturation is observed.

Since an instantaneous capture model seems to provide little information, a capture model which includes re-entrainment as a function of emulsion velocity and time is used in Run 5/6. The parameters used are shown in Table 7.6. It should be pointed out that the curvature of the oleic phase relative permeability is 1.5, and that of the aqueous phase relative permeability is 1.3.

Table 7.6

Simulation Input Parameters for Run 5/6

A. Pope's Relative Permeability Model Parameters

A.1 Interfacial Tension and Capillary Desaturation Parameters

Parameter	Value	Parameter	Value
GL1	13.1	TL1	-0.5
GL2	-14.0	TL2	0.222
GL3	0.0221	TA1	-0.428
GA1	13.1	TA2	-0.415
GA2	-14.0	TM1	0.0
GA3	0.0221	TM2	0.0
IFTW	-1.70		

A.2 End Point Relative Permeabilities and Relative Permeability Exponents for Each Phase

End Point Relative Permeability	Value	Relative Permeability Exponent	Value
$k_{rl_{nr}}^o$	0.57	e_l	1.5
$k_{rl_{lr}}^o$	1.0	e_a	1.3
$k_{ra_{nr}}^o$	0.1	e_m	1.0
$k_{ra_{lr}}^o$	1.0		
k_{rm}^o	0.8		

B. Non-Newtonian Rheology

Viscosity Parameter	Value
$K, \text{ Pa.s}^n$	0.63105
n	0.6948
$\alpha\sqrt{F}$	5.0*

* Value changed in Run 5/6 compared to Run 5/3

In comparing Run 5/6 and Run 5/3, several facts should be noted. Run 5/3 did not include the capture mechanism and used a value of 2.5 for $\alpha\sqrt{F}$ which gave an average emulsion viscosity of 0.278 Pa.s. Since this high viscosity yielded a high injection pressure, Run 5/6 has the value of $\alpha\sqrt{F}$ set to 5.0, which gives a low viscosity of 0.086 Pa.s. Run 5/6 also includes the capture mechanism in order to determine whether these two modifications together can improve the overall simulation results.

Injection pressure, cumulative oleic recovery, and oleic, aqueous, and emulsion phase cuts for Run 5/6 are shown in Fig. 7.51 to Fig. 7.56, respectively. Even though droplet capture restricts the flow and requires a higher injection pressure to maintain the same flow rate, a lower injection pressure is observed in Run 5/6 than in Run 5/3. The injection pressure stabilizes at 700 kPa compared with 980 kPa in Run 5/3. Although the fluid in the system is displaced by a much less viscous emulsion in Run 5/6, both runs display similar results for the oleic recovery and the phase cuts. Permeability is reduced from $7.9 \times 10^{-12} \text{ m}^2$ to $3.6 \times 10^{-12} \text{ m}^2$ in Run 5/6 (Fig. 7.61). This indicates that the absolute permeability reduction caused by the plugging of pores in the porous medium plays an important role during displacement. It is apparent that adjustments to the relative permeability and emulsion viscosity alone are not

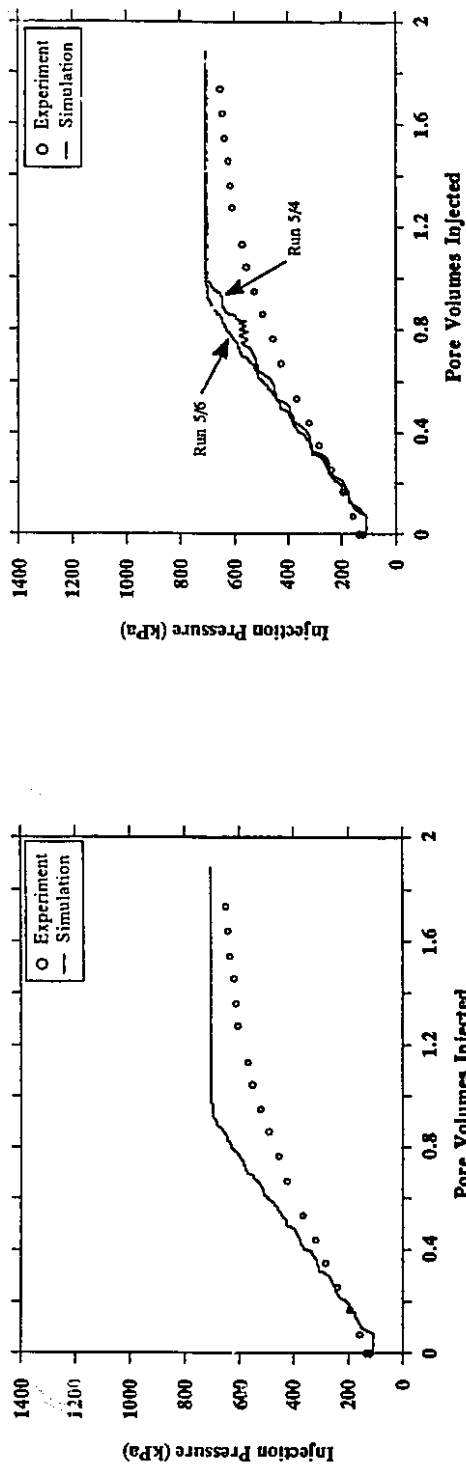


Fig. 7.51 Comparison of Experimental and Simulated Injection Pressure History for Run 5/6 for Emulsion Flooding.

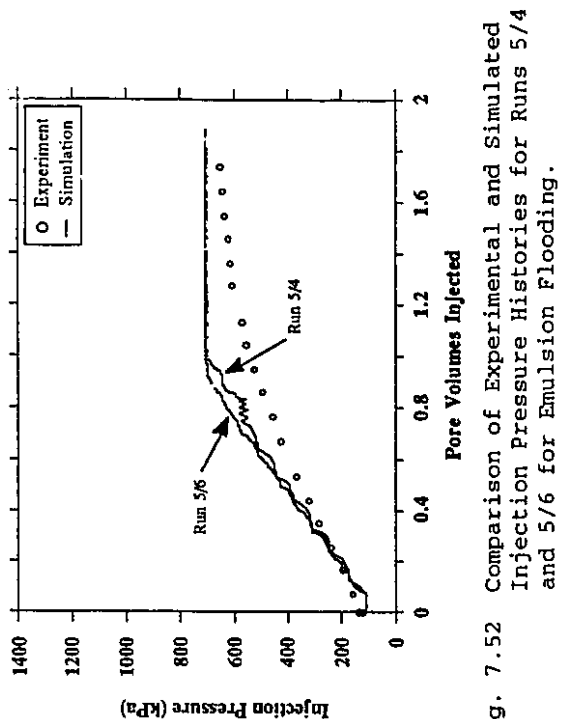


Fig. 7.52 Comparison of Experimental and Simulated Injection Pressure Histories for Runs 5/4 and 5/6 for Emulsion Flooding.

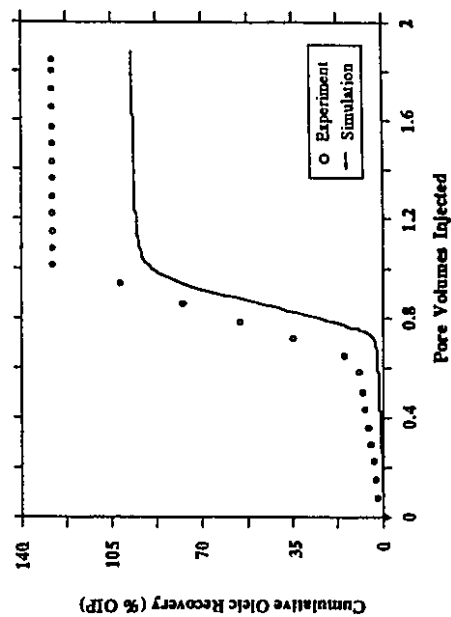


Fig. 7.53 Comparison of Experimental and Simulated Cumulative Oleic Recovery History for Run 5/6 for Emulsion Flooding.

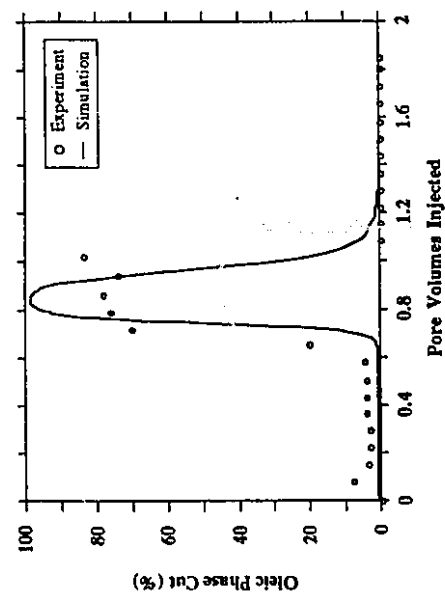


Fig. 7.54 Comparison of Experimental and Simulated Oleic Phase Cut History for Run 5/6 for Emulsion Flooding.

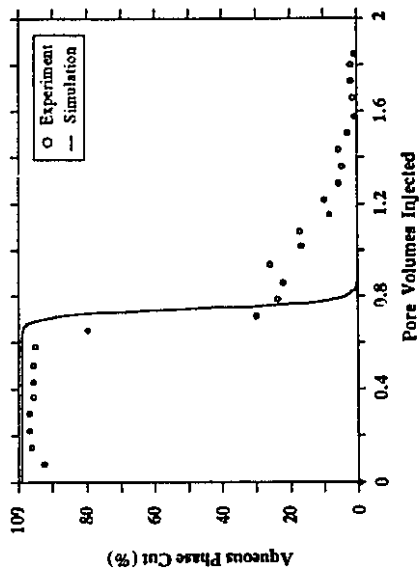


Fig. 7.55 Comparison of Experimental and Simulated Aqueous Phase Cut History for Run 5/6 for Emulsion Flooding.

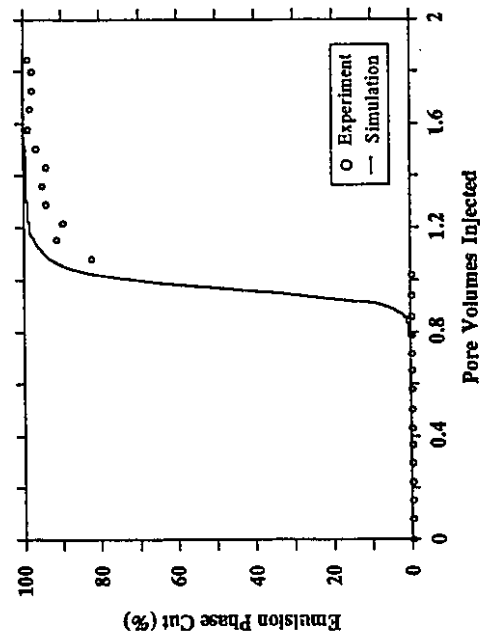


Fig. 7.56 Comparison of Experimental and Simulated Emulsion Phase Cut History for Run 5/6 for Emulsion Flooding.

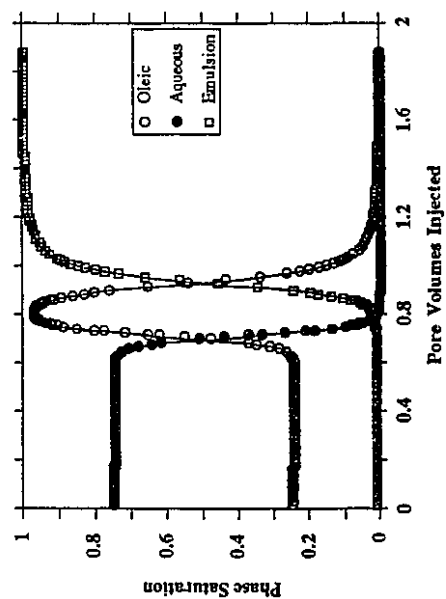


Fig. 7.57 Simulated Saturation History at Production Block for Run 5/6.

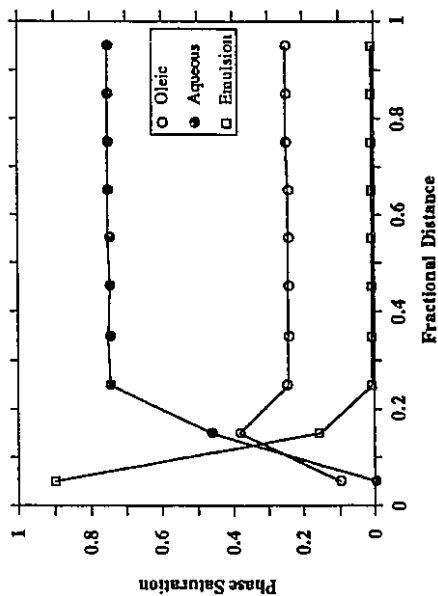


Fig. 7.58 Simulated Saturation Profile for Run 5/6 at 0.1037 PV Injected.

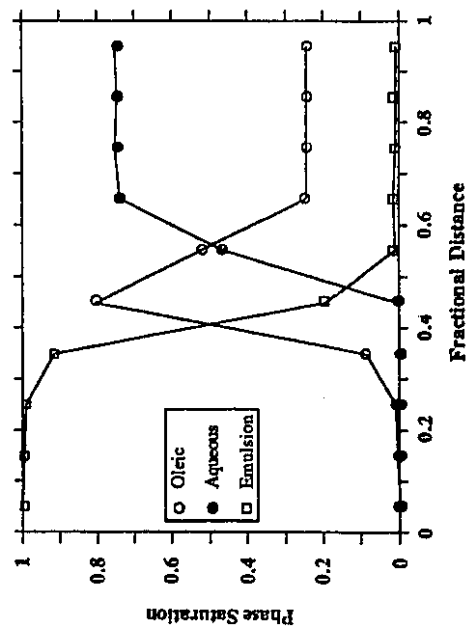


Fig. 7.59 Simulated Saturation Profile for Run 5/6 at 0.4025 PV Injected.

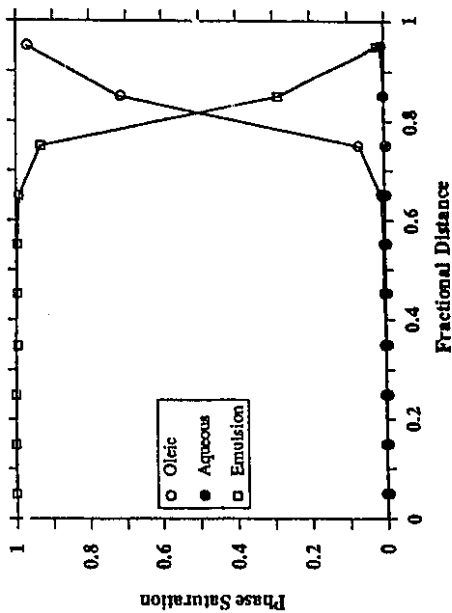


Fig. 7.60 Simulated Saturation Profile for Run 5/6 at 0.8020 PV Injected.

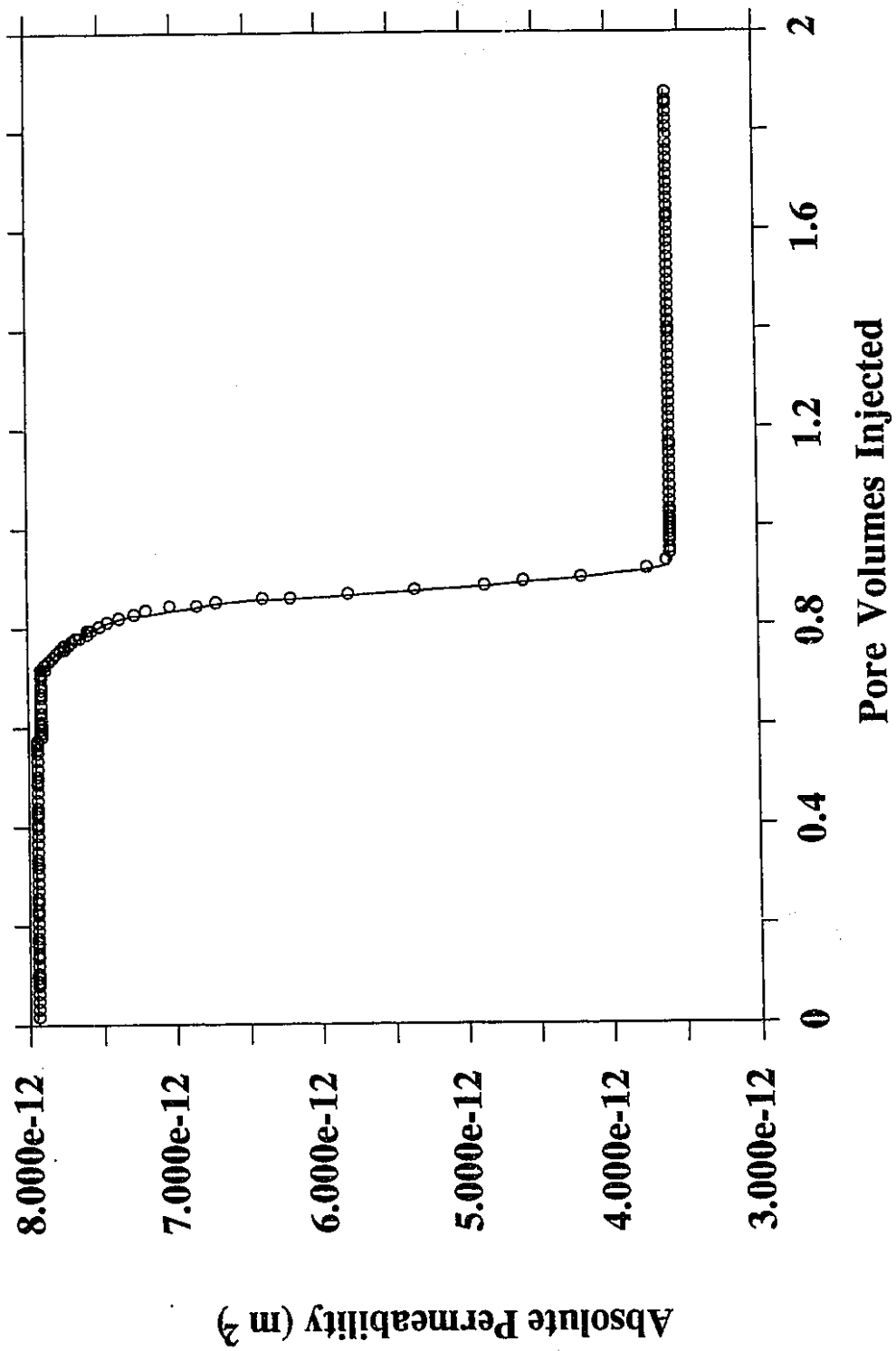


Fig. 7.61 Simulated Absolute Permeability at Production Block for Run 5/6.

sufficient to provide a better representation of the experimental observations.

7.1.5 Effect of Multiphase Emulsion Rheological Behaviour and Emulsion Relative Permeability

The simulation runs discussed above have given a clearer picture of the physical flow of emulsion in a porous medium, thereby yielding results more similar to the experimental observations. For Run 5/7, a multiphase rheological model, given by Eqns. 5.25 and 5.26, was used by entering constant values for k and n , particularly for the injected emulsion. Figure 7.74 illustrates the emulsion viscosity as a function of shear rate. The emulsion viscosity varies from 1.8 down to 0.1 Pa.s. It should be noted that a value of 6.0 was used for $\alpha\sqrt{F}$ to slightly reduce the emulsion viscosity and therefore ensure that the injection pressure would not be too high. To maintain sufficient emulsion mobility, which is increased by reducing the emulsion viscosity, the emulsion relative permeability was reduced by using an end point value of 0.7 instead of 0.8 and maintaining the same curvature. Table 7.7 gives the values of relative permeability and rheological parameters used for Run 5/7. The injection pressure in Fig. 7.62 shows a low stabilized value of 330 kPa. It can also be seen that the simulated injection pressure does not increase as sharply as the experimentally observed pressure. This may be caused by the lower emulsion viscosity at higher shear rates. Apparently, a multiphase

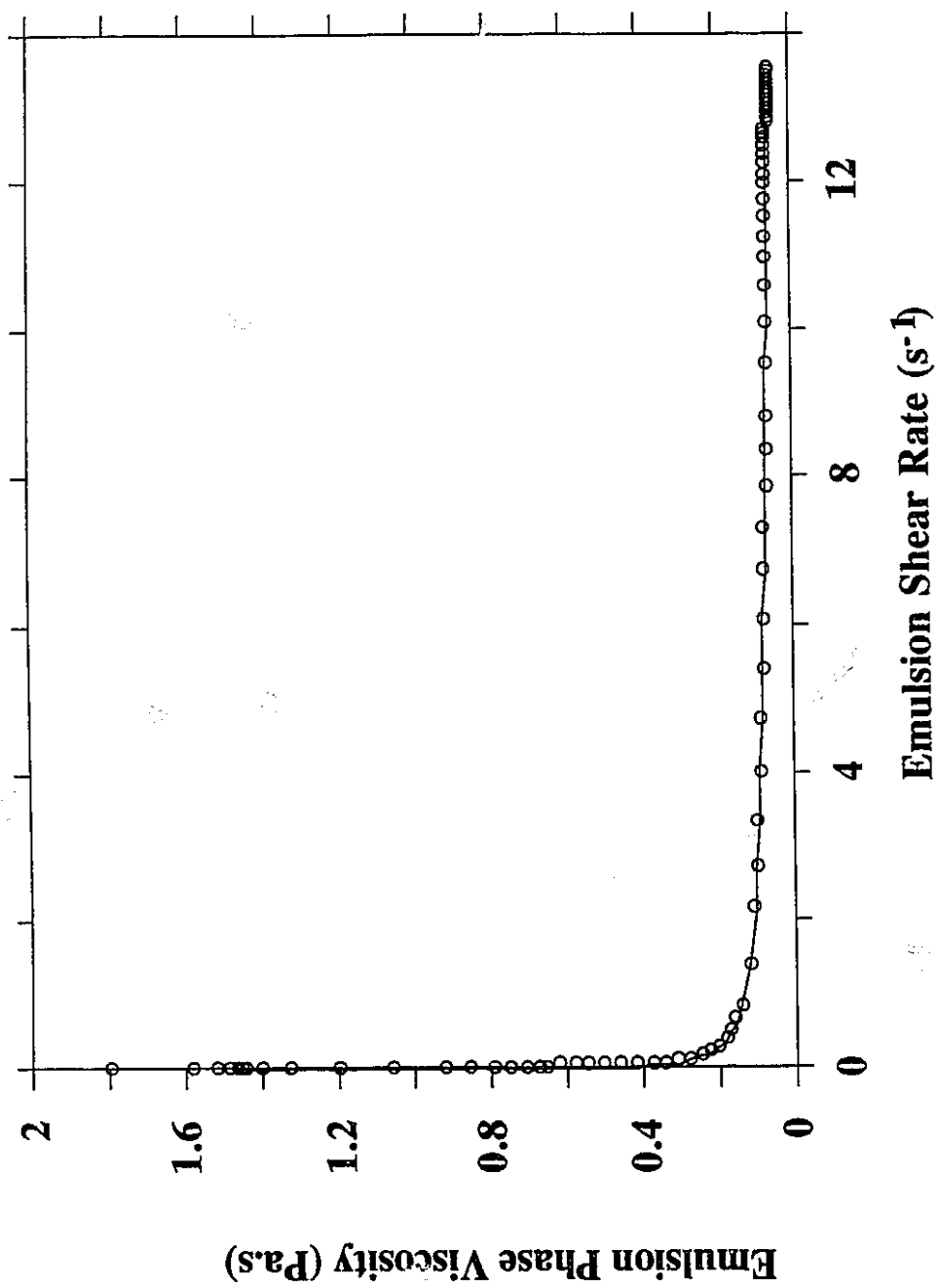


Fig. 7.74 Emulsion Rheology During Flow in Porous Medium for Run 5/7.

Table 7.7

Simulation Input Parameters for Run 5/7

A. Pope's Relative Permeability Model Parameters

A.1 Interfacial Tension and Capillary Desaturation Parameters

Parameter	Value	Parameter	Value
GL1	13.1	TL1	-0.5
GL2	-14.0	TL2	0.222
GL3	0.0221	TA1	-0.428
GA1	13.1	TA2	-0.415
GA2	-14.0	TM1	0.0
GA3	0.0221	TM2	0.0
IFTW	-1.70		

A.2 End Point Relative Permeabilities and Relative Permeability Exponents for Each Phase

End Point Relative Permeability	Value	Relative Permeability Exponent	Value
$k_{r1_{gr}}^o$	0.57	e_1	1.5
$k_{r1_{lr}}^o$	1.0	e_a	1.3
$k_{ra_{gr}}^o$	0.1	e_m	1.0
$k_{ra_{lr}}^o$	1.0		
k_{rm}^o	0.7*		

B. Non-Newtonian Rheology

Viscosity Parameter	Value
$K, \text{ Pa.s}^n$	0.63105
n	0.6948
$\alpha\sqrt{F}$	6.0*

* Values changed in Run 5/7 compared to Run 5/3

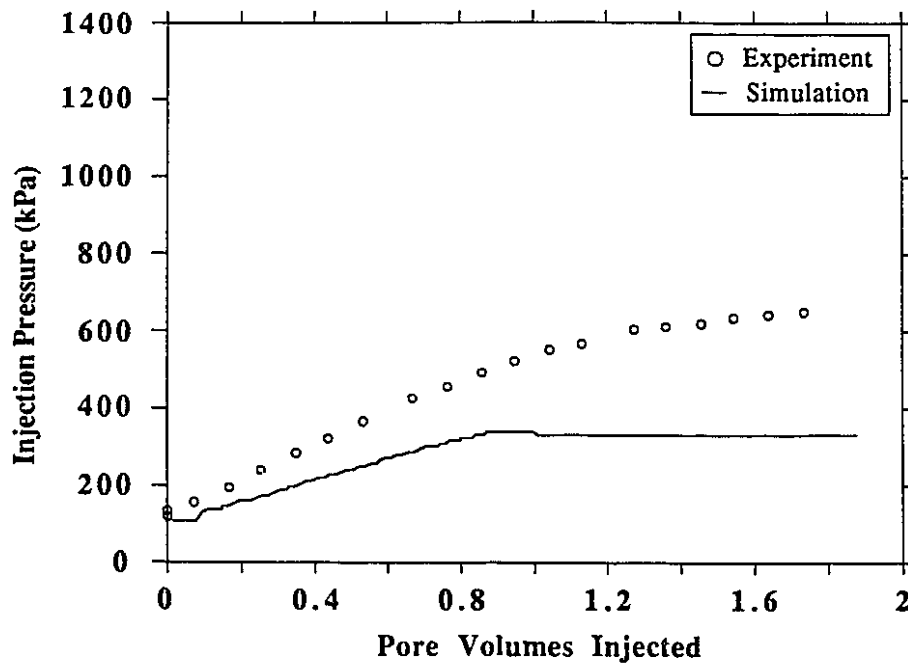


Fig. 7.62 Comparison of Experimental and Simulated Injection Pressure History for Run 5/7 for Emulsion Flooding.

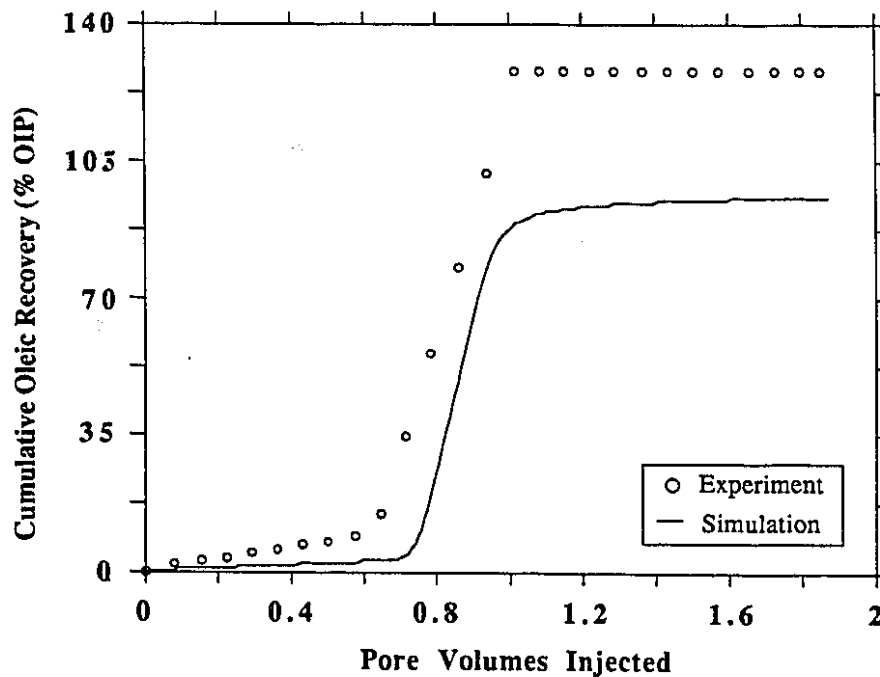


Fig. 7.63 Comparison of Experimental and Simulated Cumulative Oleic Recovery History for Run 5/7 for Emulsion Flooding.

rheological model gives a better prediction of the injection pressure than does the single-phase model. The saturation history and saturation profiles are shown in Figs. 7.67 to 7.70. The cumulative oleic recovery and phase cuts, shown in Figs. 7.63 to 7.66, are similar to those observed for Run 5/6.

7.1.6 Effect of Droplet Capture Mechanism and Permeability Reduction

At this stage it is apparent that the multiphase non-Newtonian rheological model can produce a less steep injection pressure curve than that predicted by a single phase non-Newtonian correlation due to its lower viscosity at higher shear rates. Also, the injection pressure obtained in Run 5/6 is too high. The following simulation, Run 5/8, was conducted to determine the effect of the capture mechanism in improving the injection pressure prediction. The input data used in Run 5/7 was also used in this run. Furthermore, the time-dependent capture model is included for this run. The results of Run 5/8 are shown in Figs. 7.75 to 7.88, and the input parameter data are given in Table 7.8.

An improvement in the injection pressure is obtained in Run 5/8, as expected (Fig. 7.75). For this run, the injection pressure before emulsion breakthrough was observed to be higher than that for Run 5/7. This is mainly due to pore-plugging which caused an absolute permeability reduction.

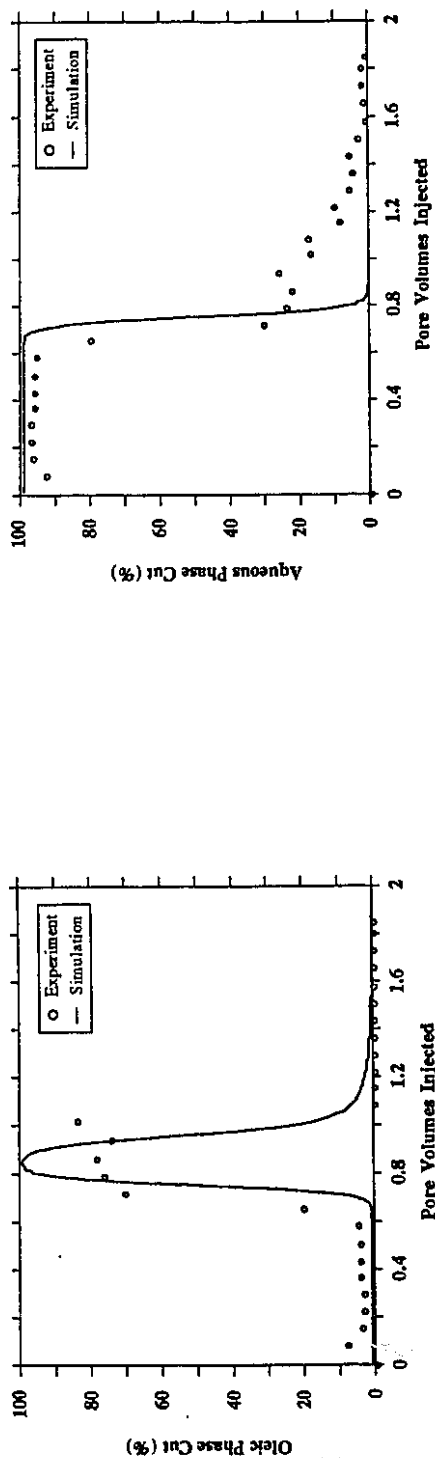


Fig. 7.64 Comparison of Experimental and Simulated Oleic Phase Cut History for Run 5/7 for Emulsion Flooding.

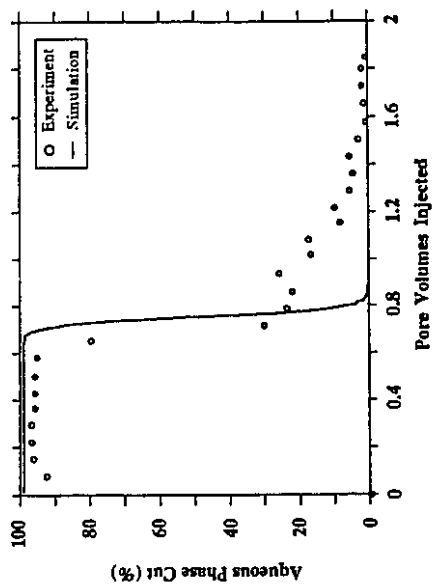


Fig. 7.65 Comparison of Experimental and Simulated Aqueous Phase Cut History for Run 5/7 for Emulsion Flooding.

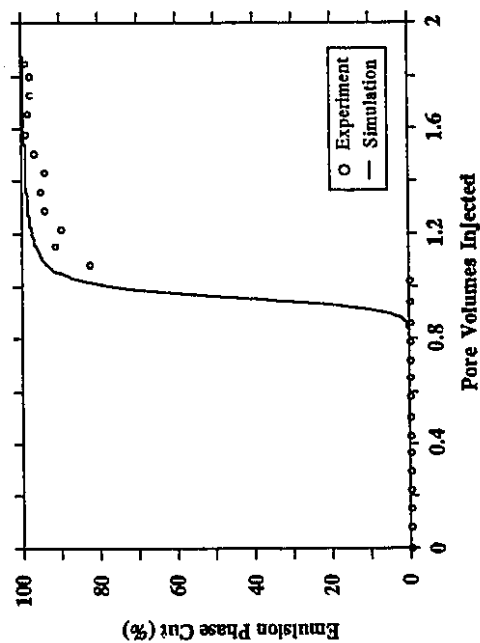


Fig. 7.66 Comparison of Experimental and Simulated Emulsion Phase Cut History for Run 5/7 for Emulsion Flooding.

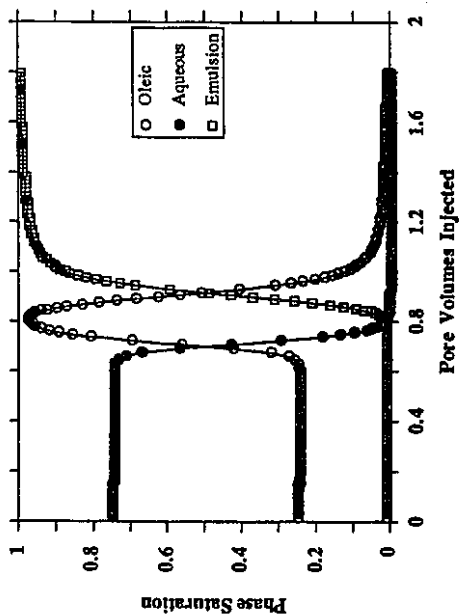


Fig. 7.67 Simulated Saturation History at Production Block for Run 5/7.

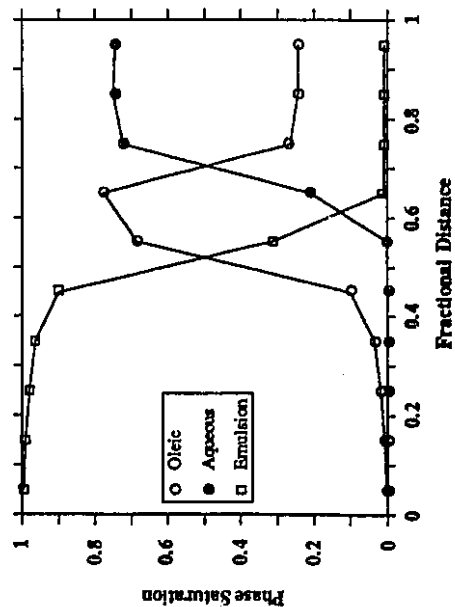


Fig. 7.69 Simulated Saturation Profile for Run 5/7 at 0.5062 PV Injected.

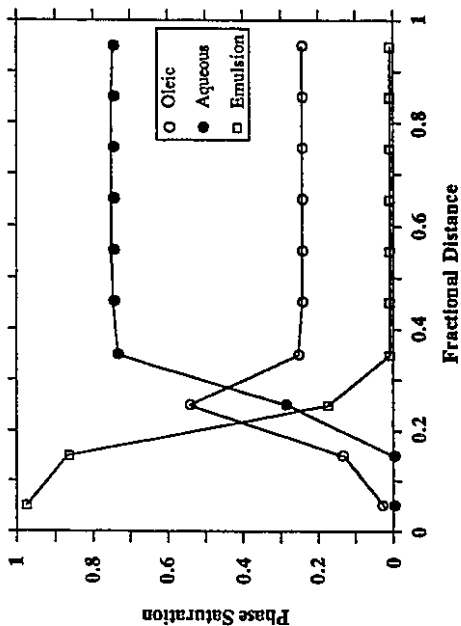


Fig. 7.68 Simulated Saturation Profile for Run 5/7 at 0.1988 PV Injected.

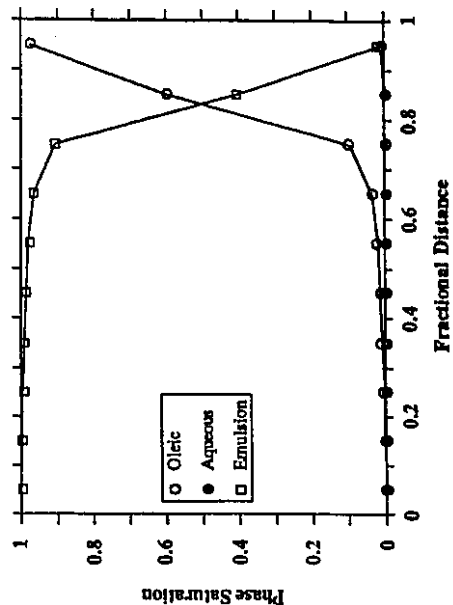


Fig. 7.70 Simulated Saturation Profile for Run 5/7 at 0.8059 PV Injected.

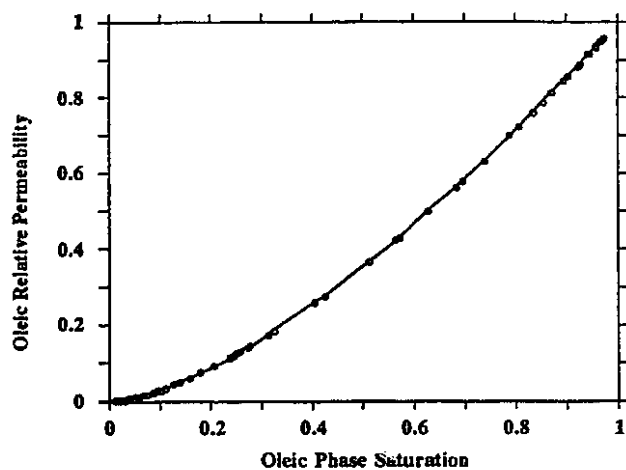


Fig. 7.71 Oleic Relative Permeability Vs. Oleic Phase Saturation for Run 5/7.

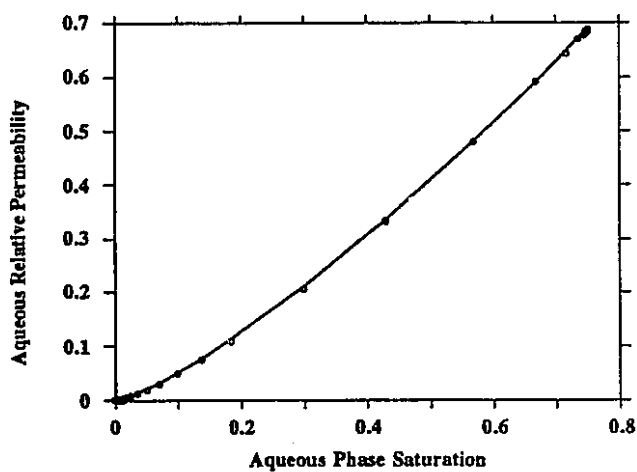


Fig. 7.72 Aqueous Relative Permeability Vs. Aqueous Phase Saturation for Run 5/7.

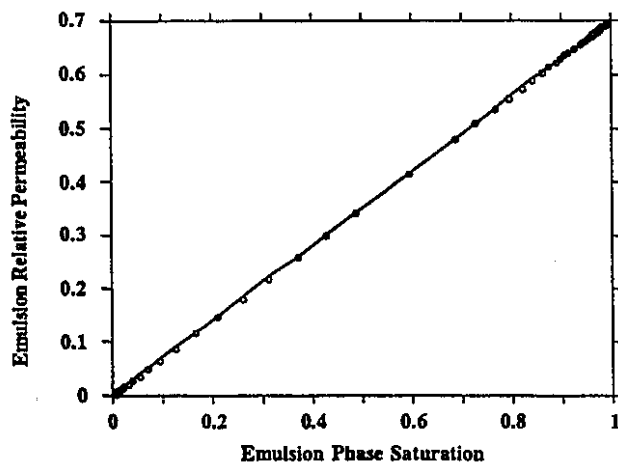


Fig. 7.73 Emulsion Relative Permeability Vs. Emulsion Phase Saturation for Run 5/7.

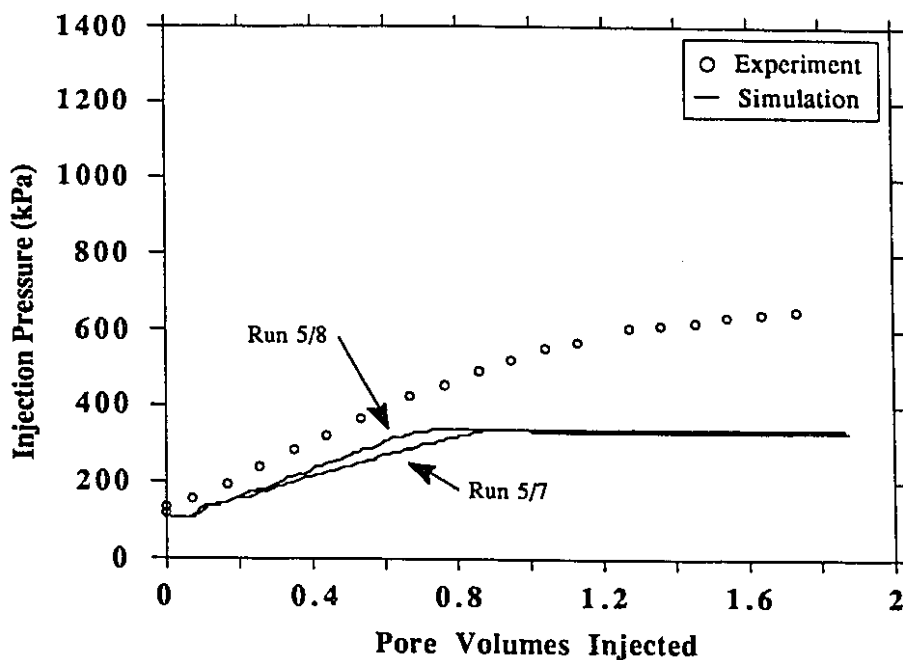


Fig. 7.75 Comparison of Experimental and Simulated Injection Pressure History for Run 5/7 and 5/8 for Emulsion Flooding.

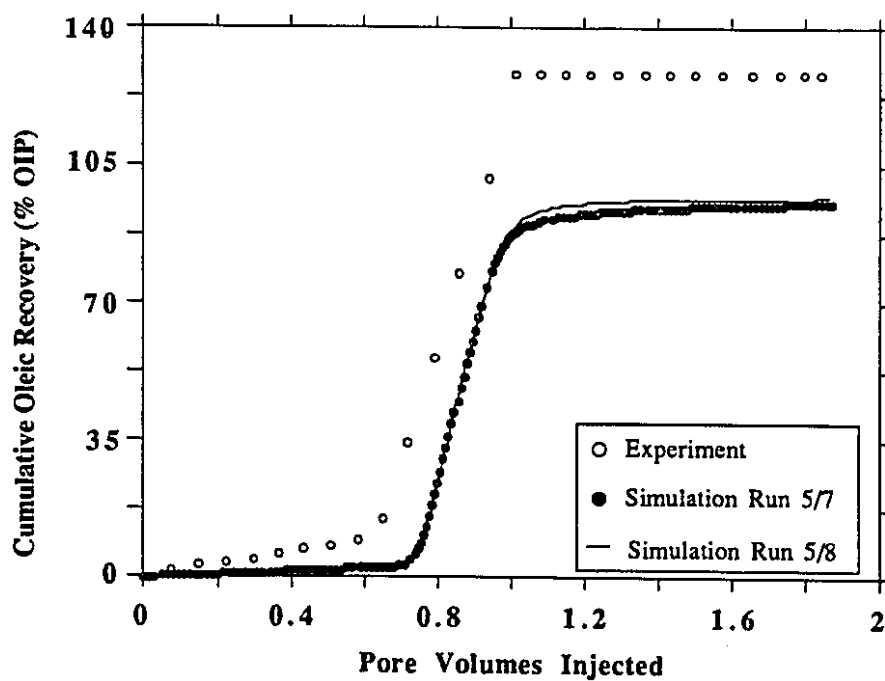


Fig. 7.76 Comparison of Experimental and Simulated Cumulative Oleic Recovery History for Runs 5/7 and 5/8 for Emulsion Flooding.

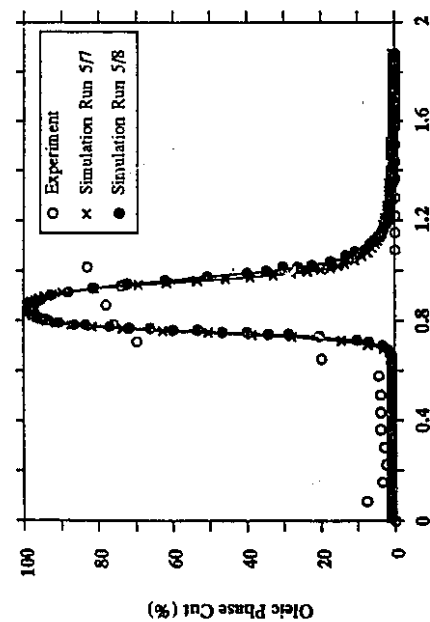


Fig. 7.77 Comparison of Experimental and Simulated Oleic Phase Cut History for Run 5/7 and 5/8 for Emulsion Flooding.

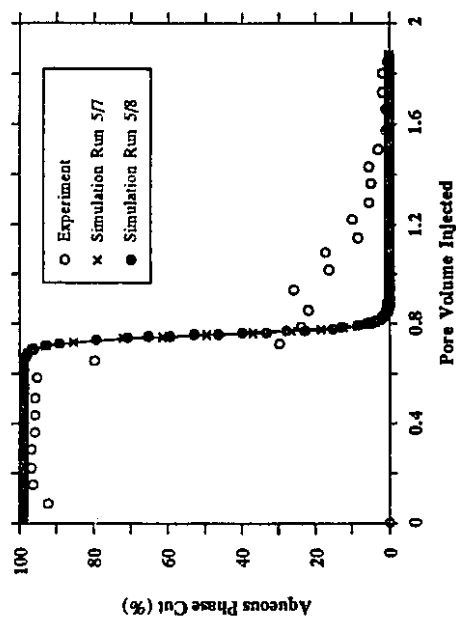


Fig. 7.78 Comparison of Experimental and Simulated Aqueous Phase Cut History for Run 5/7 and 5/8 for Emulsion Flooding.

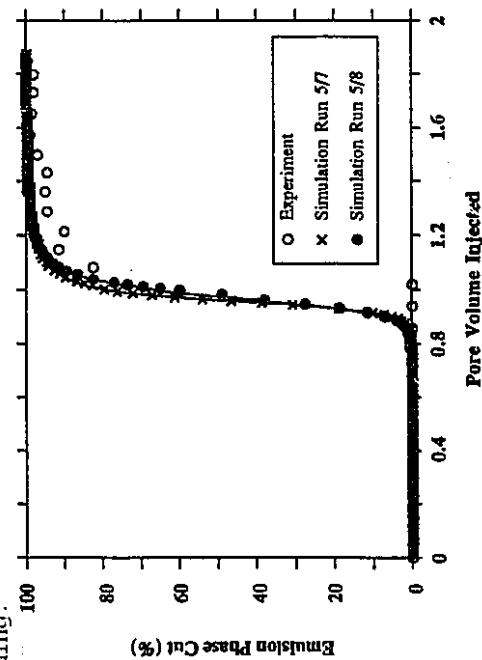


Fig. 7.79 Comparison of Experimental and Simulated Emulsion Phase Cut History for Run 5/7 and 5/8 for Emulsion Flooding.

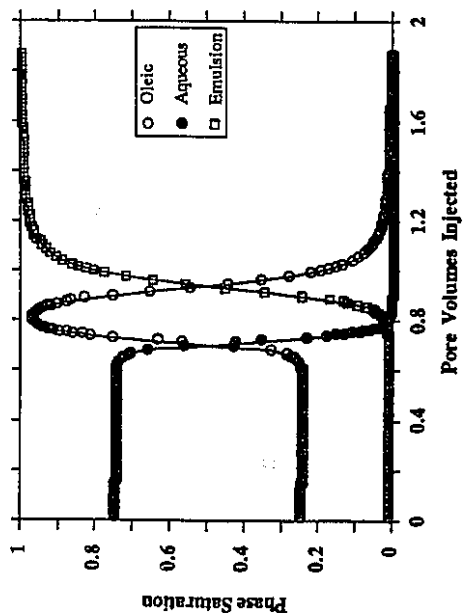


Fig. 7.80 Simulated Saturation History at Production Block for Run 5/8.

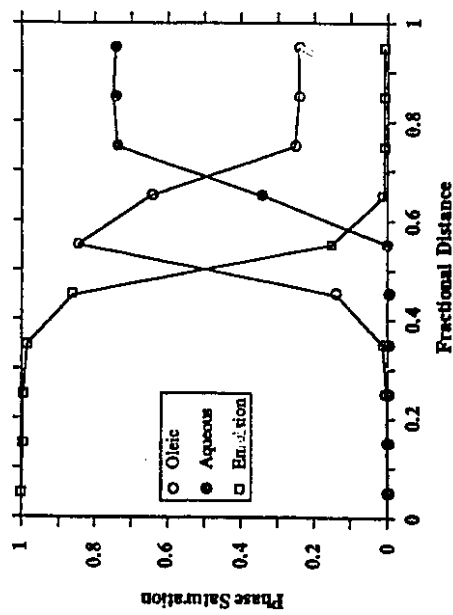


Fig. 7.82 Simulated Saturation Profile for Run 5/8 at 0.4947 PV Injected.

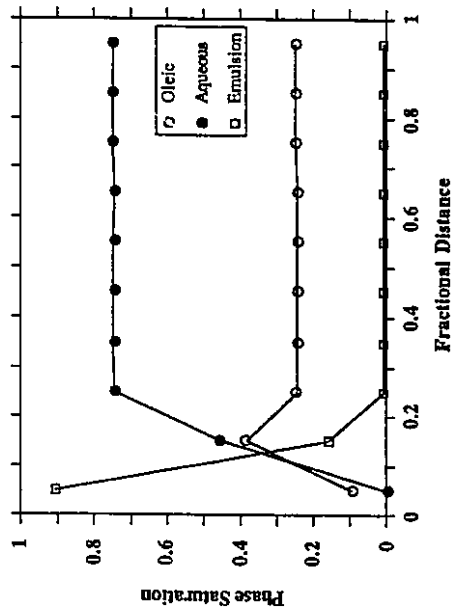


Fig. 7.81 Simulated Saturation Profile for Run 5/8 at 0.1076 PV Injected.

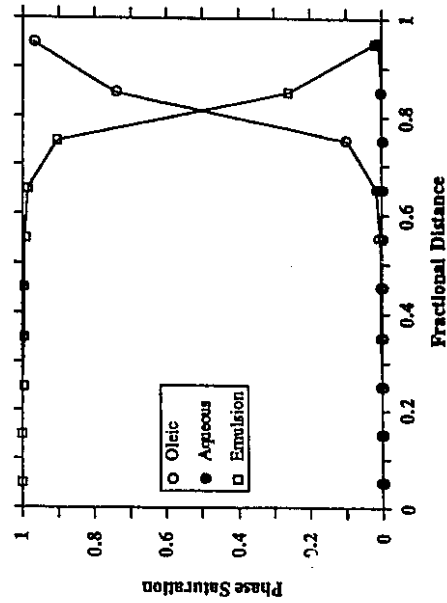


Fig. 7.83 Simulated Saturation Profile for Run 5/8 at 0.8020 PV Injected.

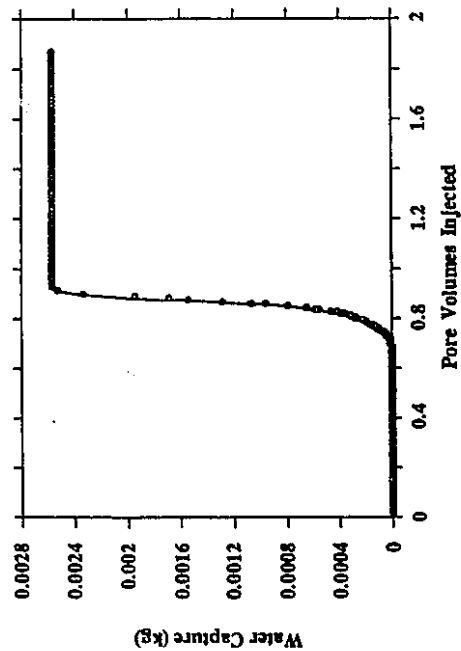


Fig. 7.84 Predicted Water Droplet Capture History at Production Block for Run 5/8.

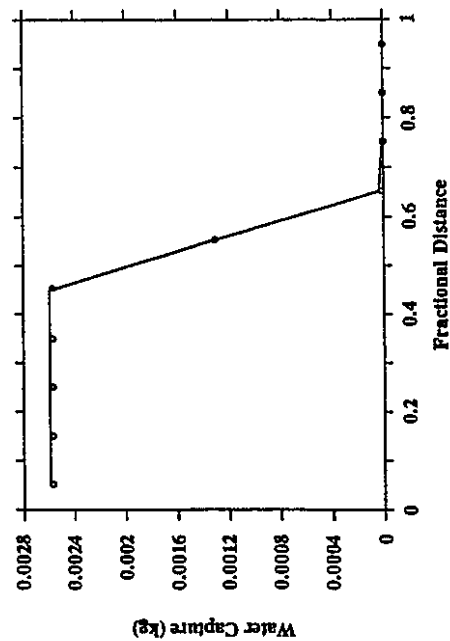


Fig. 7.86 Predicted Water Droplet Capture Profile for Run 5/8 at 0.4947 PV Injected.

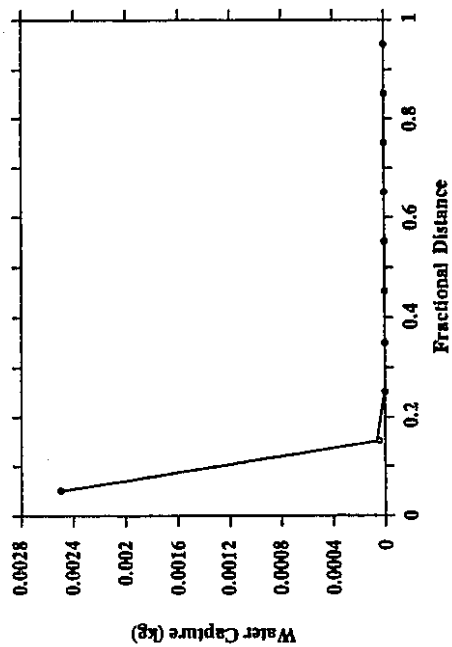


Fig. 7.85 Predicted Water Droplet Capture Profile for Run 5/8 at 0.1076 PV Injected.

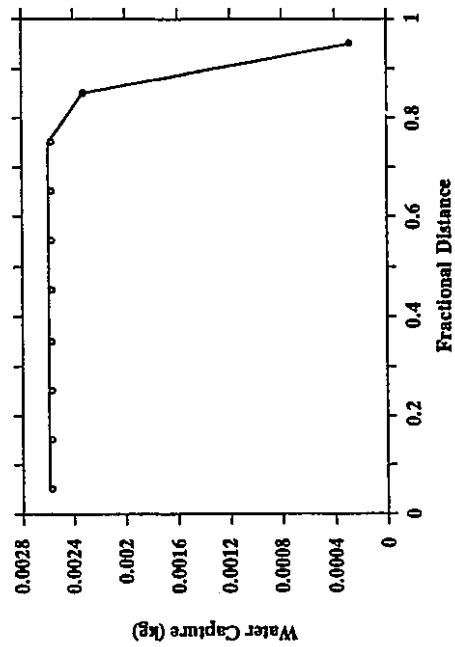


Fig. 7.87 Predicted Water Droplet Capture Profile for Run 5/8 at 0.8020 PV Injected.

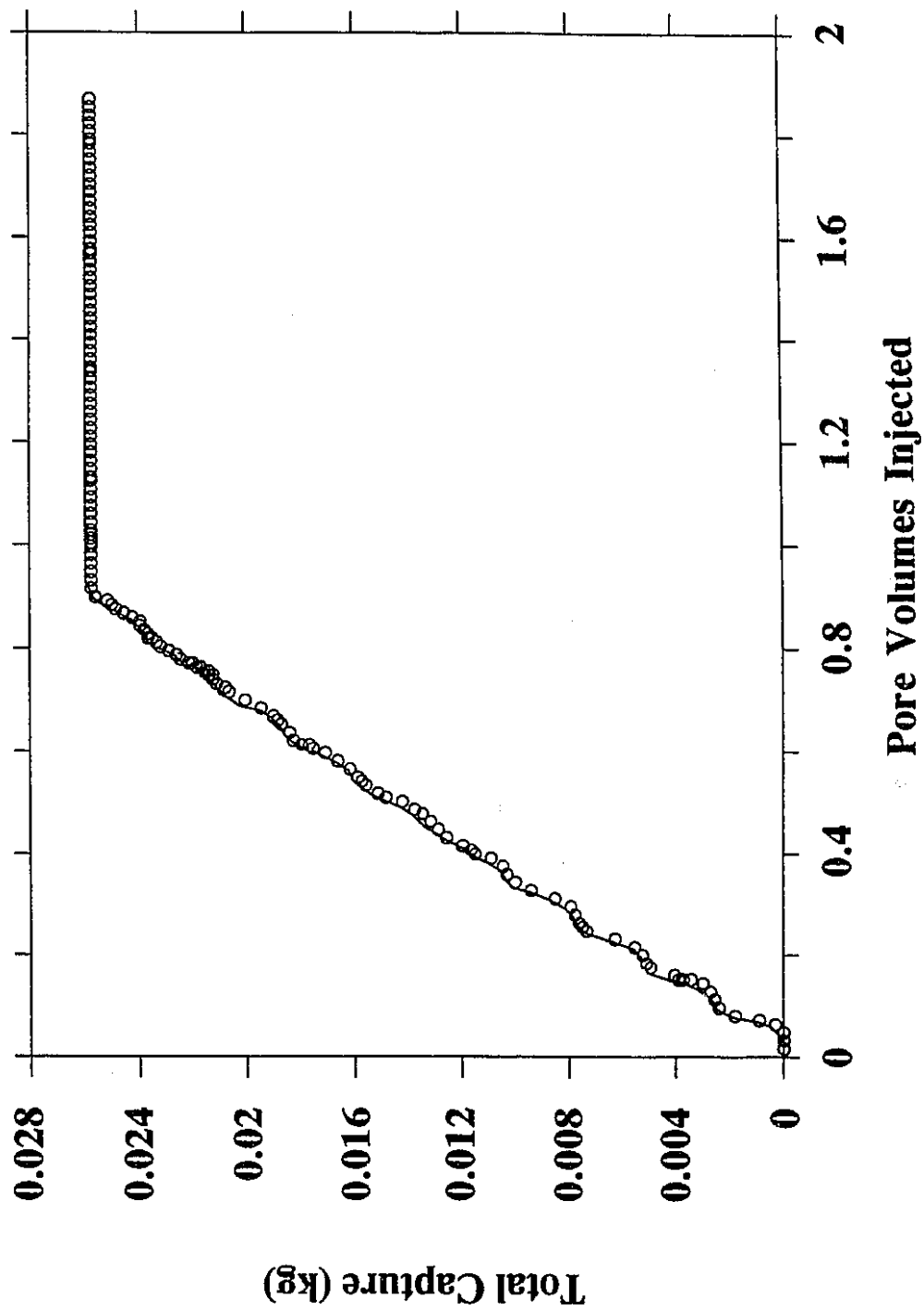


Fig. 7.88 Predicted Total Droplet Capture History for Run 5/8.

Table 7.8

Simulation Input Parameters for Run 5/8

A. Pope's Relative Permeability Model Parameters

A.1 Interfacial Tension and Capillary Desaturation Parameters

Parameter	Value	Parameter	Value
GL1	13.1	TL1	-0.5
GL2	-14.0	TL2	0.222
GL3	0.0221	TA1	-0.428
GA1	13.1	TA2	-0.415
GA2	-14.0	TM1	0.0
GA3	0.0221	TM2	0.0
IFTW	-1.70		

A.2 End Point Relative Permeabilities and Relative Permeability Exponents for Each Phase

End Point Relative Permeability	Value	Relative Permeability Exponent	Value
$k_{rl_{HT}}^o$	0.57	e_1	1.5
$k_{rl_{LT}}^o$	1.0	e_a	1.3
$k_{ra_{HT}}^o$	0.1	e_m	1.0
$k_{ra_{LT}}^o$	1.0		
k_{rm}^o	0.7*		

B. Non-Newtonian Rheology

Viscosity Parameter	Value
$K, \text{ Pa.s}^n$	0.63105
n	0.6948
$\alpha\sqrt{F}$	6.0*

* Values changed in Run 5/8 compared to Run 5/3
Run 5/8 also included droplet capture mechanism.

Furthermore, there is a lower stabilized injection pressure of 330 kPa for this run, compared to 700 kPa for Run 5/6. Cumulative oleic recovery and phase cuts are illustrated Figs. 7.76 to 7.79. The cumulative oleic recovery, oleic cut, and aqueous cut of Run 5/8 are similar to those of Run 5/7, while a slight improvement in the emulsion cut of Run 5/8 is observed. It is apparent that the modifications made to the model brought the simulation results more in line with the experimental observations. The injection pressure is higher before emulsion breakthrough and closer to the experimental data, while the oleic recovery and phase cuts still remain close to the experimental data with some improvement. This is because the multiphase non-Newtonian model and the time-dependent capture model were used in conjunction with a lower emulsion relative permeability and a lower emulsion viscosity. Finally, the saturation history, saturation profiles, instantaneous capture history and profiles, and the total capture history are shown in Figs. 7.80 to 7.88. The saturation profiles of Runs 5/6 and 5/8 are similar, while a slightly larger oil bank is formed in Run 5/8 compared to Run 5/7. This results in a slightly higher oleic recovery. Capture profiles show the propagation of drop capture along the core, with a maximum capture of 0.0026 kg of water droplets for this rock and fluid system which reduces the absolute permeability to $3.6 \times 10^{-12} \text{ m}^2$ from an initial value of $7.95 \times 10^{-12} \text{ m}^2$.

In conclusion, the simulator developed which includes the multiphase non-Newtonian emulsion rheological model, Pope's relative permeability model, and the time-dependent capture model are able to predict the production history of the laboratory core flood.

7.2 Sensitivity Study

A sensitivity study of the injection pressure, cumulative oleic recovery, and breakthrough time of core flood #5 was carried out to determine what effect the process variables have on the predictions made by the model.

7.2.1 Sensitivity Study of Injection Pressure

The injection pressure shows no response to an increase in the end point aqueous relative permeability at a high interfacial tension (Fig. 7.89). This means that no matter how permeable the porous medium is to the aqueous phase, the pressure required to inject a displacing emulsion is the same. However, an increase in the end point emulsion relative permeability leads to a lower injection pressure (Fig. 7.90). A linear increase in the pressure required to inject a more viscous emulsion is demonstrated in Fig. 7.91. Figure 7.92 shows the injection pressure necessary for the different rheological models used to predict emulsion viscosity, viz. a weighted average correlation and a single-phase non-Newtonian correlation. As expected, it was observed that the more viscous a fluid is predicted to be,

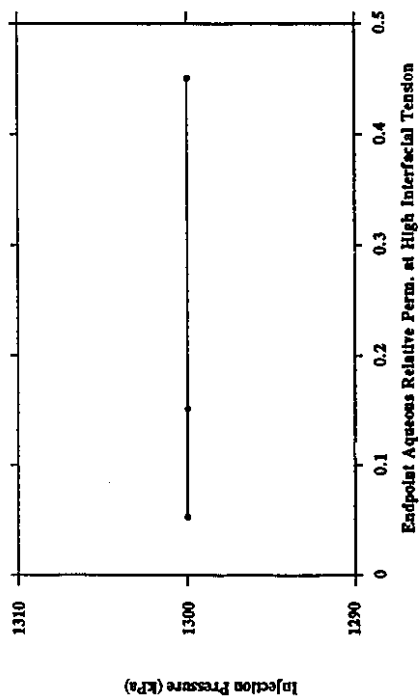


Fig. 7.89 Sensitivity of Injection Pressure to Endpoint Aqueous Relative Permeability at High Interfacial Tension.

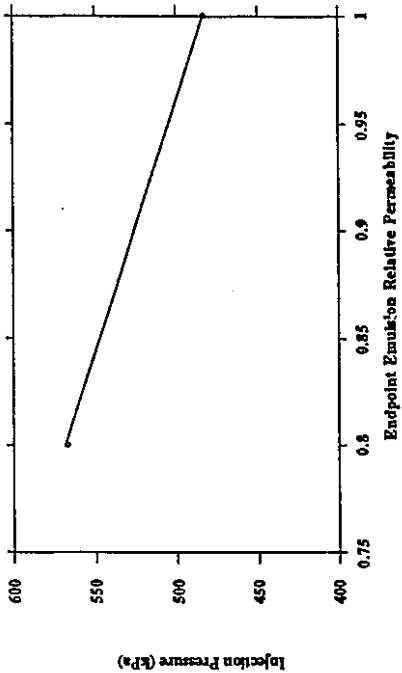


Fig. 7.90 Sensitivity of Injection Pressure to Endpoint Aqueous Relative Permeability at High Interfacial Tension.

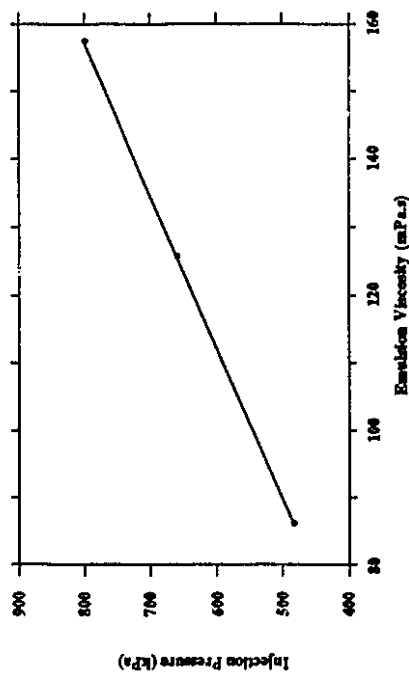


Fig. 7.91 Sensitivity of Injection Pressure to Emulsion Viscosity Predicted by Single Phase Non-Newtonian Correlation.

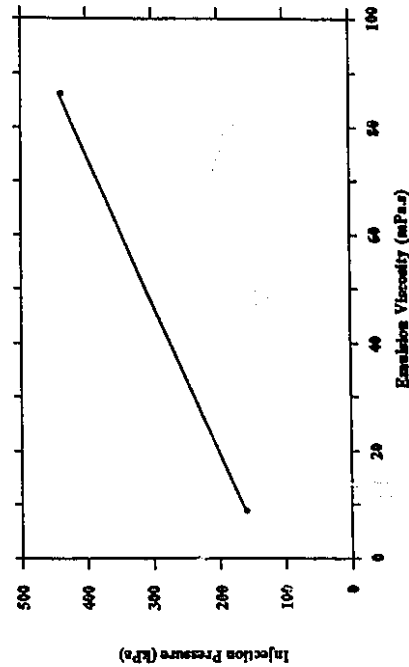


Fig. 7.92 Sensitivity of Injection Pressure to Emulsion Viscosity Predicted by Different Rheological Models.

the higher is the pressure required to make it flow at a given rate. A higher injection pressure, and thus a higher pressure drop across the core, is also required when the fluid flow rate is increased (Fig. 7.93), a result that follows from Darcy's law. Figure 7.94 indicates that no change in the injection pressure is required to displace the system in the case of different initial oil saturations in the core. However, if the oil is more viscous, a higher pressure is needed to inject a displacing fluid to displace that oil (Fig. 7.95). For oil-in-water emulsions, it is generally true that a higher mass fraction of oil in the emulsion produces a more viscous emulsion that therefore requires a higher injection pressure (Fig. 7.96). Thus, in reviewing the sensitivity of the injection pressure, it is found that it behaves in the manner anticipated.

7.2.2 Sensitivity Study of Total Oleic Recovery

The total oleic recovery is next analyzed for its sensitivity to the same process variables just examined, i.e., end point aqueous relative permeability at high interfacial tension, end point emulsion relative permeability, emulsion viscosity predicted by a single phase non-Newtonian correlation, emulsion viscosity predicted by different rheological models, and injection rate. The model predicts a lower oleic recovery if the end point aqueous relative permeability at high interfacial tension is increased (see Fig. 7.97). A possible explanation is that if the porous medium is made

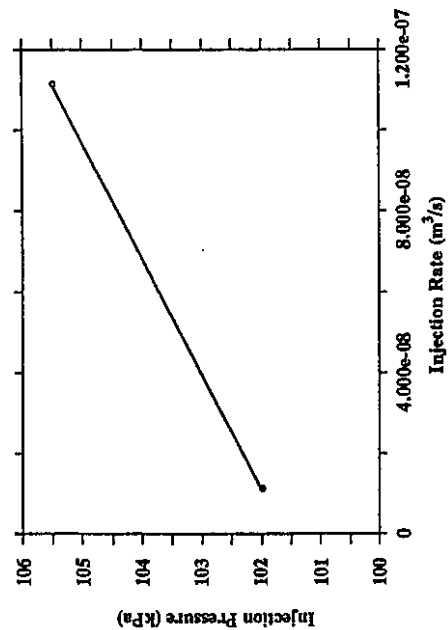


Fig. 7.93 Sensitivity of Injection Pressure to Injection Rate.

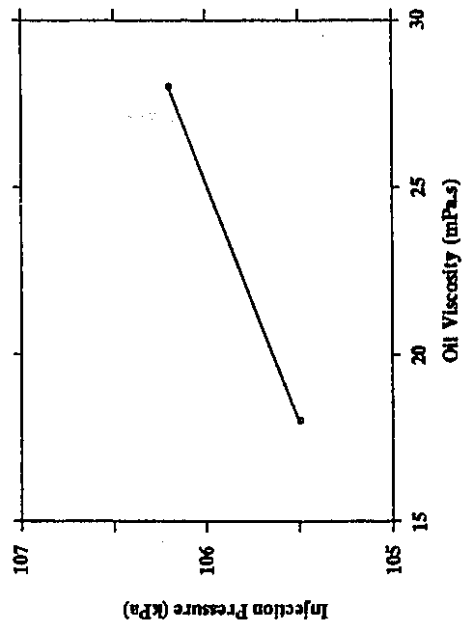


Fig. 7.95 Sensitivity of Injection Pressure to Oil Viscosity.

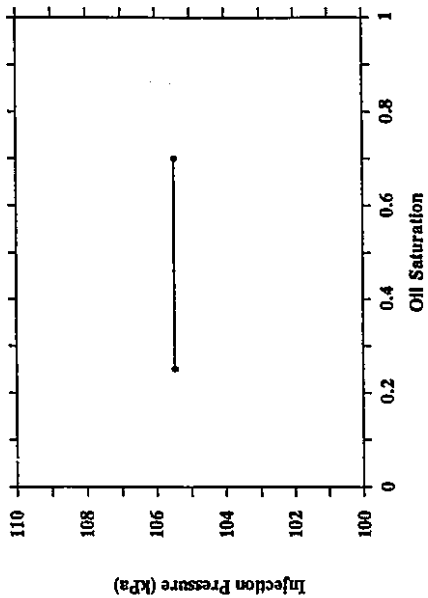


Fig. 7.94 Sensitivity of Injection Pressure to Initial Oil Saturation in the Core.

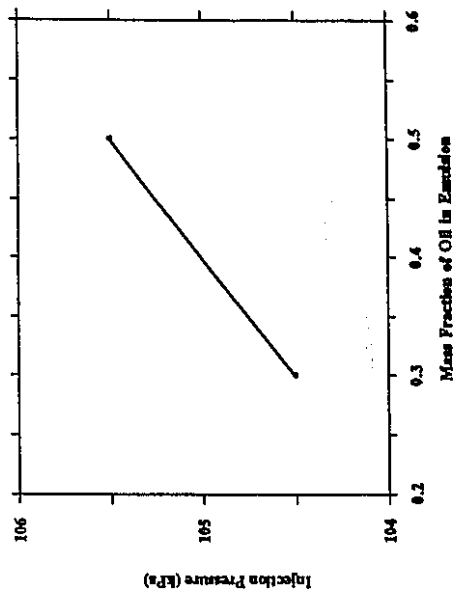


Fig. 7.96 Sensitivity of Injection Pressure to Mass Fraction of Oil in Water-in-Oil Emulsion.

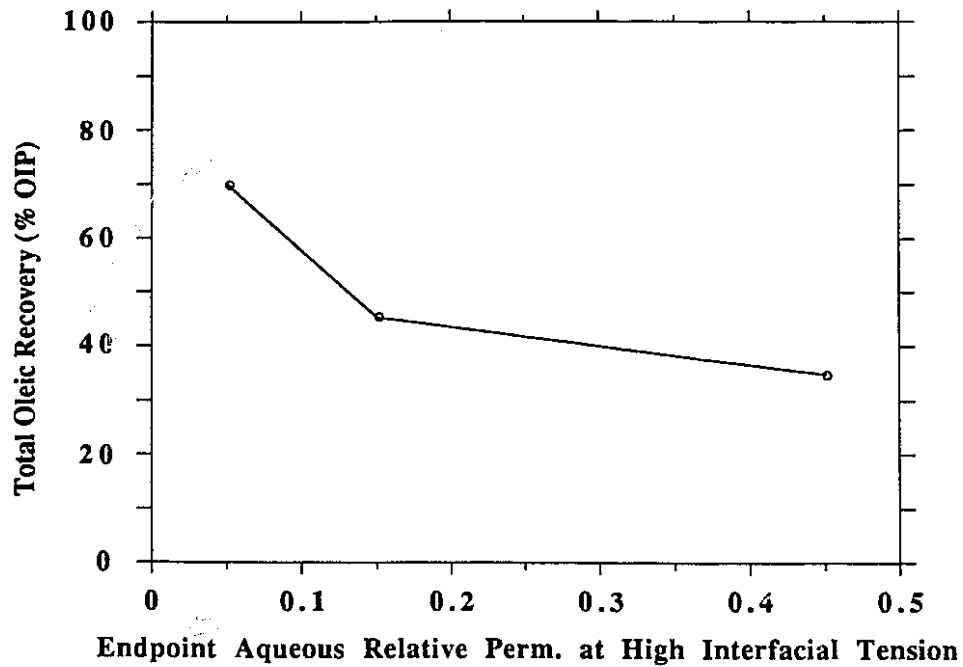


Fig. 7.97 Sensitivity of Total Oleic Recovery to Endpoint Aqueous Relative Permeability at High Interfacial Tension.

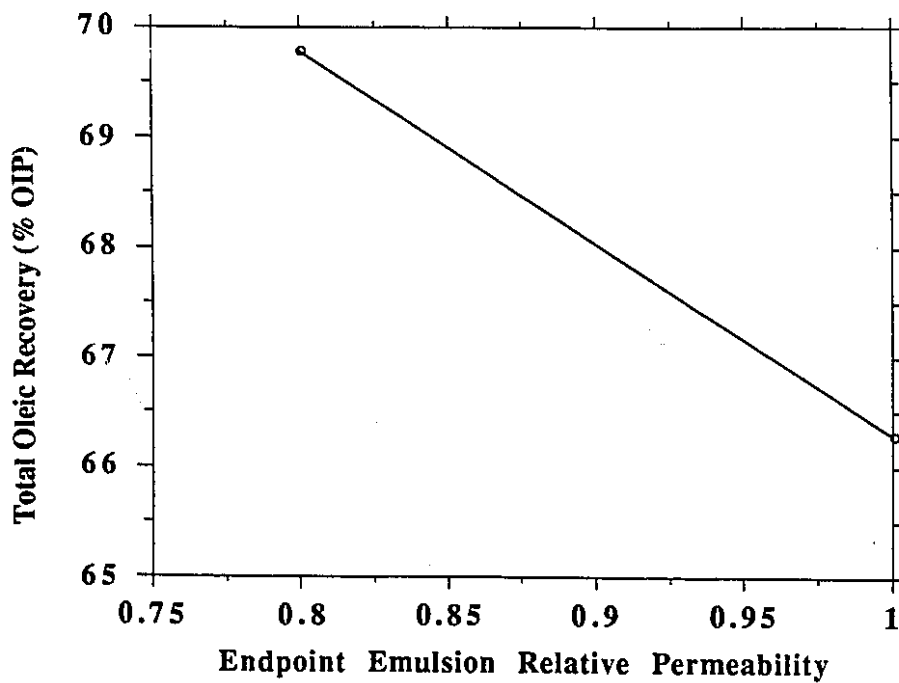


Fig. 7.98 Sensitivity of Total Oleic Recovery to Endpoint Emulsion Relative Permeability.

more permeable to the aqueous phase, more of the oil will be trapped, thereby lowering the amount of oil that can be recovered. Similarly, when the end point emulsion relative permeability is increased, the oleic recovery is again lowered. This is so because increasing the emulsion relative permeability increases the likelihood that the emulsion will finger through and bring about a poor displacement efficiency (Fig. 7.98). By using a more viscous displacing fluid, better mobility control is achieved and the oleic recovery is higher (see Fig. 7.99). A similar result is obtained when different rheological models are used (Fig. 7.100). These equations are the weighted average and single-phase non-Newtonian correlations. When the injection rate of the emulsion is increased, the total oleic recovery is increased. This can be interpreted as follows. Increasing the flow rate has the effect of increasing the viscous force acting on the trapped oil. This results in lowering the residual oil saturation and increasing the oleic recovery (Fig. 7.101).

7.2.3 Sensitivity Study of Emulsion Breakthrough Time

The last variable to be studied is the emulsion breakthrough time. It can be seen that the emulsion breakthrough time is more sensitive to the end point aqueous relative permeability than the oleic recovery based on the steeper slope shown in Fig. 7.102. The greater the ease with which the aqueous phase can flow, the later the emulsion phase will break through. Naturally, an increase in the end point emulsion

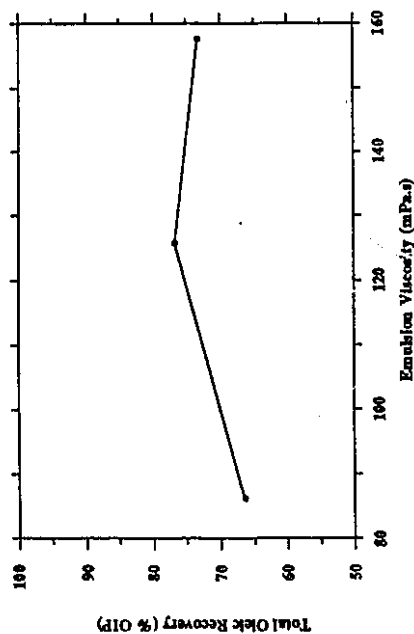


Fig. 7.99 Sensitivity of Total Oleic Recovery to Emulsion Viscosity Predicted by Single-phase Non-Newtonian Correlation.

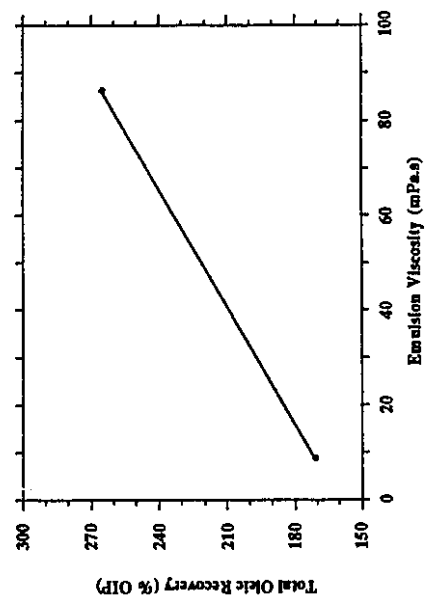


Fig. 7.100 Sensitivity of Total Oleic Recovery to Emulsion Viscosity Predicted by Different Rheological Models.

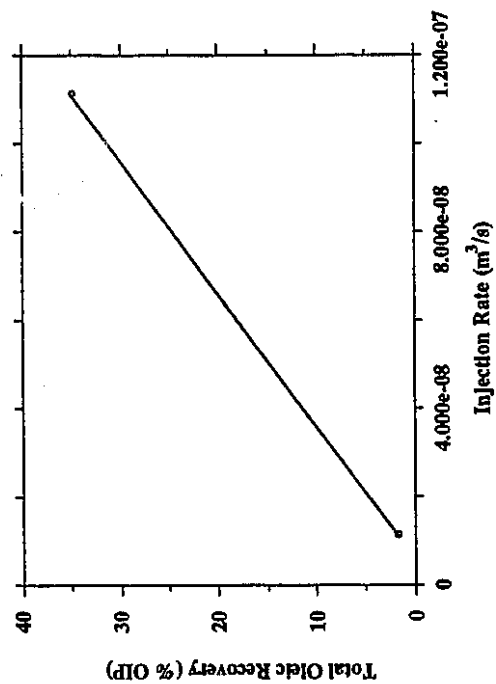


Fig. 7.101 Sensitivity of Total Oleic Recovery to Injection Rate.

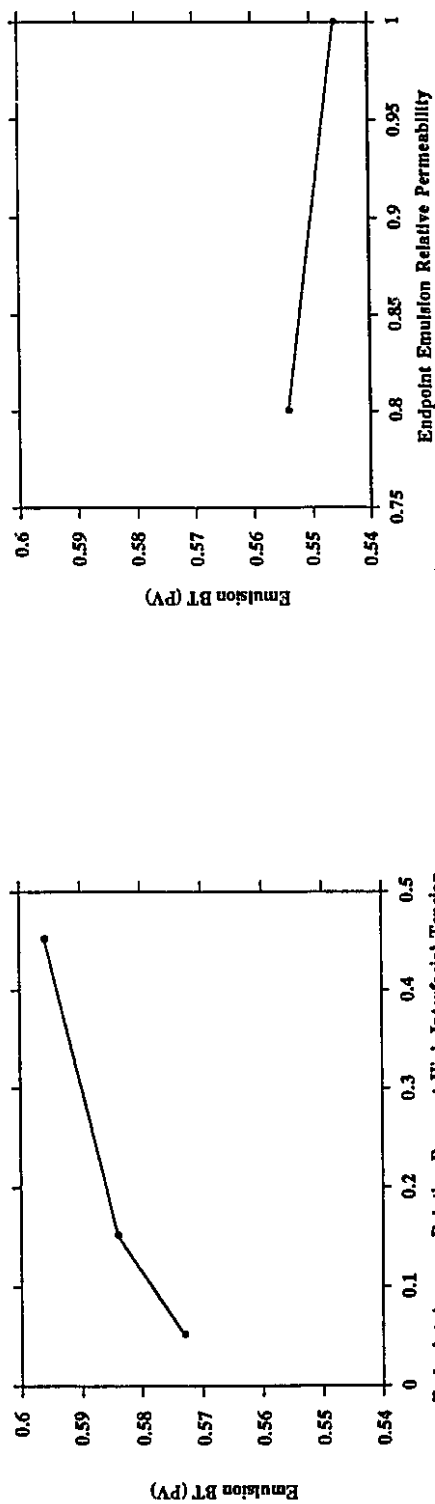


Fig. 7.102 Sensitivity of Emulsion Breakthrough Time to Endpoint Aqueous Relative Permeability at High Interfacial Tension.

Fig. 7.103 Sensitivity of Emulsion Breakthrough Time to Endpoint Emulsion Relative Permeability.

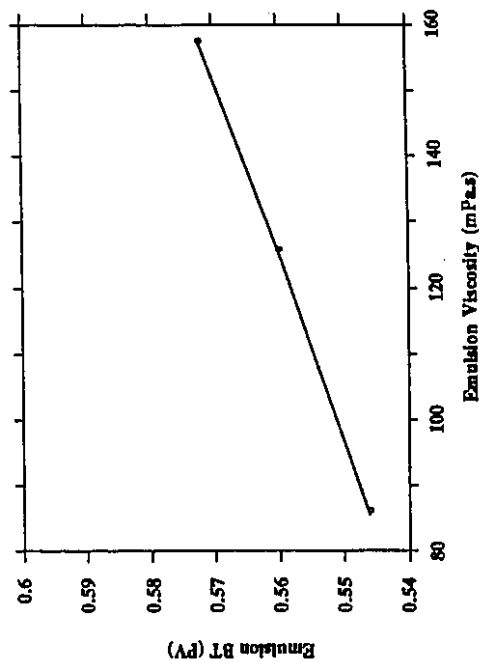


Fig. 7.104 Sensitivity of Emulsion Breakthrough Time to Emulsion Viscosity Predicted by Single-phase Non-Newtonian Correlation.

relative permeability permits the emulsion to move through the porous medium more easily. Therefore, it allows the emulsion to break through sooner, as is the case in Fig. 7.103. In addition, the expected trend in the emulsion breakthrough time is observed when the emulsion viscosity is increased. That is, a more viscous emulsion appears to be a more effective displacing fluid due to a lower emulsion mobility, a later breakthrough time, and a higher displacement efficiency (Fig. 7.104).

It should be noted that the degree of sensitivity of the injection pressure and the emulsion breakthrough time to the emulsion viscosity is about the same. Similarly, the sensitivities of the injection pressure, the cumulative oleic recovery, and the emulsion breakthrough time to the end-point emulsion relative permeability are about the same. In conclusion, the model developed gives results indicating that the physical properties and mechanisms involved in the displacement are modeled in a consistent manner.

8. CONCLUSIONS

The present study investigated the physical mechanisms when stable emulsion flows in a porous medium. These physical properties were then modeled and incorporated into a three-phase simulator. Finally, the simulator developed was tested by simulating a linear laboratory core flood using a stable emulsion. A variety of effects were examined. The following conclusions were reached based on the system studied.

1. The study of emulsion rheology shows that the rheology of an emulsion during flow in a porous medium varies while the rheology in a viscometer is consistent over the same range of shear rates for a system in which the drop sizes are comparable to the pore throat sizes. However, the overall trend shows a similarity between the rheologies when the same emulsion flows in the porous medium and in a viscometer. It is speculated that the change of emulsion quality in the pores due to droplet capture causes this effect, while the emulsion quality remains the same throughout flow in a viscometer.
2. An improved filtration model describing emulsion droplet capture in a porous medium, for both oil-in-water and water-in-oil emulsions at various mean drop size to mean pore size ratios, was developed.
3. Experiments were carried out in two types of porous media, using a series of emulsions. The production data for the

oil recovery experiments in the present study show that the emulsions used were stable enough so that there were always three phases in the system with a constant distribution of each component among phases.

4. The three-phase emulsion flood simulator incorporating various physical property models, predicted the production history with a trend similar to the experimental observations. The best production data predictions were obtained when a multiphase non-Newtonian rheological model, relative permeability model incorporating interfacial tension effects, and a time-dependent droplet capture model were used to describe emulsion rheology, three-phase relative permeabilities, and the droplet capture mechanism, respectively.
5. The sensitivity study provided information on the trends of selected process variables as the parameters controlling the investigated properties and mechanisms were varied.

REFERENCES

1. Becher, P.: Emulsions: Theory and Practice, 2nd ed., Reinhold Publishing Corp., New York (1965).
2. Alvarado, D.A.: "The Flow of Macroemulsions Through Porous Media," Ph.D. Dissertation, Department of Petroleum Engineering, Stanford University, Stanford, California (1975).
3. Egbogah, E.O.: "Interfacial Properties of Heavy Crudes in the Presence of Chemically Treated Waters," M.Sc. thesis, Department of Mineral Engineering, University of Alberta, Edmonton, Alberta (1975).
4. Flock, D.L., and Tharin, J.: "Unconventional Methods of Recovery of Bitumen and Related Research Areas Particular to the Oil Sands of Alberta," J. Can. Pet. Tech. (July-Sept. 1975) Vol. 14, No. 3, 17-27.
5. Strassner, J.E.: "Effect of pH on Interfacial Films and Stability of Crude Oil-Water Emulsions," J. Pet. Tech. (1969) 303-312.
6. Peak, E., and Hodgson, G.W.: "Alkanes in Aqueous Systems I. Exploratory Investigation on the Accommodation of C₂₀-C₃₃ n-Alkanes in Distilled Water and Occurences in Natural Water Systems," J. Am. Oil Chem. Society (1966) Vol. 43, 215-222.
7. Cash, Jr., R.L., Cayias, J.L., Hayes, J., MacAllister, D.J., and Schares, T.: "Spontaneous Emulsification - A Possible Mechanism for Enhanced Oil Recovery," paper presented at the 50th Annual Fall Meeting of the Society of AIME, Dallas, Texas, Sept. 28 - Oct. 1, 1975.
8. King, R.W.: "Heavy Oil Emulsion Rheology," M.Sc. thesis, Department of Mineral Engineering, University of Alberta, Edmonton, Alberta (1985).
9. Counsil, J.R.: "The Production and Transportation of Crude Oil as a Suspension in Water," Engineer's Thesis, Stanford University, Stanford, California (Dec. 1972) (cited in Ref. 39).

10. Marsden, Jr., S.S., and Raghavan, R.: "A System for Producing and Transporting Crude Oil as an Oil/Water Emulsion," J. Inst. Pet. (Nov. 1973) 273-278.
11. DesBrisay, C.M., Mudie, D.W., Mourits, F.M., and Kurucz, L.: "Pumping Heavy Oils with the Aid of Downhole Oil-in-Water Emulsification," Petroleum Society of CIM, paper no. 87-38-16, presented at the 38th Annual Technical Meeting of the Petroleum Society of CIM, Calgary, June 7-10, 1987.
12. Jennings, R.R., Rogers, J.H., and West, T.J.: "Oil Recovery by Alkaline Waterflooding," J. Pet. Tech. (1974) 1344-1374.
13. Chung, K.H., and Butler, R.M.: "Geometrical Effect of Steam Injection on the Formation of Emulsions in the Steam-Assisted Gravity Drainage Process," Petroleum Society of CIM, paper no. 87-38-22, presented at the 38th Annual Technical Meeting of the Petroleum Society of CIM, Calgary, June 7-10, 1987.
14. Chung, K.H., and Butler, R.M.: "In-situ Emulsification by the Condensation of Steam in Contact with Bitumen," Petroleum Society of CIM, paper no. 88-39-18, presented at the 39th Annual Technical Meeting of the Petroleum Society of CIM, Calgary, June 12-16, 1988.
15. Chen, T., Chakrabarty, T., Cullen, M.P., Thomas, R.R., and Sieben, M.C.: "Laboratory and Field Evidence of Emulsion Flow in Porous Media," Petroleum Society of CIM and AOSTRA, paper no. CIM/AOSTRA 91-78, presented at the CIM/AOSTRA 1991 Technical Conference, Banff, Alberta, April 21-24, 1991.
16. Binder, Jr., G.O., Clark, N.J., and Russell, C.D.: "Method of Secondary Recovery," U.S. Patent No. 3,203,517 (Sept. 28, 1965) (cited in Ref. 2).
17. Gogarty, W.B.: "Recovery of Petroleum by Displacement with Miscible Fluids," U.S. Patent No. 3,266,570 (Aug. 16, 1966) (cited in Ref. 2).
18. Hardy, W.C., and McArthur, B.W.: "Secondary Recovery of Petroleum Using LPG-Aqueous Liquid Emulsions," U.S. Patent No. 3,330,348 (July 11, 1967) (cited in Ref. 2).

19. Gogarty, W.B., and Tosch, W.C.: "Miscible-Type Waterflooding: Oil Recovery with Micellar Solutions," J. Pet. Tech. (Dec. 1968) 1407-1414.
20. Cartmill, J.C.: "Flow of a Disperse Emulsion of Crude Oil in Water in Porous Media," paper SPE 2881, presented at the 44th Annual Fall Meeting of the SPE of AIME, Denver, Colorado, Sept. 28 - Oct. 1, 1969.
21. Uzoigwe, A.C., and Marsden, Jr., S.S.: "Emulsion Rheology and Flow Through Unconsolidated Synthetic Porous Media," paper SPE 3004, presented at SPE-AIME 45th Annual Fall Meeting, Houston, Texas, Oct. 4-7, 1970.
22. McAuliffe, C.D.: "Oil-in-Water Emulsions and Their Flow Properties in Porous Media," J. Pet. Tech. (June 1973) 727-733.
23. McAuliffe, C.D.: "Crude-Oil-in-Water Emulsions to Improve Fluid Flow in an Oil Reservoir," J. Pet. Tech. (June 1973) 721-726.
24. Cooke, C.E., Williams, R.E., and Kolodzie, P.A.: "Oil Recovery by Alkaline Waterflooding," J. Pet. Tech. (Dec. 1974) 1365-1374.
25. Johnson, Jr., C.E.: "Status of Caustic and Emulsion Methods," J. Pet. Tech. (Jan. 1976) 85-92.
26. Radke, C.J., and Somerton, W.H.: "Enhanced Recovery with Mobility and Reactive Tension Agents," Fifth DOE Symposium on Enhanced Oil and Gas Recovery and Improved Drilling Methods," Vol. 1, Tulsa, Aug. 22-24, 1979.
27. Soo, H., and Radke, C.J.: "The Flow Mechanisms of Dilute, Stable Emulsions in Porous Media," Ind. Eng. Chem. Fund. (1984) 342-347.
28. Soo, H., and Radke, C.J.: "Flow of Dilute, Stable Liquid and Solid Dispersions in Underground Porous Media," AIChE Journal, (Nov. 1985) Vol. 31, No. 11, 1926-1928.
29. Schmidt, D.P., Soo, H., and Radke, C.J.: "Linear Oil Displacement by the Emulsion Entrapment Process," Soc. Pet. Eng. J. (June 1984) 351-360.

30. French, T.R., Broz, J.S., Lorenz, P.B., and Bertus, K.H.: "Use of Emulsions for Mobility Control During Steamflooding," paper presented at the 56th California Regional Meeting of the SPE, Oakland, California, April 2-4, 1986.
31. Islam, M.R.: "Mobility Control in Reservoirs with Bottom Water," Ph.D. Thesis, Department of Mining, Metallurgy and Petroleum Engineering, University of Alberta, Edmonton, Alberta (1987).
32. Islam, M.R., and Farouq Ali, S.M.: "Waterflooding Oil Reservoirs with Bottom Water," paper no. 87-38-26, presented at the 38th Annual Technical Meeting of the Petroleum Society of CIM, Calgary, Alberta, June 7-10, 1987.
33. Islam, M.R., and Farouq Ali, S.M.: "An Experimental and Numerical Study of Blocking of a Mobile Water Zone by an Emulsion," paper 133, presented at the Fourth UNITAR/UNDP Conference on Heavy Crude and Tar Sands, 1987.
34. Islam, M.R., and Farouq Ali, S.M.: "The Use of Oil/Water Emulsions as a Blocking and Diverting Agent," Paper 5, Session 1, presented at the Advances in Petroleum Recovery and Upgrading Technology Conference, 1987.
35. Yeung, K.: "Mobility Control by Emulsions Under Bottom Water Conditions," M.Sc. Thesis, Department of Mining, Metallurgy and Petroleum Engineering, University of Alberta, Edmonton, Alberta (1991).
36. Yeung, K., and Farouq Ali, S.M.: "Waterflooding Bottom Water Formations Using the Dynamic Blocking Method," Petroleum Society of CIM and AOSTRA, paper no. CIM/AOSTRA 91-55, presented at the CIM/AOSTRA Technical Conference, Banff, Alberta, April 21-24, 1991.
37. Mendoza, H., Thomas, S., and Farouq Ali, S.M.: "Effect of Injection Rate on Emulsion Flooding for a Canadian and a Venezuelan Crude Oil," Petroleum Society of CIM/AOSTRA Technical Conference, Banff, Alberta, April 21-24, 1991.
38. Fiori, M., and Farouq Ali, S.M.: "Optimal Emulsion Design for the Recovery of a Saskatchewan Crude," J. of Can. Pet. Tech. (March-April 1991) 123-132.

39. Alvarado, D.A., and Marsden, Jr., S.S.: "Flow of Oil-in-Water Emulsions Through Tubes and Porous Media," Soc. Pet. Eng. J. (Dec. 1979) 369-377.
40. Devereux, O.F.: "Emulsion Flow in Porous Solids I. A Flow Model," Chem. Eng. J. (1974) 121-128.
41. Devereux, O.F.: "Emulsion Flow in Porous Solids II. Experiments with a Crude Oil-in-Water Emulsion in Porous Sandstone," Chem. Eng. J. (1974) 129-136.
42. Soo, H.: "Flow of Dilute, Stable Emulsions in Porous Media," Ph.D. Dissertation, Department of Chemical Engineering, University of California, Berkeley, California (1983).
43. Abou-Kassem, J.H., and Farouq Ali, S.M.: "Evaluation of Emulsion Flow in Porous Media," submitted for publication to SPERE (1991).
44. Abou-Kassem, J.H., and Farouq Ali, S.M.: "Mathematical Representation of Single-Phase Emulsion Flow in Porous Media," submitted for publication to SPERE (1991).
45. Farouq Ali, S.M., and Abou-Kassem, J.H.: "Modelling of Emulsion Flow in Porous Media," paper no. CIM/SPE 90-97, presented at the International Technical Meeting of CIM/SPE, Calgary, Alberta, June 10-13, 1990.
46. Soo, H., and Radke, C.J.: "Velocity Effects in Emulsion Flow Through Porous Media," J. Coll. Int. Sci. (1984) 462-476.
47. Soo, H., and Radke, C.J.: "A Filtration Model for the Flow of Dilute, Stable Emulsions in Porous Media I. Theory," Chem. Eng. Sci. (1986) 263-272.
48. Soo, H., Williams, M.C., and Radke, C.J.: "A Filtration Model for the Flow of Dilute, Stable Emulsions in Porous Media II. Parameter Evaluation and Estimation," Chem. Eng. Sci. (1986) 273-281.
49. Islam, M.R., and Farouq Ali, S.M.: "Numerical Simulation of Emulsion Flow Through Porous Media," paper no. 89-40-63, presented at the 40th Annual Technical Meeting of the Petroleum Society of CIM, Banff, Alberta, May 28-31, 1989.

50. Coats, K.H., George, W.D., Chu, C., and Marcum, B.E.: "Three-Dimensional Simulation of Steamflooding," Soc. Pet. Eng. J., (Dec. 1974), 573.
51. Farouq Ali, S.M. and Ferrer, J.: "A Three-Phase, Two-Dimensional Compositional Thermal Simulator for Steam Injection Processes", J. Can. Pet. Tech. (Jan.-Mar. 1977) 1-13.
52. Al-Seehati, S.A.: "Numerical Simulation of the Micellar-Polymer Slug Process for a One-Dimensional Two-Phase and Four-Component System with Interphase Mass Transfer," Ph.D. Dissertation, Pennsylvania State University, University Park, Pennsylvania (Aug. 1979).
53. Pope, G.A., and Nelson, R.C.: "A Chemical Flooding Compositional Simulator," Soc. Pet. Eng. J. (Oct. 1978) 339-354.
54. Pope, G.A., Wang, B., and Tsaur, K.: "A Sensitivity Study of Micellar/Polymer Flooding," Soc. Pet. Eng. J. (Dec. 1979) 357-368.
55. Camilleri, D.: "Micellar/Polymer Flooding Experiments and Comparison with an Improved One-Dimensional Simulator," M.Sc. Thesis, University of Texas at Austin, Austin, Texas (May 1983).
56. Camilleri, D., Engelsen, S., Lake, L.W., Lin, E.C., Ohno, T., Pope, G., and Sepehrnoori, K.: "Description of an Improved Compositional Micellar/Polymer Simulator," SPERE (Nov. 1987) 427-432.
57. Camilleri, D., Fil, A., Pope, G.A., Rouse, B.A., and Sepehrnoori, K.: "Improvements in Physical-Property Models Used in Micellar/Polymer Flooding," SPERE (Nov. 1987) 433-440.
58. Camilleri, D., Fil, A., Pope, G.A., Rouse, B.A., and Sepehrnoori, K.: "Comparison of an Improved Compositional Micellar/Polymer Simulator with Laboratory Corefloods," SPERE (Nov. 1987) 441-451.
59. Farouq Ali, S.M., Thomas, S., and Khambharatana, F.: "Formation and Flow of Emulsions in Porous Media," Final Report AOSTRA Contract 493, June 1, 1986 - June 30, 1988.
60. Farouq Ali, S.M.: Elements of Reservoir Modelling, University of Alberta, 1989.

61. Craft, B.C., Holden, W.R., and Graves, Jr., E.D.: Well Design: Drilling and Production, Prentice-Hall, Inc., Englewood Cliffs, New Jersey (1962).
62. Solutions to Sticky Problems, Manual, Brookfield Viscometer, Brookfield Engineering Laboratories, Inc.
63. Personal Communication with Dr. M.C. Williams.

APPENDIX A

**ESTIMATION OF THE PARTITION COEFFICIENTS OF EACH
COMPONENT BETWEEN PHASES**

A.1 Sequence of Injection

Core flood #24: 10% PV of H4 followed by waterflooding.

A.2 Composition of Injected Emulsion H4

Component	Density (g/ml)	% Weight
Horsefly Crude Oil	0.886	41
1% NaCl	1.004	50
SD1000	1.127	9

**A.3 Analysis of the Aqueous Phase During Waterflooding for
Surfactant Content**

One millilitre of the effluent was first diluted to 100 ml in a volumetric flask. The sample was then analyzed for surfactant content using the UV Spectrophotometer. The following data were collected during the waterflood in core flood #24.

Sample No.	Volume (ml)	Type	Effluent Wt. (g)	Surf. Conc. (g/ml)	Total Surf. Wt. (g)	Wt. Fraction of Surf. in Effluent
1	2000	Emulsion + Brine	1922	29.5×10^{-3}	5.9	0.0031
2	1000	Brine	1004	0.19×10^{-3}	0.19	0.0002
3	500	Brine	502	0.08×10^{-3}	0.04	0.0001

A.4 Calculation of the Partition Coefficient

Using the above data, it is found that

$$K_{sam} = \frac{w_{sa}}{w_{sm}} = 0.0484.$$

It is assumed that the amount of surfactant that transfers to the aqueous phase is low enough so that the amount of oil which can dissolve in the aqueous phase is negligible. That is, no oil is transferred from the emulsion phase to the aqueous phase. Hence,

$$K_{oam} = 0.0.$$

The following table shows the weight fraction of water in each sample of effluent for core flood #24.

Sample No.	Type	Total Wt. of Water (g)	Wt. Fraction of Water in Effluent
1	Emulsion + Brine	1128	0.5869
2	Brine	1004	0.9998
3	Brine	502	0.9999

Using the assumption that $K_{oam} = 0.0$, the weights of water in the aqueous and emulsion phases can be calculated. Thus,

$$K_{wam} = \frac{w_{wa}}{w_{wm}} = 1.7037.$$

Since surfactant SD1000 is hydrophilic, it is assumed that the surfactant only dissolves in the aqueous phase. This means that the only oil present is in the oleic phase. Hence,

$$K_{olm} = 2.439, K_{wlm} = 0, \text{ and } K_{slm} = 0.$$

APPENDIX B

MATHEMATICAL DEVELOPMENT OF FLOW EQUATIONS

The mass balance equations for each component can be written as follows:

$$\begin{aligned}
 & \frac{\partial}{\partial x} \left(C_{il} \rho_l A_x k_x \frac{k_{rl}}{\mu_l} \frac{\partial \Phi_l}{\partial x} + C_{ia} \rho_a A_x k_x \frac{k_{ra}}{\mu_a} \frac{\partial \Phi_a}{\partial x} + C_{im} \rho_m A_x k_x \frac{k_{rm}}{\mu_m} \frac{\partial \Phi_m}{\partial x} \right) \Delta x \\
 & + \frac{\partial}{\partial x} \left[A_x \phi D_{il} \frac{\partial}{\partial x} (\rho_l C_{il}) + A_x \phi D_{ia} \frac{\partial}{\partial x} (\rho_a C_{ia}) + A_x \phi D_{im} \frac{\partial}{\partial x} (\rho_m C_{im}) \right] \Delta x \\
 & + \frac{\partial}{\partial y} \left(C_{il} \rho_l A_y k_y \frac{k_{rl}}{\mu_l} \frac{\partial \Phi_l}{\partial y} + C_{ia} \rho_a A_y k_y \frac{k_{ra}}{\mu_a} \frac{\partial \Phi_a}{\partial y} + C_{im} \rho_m A_y k_y \frac{k_{rm}}{\mu_m} \frac{\partial \Phi_m}{\partial y} \right) \Delta y \\
 & + \frac{\partial}{\partial y} \left[A_y \phi D_{il} \frac{\partial}{\partial y} (\rho_l C_{il}) + A_y \phi D_{ia} \frac{\partial}{\partial y} (\rho_a C_{ia}) + A_y \phi D_{im} \frac{\partial}{\partial y} (\rho_m C_{im}) \right] \Delta y \\
 & + \frac{\partial}{\partial z} \left(C_{il} \rho_l A_z k_z \frac{k_{rl}}{\mu_l} \frac{\partial \Phi_l}{\partial z} + C_{ia} \rho_a A_z k_z \frac{k_{ra}}{\mu_a} \frac{\partial \Phi_a}{\partial z} + C_{im} \rho_m A_z k_z \frac{k_{rm}}{\mu_m} \frac{\partial \Phi_m}{\partial z} \right) \Delta z \\
 & + \frac{\partial}{\partial z} \left[A_z \phi D_{il} \frac{\partial}{\partial z} (\rho_l C_{il}) + A_z \phi D_{ia} \frac{\partial}{\partial z} (\rho_a C_{ia}) + A_z \phi D_{im} \frac{\partial}{\partial z} (\rho_m C_{im}) \right] \Delta z \\
 & + Q_i^* (\text{kg}_i / \text{sec}) = ACC_i \quad \text{for } i = o, w, s, \quad (B.1)
 \end{aligned}$$

where Q_i^* is the mass flow rate of component i (positive value for injection and negative value for production) and ACC_i is the accumulation term of component i which is defined in Appendix C.

The above equation may be re-written as

$$\begin{aligned}
 & \nabla \cdot \left(\rho_l C_{il} A k \frac{k_{rl}}{\mu_l} \nabla \Phi_l \right) \Delta + \nabla \cdot \left(\rho_a C_{ia} A k \frac{k_{ra}}{\mu_a} \nabla \Phi_a \right) \Delta \\
 & + \nabla \cdot \left(\rho_m C_{im} A k \frac{k_{rm}}{\mu_m} \nabla \Phi_m \right) \Delta + \nabla \cdot [A \phi D_{il} \nabla (\rho_l C_{il})] \Delta \\
 & + \nabla \cdot [A \phi D_{ia} \nabla (\rho_a C_{ia})] \Delta + \nabla \cdot [A \phi D_{im} \nabla (\rho_m C_{im})] \Delta + Q_i^* \\
 & = ACC_i, \quad (B.2)
 \end{aligned}$$

or, by substituting $\eta_j = Ak \frac{k_j}{\mu_j}$, as

$$\begin{aligned} & \nabla \cdot (\rho_l C_{il} \eta_l \nabla \Phi_l) \Delta + \nabla \cdot (\rho_a C_{ia} \eta_a \nabla \Phi_a) \Delta + \nabla \cdot (\rho_m C_{im} \eta_m \nabla \Phi_m) \Delta \\ & + \nabla \cdot [A \phi D_{il} \nabla (\rho_l C_{il})] \Delta + \nabla \cdot [A \phi D_{ia} \nabla (\rho_a C_{ia})] \Delta \\ & + \nabla \cdot [A \phi D_{im} \nabla (\rho_m C_{im})] \Delta + Q_i^* = ACC_i. \end{aligned} \quad (B.3)$$

After writing Φ implicitly and transmissibility at the n th time level, the resulting expressions can be added and subtracted in order to write Φ in terms of $\delta\Phi$ and produce the following:

$$\begin{aligned} & \nabla \cdot [(\rho_l C_{il} \eta_l)^n \nabla \delta\Phi_l] \Delta + \nabla \cdot [(\rho_a C_{ia} \eta_a)^n \nabla \delta\Phi_a] \Delta \\ & + \nabla \cdot [(\rho_m C_{im} \eta_m)^n \nabla \delta\Phi_m] \Delta + Q_i^{*n+1} + \nabla \cdot [(\rho_l C_{il} \eta_l)^n \nabla \Phi_l^n] \Delta \\ & + \nabla \cdot [(\rho_a C_{ia} \eta_a)^n \nabla \Phi_a^n] \Delta + \nabla \cdot [(\rho_m C_{im} \eta_m)^n \nabla \Phi_m^n] \Delta \\ & + \nabla \cdot [A \phi D_{il} \nabla (\rho_l C_{il})]^n \Delta + \nabla \cdot [A \phi D_{ia} \nabla (\rho_a C_{ia})]^n \Delta \\ & + \nabla \cdot [A \phi D_{im} \nabla (\rho_m C_{im})]^n \Delta = ACC_i. \end{aligned} \quad (B.4)$$

Substituting the expressions,

$$\Phi_l = p_l - \rho_l g D, \quad (B.5)$$

$$\Phi_a = p_a - \rho_a g D, \quad (B.6)$$

$$\Phi_m = p_m - \rho_m g D, \quad (B.7)$$

$$P_{cla} = p_l - p_a, \quad (B.8)$$

and

$$P_{clm} = p_l - p_m, \quad (B.9)$$

into (B.4), the following equation arises:

$$\begin{aligned}
& \nabla \cdot [(\rho_l C_{il} \eta_l)^n \nabla \delta p_l] \Delta + \nabla \cdot [(\rho_a C_{ia} \eta_a)^n \nabla \delta p_i] \Delta \\
& + \nabla \cdot [(\rho_m C_{im} \eta_m)^n \nabla \delta p_i] \Delta + Q_i^{*n+1} - \nabla \cdot [(\rho_l C_{il} \eta_l)^n \nabla \delta(\rho_l g D)] \Delta \\
& - \nabla \cdot [(\rho_a C_{ia} \eta_a)^n \nabla \delta(P_{cla} + \rho_a g D)] \Delta \\
& - \nabla \cdot [(\rho_m C_{im} \eta_m)^n \nabla \delta(P_{clm} + \rho_m g D)] \Delta \\
& + \nabla \cdot [(\rho_l C_{il} \eta_l)^n \nabla \Phi_l^n] \Delta + \nabla \cdot [(\rho_a C_{ia} \eta_a)^n \nabla \Phi_a^n] \Delta \\
& + \nabla \cdot [(\rho_m C_{im} \eta_m)^n \nabla \Phi_m^n] \Delta + \nabla \cdot [A \phi D_{il} \nabla(\rho_l C_{il})]^n \Delta \\
& + \nabla \cdot [A \phi D_{ia} \nabla(\rho_a C_{ia})]^n \Delta + \nabla \cdot [A \phi D_{im} \nabla(\rho_m C_{im})]^n \Delta = ACC_i. \quad (B.10)
\end{aligned}$$

This may be re-written as

$$ACC_i = \nabla \cdot [T_{il} + T_{ia} + T_{im}]^n \nabla \delta p_i \Delta + Q_i^{*n+1} + R_i, \quad (B.11)$$

where

$$T_{il} = \rho_l C_{il} \eta_l,$$

$$T_{ia} = \rho_a C_{ia} \eta_a,$$

$$T_{im} = \rho_m C_{im} \eta_m,$$

and

$$\begin{aligned}
R_i = & -\nabla \cdot [T_{il}^n \nabla \delta(\rho_l g D)] \Delta - \nabla \cdot [T_{ia}^n \nabla \delta(P_{cla} + \rho_a g D)] \Delta \\
& - \nabla \cdot [T_{im}^n \nabla \delta(P_{clm} + \rho_m g D)] \Delta + \nabla \cdot (T_{il}^n \nabla \Phi_l^n) \Delta + \nabla \cdot (T_{ia}^n \nabla \Phi_a^n) \Delta \\
& + \nabla \cdot (T_{im}^n \nabla \Phi_m^n) \Delta + \nabla \cdot [A \phi D_{il} \nabla(\rho_l C_{il})]^n \Delta + \nabla \cdot [A \phi D_{ia} \nabla(\rho_a C_{ia})]^n \Delta \\
& + \nabla \cdot [A \phi D_{im} \nabla(\rho_m C_{im})]^n \Delta. \quad (B.12)
\end{aligned}$$

APPENDIX C
EXPANSION OF THE ACCUMULATION TERMS IN THE MASS
BALANCE EQUATION

The accumulation terms for each component are described by

$$ACC_o = V_b \frac{\partial}{\partial t} [\phi (C_{oi} \rho_i S_i + C_{oa} \rho_a S_a + C_{om} \rho_m S_m) + \rho_o \sigma], \quad (C.1)$$

for o/w emulsions,

$$ACC_w = V_b \frac{\partial}{\partial t} [\phi (C_{wi} \rho_i S_i + C_{wa} \rho_a S_a + C_{wm} \rho_m S_m) + \rho_w \sigma], \quad (C.2)$$

for w/o emulsions, and

$$ACC_s = V_b \frac{\partial}{\partial t} [\phi (C_{si} \rho_i S_i + C_{sa} \rho_a S_a + C_{sm} \rho_m S_m) + \frac{\rho_r A_d (1 - \phi) \rho_m C_{sm}}{1 + B_d C_{sm}}]. \quad (C.3)$$

The common terms (FLU_i) in the three previous equations can be re-written as

$$\begin{aligned} FLU_i &= V_b \frac{\partial}{\partial t} [\phi (C_{ii} \rho_i S_i + C_{ia} \rho_a S_a + C_{im} \rho_m S_m)] \\ &= \frac{V_b}{\Delta t} \delta(\phi C_{ii} \rho_i S_i) + \frac{V_b}{\Delta t} \delta(\phi C_{ia} \rho_a S_a) + \frac{V_b}{\Delta t} \delta(\phi C_{im} \rho_m S_m) \\ &= Ol_i + Aq_i + Em_i. \end{aligned} \quad (C.4)$$

For an instantaneous droplet capture, the capture term ($CAPT_i$) in (C.1) and (C.2) is developed as

$$\begin{aligned}
CAPT_i &= V_b \frac{\partial}{\partial t}(\rho_i \sigma) = V_b \frac{\partial}{\partial t} \left[\rho_i \left(\frac{A_c \frac{\rho_m C_{im}}{\rho_i}}{1 + B_c \frac{\rho_m C_{im}}{\rho_i}} \right) \right] = V_b \frac{\partial}{\partial t} \left[\rho_i \left(\frac{A_c \rho_m C_{im}}{\rho_i + B_c \rho_m C_{im}} \right) \right] \\
&= \frac{V_b}{\Delta t} \frac{\rho_i^2 A_c}{(\rho_i + B_c \rho_m C_{im})^2} \delta(\rho_m C_{im}). \quad (C.5)
\end{aligned}$$

The adsorption term ($ADSP_s$) in (C.3) can be re-written as

$$ADSP_s = V_b \frac{\partial}{\partial t} \left[\frac{\rho_r A_d (1 - \phi) \rho_m C_{sm}}{1 + B_d \rho_m C_{sm}} \right] = \frac{V_b}{\Delta t} \frac{\rho_r A_d (1 - \phi_{init})}{(1 + B_d \rho_m C_{sm})^2} \delta(\rho_m C_{sm}). \quad (C.6)$$

C.1 Expansion of the Common Flowing (FLU_i) Terms

The term Ol_i in (C.4) is further developed as follows:

$$\begin{aligned}
Ol_i &= \frac{V_b}{\Delta t} \delta(\phi C_{il} \rho_l S_l) = \frac{V_b}{\Delta t} [(\phi C_{il} \rho_l S_l)^{n+1} - (\phi C_{il} \rho_l S_l)^n] \\
&= \frac{V_b}{\Delta t} [(\phi \rho_l S_l)^{n+1} \delta C_{il} + C_{il}^n \delta(\phi \rho_l S_l)] \\
&= \frac{V_b}{\Delta t} \left\{ (\phi \rho_l S_l)^{n+1} \delta C_{il} + C_{il}^n [(\phi \rho_l)^{n+1} \delta S_l + S_l^n \delta(\phi \rho_l)] \right\} \\
&= \frac{V_b}{\Delta t} [(\phi \rho_l S_l)^{n+1} \delta C_{il} + C_{il}^n (\phi \rho_l)^{n+1} \delta S_l + C_{il}^n S_l^n (\phi^{n+1} \delta \rho_l + \rho_l^n \delta \phi)] \\
&= \frac{V_b}{\Delta t} [(\phi \rho_l S_l)^{n+1} \delta C_{il} + C_{il}^n (\phi \rho_l)^{n+1} \delta S_l + (C_{il} \rho_l S_l)^n \delta \phi \\
&\quad + (C_{il} S_l)^n \phi^{n+1} \delta \rho_l]. \quad (C.7)
\end{aligned}$$

Using the definitions,

$$\delta \phi = \left(\frac{\phi^{n+1} - \phi^n}{\rho_l^{n+1} - \rho_l^n} \right) \delta \rho_l = \phi' \delta \rho_l, \quad (C.8)$$

$$\delta \rho_l = \left(\frac{\rho_l^{n+1} - \rho_l^n}{C_{ol}^{n+1} - C_{ol}^n} \right) \delta C_{ol} + \left(\frac{\rho_l^{n+1} - \rho_l^n}{C_{wl}^{n+1} - C_{wl}^n} \right) \delta C_{wl} + \left(\frac{\rho_l^{n+1} - \rho_l^n}{C_{sl}^{n+1} - C_{sl}^n} \right) \delta C_{sl}, \quad (C.9)$$

and

$$\delta S_l + \delta S_a + \delta S_m = 0, \quad (\text{C.10})$$

substitutions are made into (C.7), giving

$$\begin{aligned} Ol_o = & \frac{V_b}{\Delta t} \phi^{n+1} \left[(\rho_l S_l)^{n+1} + (C_{ol} S_l)^n \left(\frac{\rho_l^{n+1} - \rho_l^n}{C_{ol}^{n+1} - C_{ol}^n} \right) \right] \delta C_{ol} \\ & + \frac{V_b}{\Delta t} \phi^{n+1} \left[(C_{ol} S_l)^n \left(\frac{\rho_l^{n+1} - \rho_l^n}{C_{wl}^{n+1} - C_{wl}^n} \right) \right] \delta C_{wl} \\ & + \frac{V_b}{\Delta t} \phi^{n+1} \left[(C_{ol} S_l)^n \left(\frac{\rho_l^{n+1} - \rho_l^n}{C_{sl}^{n+1} - C_{sl}^n} \right) \right] \delta C_{sl} + \frac{V_b}{\Delta t} \phi^{n+1} (C_{ol}^n \rho_l^{n+1}) \delta S_l \\ & + \frac{V_b}{\Delta t} (C_{ol} \rho_l S_l)^n \phi' \delta p_l, \end{aligned} \quad (\text{C.11})$$

$$\begin{aligned} Ol_w = & \frac{V_b}{\Delta t} \phi^{n+1} \left[(C_{wl} S_l)^n \left(\frac{\rho_l^{n+1} - \rho_l^n}{C_{ol}^{n+1} - C_{ol}^n} \right) \right] \delta C_{ol} \\ & + \frac{V_b}{\Delta t} \phi^{n+1} \left[(\rho_l S_l)^{n+1} + (C_{wl} S_l)^n \left(\frac{\rho_l^{n+1} - \rho_l^n}{C_{wl}^{n+1} - C_{wl}^n} \right) \right] \delta C_{wl} \\ & + \frac{V_b}{\Delta t} \phi^{n+1} \left[(C_{wl} S_l)^n \left(\frac{\rho_l^{n+1} - \rho_l^n}{C_{sl}^{n+1} - C_{sl}^n} \right) \right] \delta C_{sl} \\ & + \frac{V_b}{\Delta t} \phi^{n+1} (C_{wl}^n \rho_l^{n+1}) \delta S_l + \frac{V_b}{\Delta t} (C_{wl} \rho_l S_l)^n \phi' \delta p_l, \end{aligned} \quad (\text{C.12})$$

and

$$\begin{aligned} Ol_s = & \frac{V_b}{\Delta t} \phi^{n+1} \left[(C_{sl} S_l)^n \left(\frac{\rho_l^{n+1} - \rho_l^n}{C_{ol}^{n+1} - C_{ol}^n} \right) \right] \delta C_{ol} \\ & + \frac{V_b}{\Delta t} \phi^{n+1} \left[(C_{sl} S_l)^n \left(\frac{\rho_l^{n+1} - \rho_l^n}{C_{wl}^{n+1} - C_{wl}^n} \right) \right] \delta C_{wl} \\ & + \frac{V_b}{\Delta t} \phi^{n+1} \left[(\rho_l S_l)^{n+1} + (C_{sl} S_l)^n \left(\frac{\rho_l^{n+1} - \rho_l^n}{C_{sl}^{n+1} - C_{sl}^n} \right) \right] \delta C_{sl} \\ & + \frac{V_b}{\Delta t} \phi^{n+1} (C_{sl}^n \rho_l^{n+1}) \delta S_l + \frac{V_b}{\Delta t} (C_{sl} \rho_l S_l)^n \phi' \delta p_l. \end{aligned} \quad (\text{C.13})$$

These three equations can be expressed in a more general form as

$$\begin{aligned}
 Ol_i = & \frac{V_b}{\Delta t} A_{ii} \delta C_{ii} + \frac{V_b}{\Delta t} B_{ii} \delta C_{1i} + \frac{V_b}{\Delta t} C_{ii} \delta C_{2i} + \frac{V_b}{\Delta t} \phi^{n+1} (C_{ii}^n \rho_i^{n+1}) \delta S_i \\
 & + \frac{V_b}{\Delta t} (C_{ii} \rho_i S_i)^n \phi' \delta p_i,
 \end{aligned} \tag{C.14}$$

where

$$A_{ii} = \phi^{n+1} \left[(\rho_i S_i)^{n+1} + (C_{ii} S_i)^n \left(\frac{\rho_i^{n+1} - \rho_i^n}{C_{ii}^{n+1} - C_{ii}^n} \right) \right],$$

$$B_{ii} = \phi^{n+1} \left[(C_{ii} S_i)^n \left(\frac{\rho_i^{n+1} - \rho_i^n}{C_{1i}^{n+1} - C_{1i}^n} \right) \right],$$

and

$$C_{ii} = \phi^{n+1} \left[(C_{ii} S_i)^n \left(\frac{\rho_i^{n+1} - \rho_i^n}{C_{2i}^{n+1} - C_{2i}^n} \right) \right] \quad \text{for} \quad \begin{cases} 1=w \text{ and } 2=s \text{ when } i=o \\ 1=o \text{ and } 2=s \text{ when } i=w. \\ 1=o \text{ and } 2=w \text{ when } i=s \end{cases}$$

To expand (C.14) further, the oleic phase constraint must be applied. It is known from this constraint that

$$K_{ilm} = \frac{C_{il}}{C_{im}}. \tag{C.15}$$

It therefore follows that

$$C_{il} = K_{ilm} C_{im}, \tag{C.16}$$

and thus

$$\begin{aligned}
\delta C_{il} &= \delta(K_{ilm} C_{im}) \\
&= K_{ilm}^{n+1} \delta C_{im} + C_{im}^n \delta K_{ilm} \\
&= K_{ilm}^{n+1} \delta C_{im} + C_{im}^n \left[\left(\frac{K_{ilm}^{n+1} - K_{ilm}^n}{C_{im}^{n+1} - C_{im}^n} \right) \delta C_{im} + \left(\frac{K_{ilm}^{n+1} - K_{ilm}^n}{C_{1m}^{n+1} - C_{1m}^n} \right) \delta C_{1m} \right. \\
&\quad \left. + \left(\frac{K_{ilm}^{n+1} - K_{ilm}^n}{C_{2m}^{n+1} - C_{2m}^n} \right) \delta C_{2m} \right].
\end{aligned} \tag{C.17}$$

Making the substitution,

$$\delta C_{2m} = -\delta C_{im} - \delta C_{1m}, \tag{C.18}$$

the next three equations follow:

$$\begin{aligned}
\delta C_{il} &= K_{ilm}^{n+1} \delta C_{im} + C_{im}^n \left\{ \left[\left(\frac{K_{ilm}^{n+1} - K_{ilm}^n}{C_{im}^{n+1} - C_{im}^n} \right) - \left(\frac{K_{ilm}^{n+1} - K_{ilm}^n}{C_{2m}^{n+1} - C_{2m}^n} \right) \right] \delta C_{im} \right. \\
&\quad \left. + \left[\left(\frac{K_{ilm}^{n+1} - K_{ilm}^n}{C_{1m}^{n+1} - C_{1m}^n} \right) - \left(\frac{K_{ilm}^{n+1} - K_{ilm}^n}{C_{2m}^{n+1} - C_{2m}^n} \right) \right] \delta C_{1m} \right\},
\end{aligned} \tag{C.19}$$

$$\begin{aligned}
\delta C_{il} &= K_{ilm}^{n+1} \delta C_{1m} + C_{1m}^n \left\{ \left[\left(\frac{K_{ilm}^{n+1} - K_{ilm}^n}{C_{im}^{n+1} - C_{im}^n} \right) - \left(\frac{K_{ilm}^{n+1} - K_{ilm}^n}{C_{2m}^{n+1} - C_{2m}^n} \right) \right] \delta C_{im} \right. \\
&\quad \left. + \left[\left(\frac{K_{ilm}^{n+1} - K_{ilm}^n}{C_{1m}^{n+1} - C_{1m}^n} \right) - \left(\frac{K_{ilm}^{n+1} - K_{ilm}^n}{C_{2m}^{n+1} - C_{2m}^n} \right) \right] \delta C_{1m} \right\},
\end{aligned} \tag{C.20}$$

and

$$\begin{aligned}
\delta C_{2l} &= K_{2lm}^{n+1} \delta C_{2m} + C_{2m}^n \left\{ \left[\left(\frac{K_{2lm}^{n+1} - K_{2lm}^n}{C_{im}^{n+1} - C_{im}^n} \right) - \left(\frac{K_{2lm}^{n+1} - K_{2lm}^n}{C_{2m}^{n+1} - C_{2m}^n} \right) \right] \delta C_{im} \right. \\
&\quad \left. + \left[\left(\frac{K_{2lm}^{n+1} - K_{2lm}^n}{C_{1m}^{n+1} - C_{1m}^n} \right) - \left(\frac{K_{2lm}^{n+1} - K_{2lm}^n}{C_{2m}^{n+1} - C_{2m}^n} \right) \right] \delta C_{1m} \right\}.
\end{aligned} \tag{C.21}$$

Substituting (C.19), (C.20), and (C.21) into (C.14) for δC_{il} , δC_{1l} , and δC_{2l} , it follows that

$$\begin{aligned}
Ol_i &= AA_{ii} \delta C_{im} + BB_{ii} \delta C_{1m} + \frac{V_b}{\Delta t} \phi^{n+1} (C_{ii}^n \rho_i^{n+1}) \delta S_i \\
&+ \frac{V_b}{\Delta t} (C_{ii}^n \rho_i S_i)^n \phi' \delta \rho_i,
\end{aligned} \tag{C.22}$$

where

$$\begin{aligned}
AA_{ii} &= \frac{V_b}{\Delta t} \left\{ A_{ii} \left[K_{ilm}^{n+1} + C_{im}^n \left(\frac{K_{ilm}^{n+1} - K_{ilm}^n}{C_{im}^{n+1} - C_{im}^n} - \frac{K_{ilm}^{n+1} - K_{ilm}^n}{C_{2m}^{n+1} - C_{2m}^n} \right) \right] \right. \\
&+ B_{ii} C_{1m}^n \left(\frac{K_{1lm}^{n+1} - K_{1lm}^n}{C_{im}^{n+1} - C_{im}^n} - \frac{K_{1lm}^{n+1} - K_{1lm}^n}{C_{2m}^{n+1} - C_{2m}^n} \right) \\
&\left. + C_{ii} \left[-K_{2lm}^{n+1} + C_{2m}^n \left(\frac{K_{2lm}^{n+1} - K_{2lm}^n}{C_{im}^{n+1} - C_{im}^n} - \frac{K_{2lm}^{n+1} - K_{2lm}^n}{C_{2m}^{n+1} - C_{2m}^n} \right) \right] \right\},
\end{aligned}$$

$$\begin{aligned}
BB_{ii} &= \frac{V_b}{\Delta t} \left\{ A_{ii} C_{im}^n \left(\frac{K_{ilm}^{n+1} - K_{ilm}^n}{C_{1m}^{n+1} - C_{1m}^n} - \frac{K_{ilm}^{n+1} - K_{ilm}^n}{C_{2m}^{n+1} - C_{2m}^n} \right) \right. \\
&+ B_{ii} \left[K_{1lm}^{n+1} + C_{1m}^n \left(\frac{K_{1lm}^{n+1} - K_{1lm}^n}{C_{1m}^{n+1} - C_{1m}^n} - \frac{K_{1lm}^{n+1} - K_{1lm}^n}{C_{2m}^{n+1} - C_{2m}^n} \right) \right] \\
&\left. + C_{ii} \left[-K_{2lm}^{n+1} + C_{2m}^n \left(\frac{K_{2lm}^{n+1} - K_{2lm}^n}{C_{1m}^{n+1} - C_{1m}^n} - \frac{K_{2lm}^{n+1} - K_{2lm}^n}{C_{2m}^{n+1} - C_{2m}^n} \right) \right] \right\},
\end{aligned}$$

$$A_{ii} = \phi^{n+1} \left[(\rho_i S_i)^{n+1} + (C_{ii} S_i)^n \left(\frac{\rho_i^{n+1} - \rho_i^n}{C_{ii}^{n+1} - C_{ii}^n} \right) \right],$$

$$B_{ii} = \phi^{n+1} (C_{ii} S_i)^n \left(\frac{\rho_i^{n+1} - \rho_i^n}{C_{ii}^{n+1} - C_{ii}^n} \right),$$

and

$$C_{ii} = \phi^{n+1} (C_{ii} S_i)^n \left(\frac{\rho_i^{n+1} - \rho_i^n}{C_{ii}^{n+1} - C_{ii}^n} \right) \text{ for } \begin{cases} 1=w \text{ and } 2=s \text{ when } i=o \\ 1=o \text{ and } 2=s \text{ when } i=w \\ 1=o \text{ and } 2=w \text{ when } i=s \end{cases}$$

Beginning with the terms Aq_i and Em_i in (C.4), expansions similar to those made for Ol_i can be performed to arrive at the expressions

$$\begin{aligned} Aq_i = & AA_{ai}\delta C_{im} + BB_{ai}\delta C_{1m} + \frac{V_b}{\Delta t}\phi^{n+1}(C_{ia}^n\rho_a^{n+1})\delta S_a \\ & + \frac{V_b}{\Delta t}(C_{ia}^n\rho_a S_a)^n\phi'\delta p_i \end{aligned} \quad (C.23)$$

and

$$\begin{aligned} Em_i = & AA_{mi}\delta C_{im} + BB_{mi}\delta C_{1m} - \frac{V_b}{\Delta t}\phi^{n+1}(C_{im}^n\rho_m^{n+1})\delta S_i \\ & - \frac{V_b}{\Delta t}\phi^{n+1}(C_{im}^n\rho_m^{n+1})\delta S_a + \frac{V_b}{\Delta t}(C_{im}^n\rho_m S_m)^n\phi'\delta p_i, \end{aligned} \quad (C.24)$$

where

$$\begin{aligned} AA_{ai} = & \frac{V_b}{\Delta t} \left\{ A_{ai} \left[K_{iam}^{n+1} + C_{im}^n \left(\frac{K_{iam}^{n+1} - K_{iam}^n}{C_{im}^{n+1} - C_{im}^n} - \frac{K_{iam}^{n+1} - K_{iam}^n}{C_{2m}^{n+1} - C_{2m}^n} \right) \right] \right. \\ & + B_{ai} C_{1m}^n \left(\frac{K_{1am}^{n+1} - K_{1am}^n}{C_{im}^{n+1} - C_{im}^n} - \frac{K_{1am}^{n+1} - K_{1am}^n}{C_{2m}^{n+1} - C_{2m}^n} \right) \\ & \left. + C_{ai} \left[-K_{2am}^{n+1} + C_{2m}^n \left(\frac{K_{2am}^{n+1} - K_{2am}^n}{C_{im}^{n+1} - C_{im}^n} - \frac{K_{2am}^{n+1} - K_{2am}^n}{C_{2m}^{n+1} - C_{2m}^n} \right) \right] \right\}, \\ BB_{ai} = & \frac{V_b}{\Delta t} \left\{ A_{ai} C_{im}^n \left(\frac{K_{iam}^{n+1} - K_{iam}^n}{C_{1m}^{n+1} - C_{1m}^n} - \frac{K_{iam}^{n+1} - K_{iam}^n}{C_{2m}^{n+1} - C_{2m}^n} \right) \right. \\ & + B_{ai} \left[K_{1am}^{n+1} + C_{1m}^n \left(\frac{K_{1am}^{n+1} - K_{1am}^n}{C_{1m}^{n+1} - C_{1m}^n} - \frac{K_{1am}^{n+1} - K_{1am}^n}{C_{2m}^{n+1} - C_{2m}^n} \right) \right] \\ & \left. + C_{ai} \left[-K_{2am}^{n+1} + C_{2m}^n \left(\frac{K_{2am}^{n+1} - K_{2am}^n}{C_{1m}^{n+1} - C_{1m}^n} - \frac{K_{2am}^{n+1} - K_{2am}^n}{C_{2m}^{n+1} - C_{2m}^n} \right) \right] \right\}, \end{aligned}$$

$$AA_{mi} = \frac{V_b}{\Delta t} \phi^{n+1} \left[(\rho_m S_m)^{n+1} + (C_{im} S_m)^n \left(\frac{\rho_m^{n+1} - \rho_m^n}{C_{im}^{n+1} - C_{im}^n} - \frac{\rho_m^{n+1} - \rho_m^n}{C_{2m}^{n+1} - C_{2m}^n} \right) \right],$$

$$BB_{mi} = \frac{V_b}{\Delta t} \phi^{n+1} (C_{im} S_m)^n \left(\frac{\rho_m^{n+1} - \rho_m^n}{C_{1m}^{n+1} - C_{1m}^n} - \frac{\rho_m^{n+1} - \rho_m^n}{C_{2m}^{n+1} - C_{2m}^n} \right),$$

and A_{ii} , B_{ii} , and C_{ii} are the same as in (C.22).

C.2 Expansion of Adsorption ($ADSP_s$) Term

Starting with (C.6),

$$ADSP_s = V_b \frac{\partial}{\partial t} \left[\frac{\rho_r A_d (1 - \phi) \rho_m C_{sm}}{1 + B_d \rho_m C_{sm}} \right] = \frac{V_b}{\Delta t} \frac{\rho_r A_d (1 - \phi_{init})}{(1 + B_d \rho_m C_{sm})^2} \delta(\rho_m C_{sm}),$$

the equation

$$\gamma_d^{n+1} = \frac{\rho_r A_d (1 - \phi_{init})}{(1 + B_d \rho_m^{n+1} C_{sm}^{n+1})^2},$$

can be substituted in. By then using the definition of $\delta \rho_m$ from (C.9), the following expression is produced.

$$\begin{aligned} ADSP_s &= \frac{V_b}{\Delta t} \gamma_d^{n+1} (\rho_m^{n+1} \delta C_{sm} + C_{sm}^n \delta \rho_m) \\ &= \frac{V_b}{\Delta t} \gamma_d^{n+1} \left[\rho_m^{n+1} \delta C_{sm} + C_{sm}^n \left(\frac{\rho_m^{n+1} - \rho_m^n}{C_{om}^{n+1} - C_{om}^n} \delta C_{om} + \frac{\rho_m^{n+1} - \rho_m^n}{C_{wm}^{n+1} - C_{wm}^n} \delta C_{wm} \right. \right. \\ &\quad \left. \left. + \frac{\rho_m^{n+1} - \rho_m^n}{C_{sm}^{n+1} - C_{sm}^n} \delta C_{sm} \right) \right] \\ &= \frac{V_b}{\Delta t} \gamma_d^{n+1} \left\{ \left[-\rho_m^{n+1} + C_{sm}^n \left(\frac{\rho_m^{n+1} - \rho_m^n}{C_{om}^{n+1} - C_{om}^n} - \frac{\rho_m^{n+1} - \rho_m^n}{C_{sm}^{n+1} - C_{sm}^n} \right) \right] \delta C_{om} \right. \\ &\quad \left. + \left[-\rho_m^{n+1} + C_{sm}^n \left(\frac{\rho_m^{n+1} - \rho_m^n}{C_{wm}^{n+1} - C_{wm}^n} - \frac{\rho_m^{n+1} - \rho_m^n}{C_{sm}^{n+1} - C_{sm}^n} \right) \right] \delta C_{wm} \right\}. \end{aligned} \quad (C.25)$$

C.3 Expansion of Capture ($CAPT_i$) Term

Two types of droplet capture models, so called an instantaneous capture and a time-dependent capture, were used to model the droplet capture mechanism.

C.3.1 Instantaneous Capture

Beginning with (C.5),

$$CAPT_i = V_b \frac{\partial}{\partial t} \left[\rho_i \left(\frac{A_c \rho_m C_{im}}{\rho_i + B_c \rho_m C_{im}} \right) \right] = \frac{V_b}{\Delta t} \frac{\rho_i^2 A_c}{(\rho_i + B_c \rho_m C_{im})^2} \delta(\rho_m C_{im}),$$

the equation

$$\gamma_c^{n+1} = \frac{\rho_i^2 A_c}{(\rho_i + B_c \rho_m^{n+1} C_{im}^{n+1})^2}$$

can be substituted in and the expression expanded to give

$$CAPT_i = \frac{V_b}{\Delta t} \gamma_c^{n+1} (\rho_m^{n+1} \delta C_{im} + C_{im}^n \delta \rho_m). \quad (C.26)$$

By then applying the definition of $\delta \rho_m$ from (C.9), the specific expressions for the oil and water components are

$$\begin{aligned} CAPT_o = \frac{V_b}{\Delta t} \gamma_c^{n+1} & \left\{ \left[\rho_m^{n+1} + C_{om}^n \left(\frac{\rho_m^{n+1} - \rho_m^n}{C_{om}^{n+1} - C_{om}^n} - \frac{\rho_m^{n+1} - \rho_m^n}{C_{sm}^{n+1} - C_{sm}^n} \right) \right] \delta C_{om} \right. \\ & \left. + C_{om}^n \left(\frac{\rho_m^{n+1} - \rho_m^n}{C_{wm}^{n+1} - C_{wm}^n} - \frac{\rho_m^{n+1} - \rho_m^n}{C_{sm}^{n+1} - C_{sm}^n} \right) \delta C_{wm} \right\}, \end{aligned} \quad (C.27)$$

and

$$\begin{aligned} CAPT_w = \frac{V_b}{\Delta t} \gamma_c^{n+1} & \left\{ C_{wm}^n \left(\frac{\rho_m^{n+1} - \rho_m^n}{C_{om}^{n+1} - C_{om}^n} - \frac{\rho_m^{n+1} - \rho_m^n}{C_{sm}^{n+1} - C_{sm}^n} \right) \delta C_{om} \right. \\ & \left. + \left[\rho_m^{n+1} + C_{wm}^n \left(\frac{\rho_m^{n+1} - \rho_m^n}{C_{wm}^{n+1} - C_{wm}^n} - \frac{\rho_m^{n+1} - \rho_m^n}{C_{sm}^{n+1} - C_{sm}^n} \right) \right] \delta C_{wm} \right\}. \end{aligned} \quad (C.28)$$

C.3.2 Time-dependent Capture

The capture term can be represented as follows.

$$CAPT_i = V_b \frac{\partial}{\partial t}(\rho_i \sigma) = \frac{V_b}{\Delta t} \delta F, \quad (C.29)$$

where

$$F = \rho_i \sigma = \frac{\lambda_{sl_1} \phi_i \rho_i \theta}{\alpha(\lambda_{sl_1} \theta + \lambda_{sl_2})} \left[1 - e^{\frac{-\alpha u}{\phi_i} (\lambda_{sl_1} \theta + \lambda_{sl_2}) t} \right]. \quad (C.30)$$

Substituting the following relationship into (C.30),

$$\theta = \frac{\rho_m}{\rho_i} x_{im},$$

and considering that droplets are captured only from the emulsion phase, it becomes

$$\rho_i \sigma = \frac{\lambda_{sl_1} \phi_i \rho_m x_{im}}{\alpha \left(\lambda_{sl_1} \frac{\rho_m}{\rho_i} x_{im} + \lambda_{sl_2} \right)} \left[1 - e^{\frac{-\alpha u_m}{\phi_i} \left(\lambda_{sl_1} \frac{\rho_m}{\rho_i} x_{im} + \lambda_{sl_2} \right) t} \right]. \quad (C.31)$$

For one dimension and neglecting the capillary and gravity effects,

$$u_m = \frac{\lambda_{rm}}{\lambda_{ri}} u, \quad (C.32)$$

For three dimensions, \bar{u}_m can be averaged as follows.

$$\begin{aligned}
\bar{u}_{m_{i,j,k}} &= (u_{mx}^2 + u_{my}^2 + u_{mz}^2)^{1/2} \\
&= \left[(u_{m_{i+1,j,k}} + u_{m_{i-1,j,k}})^2 + (u_{m_{i,j,k+1}} + u_{m_{i,j,k-1}})^2 + (u_{m_{i,j,k+1}} + u_{m_{i,j,k-1}})^2 \right]^{1/2} \\
&= \left\{ \left[-k_x \frac{k_{rm}}{\mu_m} \right]_{i+\frac{1}{2}} \left(\frac{\Phi_{m_{i+1}} - \Phi_{m_i}}{\Delta x} \right) - k_x \frac{k_{rm}}{\mu_m} \right]_{i-\frac{1}{2}} \left(\frac{\Phi_{m_i} - \Phi_{m_{i-1}}}{\Delta x} \right) \right]^2 \\
&\quad + \left[-k_y \frac{k_{rm}}{\mu_m} \right]_{j+\frac{1}{2}} \left(\frac{\Phi_{m_{j+1}} - \Phi_{m_j}}{\Delta y} \right) - k_y \frac{k_{rm}}{\mu_m} \right]_{j-\frac{1}{2}} \left(\frac{\Phi_{m_j} - \Phi_{m_{j-1}}}{\Delta y} \right) \right]^2 \\
&\quad + \left[-k_z \frac{k_{rm}}{\mu_m} \right]_{k+\frac{1}{2}} \left(\frac{\Phi_{m_{k+1}} - \Phi_{m_k}}{\Delta z} \right) - k_z \frac{k_{rm}}{\mu_m} \right]_{k-\frac{1}{2}} \left(\frac{\Phi_{m_k} - \Phi_{m_{k-1}}}{\Delta z} \right) \right]^2 \Bigg\}^{1/2}. \quad (C.33)
\end{aligned}$$

Recalling that $CAPT_i = \frac{V_b}{\Delta t} \delta F$, where F is a function of pressure, saturation, and composition, it is clear that

$$\begin{aligned}
CAPT_i &= \frac{V_b}{\Delta t} \left[\frac{F(p_{i,j,k}^{n+1}) - F(p_{i,j,k}^n)}{p_{i,j,k}^{n+1} - p_{i,j,k}^n} \delta p_i + \frac{F(S_{m_{i,j,k}}^{n+1}) - F(S_{m_{i,j,k}}^n)}{S_{m_{i,j,k}}^{n+1} - S_{m_{i,j,k}}^n} \delta S_m \right. \\
&\quad + \frac{F(x_{om_{i,j,k}}^{n+1}) - F(x_{om_{i,j,k}}^n)}{x_{om_{i,j,k}}^{n+1} - x_{om_{i,j,k}}^n} \delta x_{om} + \frac{F(x_{wm_{i,j,k}}^{n+1}) - F(x_{wm_{i,j,k}}^n)}{x_{wm_{i,j,k}}^{n+1} - x_{wm_{i,j,k}}^n} \delta x_{wm} \\
&\quad \left. + \frac{F(x_{sm_{i,j,k}}^{n+1}) - F(x_{sm_{i,j,k}}^n)}{x_{sm_{i,j,k}}^{n+1} - x_{sm_{i,j,k}}^n} \delta x_{sm} \right]. \quad (C.34)
\end{aligned}$$

Making the substitutions $\delta S_w = -\delta S_l - \delta S_a$ and $\delta x_{sm} = -\delta x_{om} - \delta x_{wm}$, the preceding equation becomes

$$\begin{aligned}
CAPT_i = & \frac{V_b}{\Delta t} \left\{ \frac{F(p_{i,j,k}^{n+1}) - F(p_{i,j,k}^n)}{p_{i,j,k}^{n+1} - p_{i,j,k}^n} \delta p_i \right. \\
& - \frac{F(S_{m_i,j,k}^{n+1}) - F(S_{m_i,j,k}^n)}{S_{m_i,j,k}^{n+1} - S_{m_i,j,k}^n} \delta S_i - \frac{F(S_{m_i,j,k}^{n+1}) - F(S_{m_i,j,k}^n)}{S_{m_i,j,k}^{n+1} - S_{m_i,j,k}^n} \delta S_a \\
& + \left[\frac{F(x_{om_i,j,k}^{n+1}) - F(x_{om_i,j,k}^n)}{x_{om_i,j,k}^{n+1} - x_{om_i,j,k}^n} - \frac{F(x_{sm_i,j,k}^{n+1}) - F(x_{sm_i,j,k}^n)}{x_{sm_i,j,k}^{n+1} - x_{sm_i,j,k}^n} \right] \delta x_{om} \\
& \left. + \left[\frac{F(x_{wm_i,j,k}^{n+1}) - F(x_{wm_i,j,k}^n)}{x_{wm_i,j,k}^{n+1} - x_{wm_i,j,k}^n} - \frac{F(x_{sm_i,j,k}^{n+1}) - F(x_{sm_i,j,k}^n)}{x_{sm_i,j,k}^{n+1} - x_{sm_i,j,k}^n} \right] \delta x_{wm} \right\}. \quad (C.35)
\end{aligned}$$

APPENDIX D
EXPANSION OF THE REMAINDER (R_i) TERMS

The expression for R_i , as derived in (B.12), is

$$\begin{aligned}
 R_i = & \nabla \cdot [(\rho_l C_{il} \eta_l)^n \nabla \Phi_l^n] \Delta + \nabla \cdot [(\rho_a C_{ia} \eta_a)^n \nabla \Phi_a^n] \Delta \\
 & + \nabla \cdot [(\rho_m C_{im} \eta_m)^n \nabla \Phi_m^n] \Delta + \nabla \cdot [A \phi D_{il} \nabla (\rho_l C_{il})]^n \Delta \\
 & + \nabla \cdot [A \phi D_{ia} \nabla (\rho_a C_{ia})]^n \Delta + \nabla \cdot [A \phi D_{im} \nabla (\rho_m C_{im})]^n \Delta \\
 & - \nabla \cdot [(\rho_l C_{il} \eta_l)^n \nabla \delta(\rho_l g D)] \Delta - \nabla \cdot [(\rho_a C_{ia} \eta_a)^n \nabla \delta(P_{cla} + \rho_a g D)] \Delta \\
 & - \nabla \cdot [(\rho_m C_{im} \eta_m)^n \nabla \delta(P_{clm} + \rho_m g D)] \Delta. \tag{D.1}
 \end{aligned}$$

Taking the finite forward difference, and making the substitutions,

$$T_{ijx} = \frac{\rho_j C_{ij} \eta_j}{\Delta x},$$

$$T_{ijy} = \frac{\rho_j C_{ij} \eta_j}{\Delta y},$$

$$T_{ijz} = \frac{\rho_j C_{ij} \eta_j}{\Delta z},$$

$$T_{dijx} = \frac{A_x \phi D_{ij}}{\Delta x},$$

$$T_{dijy} = \frac{A_y \phi D_{ij}}{\Delta y},$$

and

$$T_{dijz} = \frac{A_z \phi D_{ij}}{\Delta z},$$

the above equation is transformed into the following:

$$\begin{aligned}
R_{i,j,k} = & T_{ilx, i+\frac{1}{2}, j, k}^n \left(\Phi_{i+1, j, k}^n - \Phi_{i, j, k}^n \right) - T_{ilx, i-\frac{1}{2}, j, k}^n \left(\Phi_{i, j, k}^n - \Phi_{i-1, j, k}^n \right) \\
& + T_{ily, i, j+\frac{1}{2}, k}^n \left(\Phi_{i, j+1, k}^n - \Phi_{i, j, k}^n \right) - T_{ily, i, j-\frac{1}{2}, k}^n \left(\Phi_{i, j, k}^n - \Phi_{i, j-1, k}^n \right) \\
& + T_{ilz, i, j, k+\frac{1}{2}}^n \left(\Phi_{i, j, k+1}^n - \Phi_{i, j, k}^n \right) - T_{ilz, i, j, k-\frac{1}{2}}^n \left(\Phi_{i, j, k}^n - \Phi_{i, j, k-1}^n \right) \\
& + T_{iax, i+\frac{1}{2}, j, k}^n \left(\Phi_{a, i+1, j, k}^n - \Phi_{a, i, j, k}^n \right) - T_{iax, i-\frac{1}{2}, j, k}^n \left(\Phi_{a, i, j, k}^n - \Phi_{a, i-1, j, k}^n \right) \\
& + T_{iay, i, j+\frac{1}{2}, k}^n \left(\Phi_{a, i, j+1, k}^n - \Phi_{a, i, j, k}^n \right) - T_{iay, i, j-\frac{1}{2}, k}^n \left(\Phi_{a, i, j, k}^n - \Phi_{a, i, j-1, k}^n \right) \\
& + T_{iaz, i, j, k+\frac{1}{2}}^n \left(\Phi_{a, i, j, k+1}^n - \Phi_{a, i, j, k}^n \right) - T_{iaz, i, j, k-\frac{1}{2}}^n \left(\Phi_{a, i, j, k}^n - \Phi_{a, i, j, k-1}^n \right) \\
& + T_{imx, i+\frac{1}{2}, j, k}^n \left(\Phi_{m, i+1, j, k}^n - \Phi_{m, i, j, k}^n \right) - T_{imx, i-\frac{1}{2}, j, k}^n \left(\Phi_{m, i, j, k}^n - \Phi_{m, i-1, j, k}^n \right) \\
& + T_{imy, i, j+\frac{1}{2}, k}^n \left(\Phi_{m, i, j+1, k}^n - \Phi_{m, i, j, k}^n \right) - T_{imy, i, j-\frac{1}{2}, k}^n \left(\Phi_{m, i, j, k}^n - \Phi_{m, i, j-1, k}^n \right) \\
& + T_{imz, i, j, k+\frac{1}{2}}^n \left(\Phi_{m, i, j, k+1}^n - \Phi_{m, i, j, k}^n \right) - T_{imz, i, j, k-\frac{1}{2}}^n \left(\Phi_{m, i, j, k}^n - \Phi_{m, i, j, k-1}^n \right) \\
& + T_{dilx, i+\frac{1}{2}, j, k}^n \left[(\rho_l C_{il})_{i+1, j, k}^n - (\rho_l C_{il})_{i, j, k}^n \right] \\
& - T_{dilx, i-\frac{1}{2}, j, k}^n \left[(\rho_l C_{il})_{i, j, k}^n - (\rho_l C_{il})_{i-1, j, k}^n \right] \\
& + T_{dily, i, j+\frac{1}{2}, k}^n \left[(\rho_l C_{il})_{i, j+1, k}^n - (\rho_l C_{il})_{i, j, k}^n \right] \\
& - T_{dily, i, j-\frac{1}{2}, k}^n \left[(\rho_l C_{il})_{i, j, k}^n - (\rho_l C_{il})_{i, j-1, k}^n \right] \\
& + T_{dilz, i, j, k+\frac{1}{2}}^n \left[(\rho_l C_{il})_{i, j, k+1}^n - (\rho_l C_{il})_{i, j, k}^n \right] \\
& - T_{dilz, i, j, k-\frac{1}{2}}^n \left[(\rho_l C_{il})_{i, j, k}^n - (\rho_l C_{il})_{i, j, k-1}^n \right]
\end{aligned}$$

$$\begin{aligned}
& + T_{d\ iax\ i+\frac{1}{2},j,k}^n \left[(\rho_a C_{ia})_{i+1,j,k}^n - (\rho_a C_{ia})_{i,j,k}^n \right] \\
& - T_{d\ iax\ i-\frac{1}{2},j,k}^n \left[(\rho_a C_{ia})_{i,j,k}^n - (\rho_a C_{ia})_{i-1,j,k}^n \right] \\
& + T_{d\ iay\ i,j+\frac{1}{2},k}^n \left[(\rho_a C_{ia})_{i,j+1,k}^n - (\rho_a C_{ia})_{i,j,k}^n \right] \\
& - T_{d\ iay\ i,j-\frac{1}{2},k}^n \left[(\rho_a C_{ia})_{i,j,k}^n - (\rho_a C_{ia})_{i,j-1,k}^n \right] \\
& + T_{d\ iaz\ i,j,k+\frac{1}{2}}^n \left[(\rho_a C_{ia})_{i,j,k+1}^n - (\rho_a C_{ia})_{i,j,k}^n \right] \\
& - T_{d\ iaz\ i,j,k-\frac{1}{2}}^n \left[(\rho_a C_{ia})_{i,j,k}^n - (\rho_a C_{ia})_{i,j,k-1}^n \right] \\
& + T_{d\ imx\ i+\frac{1}{2},j,k}^n \left[(\rho_m C_{im})_{i+1,j,k}^n - (\rho_m C_{im})_{i,j,k}^n \right] \\
& - T_{d\ imx\ i-\frac{1}{2},j,k}^n \left[(\rho_m C_{im})_{i,j,k}^n - (\rho_m C_{im})_{i-1,j,k}^n \right] \\
& + T_{d\ imy\ i,j+\frac{1}{2},k}^n \left[(\rho_m C_{im})_{i,j+1,k}^n - (\rho_m C_{im})_{i,j,k}^n \right] \\
& - T_{d\ imy\ i,j-\frac{1}{2},k}^n \left[(\rho_m C_{im})_{i,j,k}^n - (\rho_m C_{im})_{i,j-1,k}^n \right] \\
& + T_{d\ imz\ i,j,k+\frac{1}{2}}^n \left[(\rho_m C_{im})_{i,j,k+1}^n - (\rho_m C_{im})_{i,j,k}^n \right] \\
& - T_{d\ imz\ i,j,k-\frac{1}{2}}^n \left[(\rho_m C_{im})_{i,j,k}^n - (\rho_m C_{im})_{i,j,k-1}^n \right] \\
& - T_{ilx\ i+\frac{1}{2},j,k}^n g \left\{ [(\rho_i^{n+1} - \rho_i^n)D]_{i+1,j,k} - [(\rho_i^{n+1} - \rho_i^n)D]_{i,j,k} \right\} \\
& + T_{ilx\ i-\frac{1}{2},j,k}^n g \left\{ [(\rho_i^{n+1} - \rho_i^n)D]_{i,j,k} - [(\rho_i^{n+1} - \rho_i^n)D]_{i-1,j,k} \right\} \\
& - T_{ily\ i,j+\frac{1}{2},k}^n g \left\{ [(\rho_i^{n+1} - \rho_i^n)D]_{i,j+1,k} - [(\rho_i^{n+1} - \rho_i^n)D]_{i,j,k} \right\} \\
& + T_{ily\ i,j-\frac{1}{2},k}^n g \left\{ [(\rho_i^{n+1} - \rho_i^n)D]_{i,j,k} - [(\rho_i^{n+1} - \rho_i^n)D]_{i,j-1,k} \right\} \\
& - T_{ilz\ i,j,k+\frac{1}{2}}^n g \left\{ [(\rho_i^{n+1} - \rho_i^n)D]_{i,j,k+1} - [(\rho_i^{n+1} - \rho_i^n)D]_{i,j,k} \right\} \\
& + T_{ilz\ i,j,k-\frac{1}{2}}^n g \left\{ [(\rho_i^{n+1} - \rho_i^n)D]_{i,j,k} - [(\rho_i^{n+1} - \rho_i^n)D]_{i,j,k-1} \right\}
\end{aligned}$$

$$\begin{aligned}
& - T_{iax}^n_{i+\frac{1}{2},j,k} g \left\{ [(\rho_a^{n+1} - \rho_a^n)D]_{i+1,j,k} - [(\rho_a^{n+1} - \rho_a^n)D]_{i,j,k} \right\} \\
& + T_{iax}^n_{i-\frac{1}{2},j,k} g \left\{ [(\rho_a^{n+1} - \rho_a^n)D]_{i,j,k} - [(\rho_a^{n+1} - \rho_a^n)D]_{i-1,j,k} \right\} \\
& - T_{iax}^n_{i,j+\frac{1}{2},k} g \left\{ [(\rho_a^{n+1} - \rho_a^n)D]_{i,j+1,k} - [(\rho_a^{n+1} - \rho_a^n)D]_{i,j,k} \right\} \\
& + T_{iax}^n_{i,j-\frac{1}{2},k} g \left\{ [(\rho_a^{n+1} - \rho_a^n)D]_{i,j,k} - [(\rho_a^{n+1} - \rho_a^n)D]_{i,j-1,k} \right\} \\
& - T_{iax}^n_{i,j,k+\frac{1}{2}} g \left\{ [(\rho_a^{n+1} - \rho_a^n)D]_{i,j,k+1} - [(\rho_a^{n+1} - \rho_a^n)D]_{i,j,k} \right\} \\
& + T_{iax}^n_{i,j,k-\frac{1}{2}} g \left\{ [(\rho_a^{n+1} - \rho_a^n)D]_{i,j,k} - [(\rho_a^{n+1} - \rho_a^n)D]_{i,j,k-1} \right\} \\
& - T_{imx}^n_{i+\frac{1}{2},j,k} g \left\{ [(\rho_m^{n+1} - \rho_m^n)D]_{i+1,j,k} - [(\rho_m^{n+1} - \rho_m^n)D]_{i,j,k} \right\} \\
& + T_{imx}^n_{i-\frac{1}{2},j,k} g \left\{ [(\rho_m^{n+1} - \rho_m^n)D]_{i,j,k} - [(\rho_m^{n+1} - \rho_m^n)D]_{i-1,j,k} \right\} \\
& - T_{imx}^n_{i,j+\frac{1}{2},k} g \left\{ [(\rho_m^{n+1} - \rho_m^n)D]_{i,j+1,k} - [(\rho_m^{n+1} - \rho_m^n)D]_{i,j,k} \right\} \\
& + T_{imx}^n_{i,j-\frac{1}{2},k} g \left\{ [(\rho_m^{n+1} - \rho_m^n)D]_{i,j,k} - [(\rho_m^{n+1} - \rho_m^n)D]_{i,j-1,k} \right\} \\
& - T_{imx}^n_{i,j,k+\frac{1}{2}} g \left\{ [(\rho_m^{n+1} - \rho_m^n)D]_{i,j,k+1} - [(\rho_m^{n+1} - \rho_m^n)D]_{i,j,k} \right\} \\
& + T_{imx}^n_{i,j,k-\frac{1}{2}} g \left\{ [(\rho_m^{n+1} - \rho_m^n)D]_{i,j,k} - [(\rho_m^{n+1} - \rho_m^n)D]_{i,j,k-1} \right\}
\end{aligned}$$

$$\begin{aligned}
& - T_{iax}^n \left[\left(P_{cla}^{n+1} - P_{cla}^n \right)_{i+1,j,k} - \left(P_{cla}^{n+1} - P_{cla}^n \right)_{i,j,k} \right] \\
& + T_{iax}^n \left[\left(P_{cla}^{n+1} - P_{cla}^n \right)_{i,j,k} - \left(P_{cla}^{n+1} - P_{cla}^n \right)_{i-1,j,k} \right] \\
& - T_{iax}^n \left[\left(P_{cla}^{n+1} - P_{cla}^n \right)_{i,j+1,k} - \left(P_{cla}^{n+1} - P_{cla}^n \right)_{i,j,k} \right] \\
& + T_{iax}^n \left[\left(P_{cla}^{n+1} - P_{cla}^n \right)_{i,j,k} - \left(P_{cla}^{n+1} - P_{cla}^n \right)_{i,j-1,k} \right] \\
& - T_{iax}^n \left[\left(P_{cla}^{n+1} - P_{cla}^n \right)_{i,j,k+1} - \left(P_{cla}^{n+1} - P_{cla}^n \right)_{i,j,k} \right] \\
& + T_{iax}^n \left[\left(P_{cla}^{n+1} - P_{cla}^n \right)_{i,j,k} - \left(P_{cla}^{n+1} - P_{cla}^n \right)_{i,j,k-1} \right] \\
& - T_{imx}^n \left[\left(P_{clm}^{n+1} - P_{clm}^n \right)_{i+1,j,k} - \left(P_{clm}^{n+1} - P_{clm}^n \right)_{i,j,k} \right] \\
& + T_{imx}^n \left[\left(P_{clm}^{n+1} - P_{clm}^n \right)_{i,j,k} - \left(P_{clm}^{n+1} - P_{clm}^n \right)_{i-1,j,k} \right] \\
& - T_{imx}^n \left[\left(P_{clm}^{n+1} - P_{clm}^n \right)_{i,j+1,k} - \left(P_{clm}^{n+1} - P_{clm}^n \right)_{i,j,k} \right] \\
& + T_{imx}^n \left[\left(P_{clm}^{n+1} - P_{clm}^n \right)_{i,j,k} - \left(P_{clm}^{n+1} - P_{clm}^n \right)_{i,j-1,k} \right] \\
& - T_{imx}^n \left[\left(P_{clm}^{n+1} - P_{clm}^n \right)_{i,j,k+1} - \left(P_{clm}^{n+1} - P_{clm}^n \right)_{i,j,k} \right] \\
& + T_{imx}^n \left[\left(P_{clm}^{n+1} - P_{clm}^n \right)_{i,j,k} - \left(P_{clm}^{n+1} - P_{clm}^n \right)_{i,j,k-1} \right]. \tag{D.2}
\end{aligned}$$

It should be noted that when $i=0$ or w , the dispersion terms in the above equation become zero. That is,

$$\begin{aligned}
& T_{d\,ilx\,i+\frac{1}{2},j,k}^n \left[(\rho_l C_{il})_{i+1,j,k}^n - (\rho_l C_{il})_{i,j,k}^n \right] \\
& - T_{d\,ilx\,i-\frac{1}{2},j,k}^n \left[(\rho_l C_{il})_{i,j,k}^n - (\rho_l C_{il})_{i-1,j,k}^n \right] \\
& + T_{d\,ily\,i,j+\frac{1}{2},k}^n \left[(\rho_l C_{il})_{i,j+1,k}^n - (\rho_l C_{il})_{i,j,k}^n \right] \\
& - T_{d\,ily\,i,j-\frac{1}{2},k}^n \left[(\rho_l C_{il})_{i,j,k}^n - (\rho_l C_{il})_{i,j-1,k}^n \right] \\
& + T_{d\,ilz\,i,j,k+\frac{1}{2}}^n \left[(\rho_l C_{il})_{i,j,k+1}^n - (\rho_l C_{il})_{i,j,k}^n \right] \\
& - T_{d\,ilz\,i,j,k-\frac{1}{2}}^n \left[(\rho_l C_{il})_{i,j,k}^n - (\rho_l C_{il})_{i,j,k-1}^n \right] \\
& + T_{d\,iax\,i+\frac{1}{2},j,k}^n \left[(\rho_a C_{ia})_{i+1,j,k}^n - (\rho_a C_{ia})_{i,j,k}^n \right] \\
& - T_{d\,iax\,i-\frac{1}{2},j,k}^n \left[(\rho_a C_{ia})_{i,j,k}^n - (\rho_a C_{ia})_{i-1,j,k}^n \right] \\
& + T_{d\,iax\,i,j+\frac{1}{2},k}^n \left[(\rho_a C_{ia})_{i,j+1,k}^n - (\rho_a C_{ia})_{i,j,k}^n \right] \\
& - T_{d\,iax\,i,j-\frac{1}{2},k}^n \left[(\rho_a C_{ia})_{i,j,k}^n - (\rho_a C_{ia})_{i,j-1,k}^n \right] \\
& + T_{d\,iaz\,i,j,k+\frac{1}{2}}^n \left[(\rho_a C_{ia})_{i,j,k+1}^n - (\rho_a C_{ia})_{i,j,k}^n \right] \\
& - T_{d\,iaz\,i,j,k-\frac{1}{2}}^n \left[(\rho_a C_{ia})_{i,j,k}^n - (\rho_a C_{ia})_{i,j,k-1}^n \right] \\
& + T_{d\,imx\,i+\frac{1}{2},j,k}^n \left[(\rho_m C_{im})_{i+1,j,k}^n - (\rho_m C_{im})_{i,j,k}^n \right] \\
& - T_{d\,imx\,i-\frac{1}{2},j,k}^n \left[(\rho_m C_{im})_{i,j,k}^n - (\rho_m C_{im})_{i-1,j,k}^n \right] \\
& + T_{d\,imy\,i,j+\frac{1}{2},k}^n \left[(\rho_m C_{im})_{i,j+1,k}^n - (\rho_m C_{im})_{i,j,k}^n \right] \\
& - T_{d\,imy\,i,j-\frac{1}{2},k}^n \left[(\rho_m C_{im})_{i,j,k}^n - (\rho_m C_{im})_{i,j-1,k}^n \right] \\
& + T_{d\,imz\,i,j,k+\frac{1}{2}}^n \left[(\rho_m C_{im})_{i,j,k+1}^n - (\rho_m C_{im})_{i,j,k}^n \right] \\
& - T_{d\,imz\,i,j,k-\frac{1}{2}}^n \left[(\rho_m C_{im})_{i,j,k}^n - (\rho_m C_{im})_{i,j,k-1}^n \right] = 0.
\end{aligned} \tag{D.3}$$

D.1 Transmissibility Terms

The transmissibility terms in the x direction that appear in Equation (D.2) are defined as

$$T_{ilx_{i+\frac{1}{2},j,k}}^n = w_{lx} T_{ilx_{i,j,k}}^n + (1-w_{lx}) T_{ilx_{i+1,j,k}}^n, \quad (D.4)$$

$$T_{iax_{i+\frac{1}{2},j,k}}^n = w_{ax} T_{iax_{i,j,k}}^n + (1-w_{ax}) T_{iax_{i+1,j,k}}^n, \quad (D.5)$$

and

$$T_{imx_{i+\frac{1}{2},j,k}}^n = w_{mx} T_{imx_{i,j,k}}^n + (1-w_{mx}) T_{imx_{i+1,j,k}}^n, \quad (D.6)$$

where

$$T_{ilx_{i,j,k}}^n = \frac{A_x k_x}{\Delta x} \bigg|_{i+\frac{1}{2},j,k} \left(\rho_l C_{il} \frac{k_{rl}}{\mu_l} \right)_{i,j,k}^n.$$

$$T_{ilx_{i+1,j,k}}^n = \frac{A_x k_x}{\Delta x} \bigg|_{i+\frac{1}{2},j,k} \left(\rho_l C_{il} \frac{k_{rl}}{\mu_l} \right)_{i+1,j,k}^n,$$

$$T_{iax_{i,j,k}}^n = \frac{A_x k_x}{\Delta x} \bigg|_{i+\frac{1}{2},j,k} \left(\rho_a C_{ia} \frac{k_{ra}}{\mu_a} \right)_{i,j,k}^n,$$

$$T_{iax_{i+1,j,k}}^n = \frac{A_x k_x}{\Delta x} \bigg|_{i+\frac{1}{2},j,k} \left(\rho_a C_{ia} \frac{k_{ra}}{\mu_a} \right)_{i+1,j,k}^n,$$

$$T_{imx_{i,j,k}}^n = \frac{A_x k_x}{\Delta x} \bigg|_{i+\frac{1}{2},j,k} \left(\rho_m C_{im} \frac{k_{rm}}{\mu_m} \right)_{i,j,k}^n,$$

and

$$T_{imx_{i+1,j,k}}^n = \frac{A_x}{\Delta x} \bigg|_{i+\frac{1}{2},j,k} \left(\rho_m C_{im} \frac{k_{rm}}{\mu_m} \right)_{i+1,j,k}^n ,$$

and where, by using the average harmonic mean,

$$\frac{A_x k_x}{\Delta x} \bigg|_{i+\frac{1}{2},j,k} = \frac{2A_{x_{i+1,j,k}} k_{x_{i+1,j,k}} A_{x_{i,j,k}} k_{x_{i,j,k}}}{A_{x_{i+1,j,k}} k_{x_{i+1,j,k}} \Delta x_{i,j,k} + A_{x_{i,j,k}} k_{x_{i,j,k}} \Delta x_{i+1,j,k}}$$

and

$$\frac{A_x}{\Delta x} \bigg|_{i+\frac{1}{2},j,k} = \frac{2A_{x_{i+1,j,k}} A_{x_{i,j,k}}}{A_{x_{i+1,j,k}} \Delta x_{i,j,k} + A_{x_{i,j,k}} \Delta x_{i+1,j,k}} .$$

Similarly, another set of equations can be developed such that

$$T_{ilx_{i-\frac{1}{2},j,k}}^n = w_{lx}^* T_{ilx_{i,j,k}}^n + (1-w_{lx}^*) T_{ilx_{i-1,j,k}}^n , \quad (D.7)$$

$$T_{iax_{i-\frac{1}{2},j,k}}^n = w_{ax}^* T_{iax_{i,j,k}}^n + (1-w_{ax}^*) T_{iax_{i-1,j,k}}^n , \quad (D.8)$$

and

$$T_{imx_{i-\frac{1}{2},j,k}}^n = w_{mx}^* T_{imx_{i,j,k}}^n + (1-w_{mx}^*) T_{imx_{i-1,j,k}}^n . \quad (D.9)$$

Equations (D.4) to (D.9) can also be developed in the y and z directions.

D.2 Dispersion Terms

The oleic phase dispersion term at $i+\frac{1}{2}$ in the x direction that appears in (D.2) is defined as

$$T_{dilx_{i+\frac{1}{2},j,k}}^n = \frac{A_x \phi D_{il}}{\Delta x} \bigg|_{i+\frac{1}{2},j,k}^n . \quad (D.10)$$

For a constant D_{il} , and using the average harmonic mean,

$$T_{dilx}^n = \frac{2A_{x_{i+1,j,k}}(\phi D_{il})_{i+1,j,k} A_{x_{i,j,k}}(\phi D_{il})_{i,j,k}}{A_{x_{i+1,j,k}}(\phi D_{il})_{i+1,j,k} \Delta x_{i,j,k} + A_{x_{i,j,k}}(\phi D_{il})_{i,j,k} \Delta x_{i+1,j,k}} \quad (D.11)$$

Similarly,

$$T_{dilx}^n = \frac{2A_{x_{i-1,j,k}}(\phi D_{il})_{i-1,j,k} A_{x_{i,j,k}}(\phi D_{il})_{i,j,k}}{A_{x_{i-1,j,k}}(\phi D_{il})_{i-1,j,k} \Delta x_{i,j,k} + A_{x_{i,j,k}}(\phi D_{il})_{i,j,k} \Delta x_{i-1,j,k}} \quad (D.12)$$

Expressions like those in (D.11) and (D.12) can also be found for the aqueous and emulsion phases.

APPENDIX E

MASS FRACTION CONSTRAINT EXPANSION

Beginning with the oleic phase mass fraction constraint,

$$\delta C_{oi} + \delta C_{wi} + \delta C_{si} = 0, \quad (E.1)$$

an expansion can be performed similar to that in equation (C.17) such that the expression is in terms of the emulsion phase as follows:

$$\begin{aligned} & \left[K_{olm}^{n+1} + C_{om}^n \left(\frac{K_{olm}^{n+1} - K_{olm}^n}{C_{om}^{n+1} - C_{om}^n} - \frac{K_{olm}^{n+1} - K_{olm}^n}{C_{sm}^{n+1} - C_{sm}^n} \right) \right] \delta C_{om} \\ & + C_{om}^n \left(\frac{K_{olm}^{n+1} - K_{olm}^n}{C_{wm}^{n+1} - C_{wm}^n} - \frac{K_{olm}^{n+1} - K_{olm}^n}{C_{sm}^{n+1} - C_{sm}^n} \right) \delta C_{wm} \\ & + C_{wm}^n \left(\frac{K_{wlm}^{n+1} - K_{wlm}^n}{C_{om}^{n+1} - C_{om}^n} - \frac{K_{wlm}^{n+1} - K_{wlm}^n}{C_{sm}^{n+1} - C_{sm}^n} \right) \delta C_{om} \\ & + \left[K_{wlm}^{n+1} + C_{wm}^n \left(\frac{K_{wlm}^{n+1} - K_{wlm}^n}{C_{wm}^{n+1} - C_{wm}^n} - \frac{K_{wlm}^{n+1} - K_{wlm}^n}{C_{sm}^{n+1} - C_{sm}^n} \right) \right] \delta C_{wm} \\ & + \left[-K_{slm}^{n+1} + C_{sm}^n \left(\frac{K_{slm}^{n+1} - K_{slm}^n}{C_{om}^{n+1} - C_{om}^n} - \frac{K_{slm}^{n+1} - K_{slm}^n}{C_{sm}^{n+1} - C_{sm}^n} \right) \right] \delta C_{om} \\ & + \left[-K_{slm}^{n+1} + C_{sm}^n \left(\frac{K_{slm}^{n+1} - K_{slm}^n}{C_{wm}^{n+1} - C_{wm}^n} - \frac{K_{slm}^{n+1} - K_{slm}^n}{C_{sm}^{n+1} - C_{sm}^n} \right) \right] \delta C_{wm} = 0.0. \quad (E.2) \end{aligned}$$

Similarly, the aqueous phase mass fraction constraint,

$$\delta C_{oa} + \delta C_{wa} + \delta C_{sa} = 0, \quad (E.3)$$

can be expanded into

$$\begin{aligned}
& \left[K_{oam}^{n+1} + C_{om}^n \left(\frac{K_{oam}^{n+1} - K_{oam}^n}{C_{om}^{n+1} - C_{om}^n} - \frac{K_{oam}^{n+1} - K_{oam}^n}{C_{sm}^{n+1} - C_{sm}^n} \right) \right] \delta C_{om} \\
& + C_{om}^n \left(\frac{K_{oam}^{n+1} - K_{oam}^n}{C_{wm}^{n+1} - C_{wm}^n} - \frac{K_{oam}^{n+1} - K_{oam}^n}{C_{sm}^{n+1} - C_{sm}^n} \right) \delta C_{wm} \\
& + C_{wm}^n \left(\frac{K_{wam}^{n+1} - K_{wam}^n}{C_{om}^{n+1} - C_{om}^n} - \frac{K_{wam}^{n+1} - K_{wam}^n}{C_{sm}^{n+1} - C_{sm}^n} \right) \delta C_{om} \\
& + \left[K_{wam}^{n+1} + C_{wm}^n \left(\frac{K_{wam}^{n+1} - K_{wam}^n}{C_{wm}^{n+1} - C_{wm}^n} - \frac{K_{wam}^{n+1} - K_{wam}^n}{C_{sm}^{n+1} - C_{sm}^n} \right) \right] \delta C_{wm} \\
& + \left[-K_{sam}^{n+1} + C_{sm}^n \left(\frac{K_{sam}^{n+1} - K_{sam}^n}{C_{om}^{n+1} - C_{om}^n} - \frac{K_{sam}^{n+1} - K_{sam}^n}{C_{sm}^{n+1} - C_{sm}^n} \right) \right] \delta C_{om} \\
& + \left[-K_{sam}^{n+1} + C_{sm}^n \left(\frac{K_{sam}^{n+1} - K_{sam}^n}{C_{wm}^{n+1} - C_{wm}^n} - \frac{K_{sam}^{n+1} - K_{sam}^n}{C_{sm}^{n+1} - C_{sm}^n} \right) \right] \delta C_{wm} = 0.0. \quad (E.4)
\end{aligned}$$

APPENDIX F

SYSTEM OF EQUATIONS AND SOLUTION

Starting with equation (B.11) and making the appropriate substitutions of the expanded terms, the mass balances for oil, water, and surfactant may be expressed as follows.

For the oil mass balance,

$$\begin{aligned} C_{11}\delta C_{om} + C_{12}\delta C_{wm} + C_{13}\delta S_l + C_{14}\delta S_a + C_{15}\delta p_l \\ = \Delta(T_o^n \Delta \delta p_l) + Q_o^{*n+1} + R_1. \end{aligned} \quad (F.1)$$

Similarly, the water mass balance is expressible as

$$\begin{aligned} C_{21}\delta C_{om} + C_{22}\delta C_{wm} + C_{23}\delta S_l + C_{24}\delta S_a + C_{25}\delta p_l \\ = \Delta(T_w^n \Delta \delta p_l) + Q_w^{*n+1} + R_2, \end{aligned} \quad (F.2)$$

and the surfactant mass balance as

$$\begin{aligned} C_{31}\delta C_{om} + C_{32}\delta C_{wm} + C_{33}\delta S_l + C_{34}\delta S_a + C_{35}\delta p_l \\ = \Delta(T_s^n \Delta \delta p_l) + Q_s^{*n+1} + R_3. \end{aligned} \quad (F.3)$$

The expanded expression for the oleic phase mass fraction constraint, given in equation (E.2), may also be expressed as

$$C_{41}\delta C_{om} + C_{42}\delta C_{wm} + C_{43}\delta S_l + C_{44}\delta S_a + C_{45}\delta p_l = 0. \quad (F.4)$$

The aqueous phase mass fraction constraint from (E.4) can also be written in the form,

$$C_{51}\delta C_{om} + C_{52}\delta C_{wm} + C_{53}\delta S_l + C_{54}\delta S_a + C_{55}\delta p_l = 0. \quad (F.5)$$

The values of the coefficients in equations (F.1) to (F.5) are given in Appendix G.

The system of five equations just shown can be represented in matrix form as $CX = IY + R$, or

$$\begin{bmatrix} C_{11} & C_{12} & C_{13} & C_{14} & C_{15} \\ C_{21} & C_{22} & C_{23} & C_{24} & C_{25} \\ C_{31} & C_{32} & C_{33} & C_{34} & C_{35} \\ C_{41} & C_{42} & C_{43} & C_{44} & C_{45} \\ C_{51} & C_{52} & C_{53} & C_{54} & C_{55} \end{bmatrix}_{i,j,k} \cdot \begin{bmatrix} \delta C_{om} \\ \delta C_{wm} \\ \delta S_l \\ \delta S_a \\ \delta p_l \end{bmatrix}_{i,j,k} = \begin{bmatrix} 1 & 0 & 0 & 0 & 0 \\ 0 & 1 & 0 & 0 & 0 \\ 0 & 0 & 1 & 0 & 0 \\ 0 & 0 & 0 & 1 & 0 \\ 0 & 0 & 0 & 0 & 1 \end{bmatrix} \cdot \begin{bmatrix} \Delta(T_o^n \Delta \delta p_l) + Q_o^{*n+1} \\ \Delta(T_w^n \Delta \delta p_l) + Q_w^{*n+1} \\ \Delta(T_s^n \Delta \delta p_l) + Q_s^{*n+1} \\ 0 \\ 0 \end{bmatrix}_{i,j,k} + \begin{bmatrix} R_1 \\ R_2 \\ R_3 \\ 0 \\ 0 \end{bmatrix}_{i,j,k} \quad (F.6)$$

After triangularization by Gaussian elimination, the above system is transformed into $C'X = \beta Y + R'$, or

$$\begin{bmatrix} C_{11} & C_{12} & C_{13} & C_{14} & C_{15} \\ 0 & C'_{22} & C'_{23} & C'_{24} & C'_{25} \\ 0 & 0 & C''_{33} & C''_{34} & C''_{35} \\ 0 & 0 & 0 & C'''_{44} & C'''_{45} \\ 0 & 0 & 0 & 0 & C''''_{55} \end{bmatrix}_{i,j,k} \cdot \begin{bmatrix} \delta C_{om} \\ \delta C_{wm} \\ \delta S_l \\ \delta S_a \\ \delta p_l \end{bmatrix}_{i,j,k} = \begin{bmatrix} 1 & 0 & 0 & 0 & 0 \\ \beta'_{21} & 1 & 0 & 0 & 0 \\ \beta''_{31} & \beta''_{32} & 1 & 0 & 0 \\ \beta'''_{41} & \beta'''_{42} & \beta'''_{43} & 1 & 0 \\ \beta''''_{51} & \beta''''_{52} & \beta''''_{53} & \beta''''_{54} & 1 \end{bmatrix} \cdot \begin{bmatrix} \Delta(T_o^n \Delta \delta p_l) + Q_o^{*n+1} \\ \Delta(T_w^n \Delta \delta p_l) + Q_w^{*n+1} \\ \Delta(T_s^n \Delta \delta p_l) + Q_s^{*n+1} \\ 0 \\ 0 \end{bmatrix}_{i,j,k} + \begin{bmatrix} R_1 \\ R'_2 \\ R''_3 \\ R'''_4 \\ R''''_5 \end{bmatrix}_{i,j,k} \quad (F.7)$$

The last equation in the above system,

$$C_{55,i,j,k}'''' \delta p_{i,j,k} = \beta_{51}'''' \Delta(T_o^n \Delta \delta p_i) + \beta_{52}'''' \Delta(T_w^n \Delta \delta p_i) + \beta_{53}'''' \Delta(T_s^n \Delta \delta p_i) \\ + \beta_{51}'''' Q_{o,i,j,k}^{*n+1} + \beta_{52}'''' Q_{w,i,j,k}^{*n+1} + \beta_{53}'''' Q_{s,i,j,k}^{*n+1} + R_{5,i,j,k}'''' , \quad (F.8)$$

is a parabolic difference equation in p . By expanding it using the forward difference method, it becomes

$$\begin{aligned} & \beta_{51}'''' \left[T_{o,i,j,k+\frac{1}{2}}^n (\delta p_{i+1,j,k} - \delta p_{i,j,k}) - T_{o,i-\frac{1}{2},j,k}^n (\delta p_{i,j,k} - \delta p_{i-1,j,k}) \right. \\ & \quad + T_{o,i,j+\frac{1}{2},k}^n (\delta p_{i,j+1,k} - \delta p_{i,j,k}) - T_{o,i,j-\frac{1}{2},k}^n (\delta p_{i,j,k} - \delta p_{i,j-1,k}) \\ & \quad \left. + T_{o,i,j,k+\frac{1}{2}}^n (\delta p_{i,j,k+1} - \delta p_{i,j,k}) - T_{o,i,j,k-\frac{1}{2}}^n (\delta p_{i,j,k} - \delta p_{i,j,k-1}) \right] \\ & + \beta_{52}'''' \left[T_{w,i,j,k+\frac{1}{2}}^n (\delta p_{i+1,j,k} - \delta p_{i,j,k}) - T_{w,i-\frac{1}{2},j,k}^n (\delta p_{i,j,k} - \delta p_{i-1,j,k}) \right. \\ & \quad + T_{w,i,j+\frac{1}{2},k}^n (\delta p_{i,j+1,k} - \delta p_{i,j,k}) - T_{w,i,j-\frac{1}{2},k}^n (\delta p_{i,j,k} - \delta p_{i,j-1,k}) \\ & \quad \left. + T_{w,i,j,k+\frac{1}{2}}^n (\delta p_{i,j,k+1} - \delta p_{i,j,k}) - T_{w,i,j,k-\frac{1}{2}}^n (\delta p_{i,j,k} - \delta p_{i,j,k-1}) \right] \\ & + \beta_{53}'''' \left[T_{s,i,j,k+\frac{1}{2}}^n (\delta p_{i+1,j,k} - \delta p_{i,j,k}) - T_{s,i-\frac{1}{2},j,k}^n (\delta p_{i,j,k} - \delta p_{i-1,j,k}) \right. \\ & \quad + T_{s,i,j+\frac{1}{2},k}^n (\delta p_{i,j+1,k} - \delta p_{i,j,k}) - T_{s,i,j-\frac{1}{2},k}^n (\delta p_{i,j,k} - \delta p_{i,j-1,k}) \\ & \quad \left. + T_{s,i,j,k+\frac{1}{2}}^n (\delta p_{i,j,k+1} - \delta p_{i,j,k}) - T_{s,i,j,k-\frac{1}{2}}^n (\delta p_{i,j,k} - \delta p_{i,j,k-1}) \right] \\ & - C_{55,i,j,k}'''' \delta p_{i,j,k} = -\beta_{51}'''' Q_{o,i,j,k}^{*n+1} - \beta_{52}'''' Q_{w,i,j,k}^{*n+1} - \beta_{53}'''' Q_{s,i,j,k}^{*n+1} - R_{5,i,j,k}'''' . \end{aligned} \quad (F.9)$$

This may be re-written as

$$\begin{aligned} & Z_{i,j,k} \delta p_{i,j,k-1} + B_{i,j,k} \delta p_{i,j-1,k} + D_{i,j,k} \delta p_{i-1,j,k} + E_{i,j,k} \delta p_{i,j,k} \\ & \quad + F_{i,j,k} \delta p_{i,j+1,k} + H_{i,j,k} \delta p_{i+1,j,k} + S_{i,j,k} \delta p_{i,j,k+1} \\ & = -\beta_{51}'''' Q_{o,i,j,k}^{*n+1} - \beta_{52}'''' Q_{w,i,j,k}^{*n+1} - \beta_{53}'''' Q_{s,i,j,k}^{*n+1} - R_{5,i,j,k}'''' , \end{aligned} \quad (F.10)$$

where

$$Z_{i,j,k} = \beta_{51}''''T_o^n_{i,j,k-\frac{1}{2}} + \beta_{52}''''T_w^n_{i,j,k-\frac{1}{2}} + \beta_{53}''''T_s^n_{i,j,k-\frac{1}{2}},$$

$$B_{i,j,k} = \beta_{51}''''T_o^n_{i,j-\frac{1}{2},k} + \beta_{52}''''T_w^n_{i,j-\frac{1}{2},k} + \beta_{53}''''T_s^n_{i,j-\frac{1}{2},k},$$

$$D_{i,j,k} = \beta_{51}''''T_o^n_{i,\frac{1}{2},k} + \beta_{52}''''T_w^n_{i,\frac{1}{2},k} + \beta_{53}''''T_s^n_{i,\frac{1}{2},k},$$

$$F_{i,j,k} = \beta_{51}''''T_o^n_{i+\frac{1}{2},j,k} + \beta_{52}''''T_w^n_{i+\frac{1}{2},j,k} + \beta_{53}''''T_s^n_{i+\frac{1}{2},j,k},$$

$$H_{i,j,k} = \beta_{51}''''T_o^n_{i,j,k+\frac{1}{2}} + \beta_{52}''''T_w^n_{i,j,k+\frac{1}{2}} + \beta_{53}''''T_s^n_{i,j,k+\frac{1}{2}},$$

$$S_{i,j,k} = \beta_{51}''''T_o^n_{i,j,k+\frac{1}{2}} + \beta_{52}''''T_w^n_{i,j,k+\frac{1}{2}} + \beta_{53}''''T_s^n_{i,j,k+\frac{1}{2}},$$

and

$$E_{i,j,k} = -(Z_{i,j,k} + B_{i,j,k} + D_{i,j,k} + F_{i,j,k} + H_{i,j,k} + S_{i,j,k} + C_{55,i,j,k}''').$$

The one-dimensional pressure distribution can now be solved by specifying a pressure for block $N_x,1,1$, the last block, and then solving for δp from block $1,1,1$ to block $(N_x-1),1,1$, the second last block.

The next step is to calculate the production rate at block $N_x,1,1$. This is accomplished, based on the core floods experiment carried out, by specifying a pressure of one atmosphere for the last block, and then calculating the flow rate required to satisfy this constant pressure. The resulting relationship is

$$\beta_{51}''''Q_{o_{N_x,1,1}}^{*n+1} + \beta_{52}''''Q_{w_{N_x,1,1}}^{*n+1} + \beta_{53}''''Q_{s_{N_x,1,1}}^{*n+1} = -D_{N_x,1,1}\delta p_{l_{N_x-1,1,1}} - R_{5_{N_x,1,1}}'''' . \quad (F.11)$$

Substituting for the variables $Q_{o_{N_x,1,1}}^{*n+1}$, $Q_{w_{N_x,1,1}}^{*n+1}$, and $Q_{s_{N_x,1,1}}^{*n+1}$, the following equation arises:

$$\begin{aligned} & \beta_{51}'''' \left(q_l \rho_l C_{ol} + q_l \frac{\lambda_a}{\lambda_l} \rho_a C_{oa} + q_l \frac{\lambda_m}{\lambda_l} \rho_m C_{om} \right)_{N_x,1,1}^{n+1} \\ & + \beta_{52}'''' \left(q_l \rho_l C_{wl} + q_l \frac{\lambda_a}{\lambda_l} \rho_a C_{wa} + q_l \frac{\lambda_m}{\lambda_l} \rho_m C_{wm} \right)_{N_x,1,1}^{n+1} \\ & + \beta_{53}'''' \left(q_l \rho_l C_{sl} + q_l \frac{\lambda_a}{\lambda_l} \rho_a C_{sa} + q_l \frac{\lambda_m}{\lambda_l} \rho_m C_{sm} \right)_{N_x,1,1}^{n+1} \\ & = -D_{N_x,1,1} \delta p_{l_{N_x-1,1,1}} - R_{5_{N_x,1,1}}'''' . \end{aligned} \quad (F.12)$$

Solving for $q_{l_{N_x,1,1}}^{n+1}$ it is found that

$$q_{l_{N_x,1,1}}^{n+1} = \frac{-D_{N_x,1,1} \delta p_{l_{N_x-1,1,1}} - R_{5_{N_x,1,1}}''''}{\beta_{51}''''(\rho_l C_{ol} + \dots)_{N_x,1,1}^{n+1} + \beta_{52}''''(\rho_l C_{wl} + \dots)_{N_x,1,1}^{n+1} + \beta_{53}''''(\rho_l C_{sl} + \dots)_{N_x,1,1}^{n+1}} . \quad (F.13)$$

The cases where $q_{a_{N_x,1,1}}^{n+1} = \left(\frac{\lambda_a}{\lambda_l} q_l \right)_{N_x,1,1}^{n+1}$ and $q_{m_{N_x,1,1}}^{n+1} = \left(\frac{\lambda_m}{\lambda_l} q_l \right)_{N_x,1,1}^{n+1}$ can now be solved. Following this, values can be found for the variables $Q_{o_{N_x,1,1}}^{*n+1}$, $Q_{w_{N_x,1,1}}^{*n+1}$, and $Q_{s_{N_x,1,1}}^{*n+1}$.

The next steps involve solutions for the saturation and composition. Starting with equation (F.7), the relation involving δS_a ,

$$\begin{aligned}
C_{44,i,j,k}''' \delta S_{a,i,j,k} + C_{45,i,j,k}''' \delta p_{i,i,j,k} &= \beta_{41}''' \Delta(T_o^n \Delta \delta p_i) + \beta_{42}''' \Delta(T_w^n \Delta \delta p_i) \\
+ \beta_{43}''' \Delta(T_s^n \Delta \delta p_i) + \beta_{41}''' Q_{o,i,j,k}^{*n+1} + \beta_{42}''' Q_{w,i,j,k}^{*n+1} + \beta_{43}''' Q_{s,i,j,k}^{*n+1} + R_4''',
\end{aligned}
\tag{F.14}$$

can be re-written as

$$\begin{aligned}
\delta S_{a,i,j,k} &= \frac{1}{C_{44,i,j,k}'''} \left(Z_{i,j,k} \delta p_{i,i,j,k-1} + B_{i,j,k} \delta p_{i,i,j-1,k} + D_{i,j,k} \delta p_{i,i-1,j,k} \right. \\
+ E_{i,j,k} \delta p_{i,i,j,k} + F_{i,j,k} \delta p_{i+1,i,j,k} + H_{i,j,k} \delta p_{i,i,j+1,k} + S_{i,j,k} \delta p_{i,i,j,k+1} + \beta_{41}''' Q_{o,i,j,k}^{*n+1} \\
+ \beta_{42}''' Q_{w,i,j,k}^{*n+1} + \beta_{43}''' Q_{s,i,j,k}^{*n+1} + R_4'''),
\end{aligned}
\tag{F.15}$$

in order to solve for δS_a , where

$$Z_{i,j,k} = \beta_{41}''' T_{o,i,j,k-\frac{1}{2}}^n + \beta_{42}''' T_{w,i,j,k-\frac{1}{2}}^n + \beta_{43}''' T_{s,i,j,k-\frac{1}{2}}^n,$$

$$B_{i,j,k} = \beta_{41}''' T_{o,i,j-\frac{1}{2},k}^n + \beta_{42}''' T_{w,i,j-\frac{1}{2},k}^n + \beta_{43}''' T_{s,i,j-\frac{1}{2},k}^n,$$

$$D_{i,j,k} = \beta_{41}''' T_{o,i-\frac{1}{2},j,k}^n + \beta_{42}''' T_{w,i-\frac{1}{2},j,k}^n + \beta_{43}''' T_{s,i-\frac{1}{2},j,k}^n,$$

$$F_{i,j,k} = \beta_{41}''' T_{o,i+\frac{1}{2},j,k}^n + \beta_{42}''' T_{w,i+\frac{1}{2},j,k}^n + \beta_{43}''' T_{s,i+\frac{1}{2},j,k}^n,$$

$$H_{i,j,k} = \beta_{41}''' T_{o,i,j+\frac{1}{2},k}^n + \beta_{42}''' T_{w,i,j+\frac{1}{2},k}^n + \beta_{43}''' T_{s,i,j+\frac{1}{2},k}^n,$$

$$S_{i,j,k} = \beta_{41}''' T_{o,i,j,k+\frac{1}{2}}^n + \beta_{42}''' T_{w,i,j,k+\frac{1}{2}}^n + \beta_{43}''' T_{s,i,j,k+\frac{1}{2}}^n,$$

and

$$E_{i,j,k} = -(Z_{i,j,k} + B_{i,j,k} + D_{i,j,k} + F_{i,j,k} + H_{i,j,k} + S_{i,j,k} + C_{45,i,j,k}''').$$

Starting again with (F.7), the expression containing δS_i ,

$$\begin{aligned}
C_{33,i,j,k}'' \delta S_{i,i,j,k} + C_{34,i,j,k}'' \delta S_{a,i,j,k} + C_{35,i,j,k}'' \delta p_{i,i,j,k} &= \beta_{31}'' \Delta(T_o^n \Delta \delta p_i) \\
+ \beta_{32}'' \Delta(T_w^n \Delta \delta p_i) + \beta_{33}'' \Delta(T_s^n \Delta \delta p_i) + \beta_{31}'' Q_{o,i,j,k}^{*n+1} + \beta_{32}'' Q_{w,i,j,k}^{*n+1} + \beta_{33}'' Q_{s,i,j,k}^{*n+1} \\
+ R_3'',
\end{aligned}
\tag{F.16}$$

can be solved by re-writing it as

$$\begin{aligned} \delta S_{i,j,k} = & \frac{1}{C''_{33,i,j,k}} \left(Z_{i,j,k} \delta p_{i,j,k-1} + B_{i,j,k} \delta p_{i,j-1,k} + D_{i,j,k} \delta p_{i-1,j,k} \right. \\ & + E_{i,j,k} \delta p_{i,j,k} + F_{i,j,k} \delta p_{i+1,j,k} + H_{i,j,k} \delta p_{i,j+1,k} + S_{i,j,k} \delta p_{i,j,k+1} + \beta''_{31} Q_{o,i,j,k}^{*n+1} \\ & \left. + \beta''_{32} Q_{w,i,j,k}^{*n+1} + \beta''_{33} Q_{s,i,j,k}^{*n+1} + R_3'' - C''_{34,i,j,k} \delta S_{o,i,j,k} \right), \quad (F.17) \end{aligned}$$

where

$$Z_{i,j,k} = \beta''_{31} T_o^n_{i,j,k-\frac{1}{2}} + \beta''_{32} T_w^n_{i,j,k-\frac{1}{2}} + \beta''_{33} T_s^n_{i,j,k-\frac{1}{2}},$$

$$B_{i,j,k} = \beta''_{31} T_o^n_{i,j-\frac{1}{2},k} + \beta''_{32} T_w^n_{i,j-\frac{1}{2},k} + \beta''_{33} T_s^n_{i,j-\frac{1}{2},k},$$

$$D_{i,j,k} = \beta''_{31} T_o^n_{i-\frac{1}{2},j,k} + \beta''_{32} T_w^n_{i-\frac{1}{2},j,k} + \beta''_{33} T_s^n_{i-\frac{1}{2},j,k},$$

$$F_{i,j,k} = \beta''_{31} T_o^n_{i+\frac{1}{2},j,k} + \beta''_{32} T_w^n_{i+\frac{1}{2},j,k} + \beta''_{33} T_s^n_{i+\frac{1}{2},j,k},$$

$$H_{i,j,k} = \beta''_{31} T_o^n_{i,j+\frac{1}{2},k} + \beta''_{32} T_w^n_{i,j+\frac{1}{2},k} + \beta''_{33} T_s^n_{i,j+\frac{1}{2},k},$$

$$S_{i,j,k} = \beta''_{31} T_o^n_{i,j,k+\frac{1}{2}} + \beta''_{32} T_w^n_{i,j,k+\frac{1}{2}} + \beta''_{33} T_s^n_{i,j,k+\frac{1}{2}},$$

and

$$E_{i,j,k} = - \left(Z_{i,j,k} + B_{i,j,k} + D_{i,j,k} + F_{i,j,k} + H_{i,j,k} + S_{i,j,k} + C''_{35,i,j,k} \right).$$

The expression containing δC_{wm} in (F.7),

$$\begin{aligned} & C'_{22,i,j,k} \delta C_{wm,i,j,k} + C'_{23,i,j,k} \delta S_{i,j,k} + C'_{24,i,j,k} \delta S_{o,i,j,k} + C'_{25,i,j,k} \delta p_{i,j,k} \\ & = \beta'_{21} \Delta(T_o^n \Delta \delta p_i) + \beta'_{22} \Delta(T_w^n \Delta \delta p_i) + \beta'_{21} Q_{o,i,j,k}^{*n+1} + \beta'_{22} Q_{w,i,j,k}^{*n+1} + R'_2, \end{aligned} \quad (F.18)$$

is re-written to solve for δC_{wm} as

$$\begin{aligned}
\delta C_{wm, i, j, k} = & \frac{1}{C'_{22, i, j, k}} \left(Z_{i, j, k} \delta p_{i, j, k-1} + B_{i, j, k} \delta p_{i, j-1, k} + D_{i, j, k} \delta p_{i-1, j, k} \right. \\
& + E_{i, j, k} \delta p_{i, j, k} + F_{i, j, k} \delta p_{i+1, j, k} + H_{i, j, k} \delta p_{i, j+1, k} + S_{i, j, k} \delta p_{i, j, k+1} \\
& \left. + \beta'_{21} Q_{o, i, j, k}^{*n+1} + \beta'_{22} Q_{w, i, j, k}^{*n+1} + R'_2 - C'_{23, i, j, k} \delta S_{i, j, k} - C'_{24, i, j, k} \delta S_{a, i, j, k} \right),
\end{aligned}
\tag{F.19}$$

where

$$Z_{i, j, k} = \beta'_{21} T_{o, i, j, k-\frac{1}{2}}^n + \beta'_{22} T_{w, i, j, k-\frac{1}{2}}^n,$$

$$B_{i, j, k} = \beta'_{21} T_{o, i, j-\frac{1}{2}, k}^n + \beta'_{22} T_{w, i, j-\frac{1}{2}, k}^n,$$

$$D_{i, j, k} = \beta'_{21} T_{o, i-\frac{1}{2}, j, k}^n + \beta'_{22} T_{w, i-\frac{1}{2}, j, k}^n,$$

$$F_{i, j, k} = \beta'_{21} T_{o, i+\frac{1}{2}, j, k}^n + \beta'_{22} T_{w, i+\frac{1}{2}, j, k}^n,$$

$$H_{i, j, k} = \beta'_{21} T_{o, i, j+\frac{1}{2}, k}^n + \beta'_{22} T_{w, i, j+\frac{1}{2}, k}^n,$$

$$S_{i, j, k} = \beta'_{21} T_{o, i, j, k+\frac{1}{2}}^n + \beta'_{22} T_{w, i, j, k+\frac{1}{2}}^n,$$

and

$$E_{i, j, k} = -\left(Z_{i, j, k} + B_{i, j, k} + D_{i, j, k} + F_{i, j, k} + H_{i, j, k} + S_{i, j, k} + C'_{25, i, j, k} \right).$$

Finally, the relationship involving δC_{om} in (F.7),

$$\begin{aligned}
C_{11, i, j, k} \delta C_{om, i, j, k} + C_{12, i, j, k} \delta C_{wm, i, j, k} + C_{13, i, j, k} \delta S_{i, j, k} + C_{14, i, j, k} \delta S_{a, i, j, k} \\
+ C_{15, i, j, k} \delta p_{i, j, k} = \beta_{11} \Delta(T_o^n \Delta \delta p_i) + \beta_{11} Q_{o, i, j, k}^{*n+1} + R_1,
\end{aligned}
\tag{F.20}$$

is solved by rearranging it as

$$\begin{aligned}
\delta C_{om_{i,j,k}} = & \frac{1}{C_{11_{i,j,k}}} \left(Z_{i,j,k} \delta p_{i,j,k-1} + B_{i,j,k} \delta p_{i,j-1,k} + D_{i,j,k} \delta p_{i-1,j,k} \right. \\
& + E_{i,j,k} \delta p_{i,j,k} + F_{i,j,k} \delta p_{i+1,j,k} + H_{i,j,k} \delta p_{i,j+1,k} + S_{i,j,k} \delta p_{i,j,k+1} + \beta_{11} Q_{o_{i,j,k}}^{*n+1} \\
& \left. + R_1 - C_{12_{i,j,k}} \delta C_{wm_{i,j,k}} - C_{13_{i,j,k}} \delta S_{i,j,k} - C_{14_{i,j,k}} \delta S_{o_{i,j,k}} \right), \quad (F.21)
\end{aligned}$$

where

$$Z_{i,j,k} = \beta_{11} T_{o_{i,j,k-\frac{1}{2}}}^n,$$

$$B_{i,j,k} = \beta_{11} T_{o_{i,j-\frac{1}{2},k}}^n,$$

$$D_{i,j,k} = \beta_{11} T_{o_{i-\frac{1}{2},j,k}}^n,$$

$$F_{i,j,k} = \beta_{11} T_{o_{i+\frac{1}{2},j,k}}^n,$$

$$H_{i,j,k} = \beta_{11} T_{o_{i,j+\frac{1}{2},k}}^n,$$

$$S_{i,j,k} = \beta_{11} T_{o_{i,j,k+\frac{1}{2}}}^n,$$

and

$$E_{i,j,k} = - \left(Z_{i,j,k} + B_{i,j,k} + D_{i,j,k} + F_{i,j,k} + H_{i,j,k} + S_{i,j,k} + C_{15_{i,j,k}} \right).$$

APPENDIX G **DEFINITION OF COEFFICIENTS**

For the oil mass balance, equation (F.1),

$$C_{11} = AA_{lo} + AA_{ao} + AA_{mo},$$

$$C_{12} = BB_{lo} + BB_{ao} + BB_{mo},$$

$$C_{13} = \frac{V_b}{\Delta t} \phi^{n+1} (C_{ol}^n \rho_l^{n+1} - C_{om}^n \rho_m^{n+1}),$$

$$C_{14} = \frac{V_b}{\Delta t} \phi^{n+1} (C_{oa}^n \rho_a^{n+1} - C_{om}^n \rho_m^{n+1}),$$

and

$$C_{15} = \frac{V_b}{\Delta t} [(C_{ol}^n \rho_l S_l)^n \phi' + (C_{oa}^n \rho_a S_a)^n \phi' + (C_{om}^n \rho_m S_m)^n \phi'].$$

The terms AA_{li} , AA_{ai} , AA_{mi} , BB_{li} , BB_{ai} , and BB_{mi} have already been defined in Appendix C in equations (C.22) and (C.24).

For an o/w emulsion, oil capture should be included in the accumulation coefficients shown above. Hence,

$$C_{11} = C_{11} + \frac{V_b}{\Delta t} \gamma_c^{n+1} \left[\rho_m^{n+1} + C_{om}^n \left(\frac{\rho_m^{n+1} - \rho_m^n}{C_{om}^{n+1} - C_{om}^n} - \frac{\rho_m^{n+1} - \rho_m^n}{C_{sm}^{n+1} - C_{sm}^n} \right) \right],$$

$$C_{12} = C_{12} + \frac{V_b}{\Delta t} \gamma_c^{n+1} \left[C_{om}^n \left(\frac{\rho_m^{n+1} - \rho_m^n}{C_{wm}^{n+1} - C_{wm}^n} - \frac{\rho_m^{n+1} - \rho_m^n}{C_{sm}^{n+1} - C_{sm}^n} \right) \right],$$

$$C_{13} = C_{13},$$

$$C_{14} = C_{14},$$

and

$$C_{15} = C_{15}.$$

For the water mass balance, equation (F.2),

$$C_{21} = BB_{hw} + BB_{aw} + BB_{mw},$$

$$C_{22} = AA_{hw} + AA_{aw} + AA_{mw},$$

$$C_{23} = \frac{V_b}{\Delta t} \phi^{n+1} (C_{wl}^n \rho_l^{n+1} - C_{wm}^n \rho_m^{n+1}),$$

$$C_{24} = \frac{V_b}{\Delta t} \phi^{n+1} (C_{wa}^n \rho_a^{n+1} - C_{wm}^n \rho_m^{n+1}),$$

and

$$C_{25} = \frac{V_b}{\Delta t} [(C_{wl}^n \rho_l S_l)^n \phi' + (C_{wa}^n \rho_a S_a)^n \phi' + (C_{wm}^n \rho_m S_m)^n \phi'].$$

For a w/o emulsion, water capture should be included in the accumulation coefficients above. Hence,

$$C_{21} = C_{21} + \frac{V_b}{\Delta t} \gamma_c^{n+1} \left[C_{wm}^n \left(\frac{\rho_m^{n+1} - \rho_m^n}{C_{om}^{n+1} - C_{om}^n} - \frac{\rho_m^{n+1} - \rho_m^n}{C_{sm}^{n+1} - C_{sm}^n} \right) \right],$$

$$C_{22} = C_{22} + \frac{V_b}{\Delta t} \gamma_c^{n+1} \left[\rho_m^{n+1} + C_{wm}^n \left(\frac{\rho_m^{n+1} - \rho_m^n}{C_{wm}^{n+1} - C_{wm}^n} - \frac{\rho_m^{n+1} - \rho_m^n}{C_{sm}^{n+1} - C_{sm}^n} \right) \right],$$

$$C_{23} = C_{23},$$

$$C_{24} = C_{24},$$

and

$$C_{25} = C_{25}.$$

To determine the coefficients in the surfactant mass balance, the equation,

$$\delta C_{sm} = -\delta C_{om} - \delta C_{wm},$$

is substituted into the general equations for Ol_i , Aq_i , and Em_i , namely (C.22), (C.23), and (C.24). Hence,

$$Ol_i = (-AA_{ls} + BB_{ls})\delta C_{om} - AA_{ls}\delta C_{wm} + \frac{V_b}{\Delta t}\phi^{n+1}(C_{sl}^n\rho_l^{n+1})\delta S_l \\ + \frac{V_b}{\Delta t}(C_{sl}\rho_l S_l)^n\phi'\delta p_l,$$

$$Aq_i = (-AA_{as} + BB_{as})\delta C_{om} - AA_{as}\delta C_{wm} + \frac{V_b}{\Delta t}\phi^{n+1}(C_{sa}^n\rho_a^{n+1})\delta S_a \\ + \frac{V_b}{\Delta t}(C_{sa}\rho_a S_a)^n\phi'\delta p_l,$$

and

$$Em_s = (-AA_{ms} + BB_{ms})\delta C_{om} - AA_{ms}\delta C_{wm} - \frac{V_b}{\Delta t}\phi^{n+1}(C_{sm}^n\rho_m^{n+1})\delta S_l \\ - \frac{V_b}{\Delta t}\phi^{n+1}(C_{sm}^n\rho_m^{n+1})\delta S_m + \frac{V_b}{\Delta t}(C_{sm}\rho_m S_m)^n\phi'\delta p_l.$$

Therefore, the accumulation coefficients in equation (F.3), including surfactant adsorption, are:

$$C_{31} = -AA_{ls} + BB_{ls} - AA_{as} + BB_{as} - AA_{ms} + BB_{ms} \\ + \frac{V_b}{\Delta t}\gamma_d^{n+1}\left[-\rho_m^{n+1} + C_{sm}^n\left(\frac{\rho_m^{n+1} - \rho_m^n}{C_{om}^{n+1} - C_{om}^n} - \frac{\rho_m^{n+1} - \rho_m^n}{C_{sm}^{n+1} - C_{sm}^n}\right)\right],$$

$$C_{32} = -AA_{ls} - AA_{as} - AA_{ms} \\ + \frac{V_b}{\Delta t}\gamma_d^{n+1}\left[-\rho_m^{n+1} + C_{sm}^n\left(\frac{\rho_m^{n+1} - \rho_m^n}{C_{wm}^{n+1} - C_{wm}^n} - \frac{\rho_m^{n+1} - \rho_m^n}{C_{sm}^{n+1} - C_{sm}^n}\right)\right],$$

$$C_{33} = \frac{V_b}{\Delta t}\phi^{n+1}(C_{sl}^n\rho_l^{n+1} - C_{sm}^n\rho_m^{n+1}),$$

$$C_{34} = \frac{V_b}{\Delta t}\phi^{n+1}(C_{sa}^n\rho_a^{n+1} - C_{sm}^n\rho_m^{n+1}),$$

and

$$C_{35} = \frac{V_b}{\Delta t}[(C_{sl}\rho_l S_l)^n\phi' + (C_{sa}\rho_a S_a)^n\phi' + (C_{sm}\rho_m S_m)^n\phi'].$$

For the oleic phase mass fraction constraint, equation (F.4),

$$\begin{aligned}
 C_{41} &= K_{olm}^{n+1} - K_{slm}^{n+1} + C_{om}^n \left(\frac{K_{olm}^{n+1} - K_{olm}^n}{C_{om}^{n+1} - C_{om}^n} - \frac{K_{olm}^{n+1} - K_{olm}^n}{C_{sm}^{n+1} - C_{sm}^n} \right) \\
 &+ C_{wm}^n \left(\frac{K_{wlm}^{n+1} - K_{wlm}^n}{C_{om}^{n+1} - C_{om}^n} - \frac{K_{wlm}^{n+1} - K_{wlm}^n}{C_{sm}^{n+1} - C_{sm}^n} \right) \\
 &+ C_{sm}^n \left(\frac{K_{slm}^{n+1} - K_{slm}^n}{C_{om}^{n+1} - C_{om}^n} - \frac{K_{slm}^{n+1} - K_{slm}^n}{C_{sm}^{n+1} - C_{sm}^n} \right), \\
 C_{42} &= K_{wlm}^{n+1} - K_{slm}^{n+1} + C_{om}^n \left(\frac{K_{olm}^{n+1} - K_{olm}^n}{C_{wm}^{n+1} - C_{wm}^n} - \frac{K_{olm}^{n+1} - K_{olm}^n}{C_{sm}^{n+1} - C_{sm}^n} \right) \\
 &+ C_{wm}^n \left(\frac{K_{wlm}^{n+1} - K_{wlm}^n}{C_{wm}^{n+1} - C_{wm}^n} - \frac{K_{wlm}^{n+1} - K_{wlm}^n}{C_{sm}^{n+1} - C_{sm}^n} \right) \\
 &+ C_{sm}^n \left(\frac{K_{slm}^{n+1} - K_{slm}^n}{C_{wm}^{n+1} - C_{wm}^n} - \frac{K_{slm}^{n+1} - K_{slm}^n}{C_{sm}^{n+1} - C_{sm}^n} \right),
 \end{aligned}$$

$$C_{43} = 0.0,$$

$$C_{44} = 0.0,$$

and

$$C_{45} = 0.0.$$

For the aqueous phase mass fraction constraint, equation (F.5),

$$\begin{aligned}
C_{51} = & K_{oam}^{n+1} - K_{sam}^{n+1} + C_{om}^n \left(\frac{K_{oam}^{n+1} - K_{oam}^n}{C_{om}^{n+1} - C_{om}^n} - \frac{K_{oam}^{n+1} - K_{oam}^n}{C_{sm}^{n+1} - C_{sm}^n} \right) \\
& + C_{wm}^n \left(\frac{K_{wam}^{n+1} - K_{wam}^n}{C_{om}^{n+1} - C_{om}^n} - \frac{K_{wam}^{n+1} - K_{wam}^n}{C_{sm}^{n+1} - C_{sm}^n} \right) \\
& + C_{sm}^n \left(\frac{K_{sam}^{n+1} - K_{sam}^n}{C_{om}^{n+1} - C_{om}^n} - \frac{K_{sam}^{n+1} - K_{sam}^n}{C_{sm}^{n+1} - C_{sm}^n} \right),
\end{aligned}$$

$$\begin{aligned}
C_{52} = & K_{wam}^{n+1} - K_{sam}^{n+1} + C_{om}^n \left(\frac{K_{oam}^{n+1} - K_{oam}^n}{C_{wm}^{n+1} - C_{wm}^n} - \frac{K_{oam}^{n+1} - K_{oam}^n}{C_{sm}^{n+1} - C_{sm}^n} \right) \\
& + C_{wm}^n \left(\frac{K_{wam}^{n+1} - K_{wam}^n}{C_{wm}^{n+1} - C_{wm}^n} - \frac{K_{wam}^{n+1} - K_{wam}^n}{C_{sm}^{n+1} - C_{sm}^n} \right) \\
& + C_{sm}^n \left(\frac{K_{sam}^{n+1} - K_{sam}^n}{C_{wm}^{n+1} - C_{wm}^n} - \frac{K_{sam}^{n+1} - K_{sam}^n}{C_{sm}^{n+1} - C_{sm}^n} \right),
\end{aligned}$$

$$C_{53} = 0.0,$$

$$C_{54} = 0.0,$$

and

$$C_{55} = 0.0.$$

APPENDIX H **ESTIMATION OF RHEOLOGICAL PARAMETERS**

The following analytical correlation suggested by Abou-Kassem and Farooq Ali⁴⁴ is used to estimate the parameter .

$$\alpha\sqrt{F} = \left[\frac{2^{2n+1}KL_c \left(\frac{3n+1}{4n}\right)^n}{\left(\frac{k}{\phi}\right)^{\frac{n+1}{2}} \phi^n I} \right]^{\frac{1}{n+1}} .$$

where,

$$K = \frac{K'}{\varepsilon^n},$$

and

$$\varepsilon = \left(\frac{\zeta^{2/n}}{n\zeta^2} \right) \left(\frac{\zeta^2 - 1}{\zeta^{2/n} - 1} \right).$$

Viscometric Data of Emulsion (Batch 1) and Flow Data in
Ottawa Sand Pack for Core Flood #2

Consistency, K'	0.6311 Pa.s ⁿ
$\zeta = \frac{r_{outer}}{r_{inner}}$	1.0976
Flow Behaviour Index, n	0.6948
Intercept of Log-Log Plot of Δp Versus Q, I	$1.785 \times 10^9 \text{ Pa/(m}^3/\text{s)}^n$

Core Data for Core Flood #5

Core Length, L_c	0.61 m
Absolute Permeability, k	$7.95 \times 10^{-12} \text{ m}^2$
Porosity, ϕ	0.3851

Hence,

$$\alpha\sqrt{F} = 1.8.$$

APPENDIX I **DERIVATION OF SINGLE PHASE NON-NEWTONIAN RHEOLOGICAL** **MODEL**

Alvarado and Marsden found a similarity between the rheological behaviour of macroemulsion flow through a porous medium and a capillary tube viscometer for the range of shear rates between 10^3 and 10^4 sec^{-1} . Therefore, the correlation for modeling non-Newtonian behaviour can be derived by coupling the capillary model (or the hydraulic radius model) for porous media with a specific rheological model, the Ostwald-de Waele model, which is also widely known as the power-law model.

I.1 Flow of Fluids Through Capillary Tubes

For steady state laminar flow of an incompressible non-Newtonian fluid in a long uniform capillary tube having a radius r_c and length L_c , Alvarado² and Alvarado and Marsden³⁹ reported the equation

$$\tau_{rc} = K \dot{\gamma}_{rc}^n, \quad (\text{I.1})$$

where

$$\tau_{rc} = \frac{r_c \Delta p_c}{2L_c}, \quad (\text{I.2})$$

and

$$\dot{\gamma}_{rc} = \left(-\frac{dV_c}{dr} \right)_{r=r_c} = \left(\frac{3n+1}{4n} \right) \left(\frac{4\bar{V}_c}{r_c} \right). \quad (I.3)$$

A logarithmic plot of τ_{rc} versus $\dot{\gamma}_{rc}$ yields a straight line with a slope equal to n and an intercept (at $\dot{\gamma}_{rc} = 1$) equal to K . It is noted in Ref. 61 that the values of K and n are independent of the type of viscometer used to measure the rheological properties of a particular fluid. That is, K and n represent the true physical indices. However, the shear rates obtained from a Brookfield viscometer are the apparent shear rates. Therefore, shear stress and shear rate data obtained from a Brookfield viscometer⁶³ give the intercept value K' , not K . By using the following relationship, the value of K can be obtained.

$$K = \frac{K'}{\varepsilon^n}, \quad (I.4)$$

where

$$\varepsilon = \left(\frac{\zeta^{2/n}}{n\zeta^2} \right) \left(\frac{\zeta^2 - 1}{\zeta^{2/n} - 1} \right), \quad (I.5)$$

and

$$\zeta = \frac{r_{outer}}{r_{inner}}. \quad (I.6)$$

I.2. Flow of Fluids Through Porous Media

The following assumptions, which are mentioned in Abou-Kassem and Farouq Ali⁴⁴, are incorporated in the flow model of non-Newtonian fluids through porous media.

1. The emulsion is homogeneous on a macroscopic scale.
2. The porous medium is represented by a bundle of uniform capillary tubes.
3. The average pore velocity is related to flow velocity through the Dupuit-Forchheimer equation; i.e., $\bar{V}_c = \frac{\bar{V}_c}{\phi}$.
4. The rheological behaviour of the flowing fluid is of purely viscous nature; i.e., it is independent of the geometry of the porous medium.
5. The rheological behaviour of the flowing fluid is represented by the power law which is valid in the range of shear rates over which its parameters were estimated.
6. Laminar flow conditions prevail and viscoelastic effects are absent.
7. Pore blockage and adsorption on rock surfaces as a result of fluid flow through a porous medium may cause permanent permeability damage regardless of the subsequent flowing fluid. This damage reaches a limiting value depending on the quality of the emulsion. Plugging affects permeability significantly. The effect on porosity is negligible. Therefore, the new permeability of the porous medium k_f , which is called the flowing or flushed permeability, can be expressed as $k_f = Fk$.

For steady state laminar flow of a Newtonian fluid in a bundle of uniform tubes, the Hagen-Poiseuille law may be written as

$$\bar{V}_c = \frac{1}{2} \left(\frac{r_c}{2} \right)^2 \frac{\Delta p_c}{\mu L_c}. \quad (\text{I.7})$$

By using the Dupuit-Forchheimer equation,

$$\bar{V}_c = \frac{\bar{V}_c}{\phi}, \quad (\text{I.8})$$

Darcy's law can be written as

$$\bar{V}_c = \frac{k_f}{\phi} \frac{\Delta P_c}{\mu L_c}. \quad (\text{I.9})$$

Combining Eqns. (I.7) and (I.9) gives

$$\frac{1}{2} \left(\frac{r_c}{2} \right)^2 = \frac{k_f}{\phi},$$

or

$$r_c = 2\sqrt{2} \sqrt{\frac{k_f}{\phi}}. \quad (\text{I.10})$$

As the porous medium usually deviates from the model of a bundle of capillary tubes, the equivalent capillary radius may be expressed as

$$r_c = \alpha \sqrt{\frac{k_f}{\phi}} = \alpha \sqrt{\frac{Fk}{\phi}} = \left(\frac{\alpha^2 Fk}{\phi} \right)^{1/2}, \quad (\text{I.11})$$

where

α = a parameter that depends on pore size distribution and tortuosity of the porous medium

F = ratio of flushed permeability (k_f) to initial permeability (k), fraction

It should be noted that both k and k_f can be obtained by flowing a Newtonian fluid through the porous medium before and after an emulsion flood, respectively, and applying Darcy's law.

The average shear stress in a porous medium, $\bar{\tau}_c$, can be defined by using Eqn. (I.11) to define an r_c for Eqn. (I.2) as follows.

$$\bar{\tau}_c = \frac{\left(\frac{\alpha^2 F k}{\phi} \right)^{1/2} \Delta P_c}{2L_c} \quad (I.12)$$

Similarly, the average shear rate in a porous medium, $\bar{\gamma}_c$, can be defined by substituting Eqns. (I.8) and (I.11) into Eqn. (I.3), giving,

$$\bar{\gamma}_c = \left(\frac{3n+1}{4n} \right) \left(\frac{4\bar{V}_c}{\phi \left(\frac{\alpha^2 F k}{\phi} \right)^{1/2}} \right) \quad (I.13)$$

Based on the assumption that the rheological behaviour of the flowing fluid is independent of the geometry of porous media,

the rheological equation describing the flow of emulsions through porous media can be expressed in a similar way to that of the capillary tube Eqn. (I.1) for a given range of shear rates. This expression is

$$\bar{\tau}_c = K\bar{\gamma}_c^n. \quad (\text{I.14})$$

Substituting Eqns. (I.12) and (I.13) into Eqn. (I.14) and solving for \bar{V}_c gives

$$\bar{V}_c^n = \frac{\left(\frac{\alpha^2 F k}{\phi}\right)^{\frac{n+1}{2}} \phi^n}{2^{(2n+1)} \left(\frac{3n+1}{4n}\right)^n K L_c} \Delta P_c, \quad (\text{I.15})$$

Equation (I.15) can be expressed in the form of the modified Darcy's law for non-Newtonian fluid flow through porous media,

$$\bar{V}_c = \frac{k}{\mu_{\text{eff}}} \frac{\Delta P_c}{L_c}, \quad (\text{I.16})$$

where

$$\mu_{\text{eff}} = 2 \left(\frac{2}{\alpha\sqrt{F}}\right)^{\frac{n+1}{n}} \left(\frac{3n+1}{4n}\right)^{\frac{1}{n}} K^{\frac{1}{n}} \left(\frac{k}{\phi}\right)^{\frac{n-1}{2n}} \left(\frac{\Delta P_c}{L_c}\right)^{\frac{n-1}{n}}, \quad (\text{I.17})$$

or

$$\mu_{\text{eff}} = 2^n \left(\frac{2}{\alpha\sqrt{F}}\right)^{n+1} \left(\frac{3n+1}{4n}\right)^n K \left(\frac{k}{\phi}\right)^{\frac{n-1}{2}} \left(\frac{\bar{V}_c}{k}\right)^{n-1}. \quad (\text{I.18})$$

For Newtonian fluids $n = 1$, $K = \mu$, $F = 1$, and $\alpha = 2\sqrt{2}$.

Alvarado and Marsden³⁹ suggested a trial-and-error graphical procedure to calculate a parameter that forces the core rheogram and the viscometry (capillary) rheogram to coincide. Their parameter β as mentioned by Abou-Kassem and Farouq Ali⁴⁴ is related to the parameter $\alpha\sqrt{F}$ by

$$\beta = (\alpha^2 F)^{\frac{n+1}{2}}. \quad (\text{I.19})$$

Abou-Kassem and Farouq Ali⁴⁴ estimated analytically the parameter $\alpha\sqrt{F}$ which brought the porous medium rheogram and the viscometry rheogram into agreement. Core data (ΔP_c and \bar{V}_c) plotted on a log-log scale yields a straight line with a slope n and an intercept I . Mathematically,

$$\Delta P_c = I \bar{V}_c^n,$$

or

$$\log \Delta P_c = \log I + n \log \bar{V}_c. \quad (\text{I.20})$$

Solving for the best estimate of I by the least squares method gives

$$I = \left[\frac{\Delta P_{c_1} \times \Delta P_{c_2} \times \dots}{(\bar{V}_{c_1} \times \bar{V}_{c_2} \times \dots)^n} \right]^{1/N}, \quad (\text{I.21})$$

where N equals the number of core flow data points.

As explained previously, the rheological equation for a porous medium can be written as

$$\bar{\tau}_c = K \bar{\gamma}_c^n, \quad (\text{I.22})$$

where the intercept K is expressed by an equation similar to Eqn. (I.21),

$$K = \left[\frac{\bar{\tau}_{c_1} \times \bar{\tau}_{c_2} \times \dots}{(\bar{\gamma}_{c_1} \times \bar{\gamma}_{c_2} \times \dots)^n} \right]^{1/N}. \quad (\text{I.23})$$

Substituting for $\bar{\tau}_c$ and $\bar{\gamma}_c$ from Eqns. (I.12) and (I.13), respectively, Eqn. (I.23) becomes

$$K = \frac{\left(\frac{\alpha^2 F k}{\phi} \right)^{\frac{n+1}{2}} \phi^n}{2^{(2n+1)} L_c} \left(\frac{4n}{3n+1} \right)^n \left[\frac{\Delta P_{c_1} \times \Delta P_{c_2} \times \dots}{(\bar{V}_{c_1} \times \bar{V}_{c_2} \times \dots)^n} \right]^{1/N}, \quad (\text{I.24})$$

or

$$K = \frac{\left(\frac{\alpha^2 F k}{\phi} \right)^{\frac{n+1}{2}} \phi^n I}{2^{(2n+1)} L_c} \left(\frac{4n}{3n+1} \right)^n. \quad (\text{I.25})$$

Then, solving for $\alpha\sqrt{F}$,

$$\alpha\sqrt{F} = \left[\frac{2^{(2n+1)} K L_c \left(\frac{3n+1}{4n} \right)^n}{\left(\frac{k}{\phi} \right)^{\frac{n+1}{2}} \phi^n I} \right]^{\frac{1}{n+1}}. \quad (\text{I.26})$$

Recalling Eqn. (I.18),

$$\mu_{eff} = 2^n \left(\frac{2}{\alpha \sqrt{F}} \right)^{n+1} \left(\frac{3n+1}{4n} \right)^n K \left(\frac{k}{\phi} \right)^{\frac{n-1}{2}} \left(\frac{\bar{V}_c}{k} \right)^{n-1}.$$

The apparent viscosity of the emulsion can also be written in the form,

$$\mu_m = \frac{8K}{(\alpha \sqrt{F})^2} \left(\frac{3n+1}{4n} \right) (\bar{\gamma})^{n-1}, \quad (\text{I.27})$$

where

$$\bar{\gamma} = \left(\frac{3n+1}{4n} \right) \frac{4\bar{V}}{\phi \left(\frac{\alpha^2 F k}{\phi} \right)^{1/2}}. \quad (\text{I.28})$$